A STUDY OF REACTIVELY EVAPORATED AMORPHOUS HYDROGENATED SILICON & AMORPHOUS HYDROGENATED GERMANIUM AND RECRYSTALLIZATION OF AMORPHOUS GERMANIUM BY RAPID THERMAL ANNEALING METHOD

---

by

Lui Ka Man, Raymond
（雷家文）

A Thesis Submitted in Partial Fulfillment
of the Requirements for the Degree of
Master of Philosophy in Physics

The Chinese University of Hong Kong
June 1993

UL

Acknowledgements

I would like to express my sincere gratitude to Dr. K.P. Chik, my supervisor, for his excellent guidance, constant encouragement and great patience in reading as well as providing invaluable suggestions on correcting this thesis. I would like to thank Dr. H.K. Wong, also my supervisor, for his helpful suggestions from time to time and enlightening discussions, especially on the subject of X-ray diffraction. Both my supervisors not only widen my horizon in physics, but also enrich my life as a graduate student.

I would like to thank Mr. P.C. Wong, for his excellent technical assistance and his willingness in sharing my ups and downs in the past two years. Also, his positive attitude towards physics is really impressive and I learn much from him. Thank also goes to Mr. W.H. Wong. I benefit much from his clear and clean explanations on many physics problems.

Last but not the least, I would like to thank my parents for their selfless support, caring, understanding and love.

Abstract

Amorphous Si:H films were prepared by high vacuum evaporation onto a glass substrate (Corning 7059) immersed in a beam of atomic hydrogen. The film properties depend on the substrate temperature T_s. Films of highest quality were prepared around $T_s = 250^{\circ}C$ with the following properties, namely, $\sigma_{dark} \cong 8 \times 10^{-11}\ \Omega^{-1}\ cm^{-1}$, σ_{photo} under AM1 illumination $\cong 2 \times 10^{-6}\ \Omega^{-1}cm^{-1}$, ESR spin density $\cong 10^{17}\ cm^{-3}$ with a g value of 2.0043, optical band gap = 1.7 eV and a valence band tail width ≅ 65 meV. The films are thermally stable up to 510°C without Staebler-Wronski effect. IR measurements indicate that hydrogen in the films exists predominantly in monohydride form. Films prepared at T_s above and below 250°C have inferior qualities.

The annealing behaviour of electron beam evaporated a-Ge and reactively evaporated a-Ge:H has been examined by rapid thermal annealing method. For a-Ge deposited at different T_s, it was observed that under isothermal annealing condition, samples prepared at lower T_s took longer time to complete crystallization and tended to have higher final resistivities after complete cryatallization. Besides, a preferred crystal orientation in <111> was observed from the recrystallization of a-Ge on glass substrates, which was independent of substrate temperatures and annealing methods. Moreover, the crystallization process can be described by a nucleation and growth process and a negative incubation time was obtained. This led one to suspect that nuclei for recrystallization were already present and were formed during the film growth process. The isochronal annealing behaviour of a-Ge:H was also studied. A plot of resistivity against annealing temperature showed three peaks, which can be attributed to the evolution of hydrides of different forms with subsequent lattice reconstruction.

Table of Contents

Chapter 1

Introduction

A) General Description On Amorphous Materials:

In order to define amorphous materials, we have first to define a perfect crystal. Here we adopt the following definition:

A perfect crystal is that in which the atoms (or groups of atoms) are arranged in a pattern that repeats periodically in three dimensions to an infinite extent (Elliott, 1984).

With the above definition as a comparison standard, we define amorphous materials as those which **do not possess the long range order (periodicity) characteristic of a crystal.** Experimentally, we define whether a material is amorphous by observing if its X-ray diffraction pattern consists of diffuse haloes rather than sharp rings or spotty characteristics of polycrystalline or single crystal.

Although the long range order in an amorphous material is destroyed, the short range order is preserved. So, we retain the concept of density of states, N(E), and the quantity N(E) dE denotes the number of single particle states per unit volume between E and E + dE. However, due to the effect of disorder, new features evolve in the density of states. In an amorphous material, variation in bond lengths and distortion in bond angles induce random fluctuations in atomic potentials, which can be treated as a perturbation on the original crystalline density of states (Anderson, 1958). This results in the smearing out of sharp features on the original density of states and tailing of states from the band edges. What is more is that all these tail states are localized. The concept of localized states is nothing new as they are simply traps. Yet what is new for amorphous materials is that a continuous density of states, N(E), can exist in a range of energies which are all traps, and for which the mobility at zero temperature vanishes, even though the wavefunctions of

neighbouring states overlap (Mott, 1979). Since a state cannot be both localized and extended, there should be a critical energy E_c separating the localized and the non-localized states and this energy is termed as the mobility edge (Figure 1-1). The physical significance of mobility edge is that it separates the extended states from the localized states which at zero temperature, there is no diffusion of electron from one state to another state, even though the wavefunctions of the corresponding states are overlapping. Although there is a general agreement on the existence of mobility edge, the change of $\mu(E)$ across the edge is still not certain. Several possibilities are given in Figure 1-2.

B) Reasons For Studying Reactively Evaporated a-Si:H And a-Ge:H:

Intrinsic amorphous silicon and amorphous germanium are of little practical interest, because of the presence of vast amount of structural defects, leading to poor semiconducting properties and nearly absence of photo-response. Besides, attempts in doping both materials have been unsuccessful, due to the Fermi level being strongly pinned by the gap states within the mobility gap.

In 1975, Spear and Le Comber were able to prepare doped amorphous silicon thin films by glow discharge method, which made use of a simultaneous decomposition of silane gas and relevent doping gases. This success has been attributed to the incorporation of hydrogen into the silicon lattice, which passivated most of the gap states. However, the use of silane is highly undesirable due to its highly explosive nature. Besides, the properties of the glow-discharge a-Si film depend sensitively on the plasma conditions during film formation. Hence, it is difficult to control all the deposition parameters since a complex reaction is taking place during silane decomposition (K.P. Chik et al, 1983). Furthermore, the presence of Staebler-Wronski effect (an optical induced degradation of the sample) among the glow-discharge sample urges one to seek other methods which can produce high quality a-Si:H. Many attempts have been made, to name a few, the method of posthydrogenation (P.K. John et al., 1981),

biased activated reactive evaporation (J.C. Anderson et al., 1986)and ionized-cluster beam deposition (I. Yamada et al.,1982). The common feature of the above methods is that only a direct reaction between hydrogen and silicon atoms is involved,and complex chemical decomposition process can be bypassed, hence resulting in a simpler growth kinetic.

C) A Brief Review On Deposition Techniques:

C.1 The Glow-Discharge Method:

This technique relies on the production of plasma in a low-pressure gas and subsequent chemical decomposition of the gas itself, leading to deposition of a solid film on a substrate placed inside the plasma. The plasma is produced by a r.f. field in one of two ways, either by inductive coupling or by capacitive coupling (Figure 1-3 - 1-5). Typical reactant gas pressures lie between 0.05 and 1.0 torr. A 14 MHz r.f. source operating at a power of 1 - 10 W can produce deposition rates of 1 - 10 Å/s.

The GD process, depending on plasma formation, has a number of significant parameters that can affect the characteristics of a particular film. Some of them are listed below:

1) Gas pressure and temperature;
2) Ratio of reactant gas flow to carrier gas flow;
3) Gas flow rate and consequent dwell time in the chamber;
4) Chamber geometry and substrate position relative to the plasma;
5) R.F. power applied to plasma;
6) Method of coupling of r.f. power to plasma;
7) Substrate bias;
8) Substrate temperature.

C.2) The Posthydrogenation Method: (P.K. John et al., 1981)

A-Si films are first prepared by electron beam evaporation in a conventional high vaccum system and are subsequently hydrogenated in a theta-pinch plasma machine (Figure 1-6). Hydrogen admitted from one end is dissociated by a standard θ-pinch plasma set-up. The ions are accelerated and focused on the sample by a pair of grid electrodes. Films after hydrogenation showed no observable structural damage. They were thermally stable up to the temperature of recrystallization and were free of S-W effect.

C.3 Ionized-Cluster Beam Deposition: (I. Yamada et al., 1982)

(Figure 1-7). The crucible containing the silicon source is heated up to 2000°C by means of electron bombardment, and silicon vapour of a few torr is ejected from a tiny nozzle into the vaccum where hydrogen is introduced in a range of 10^{-5} - 10^{-4} torr. During expansion, clusters of loosely coupled Si atoms are formed and are partially ionized. The ionized clusters are then accelerated towards the substrate by an acceleration electrode. The parameters governing the films' qualities are:

1) the crucible temperature;
2) the acceleration voltage;
3) the ionization current;
4) the substrate temperature;
5) the hydrogen pressure.

Amorphous Si:H produced by this method can have a maximum photosensitvity of 10^{4}.

C.4) The Biased Activated Reactive Evaporation:
(J.C. Anderson et al., 1986)

In the BARE process, silicon evaporates from the

electron-beam melted ingot (Figure 1-8) into the vaccum where a hydrogen pressure of 10^{-2} torr is maintained. A circular probe electrode situated above the molten silicon pool is maintained at 300 V and collects thermionic electrons from the pool, causing ionization of the hydrogen and the creation of plasma above silicon. The substrate, 10 cm above the probe, is mounted on a r.f. sputtering electrode and the r.f. power is 300 - 400 W. In this method, gaseous doping can be achieved by the admission of doping gas through extra gas pipes.

D) The Present Study:

In the present study, a new method which also belongs to the family of reactive evaporation has been developed. Only a commercially available atom gun has to be added into a conventional electron beam evaporation system, and device-grade a-Si:H highly comparable to that of glow-discharge sample yet without the Staebler-Wronski effect can be produced. The details of the configuration of the system and operation procedure will be fully described in Chapter 2. The best samples were obtained by optimizing the substrate temperature during film growth and their properties were studied by a series of experiments. The results will be presented in Chapter 4 - 6. Detailed analysis of experimental results led to a simple band model and a growth mechanism for our a-Si:H. The same deposition method has been applied to produce a-Ge:H and preliminary results concerning its behaviour under annealing, together with a detailed study on the recrystallization of a-Ge by the method of rapid thermal processing, will be presented in Chapter 7. Finally, Chapter 8 marks the end of this thesis by drawing proper conclusions and giving some suggestions on further development and improvement of the present system.

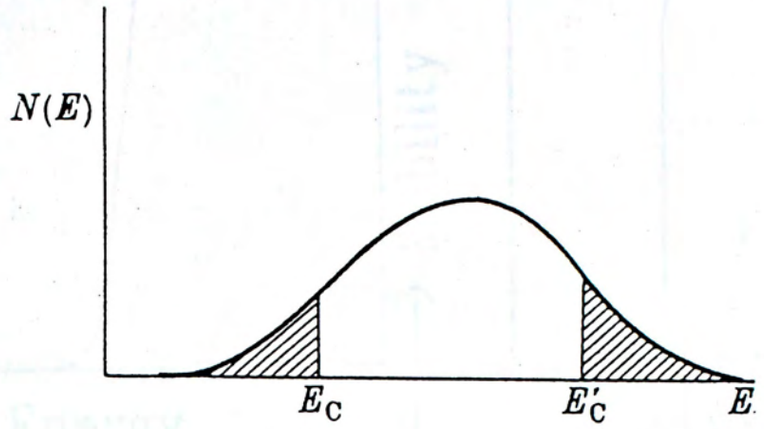

Figure 1-1. Density of states in the Anderson model when states are non-localized in the centre of the band. Localized states are shown shaded. Ec, Ec' separate the ranges of energy where states are localized and non-localized and are termed as the mobility edges. (Mott and Davis, 1979).

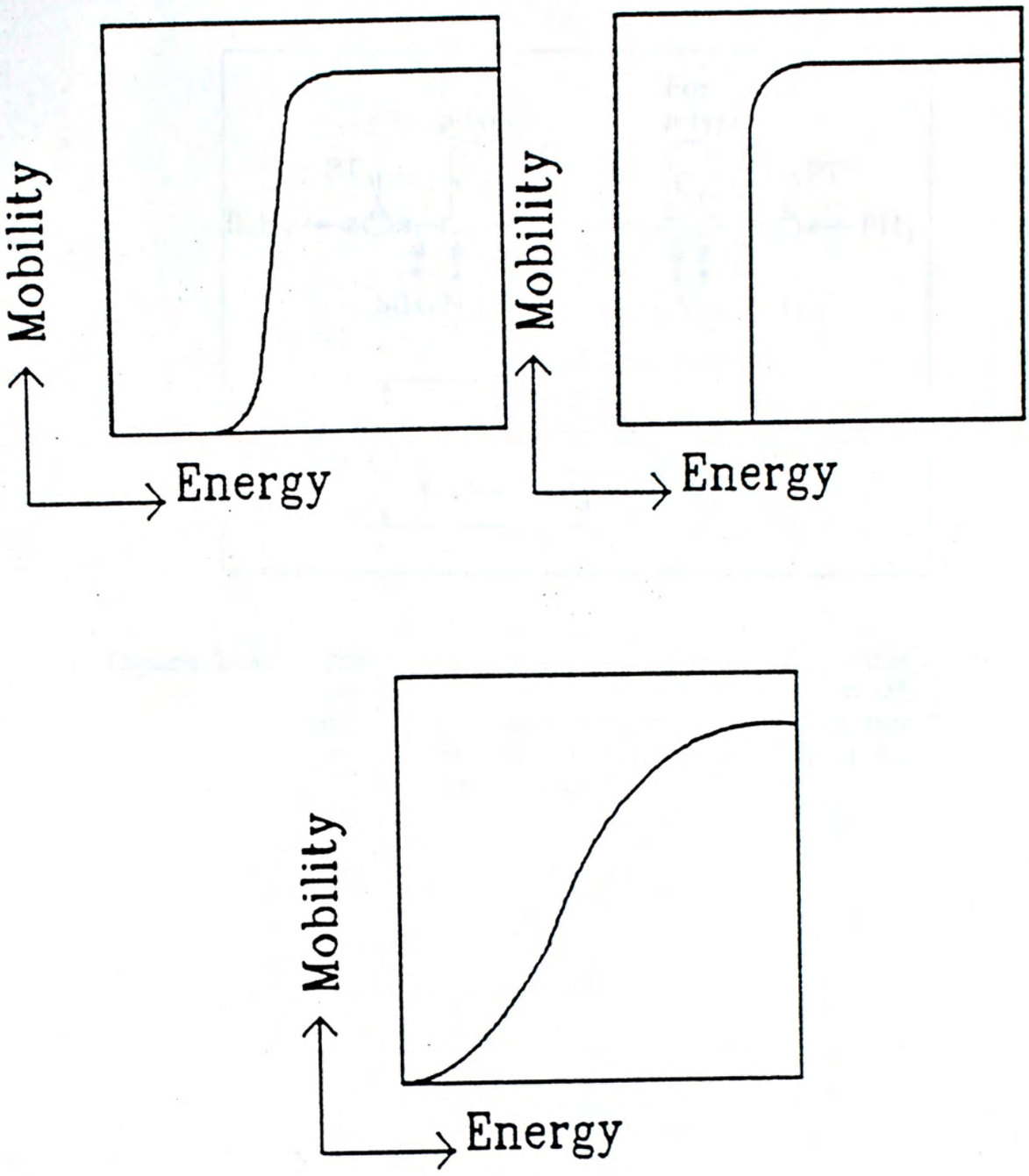

Figure 1-2. Three models for the increase of mobility as the energy increases from the band tail to the dense portion of the band.

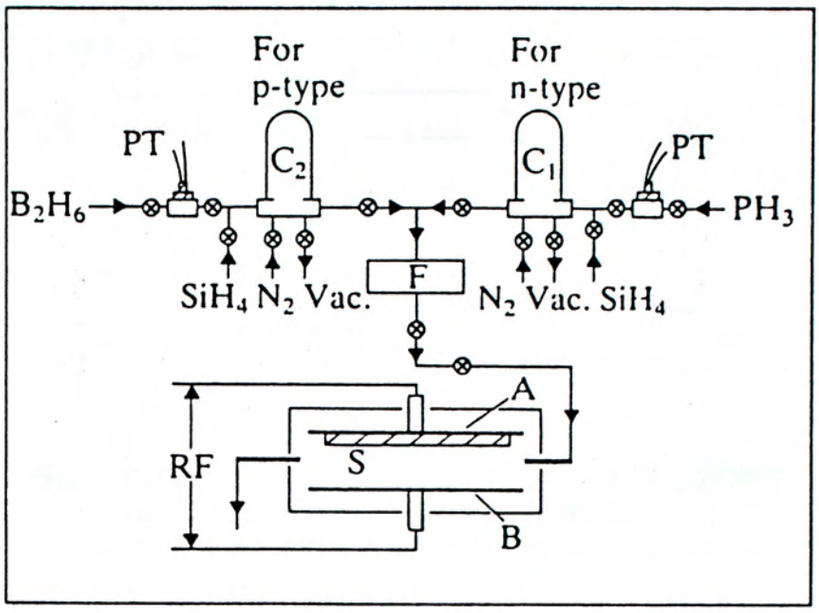

Figure 1-3. Schematic illustration of the preparative unit for the deposition of n- and p- type a-Si:H (C1, C2, glass cylinders; PT, pressure transducer; F, flow meter; S, substrate).

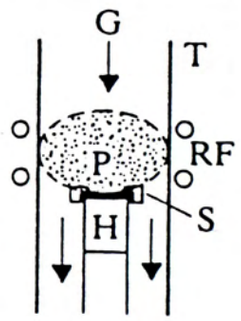

Figure 1-4. Inductive coupling of the r.f. power to the plasma.

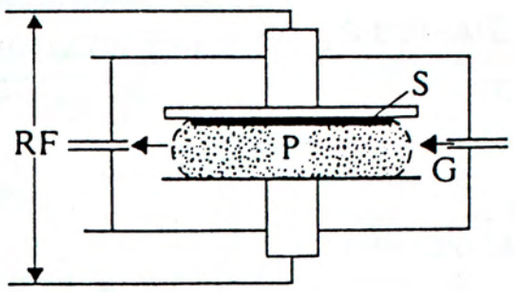

Figure 1-5. Capacitive coupling of the r.f. power to the plasma (Spear 1977).

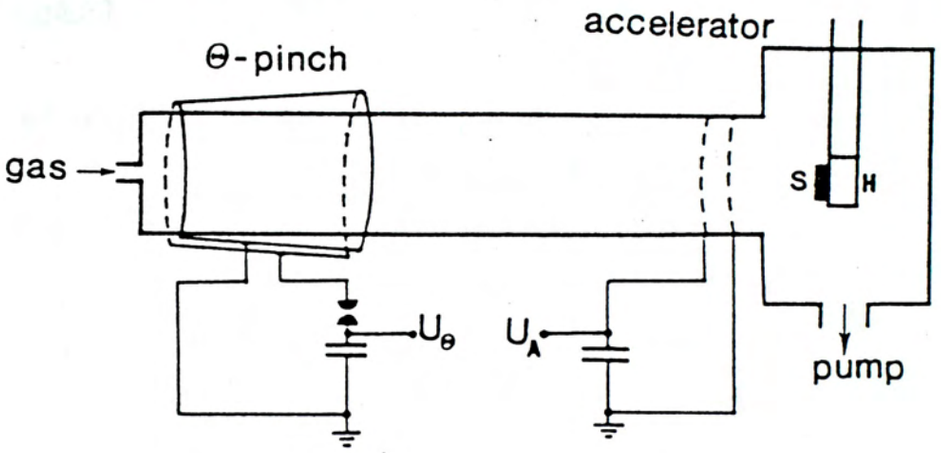

Figure 1-6. Theta-pinch plasma apparatus used in the hydrogenation of evaporated a-Si films. S, the sample and H, the sample holder (P.K. John et al., 1981).

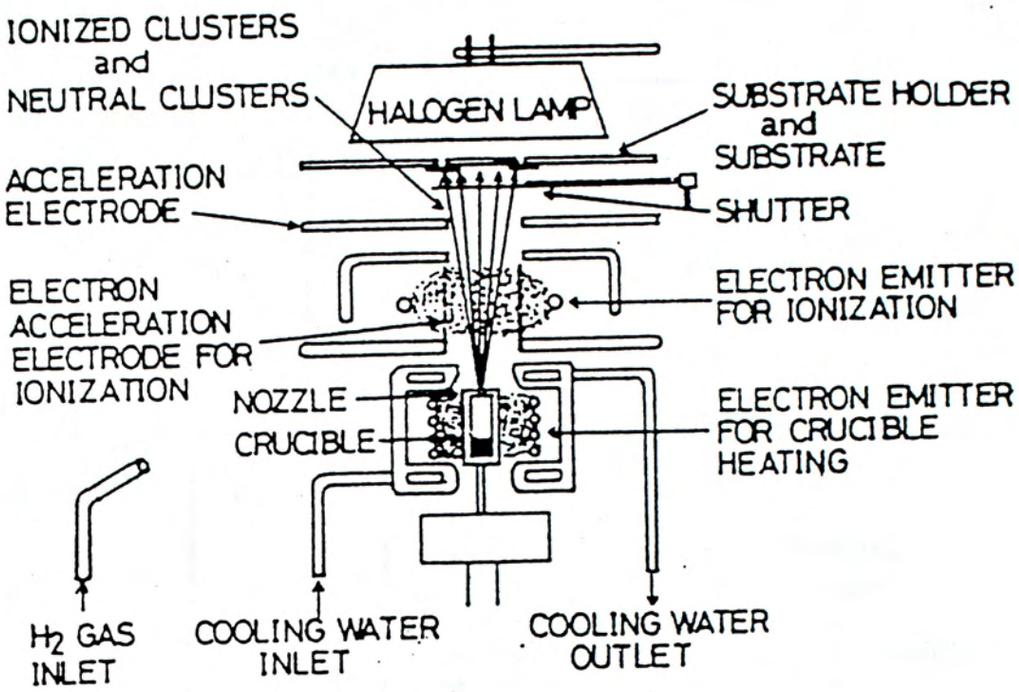

Figure 1-7. Schemaic diagram of the ion source for the ionized cluster beam deposition (I. Yamada et al., 1982).

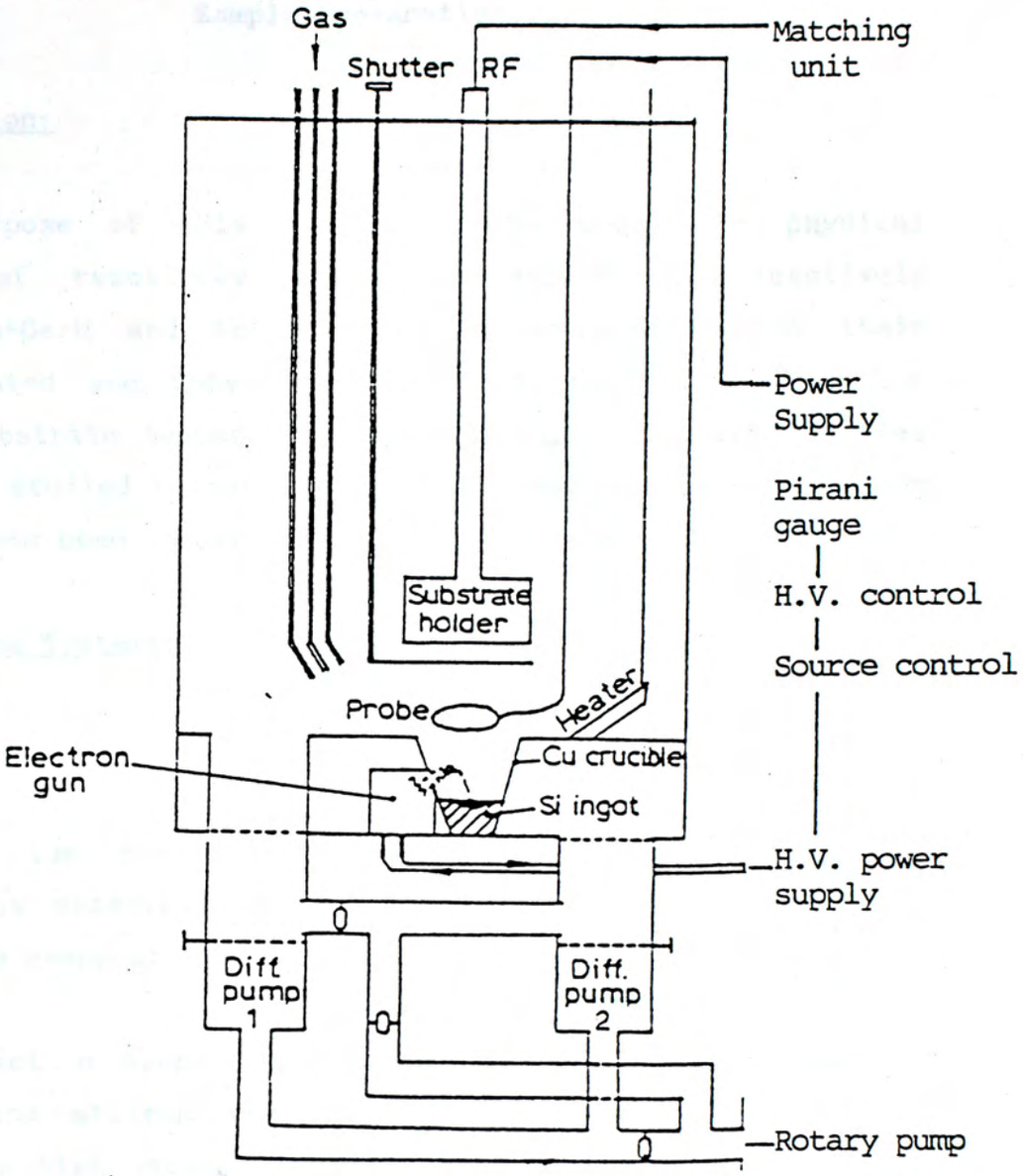

Figure 1-8. Schemaic of deposition system for biased activated reactive evaporation (J.C. Anderson et al.,1986).

Chapter 2

Sample Preparation

A) Introduction:

The purpose of this project is to study the physical properties of reactively evaporated a-Si:H and reactively evaporated a-Ge:H and to compare the properties with their posthydrogenated and unhydrogenated counterparts. Besides, the effect of substrate temperature on reactively evaporated samples will also be studied in details. This chapter reports the methods and the systems used to produce all these samples.

B) The Working Systems:

General Description:

In the present study, hydrogen incorporation into amorphous materials can be done in two ways, namely, by reactive evaporation and by posthydrogenation.

Reactive evaporation is the co-deposition of hydrogen atoms and silicon/germanium atoms onto heated substrates inside a high vacuum coating unit (Model BA 510 Automatic, Balzers) (Figure 2-1), which is provided with an electron beam source (Model SFIH-270-1, Temescal), a crystal thickness monitor (Leybold Inficon Inc.) and a substrate heater. Neutral hydrogen atoms coming out of an atom gun (Model FAB 100W) are directed towards the substrates, so that atomic hydrogen reacts with the silicon atoms at the substrate surface throughout the deposition process. Posthydrogenation is a kind of post-deposition treatment, which is also carried out in a high vacuum chamber (Figure 2-2) equipped with an atom gun. Hydrogen atoms from the gun hit the samples which are kept at an elevated temperature by a heater throughout the whole posthydrogenation process. In both cases, ultra high purity hydrogen gas is used (supplied by HKO Ltd.)

The Atom Guns:

The atom guns used in reactive evaporation and posthydrogenation operate on the same principle but differ only by the beam size. For reactive evaporation, the atom gun used (Model FAB 100W) has a beam aperture in the form of 16-hole carbon grid. In the present system configuration (Figure 2-3), the separation between the grid surface and the substrates is about 100 mm. Thus the area covered by the atom beam at the substrates is about 20×20 mm^2. Within this area, the beam current density is about 100 $\mu A/cm^2$ and its variation should be less than 10%. The above features offer an advantage of uniform coverage of atomic hydrogen over the whole substrate surface during deposition. For posthydrogenation, the atom gun used (Model FAB 11NF) has a beam aperture of 15 mm in diameter. Within the posthydrogenation chamber, the separation between the aperture and the sample is about 100 mm (Figure 2-4). After taking the beam divergence of $\cong 2^\circ$ into consideration, the area covered by hydrogen beam at the position of the sample is about 57mm^2, and the corresponding beam current density is about 70 $\mu A/cm^2$. Although the outcoming atomic beam is in the form of a spot, the uniformity of hydrogen diffusion into the sample can be improved by means of a rotatable sample holder. However, since the beam current of the atom guns is controlled by the gas pressure, so it can only be varied in a very limited range.

The Electron Beam Source And Other Components:

The electron beam source (Model SFIH-270-1, Temescal) is composed of a 7 cc water-cooled crucible and a hidden electron beam emitter with 270° beam deflection (Figure 2-5). The beam spot hitting on the source material can be horizontally and vertically deflected by an electromagnet provided. The maximum power output of the electron beam source is of 10 KW (10 kV × 1 A). However, it was discovered

that the problems of electrical leakage and spitting of source material out of the crucible could be minimized when the high tension operates at a lower voltage. In the present study, it has been fixed at 6 kV. The separation between the crucible and the substrate is about 25 cm, and so is the separation between the crucible and the crystal thickness monitor. During the deposition, the thickness monitor (Leybold Inficon Inc.) detects the frequency shift in a gold-coated quartz crystal (6 MHz) which is caused by a coating of source material on its surface, and according to a thickness-frequency equation provides a real time monitoring on both the deposition rate and the thickness of film grown.

Since the effect of substrate temperature on the resultant film properties has to be studied, a 1000 W quartz lamp is installed as the substrate heater, which is placed at a height of about 2 cm from the back of the substrates. The power of the quartz lamp is supplied by a power regulator (Shimaden) under the control of a temperature controller, and it obtains its control feedback from a K-type (chromel-alumel) thermocouple, which has already been pasted by ceramic cement on a dummy substrate in the vicinity of the real substrates (Figure 2-6).

C) Sample Preparation:

C.1) The Method Of Reactive Evaporation:

After the coating system has been evacuated to a base pressure of $\cong 4\times10^{-7}$ torr, the chamber was degassed with a temperature at least equal to that of the desired substrate temperature, followed by flushing several times with ultra high purity hydrogen whose admittance was controlled by means of a needle valve. Then the electron beam (E-beam) source was turned on to degass the source material for an hour. During this period, the high tension and the emission current of the E-beam source was kept at 6 kV and 0.02 A respectively. In

order to degass also the carbon grid of the atom gun, its power supply (B50, Ion Tech Ltd.) was also turned on. The degassing of atom gun can be finished in a time of 15 minutes, indicated by a stabilized high tension and plasma current. Any change on these values later on can only be achieved by adjusting a combination of the needle valve for regulating the hydrogen gas pressure, the high voltage knob and the plasma current knob on the power supply. Usually, the high voltage was fixed at 5 - 6 kV with a plasma current at 6 mA. Throughout the deposition process, atomic hydrogen reacted continuously with silicon/germanium atoms at the heated substrate surfaces. In order to obtain a steady and safe deposition condition, from time to time inspection on the emission current of the E-beam source, the hitting spot on the source material, the backing pressure (should be lower than 10^{-1} torr) and the plasma current within the atom gun was needed.

C.2) The Method Of Posthydrogenation:

Before performing the posthydrogenation process, the sample had to be firstly annealed at a temperature of 500°C for 20 minutes (W.H. Ho, 1988). Then the annealed sample was placed on a rotatable sample holder directly below the aperture of the atom gun inside a high vacuum chamber as described previously. During the process of posthydrogenation, the sample was heated to 450°C and continuously hit by a beam of atomic hydrogen for 15 minutes. As mentioned before, the outcoming beam size on the sample is about 57 mm^2. Uniform hydrogen diffusion within the sample was achieved by rotating the sample back and forth by means of a dc motor, so that the atomic beam can hit the whole surface of the sample throughout the posthydrogenation process.

D) The Substrates:

Three kinds of substrates have been used in the present study, namely, 7059 Corning glass, silicon wafer and quartz.

7059 Corning glasses were used to deposit samples for conductivity measurements, ESR measurements and PDS measurements in the near IR to visible region, while silicon wafer and quartz substrates were used to prepare samples for performing IR absorption spectroscopy and optical absorption spectroscopy in the UV to visible region respectively.

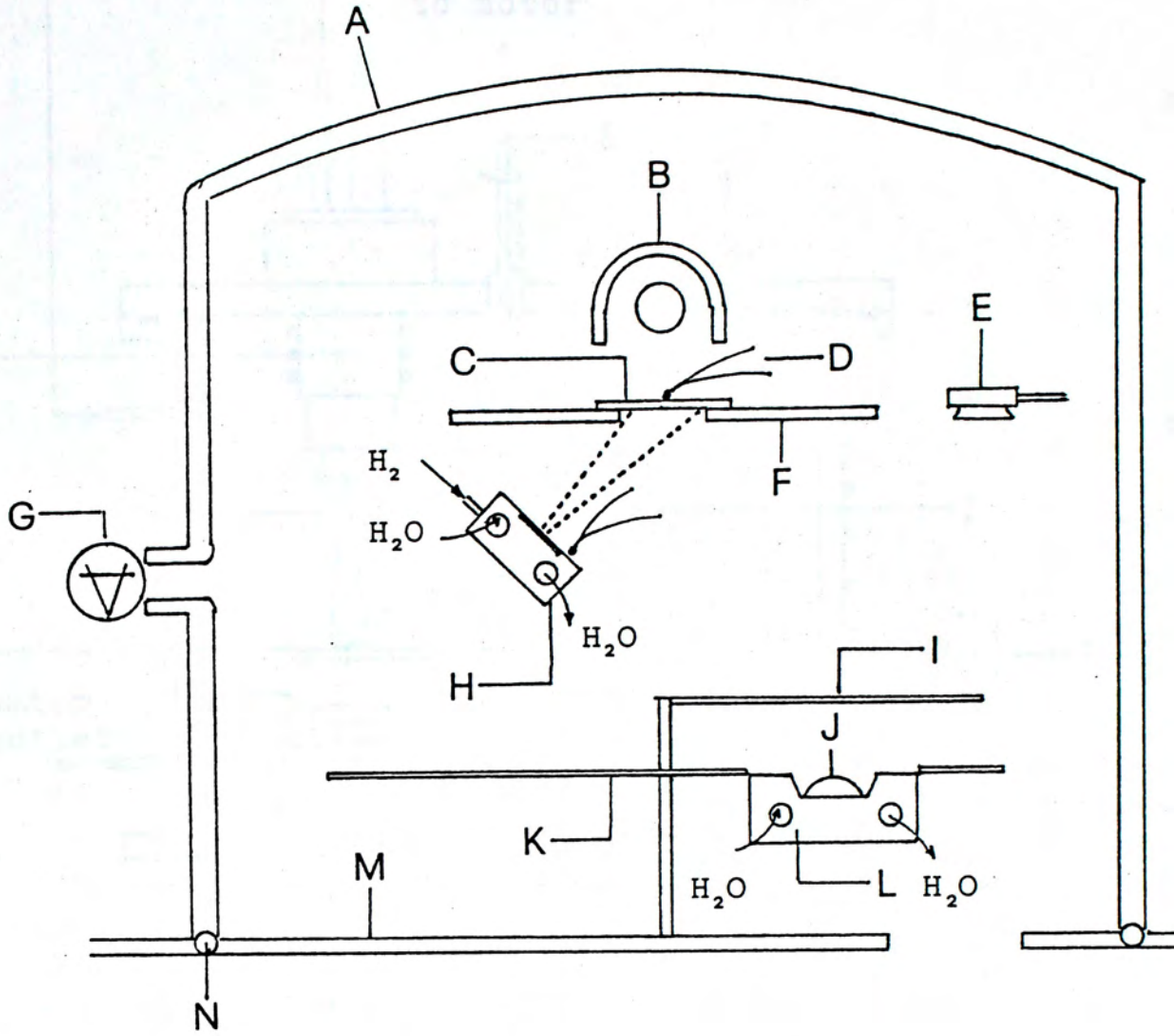

Figure 2-1. A : Stainless steel chamber wall;
B : Substrate heater;
C : Substrate;
D : K-type thermocouple;
E : Crystal thickness monitor;
F : Stainless steel substrate holder;
G : Penning gauge;
H : Atom gun;
I : Shutter;
J : Source material;
K : Stainless steel plate;
L : Electron beam gun;
M : Stainless steel base plate;
N : O-ring.

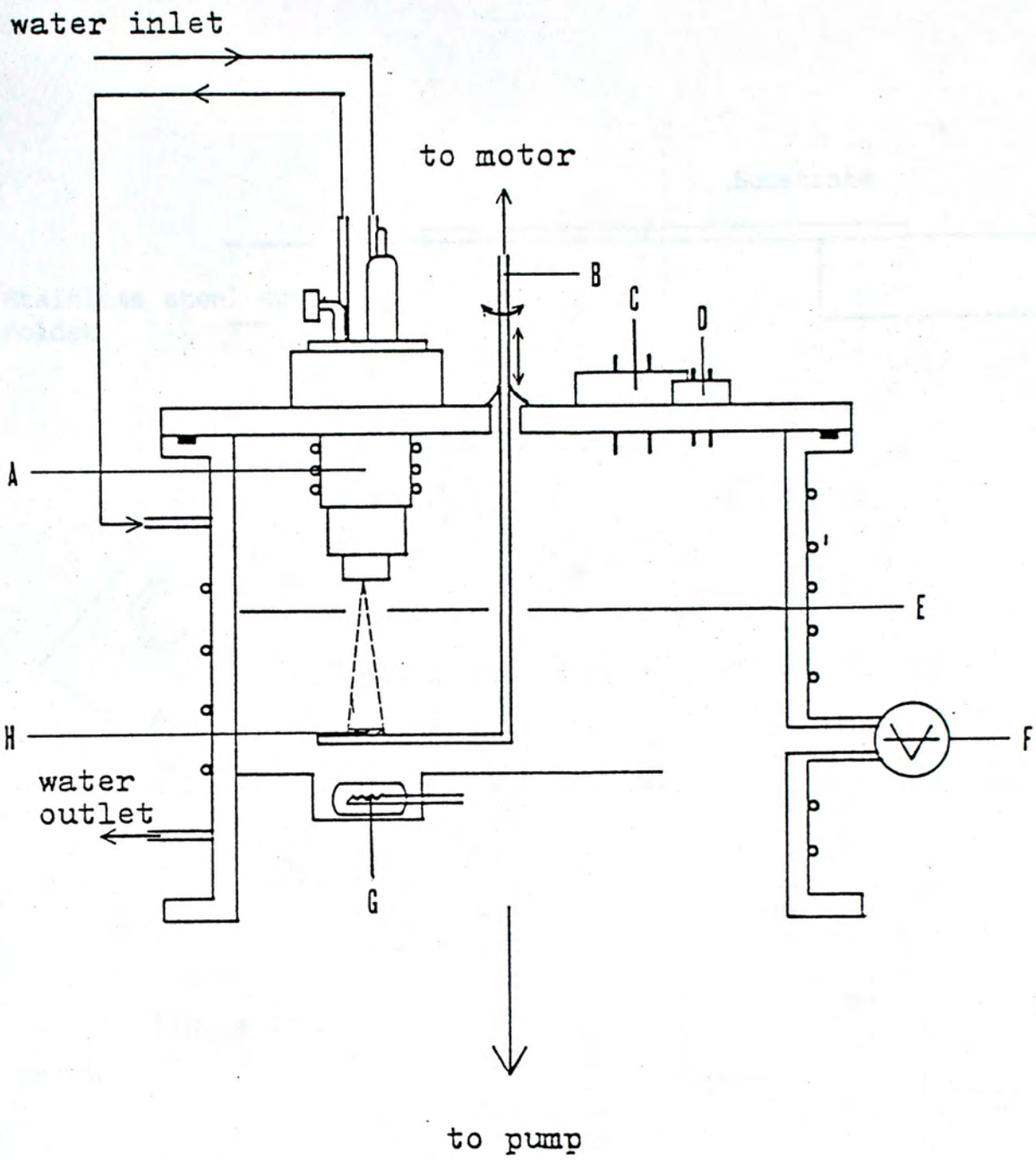

Figure 2-2. The working chamber for posthydrogenation.
A : Saddle field fast atom source
B : Rotatable axis
C : Heater feedthrough
D : Thermocouple
E : Radiation shield
F : Penning gauge head
G : Tungsten halogen lamp
H : Sample

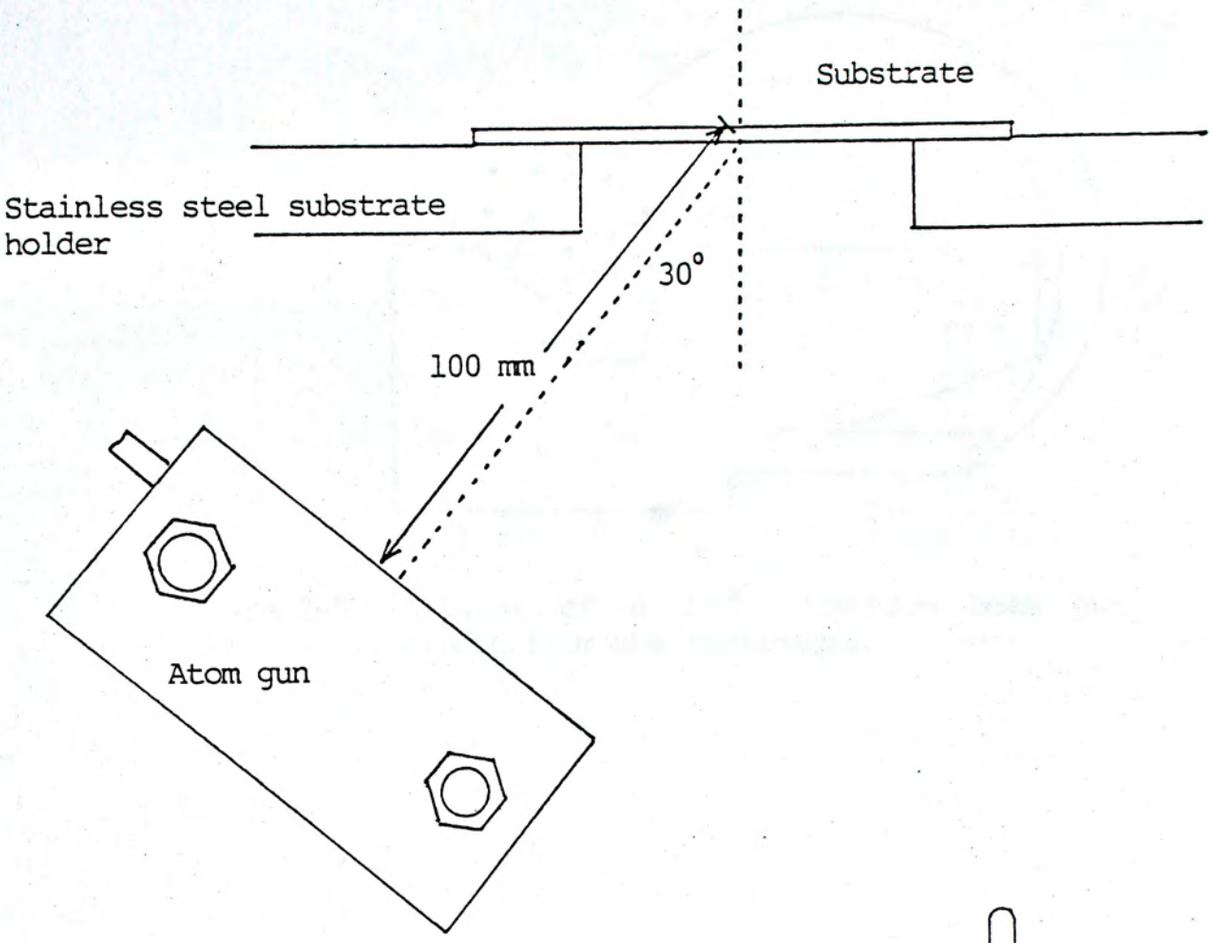

Figure 2-3.

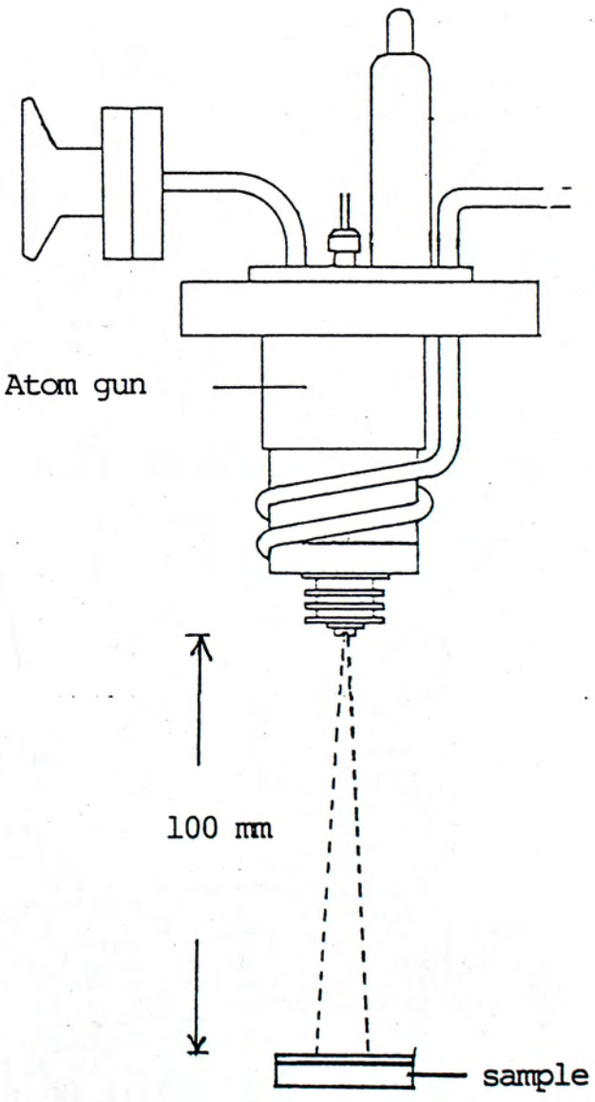

Figure 2-4.

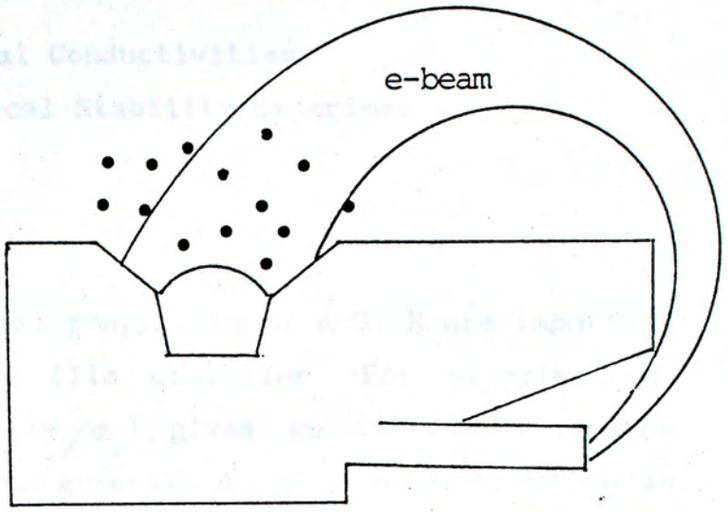

Figure 2-5. Diagram of a 270° electron beam gun hidden from the condensate.

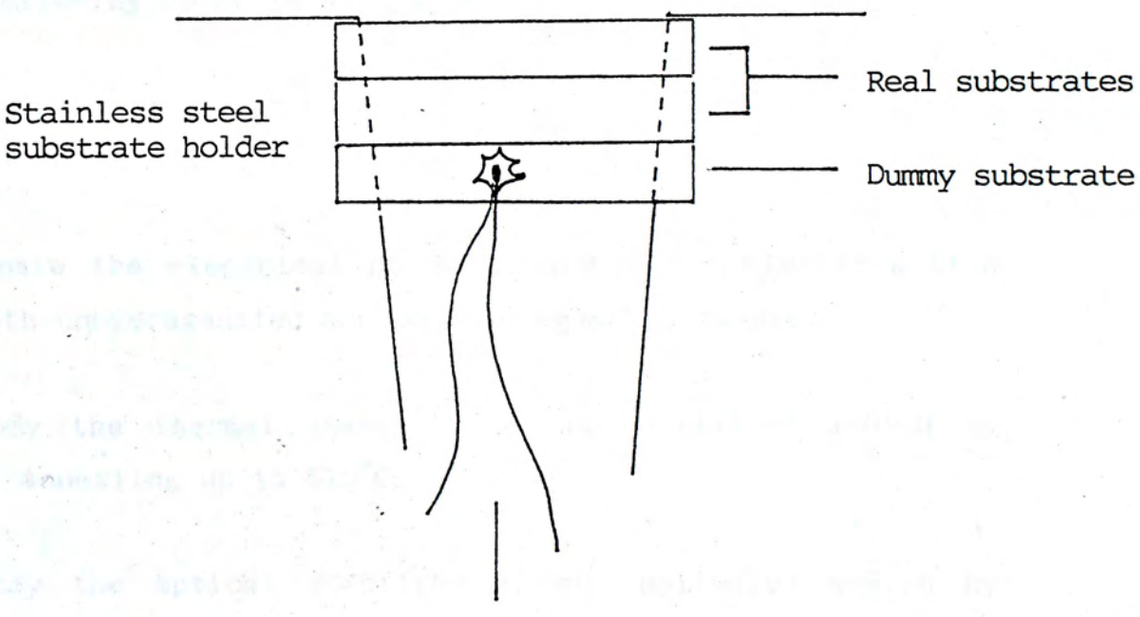

Figure 2-6.

Chapter 3

Electrical Conductivities, Thermal and Optical Stability Experiments

A) Introduction:

Measurements of electrical properties of a-Si:H are important for the characterization of film qualities. For example, the photosensitivity defined as (σ_p/σ_d) gives an indication on the effectiveness of photo-carrier generation and transport, which is particularly important for solar cell fabrication. The temperature dependence of σ_d allows a rough estimation of the Fermi level within the mobility gap, while an Arrhenius plot of σ_d can give some inference on the mechanism of electronic transport. In addition, the thermal and optical stability of a-Si:H are readily reflected from the electrical properties after either annealing or light soaking. With the help of such measurements, it is possible to find optimum conditions to prepare films with the best photoconductivity and stability. This chapter reports such results with the following objectives in mind:

1) To search for an optimum substrate temperature for reactive evaporation of a-Si:H in our present system;

2) To compare the electrical properties of our optimized a-Si:H with both unhydrogenated and posthydrogenated samples;

3) To study the thermal stability of our optimized a-Si:H by thermal annealing up to 510°C;

4) To study the optical stability of our optimized a-Si:H by prolonged illumination.

B) Theory:

B.1) Electronic transport in Amorphous Semiconductor:

Without a model, many experimental results concerning electronic transport cannot be interpreted properly. Several well-known models are now summarized.

B.1.1) The Cohen-Fritzsche-Ovshinsky Model: (P.Nagels, 1979)

The CFO Model (Figure 3-1a) assumes that tail states extend across the gap in a structureless distribution. While the gradual decrease of the localized states destroys the sharpness of the conduction and valence band edges, the disorder-induced tailing from the valence and conduction bands overlaps in the middle of the gap. This leads to a redistribution of charges, hence pinning the Fermi level close to the mid-gap. The main problem with the CFO Model lies in the difficulty in explaining the high transparency of amorphous chalcogenides below a well defined absorption edge.

B.1.2) The Davis-Mott Model: (P. Nagels, 1979)

According to Davis and Mott, the tails of localized states should be rather narrow and should extend a few tenths of an electron volt into the forbidden gap. Besides, they proposed the existence of a band of compensated levels near the middle of the gap, originating from defects in the random network (Figure 3-1b). Moreover, the center of the band may be split into a donor and an acceptor band, which will also pin the Fermi level (Figure 3-1c).

B.1.3) The Small-Polaron Model: (P. Nagels, 1979)

Emin took an entirely different approach to the problem. He suggested that charge carriers in some amorphous semiconductors may enter a self-trapped (small polaron)

state as a result of the polarization of the surrounding atomic lattice. To support his views, he proposed that a charge carrier will be slowed down in a disordered medium and this slow-down essentially leads to a localization. If the carrier stays at an atomic site long enough for atomic rearrangements to take place, it may induce displacements of the atoms in its vicinity, causing small polaron formation. Conduction by polarons can be achieved in two ways: band conduction at low temperatures involves the motion of a small polaron without any change in the phonon population while at high temperatures, the small polaron moves by phonon assisted hopping between adjacent sites. It is worth noting that in this model, the concepts of mobility edges and localized tail states are not needed.

However, from electron spin resonance experiment (Chapter 5) and optical absorption experiment (Chapter 6), it was found that the band model needed to interpret our experimental results highly resembles that of Davis and Mott. So conduction mechanisms suggested by this model will be considered in details. The existence of narrow tails of localized states and two localized impurity bands within the gap lead to basically three different channels for conduction (Mott and Davis, 1979) (Figure 3-2).

B.2) dc Electrical Conductivity In Davis-Mott Model:

B.2.1) Extended States Conduction:

The conductivity for any semiconductor can be written as:

$$\sigma = - e \int N(E)\ \mu(E)\ kT\ \frac{\partial f}{\partial E}\ dE \qquad (3.1)$$

where N(E) is the density of states at energy E
$\mu(E)$ is the mobility at energy E
f is the Fermi-Dirac distribution function

Since

$$\frac{\partial f}{\partial E} = -f(E)\,[1 - f(E)] \,/\, kT$$

$$\Rightarrow \quad \sigma = e \int N(E)\,\mu(E)\,f(E)\,[1 - f(E)]\,dE \qquad (3.2)$$

In Davis-Mott model, electrical conduction is implicitly assumed to be non-degenerate (i.e. E_f far from mobility edges). So Boltzmann statistics can be used to describe the occupancy of states. As a result, the conductivity for electrons can be written as:

$$\sigma \cong e \int_{E_c}^{\infty} N(E)\,\mu(E)\,e^{-(E-E_f)/kT}\,dE \qquad (3.3)$$

Under the assumption of a constant density of states and constant mobility, the conductivity due to electrons excited beyond the mobility edge of conduction band is given by:

$$\sigma = e\,N(E_c)\,\mu_c\,kT\,\exp[-(E_c - E_f)/kT] \qquad (3.4)$$

To account for the temperature dependence of $E_c - E_f$ a linear temperature variation is assumed:

$$E_c - E_f = E_a - \gamma T \qquad (3.5)$$

Eqt. (3.4) can be rewritten as:

$$\sigma = e\,N(E_c)\,\mu_c\,e^{\gamma/k}\,kT\,\exp\,[-E_a/kT]$$
$$\equiv \sigma_0\,\exp\,[-E_a/kT] \qquad (3.6)$$

where σ_o is the pre-exponential factor
E_a is the activation energy

B.2.2) Conduction in Band Tails:

Conduction in band tails is by thermally activated hopping. Everytime an electron hops from one localized state to another, it exchanges energy with a phonon. According to Mott (1979),

$$\mu_{hop} = \mu_o \exp [-W_1(E)/kT] \qquad (3.7)$$

and $\mu_o = (1/6)\ \nu_{ph}\ eR^2/kT$ (3.8)

where ν_{ph} is the phonon frequency and R is the distance covered in one hop.

By assuming a linear band tail with a width $E_c - E_A = \Delta E$, the conductivity is found to be:

$$\sigma_{hop} = \mu_{hop} \left(\frac{kT}{\Delta E}\right) C_1 \exp [-(E_A - E_f + W_1)/kT] \qquad (3.9)$$

where $C_1 = 1 - \{\exp [-\Delta E/kT]\} [1 + (\Delta E/kT)]$

B.2.3) Conduction in Localized States at Fermi energy:

If the Fermi energy lies in a band of localized states, the carriers can move between the states via a phonon assisted hopping process. Following the analysis made by Mott (1969), let us consider an electron which hops from one localized state to another at Fermi energy. The energy difference between the states is W_2. The probability that an electron performs a jump is determined by three factors:

1) The probability of finding a phonon with an excitation energy equal to W_2, given by Boltzmann expression $\exp(-W_2/kT)$;

2) An attempt frequency ν_{ph}, which cannot be greater than the maximum phonon frequency (in the range 10^{12}-10^{13} Hz);

3) The probability of an electronic transfer from one state to another depends on the degree of overlapping of electron wavefunctions, and is given by $\exp(-2\alpha R)$. At high temperatures, R is the distance for nearest neighbour hopping. α indicates the rate of fall off of the wavefunction at a site.

Altogether, the probability for an electron jump is:

$$p = \nu_{ph} \exp(-2\alpha R - W_2/kT) \tag{3.10}$$

By making use of Einstein's relation, the mobility can be written as:

$$\mu = e\, p\, R^2 / 6kT \tag{3.11}$$

and the conductivity is found to be:

$$\sigma = \frac{1}{6} e^2\, p\, R^2\, N(E_f)$$

$$= \frac{1}{6} e^2\, R^2\, \nu_{ph} N(E_f) \exp(-2\alpha R) \exp(-W_2/kT) \tag{3.12}$$

where $N(E_f)kT$ is the number of electrons around Fermi energy that contribute to conduction.

However when the temperature is lowered, carriers will tend to hop to larger distances in order to find sites which are energetically closer than the nearest neighbours, and Mott found that the conductivity for variable range hopping becomes:

$$\sigma = (\frac{1}{6})\ e^2\ R^2\ \nu_{ph}\ N(E_f)\ \exp(-\frac{A}{kT^{1/4}}) \qquad (3.13)$$

B.3) Photoconductivity:

Besides dark conductivity, another important electrical property of a-Si:H is the observed increase in conductivity of the sample upon illumination. This excess conductivity $\Delta\sigma$ originates from excess charge carriers due to photoexcitation. Explicitly:

$$\Delta\sigma = e\ (\Delta n\ \mu_n + \Delta p\ \mu_p) \qquad (3.14)$$

where Δn (Δp) is the excess density of electrons (holes)
μ_n (μ_p) is the mobility of electrons (holes)

Under steady conditions, the excess densities equal to their rate of generation g (i.e. the number of carriers generated per unit time per unit volume) multiplied by their average life time τ :

$$\Delta n = g\ \tau_n \text{ and } \Delta p = g\ \tau_p \qquad (3.15)$$

The generation rate is governed by the quantum yield η, which is the number of electron-hole pairs generated by the absorption of a photon. These excess charge carriers will exist until recombination takes place. In general, there are three channels for recombination: 1) direct recombination of a free electron with a free hole; 2) capture of an electron by a center in which a hole is localized; 3) capture of a hole by a center in which there is a bound electron. In steady state, the generation rate equals the recombination rate.

B.4) Staebler-Wronski Effect:

Staebler-Wronski effect is a kind of reversible light-induced changes in optoelectronic properties of a-Si:H. Upon illumination, the conductivities of glow-discharge produced a-Si:H decrease (Figure 3-3). However the above changes can be reversed by annealing the sample above 150°C (Staebler and Wronski, 1980). It is generally believed that such a kind of light induced instability is due to defect formation within the sample after prolonged illumination (Street, 1982). Such induced change in conductivities and gap states can in principle have very large effects on the application of a-Si:H. For example, the change in bulk conductivity directly affects the series resistance of photovoltaic cells, while the change in the gap states and carrier recombination can have a serious effect on the junction properties and on the collection of free carriers. So efforts have been made to produce a-Si:H free from such effect (P.K. John et al.,1981) (J.C. Anderson et al.,1986).

C) Experimental method:

Three kinds of samples have been used in this study. They are all electron beam evaporated (Temescal CV-14) in a high vacuum unit (Balzer Model BA510) but they are either unhydrogenated or hydrogenated in different ways. The detail procedure and experimental set-up for deposition and subsequent treatments have been described in Chapter 2. Briefly, all samples were deposited on 7059 Corning glass substrates (≅ 3x25 mm^2). Samples were of 10^3 Å thick measured by Alpha step. The samples without hydrogenation were deposited at a substrate temperature of 250°C. Posthydrogenation was done on some of these samples at a temperature of 450°C for 25 minutes. Reactively evaporated samples were obtained by co-evaporating silicon atoms with hydrogen atoms produced from an atom gun (Ion Tech FAB 100W), with substrate temperatures ranging from ≤ 150°C to 300°C. The coating rate was the same for each kind of deposition, being ≅ 0.5 Å/s.

The following experiments were performed on all these three kinds of samples:

1) Room temperature dark conductivity and photoconductivity measurements;
2) Temperature dependence of dark conductivity from 30°C to 220°C;
3) Temperature dependence of photoconductivity from 30°C to 220°C.

The following experiments were further performed on reactively evaporated a-Si:H deposited at 250°C:

1) Conductivity (both σ_d and σ_p) measurements along with prolonged illumination;
2) Conductivity (both σ_d and σ_p) measurements after each step of isochronal annealing from 300°C up to 510°C.

C.1 Dark and Photo Conductivities Measurements:

The working chamber has been described by P.H. Chan (1988) (Figure 3-4). All measurements were done under a vaccum of $\cong 10^{-6}$ torr. Thin copper wire electrodes were pasted onto the sample with silver paste (Figure 3-5), with a typical gap width of $\cong$ 1 mm. When performing temperature dependence measurements, thermal contact between the sample holder and the sample was improved by adding vaccum grease (Dow Corning) between them.

For room temperature σ_d and σ_p measurements, voltage dropped across a standard resistor (Figure 3-6a) with resistance of 9.53×10^9 Ω was taken with an electrometer (Keithley 617), whose input impedance is about 10^{16} Ω. Then, the corresponding conductivities were calculated according to the following formula:

$$\sigma_i = \frac{l}{w\ t}\ \frac{V}{(\varepsilon - V)\ R_s} \qquad (3.16)$$

where i = d, L for the sample being in darkness or under illumination;

l : gap width in mm;

w : strip width in mm;

t : film thickness in cm;

V : voltage dropped across the standard resistor in Volt;

ε : total voltage supplied in Volt;

R_s : resistance of the standard resistor in Ω.

The photoconductivity was then given by:

$$\sigma_p = \sigma_L - \sigma_d \qquad (3.17)$$

The typical voltage supplied in this configuration was ≅ 200 V by an external dc power supply (Metronix HSV1K-60). The illumination source was a quartz lamp producing white light which was shone directly on the sample surface through an infrared filter (whose function was to avoid heating up the sample by the light source), a combination of an optical fibre and a quartz rod. The light intensity at about 1 cm below the lower end of the quartz rod has been checked by a power radiometer (IL1500, International Light) and was equal to 100 mW/cm^2. So the measurements were done with the sample placed ≅ 1 cm below the lower end of the quartz rod.

The temperature dependence of conductivity measurements were done automatically in a system developed by C.Y. Tang (1991),which makes use of the V/I mode of a programmable electrometer (Figure 3-6b). During measurements, the temperature of the sample was controlled by a computer, which obtained its control feedback from a T-type

$$\sigma_i = \frac{l}{w\ t}\ \frac{V}{(\varepsilon - V)\ R_s} \qquad (3.16)$$

where i = d, L for the sample being in darkness or under illumination;

l : gap width in mm;

w : strip width in mm;

t : film thickness in cm;

V : voltage dropped across the standard resistor in Volt;

ε : total voltage supplied in Volt;

R_s : resistance of the standard resistor in Ω.

The photoconductivity was then given by:

$$\sigma_p = \sigma_L - \sigma_d \qquad (3.17)$$

The typical voltage supplied in this configuration was ≅ 200 V by an external dc power supply (Metronix HSV1K-60). The illumination source was a quartz lamp producing white light which was shone directly on the sample surface through an infrared filter (whose function was to avoid heating up the sample by the light source), a combination of an optical fibre and a quartz rod. The light intensity at about 1 cm below the lower end of the quartz rod has been checked by a power radiometer (IL1500, International Light) and was equal to 100 mW/cm^2. So the measurements were done with the sample placed ≅ 1 cm below the lower end of the quartz rod.

The temperature dependence of conductivity measurements were done automatically in a system developed by C.Y. Tang (1991), which makes use of the V/I mode of a programmable electrometer (Figure 3-6b). During measurements, the temperature of the sample was controlled by a computer, which obtained its control feedback from a T-type

(copper-constantan) thermocouple pasted on a dummy glass (Figure 3-7) in the vicinity of the sample. Thermovoltages from the thermocouple were read into the computer through a RS232 interface. Should any deviation of temperature from a preset value arise, correction was made by adjusting the current passing through a couple of 1.5 Ω heaters through the computer with the PID algorithm. The regulated temperature ranged from 30°C to 220°C. A typical voltage of 100 V, supplied by the electrometer, was applied across the gap of the pasted electrodes. Readings of the resistances of the sample at various temperatures were sent from the Keithley 617 electrometer (which was set at the V/I mode) to the computer through an IEEE 488 bus for every 360 ms. Nevertheless, the computer recorded data only for every 5°C interval. The whole measuring process was done automatically, with the programme initialized to start at 220°C, ramping down at a rate of 0.8°C/min. and to stop when 30°C was reached. All data acquired were stored in a magnetic disk for later processing.

C.2) Optical Stability Measurement:

The same working chamber was used for the investigation of optical stability of reactively evaporated a-Si:H (T_s = 250°C). The sample was illuminated by white light with an intensity of 100 mW/cm^2 (as described previously) for different periods of time, namely, 3 hours, 3 hours and 5 hours respectively. During and between each illumination interval, both σ_p and σ_d were recorded.

C.3) Thermal Stability Measurement:

Reactively evaporated a-Si:H (T_s = 250°C) was isochronally annealed with a rapid thermal processing furnace (Figure 3-8) (to be described in a later chapter). Each processing time were 300 s. After each annealing, thin copper wire electrodes were painted onto the sample for electrical

measurements. Between each annealing step, both σ_d and σ_p were recorded. Before replacing the sample into the furnace for annealing, the silver paste for pasting the electrodes was washed away with technical acetone, followed by 99% alcohol. The annealing temperature was from 300°C to 510°C.

D) Results:

According to Eqt.(3.6), a plot of $\ln(\sigma_d)$ vs 1/T should give a straight line whose slope gives the activation energy (E_a) for extended states conduction. From the experimental results, it was found that Eqt.(3.6) was applicable in the temperature range from 127°C to 220°C for all three types of samples. Of course, for samples with a higher quality the temperature range can be extended to include lower temperature values. However, the above mentioned range was simply used to get E_a.

Results for the three kinds of samples were tabulated in Table 3-1.

Types of deposition	T_s (°C)	E_a (eV)	σ_o $\times 10^{-5}$	(room temp.) σ_d $\times 10^{11}$ ($\Omega^{-1}cm^{-1}$)	σ_p $\times 10^{9}$	σ_p/σ_d
Reactively evaporated	< 150	1.01	0.896	110	3.69	3.36
	200	1.03	4.50	55	455	827
	250	0.87	0.119	8.56	2000	23400
	300	1.15	54.0	10	685	6800
Posthydrogenated	250	0.783	0.113	78.6	274	348
Unhydrogenated	250	0.774	0.136	6100	16.6	0.27

Table 3-1: T_s : substrate temperature;
E_a : activation energy for extended states conduction, assuming one dominant type of conduction;
σ_o : pre-exponential factor for extended states conduction;

σ_d : dark conductivity;

σ_p : photoconductivity under 100 mW/cm^2 illumination

σ_p/σ_d : photosensitivity.

D.1) Reactively Evaporated Samples:

In view of the above table, the following observations were made for reactively evaporated samples:

1) (See Figure 3-9a). E_a has a minimum value for $T_s \cong 250^\circ C$. Activation energies for samples deposited at T_s other than $250^\circ C$ are found to be ≥ 1 eV.

2) (See Figure 3-9b). The pre-exponential factor has also a minimum value at $T_s \cong 250^\circ C$.

3) (See Figure 3-9c). As T_s increases from $15^\circ C$ to $250^\circ C$, the photoconductivity increases and reaches a maximum value at $T_s \cong 250^\circ C$. Further rise in T_s produces a decrease in photoconductivity. The maximum value coincides with a minimum dark conductivity at $T_s \cong 250^\circ C$.

4) (See Figure 3-9d). Increasing T_s from $150^\circ C$ to $250^\circ C$, the photosensitivity reaches a maximum value of $\cong 10^4$ at $T_s \cong 250^\circ C$ and decreases again with further increase in T_s.

D.2) Temperature Dependence of Conductivities:

The results for temperature dependence of conductivities measurements are shown from Figure 3-10a to 3-10f.

Firstly, it can be observed that the temperature above which thermally excited charge carriers become dominant in the conduction process was different for different sample. This temperature is arbitrarily set at $\sigma_p = \sigma_d$. Table 3-2 summarizes the results:

Type of deposition	T_s (°C)	Temp. at $\sigma_p = \sigma_d$ (°C)
Reactively evaporated	<150	≅ 196
	200	≅ 194
	250	> 220 } above measuring temp. range
	300	> 220 } above measuring temp. range
Posthydrogenated	250	≅ 159
Unhydrogenated	250	≅ 46

Table 3-2. σ_p was measured under 100 mW/cm^2 white light.

From the above table, it can be seen that the temperature above which thermal excitations dominate is higher for reactively evaporated samples than those of posthydrogenated and unhydrogenated samples. Also, among the reactively evaporated samples, as $T_s \geq 250^\circ C$, photo excitations dominate the conduction process over the whole range of measurement (i.e. > 220°C) . From Figure 3-11a, one can see that the photoconductivity curve for $T_s = 250^\circ C$ is well above all other curves. Finally, from Figure 3.11b, reactively evaporated samples in general have lower dark conductivities than both posthydrogenated and unhydrogenated samples. This means that these samples have lower density of defects.

D.3) Optical Stability Measurements:

From Figure 3-12, both photoconductivity and dark conductivity for reactively evaporated a-Si:H ($T_s = 250^\circ C$) show a small initial irreversible change upon illumination, but then remain constant thereafter even after a total of 11 hours of illumination under a 100 m W/cm^{2}white light. So the sample is free from S-W effect.

D.4) Thermal Stability Measurement:

From Figure 3-13, it can be observed that the photoconductivity, dark conductivity and photosensitivity of reactively evaporated a-Si:H (T_s = 250°C) show no significant changes even after an annealing up to 510°C.

E) Discussions:

E.1) Electrical Properties of Reactively Evaporated a-Si:H:

Our experimental findings give an optimum substrate temperature for reactively evaporated a-Si:H at 250°C. This value is in close agreement with the findings of other authors, (e.g. G. Lucovsky, 1989; I. Yamada et al. 1982), although the deposition methods employed are not the same. This shows that the effect of substrate temperature on the resultant film quality is quite independent of deposition methods. Indeed, from infrared absorption experiment (Chapter 4), it was found that substrate temperature controls the mode of hydrogen bonding configurations within the silicon lattice. At low T_s (i.e. < 250°C), hydrogen is mainly bonded in dihydride or even polyhydride configurations, which as one believes can degrade the opto-electronic properties of a-Si:H. At temperatures higher than 250°C, less hydrogen can be retained in the lattice. These explain why an optimum T_s should be present.

From Figure 3-9a, the local minimum observed in the activation energies implies two things. 1) at the optimum substrate temperature, the Fermi level moves towards the mid-gap, consistent with the finding from optical absorption experiment (Chapter 6). 2) The mobility gap is not expected to exceed 2 eV. When the observed activation energies are larger than 1 eV, a single dominant type of conduction is implied as in the case of our a-Si:H produced by reactive evaporation.

According to equation (3.6), the pre-exponential factor σ_o can be written as $e\,N(E_c)\,\mu_c\,kT\exp(\gamma/k)$, (under the assumptions of constant density of states and mobility), where $N(E_c)\,kT$ is merely the number of charge carriers above the mobility edge. This formula has difficulty in explaining the two order of magnitude difference observed in σ_o (See Table 3-1) for reactively evaporated samples, unless $N(E_c)$, μ_c and γ vary substantially from sample to sample. More experimental and theoretical work have to be done before a proper explanation can be provided.

Moreover, reactively evaporated sample prepared at $T_s = 250^{\circ}C$ provides the highest photosensitivity and photo conductivity. Posthydrogenation does improve the opto-electronic properties of electron beam evaporated sample, yet its σ_p/σ_d is still a factor of 10^2 below that of reactively evaporated samples. This can be understood if their ESR spin densities are taken into consideration (Chapter 5). The spin densities for reactively evaporated, posthydrogenated and unhydrogenated samples are $\cong 3\times10^{17}\ cm^{-3}$, $\cong 5\times10^{18}\ cm^{-3}$ and $8\times10^{18}\ cm^{-3}$ respectively. Since gap states act as either trapping or recombination centers for optically created electron-hole pairs, one expects the larger the spin density, the smaller the photoconductivity. In fact, the low-defect-density nature of reactively evaporated samples is already reflected from their generally lower dark conductivities and the domination of photo-carriers in photoconduction.

E.2) A Comparative Study Between Reactively Evaporated Samples With Those From Other Reactive Deposition Techniques And Glow-Discharge Process:

J.C. Anderson et al. (1986) used biased active reactive evaporation to produce undoped a-Si:H. The results for their optimized film are shown in Figure 3-14. From the graph, it can be estimated that at room temperature, $\sigma_p \cong 2\times10^{-7}$

$(\Omega cm)^{-1}$ under a 100 mW/cm^2 light, while $\sigma_d \cong 2\times10^{-11}$ $(\Omega cm)^{-1}$. Hence, the photosensitivity was about 1×10^4. Besides, the authors showed that BARE films were free from Staebler-Wronski effect (Figure 3-15).

I. Yamada et al. (1982) used ionized-cluster beam deposition to produce undoped a-Si:H. Their results are shown in Figure 3-16. The optimized film deposited at T_S= 220°C with acceleration voltage of 5 kV gives a room temperature $\sigma_p \cong 10^{-5}$ $(\Omega cm)^{-1}$ under a 100 m Watt/cm^2 light and $\sigma_d \cong 8\times10^{-10}$ $(\Omega cm)^{-1}$. Hence, the photosensitivity was about 1.25×10^4.

A comparison among the reactively deposited a-Si:H and that from glow-discharge process was tabulated in Table 3-3.

Method of deposition	$\sigma_p (\Omega cm)^{-1}$	$\sigma_d (\Omega cm)^{-1}$	σ_p/σ_d
Reactively evaporated	2×10^{-6}	8.56×10^{-11}	2.34×10^4
Ionized-cluster beam	1×10^{-5}	8×10^{-10}	1.25×10^4
BARE process	2×10^{-7}	2×10^{-11}	1×10^4
Glow-discharge	———	10^{-9} - 10^{-11}†	10^4 - 10^6‡

Table 3-3: σ_p was measured under a 100 mW/cm^2 light at room temperature;
† V.Augelli (1989); ‡ D.Han (1988).

It can be seen from the above table that reactively evaporated a-Si:H has the highest photosensitivity among the reactively deposited samples and both of its dark conductivity and photosensitivity are comparable to the quoted values of glow-discharge samples.

F) Conclusions:

The electrical properties of reactively evaporated a-Si:H with substrate temperatures ranging from <150°C to 300°C were

studied. Optimized film was prepared at T_s = 250°C, whose room temperature dark conductivity was $8.56\times10^{-11}(\Omega cm)^{-1}$ and photoconductivity equaled 2×10^{-6} $(\Omega cm)^{-1}$ under a 100 mW/cm^2 white light illumination. This gave a photosensitivity of 2.34×10^{4}, which is comparable to that of glow-discharge produced samples . Films deposited at lower or higher substrate temperatures had inferior qualities. Besides, from temperature dependent electrical measurement, the pre-exponential factor and activation energy for extended states conduction were found to be 1.19×10^{4} $(\Omega cm)^{-1}$ and 0.87 eV respectively, being comparable to those produced by glow-discharge method (A. Madan and M.P. Shaw, 1988). The optimized film has no Staebler-Wronski effect and is thermally stable up to 510°C.

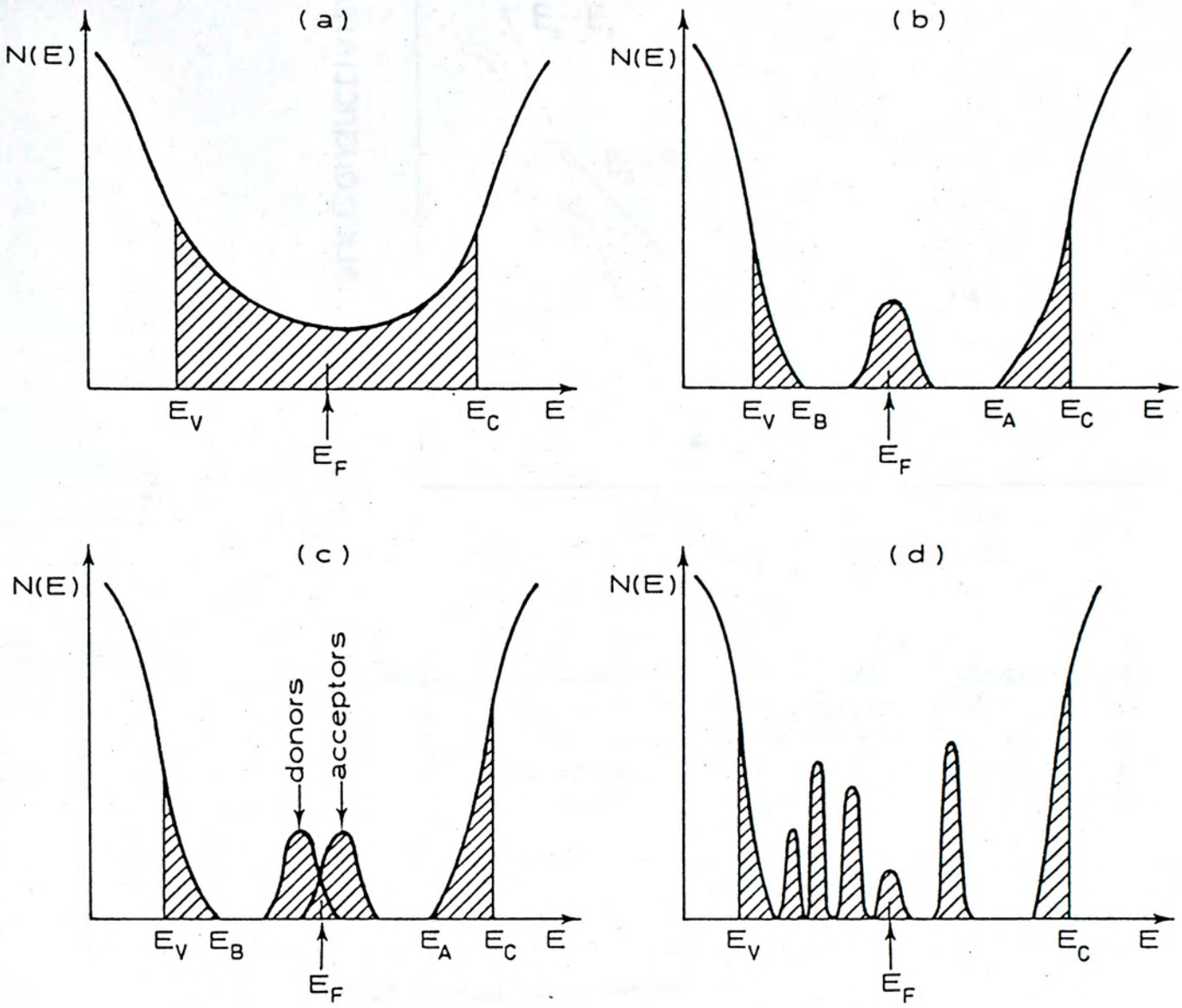

Figure 3-1. Schematic density of states diagrams for amorphous semiconductors. (a) The Cohen-Fritzsche-Ovshinsky model, (b) the Davis-Mott model showing a band of compensated levels near the middle of the gap, (c) modified Davis-Mott model, (d) a "real" glass with defect states (P. Nagels,1979).

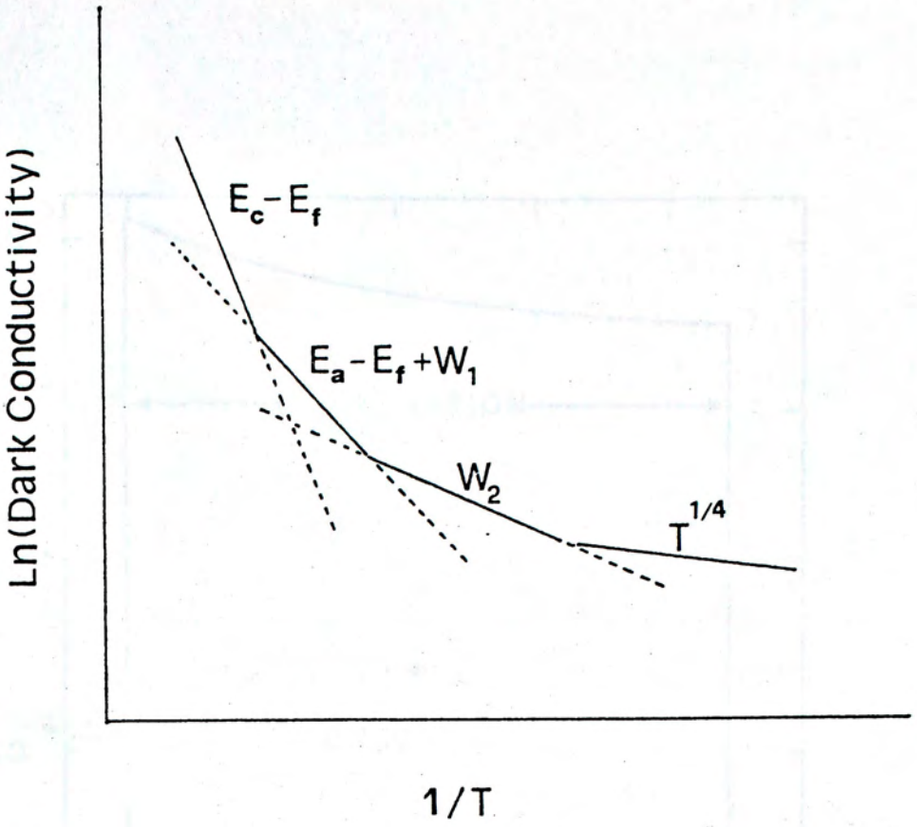

Figure 3-2. Illustration of the temperature dependence of conductivity according to Mott's model. The acivation energies associated with various processes are indicated.

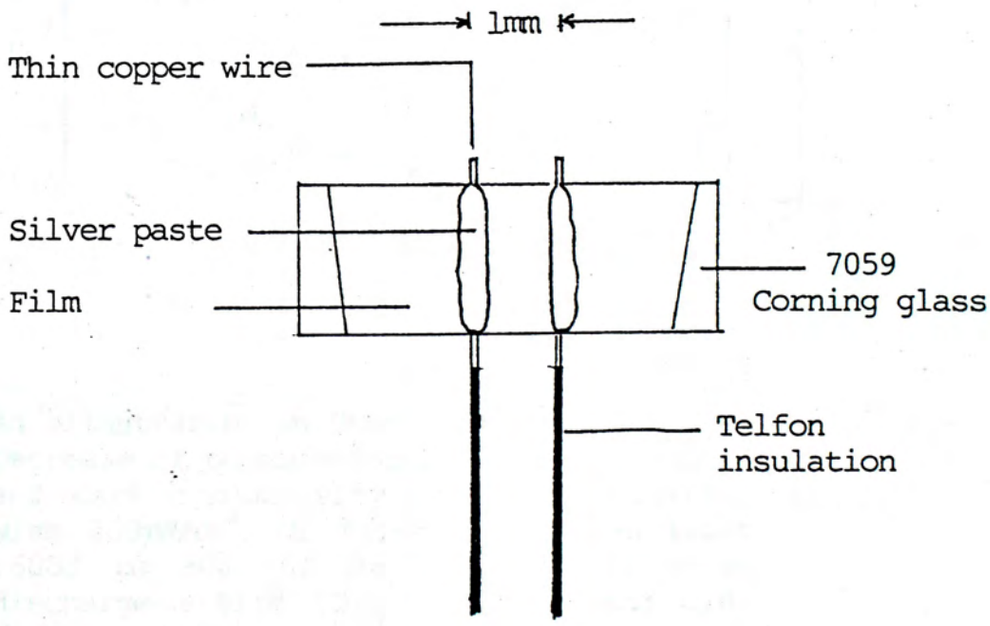

Figure 3-5.

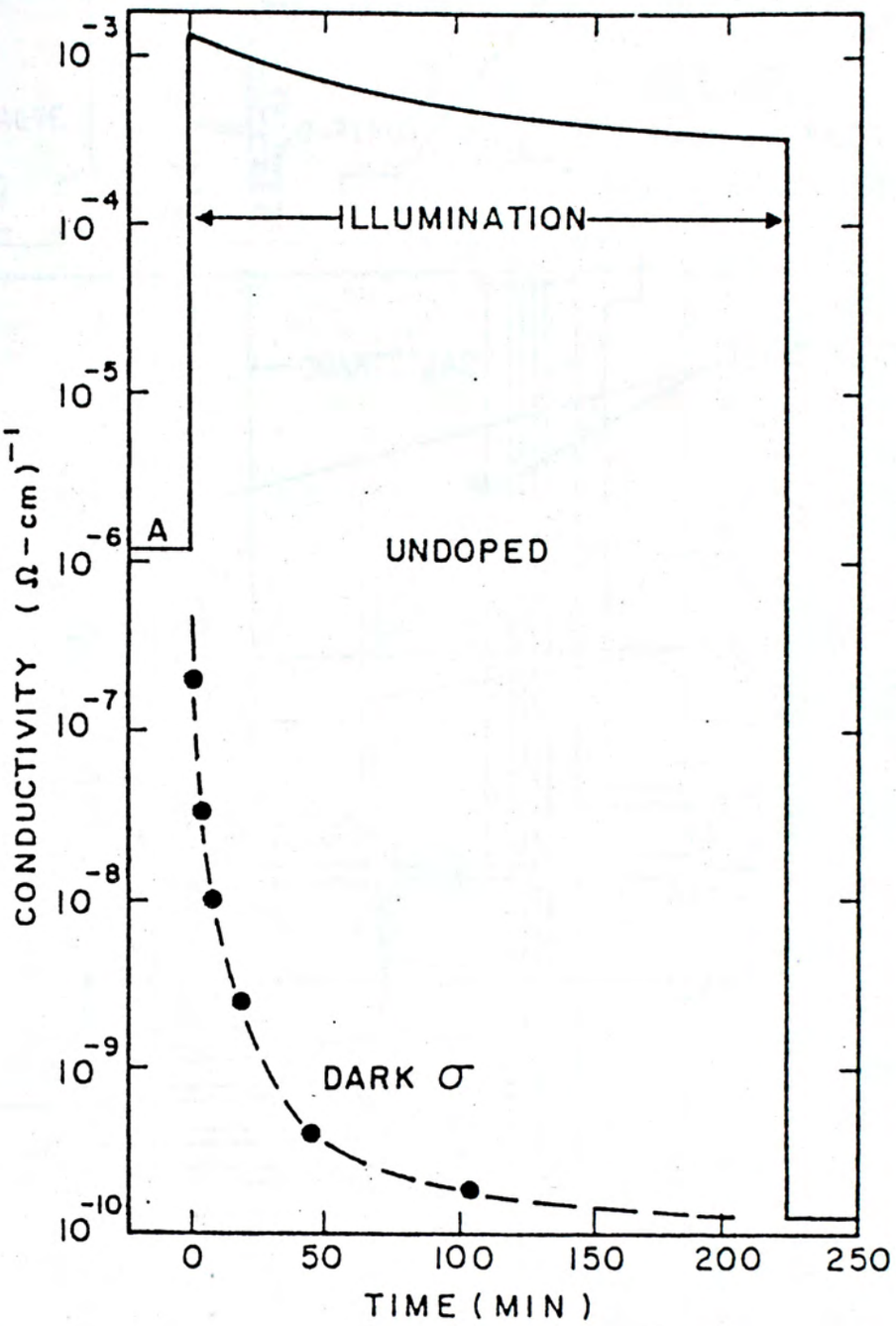

Figure 3-3. An illustration on Staebler-Wronski effect. Decrease of photoconductivity (solid curve) and dark conductivity during illumination with 200mW/cm^2 of filtered tungsten light (6000 to 9000 A) for undoped r.f. glow-discharge a-Si:H (D.L. Staebler and C.R. Wronski, 1980).

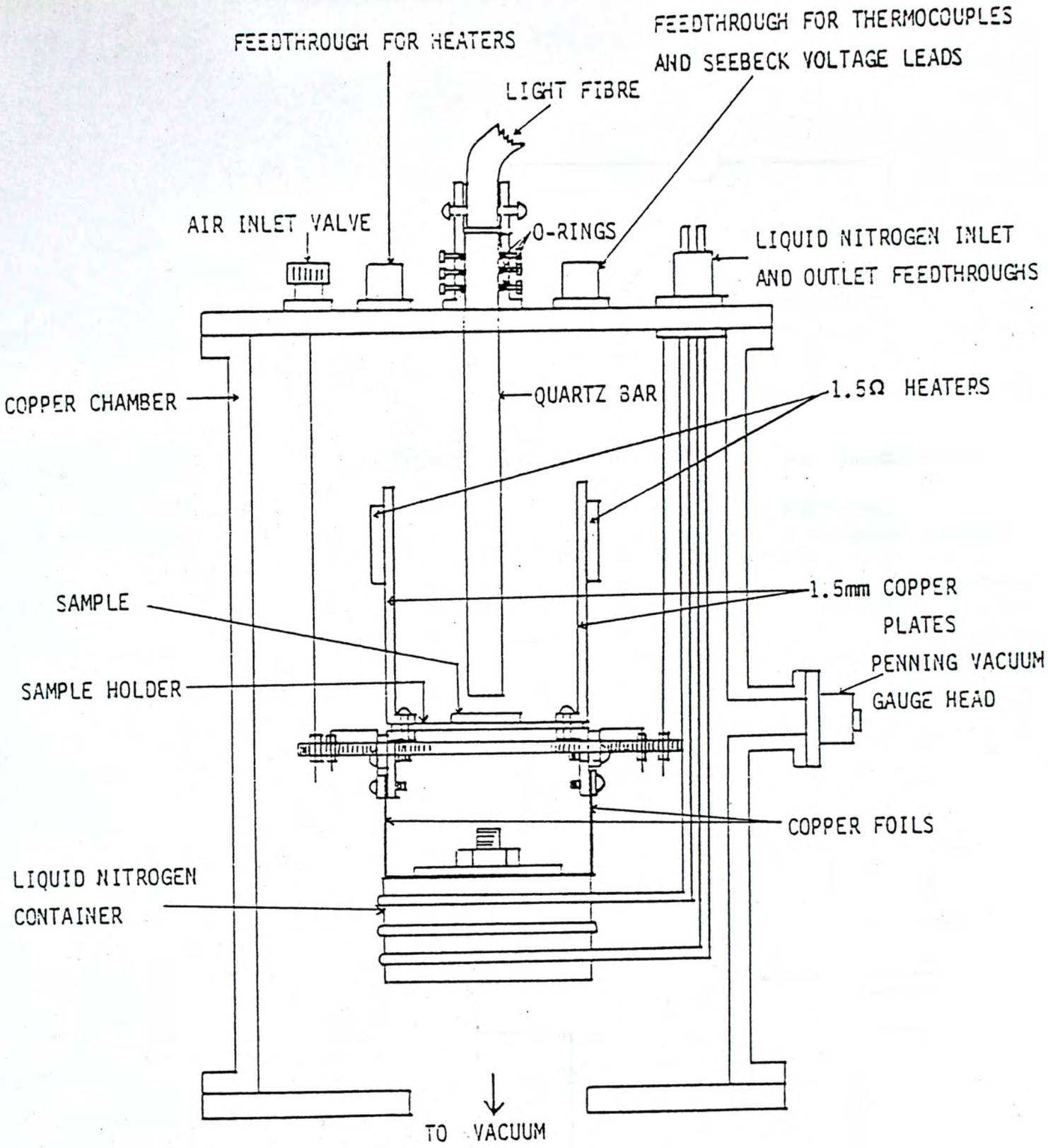

Figure 3-4. The working chamber for conductivity measurements.

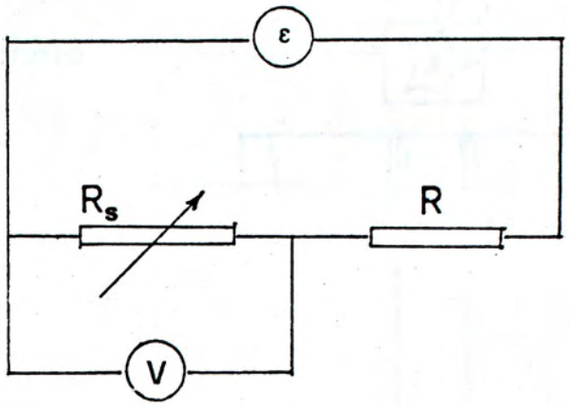

Figure 3-6a. Circuit diagram for conductivity measurements.
: Total voltage supplied;
R : Resistance of a standard resistor;
R : Resistance of the sample;
V : Voltage dropped across the standard resistor.

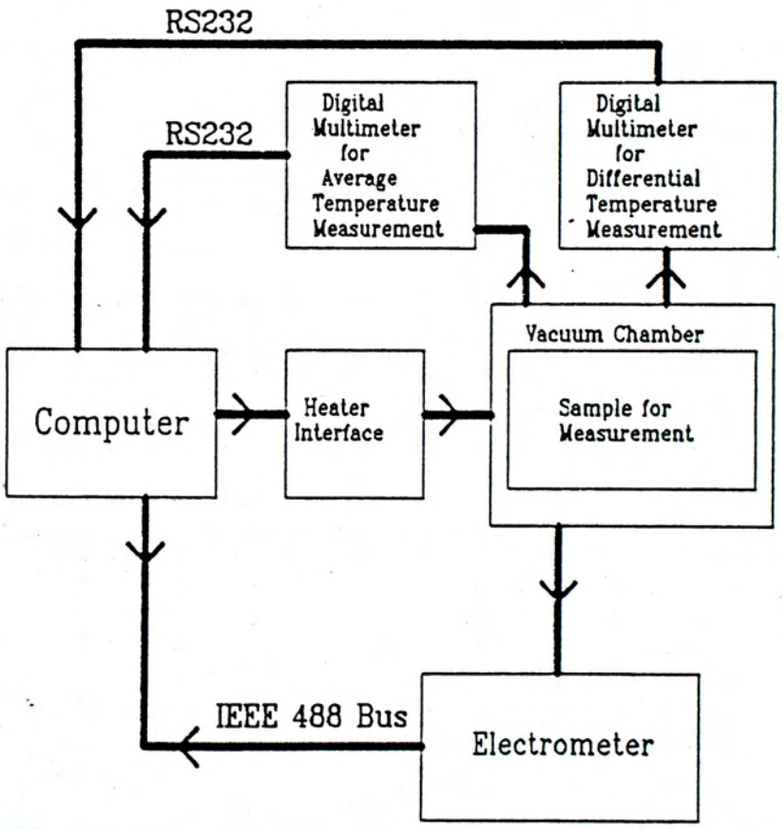

Figure 3-6b. The block diagram of the computer controlled conductivity measurement set-up (C.Y. Tang, 1991).

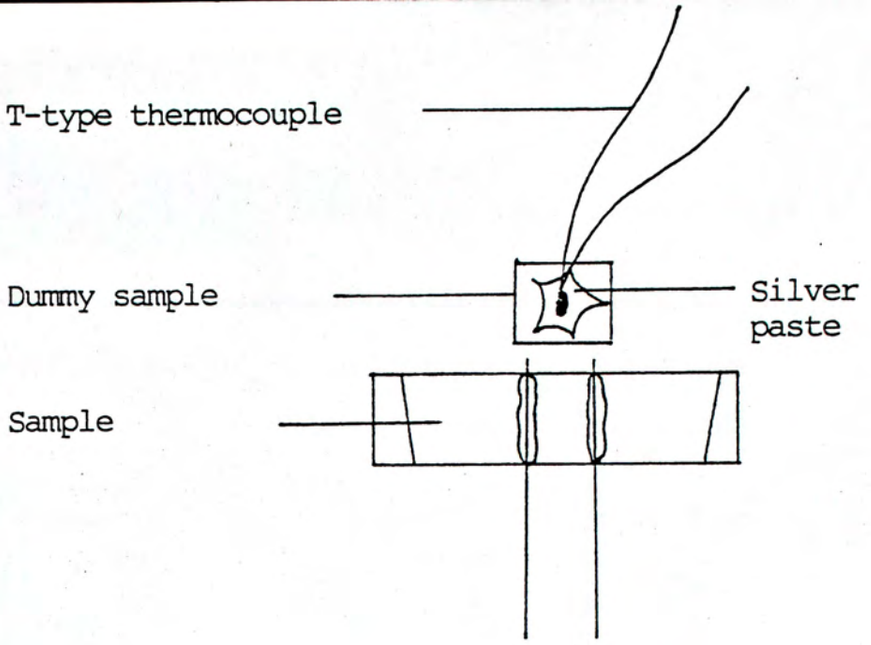

Figure 3-7.

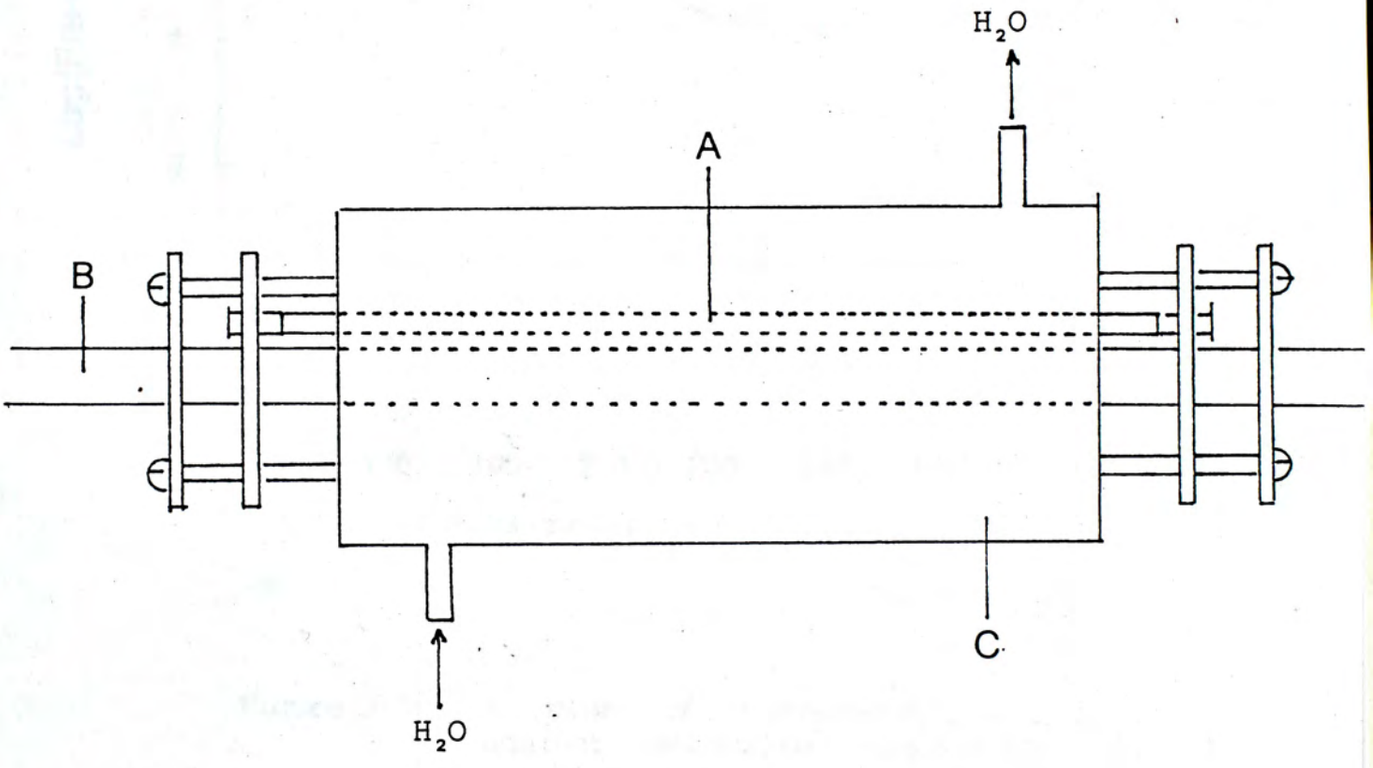

Figure 3-8. A schematic diagram showing the RTP furnace.
A : 1250 W quartz lamp as the heating source (6 altogether);
B : Quartz tube as the processing chamber;
C : Water-cooled stainless steel furnace wall.

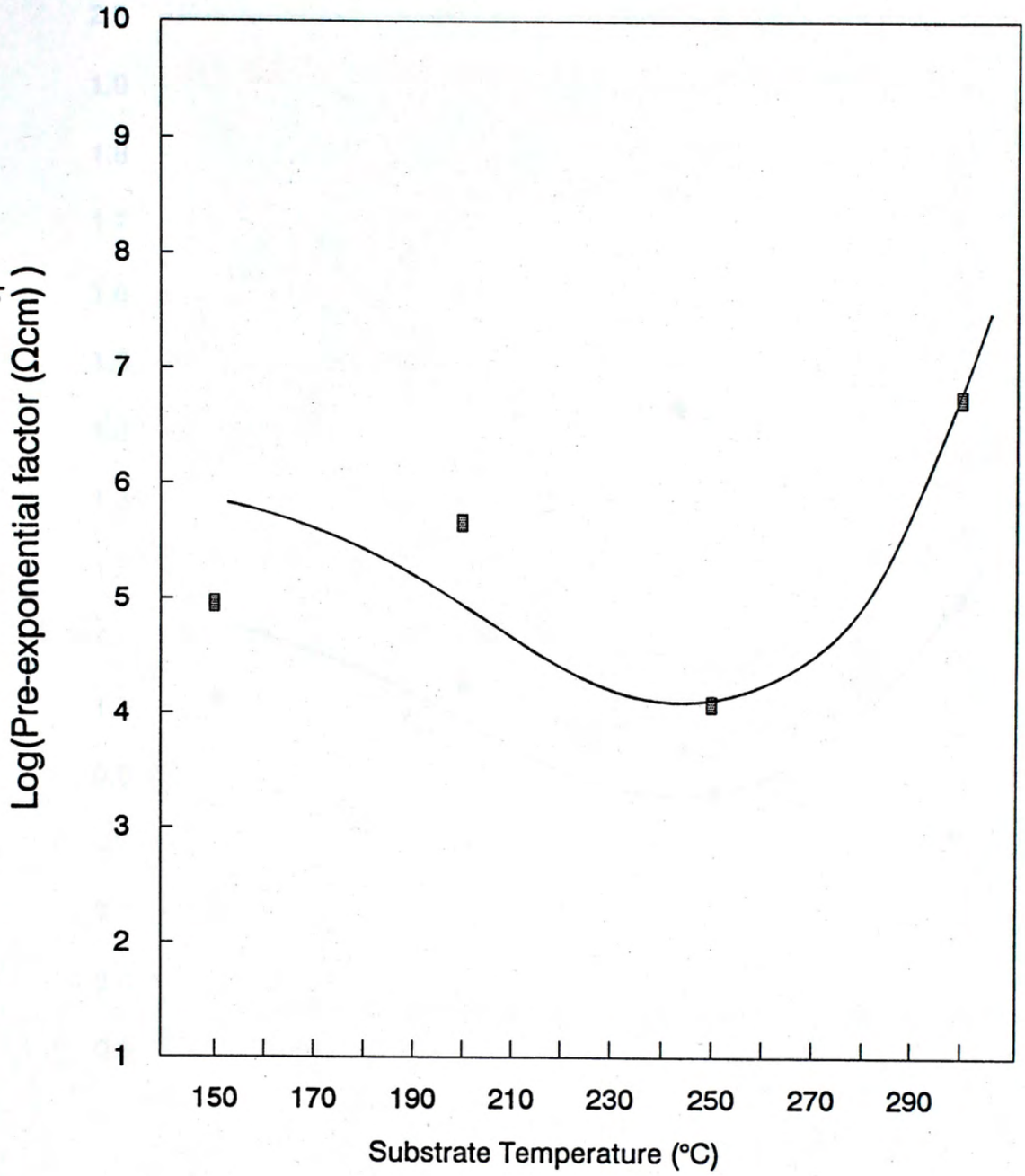

Figure 3-9a. A plot of pre-exponential factor against substrate temperature for extended states conduction in the temperature range 127 °C - 220 °C for reactively evaporated a-Si:H.

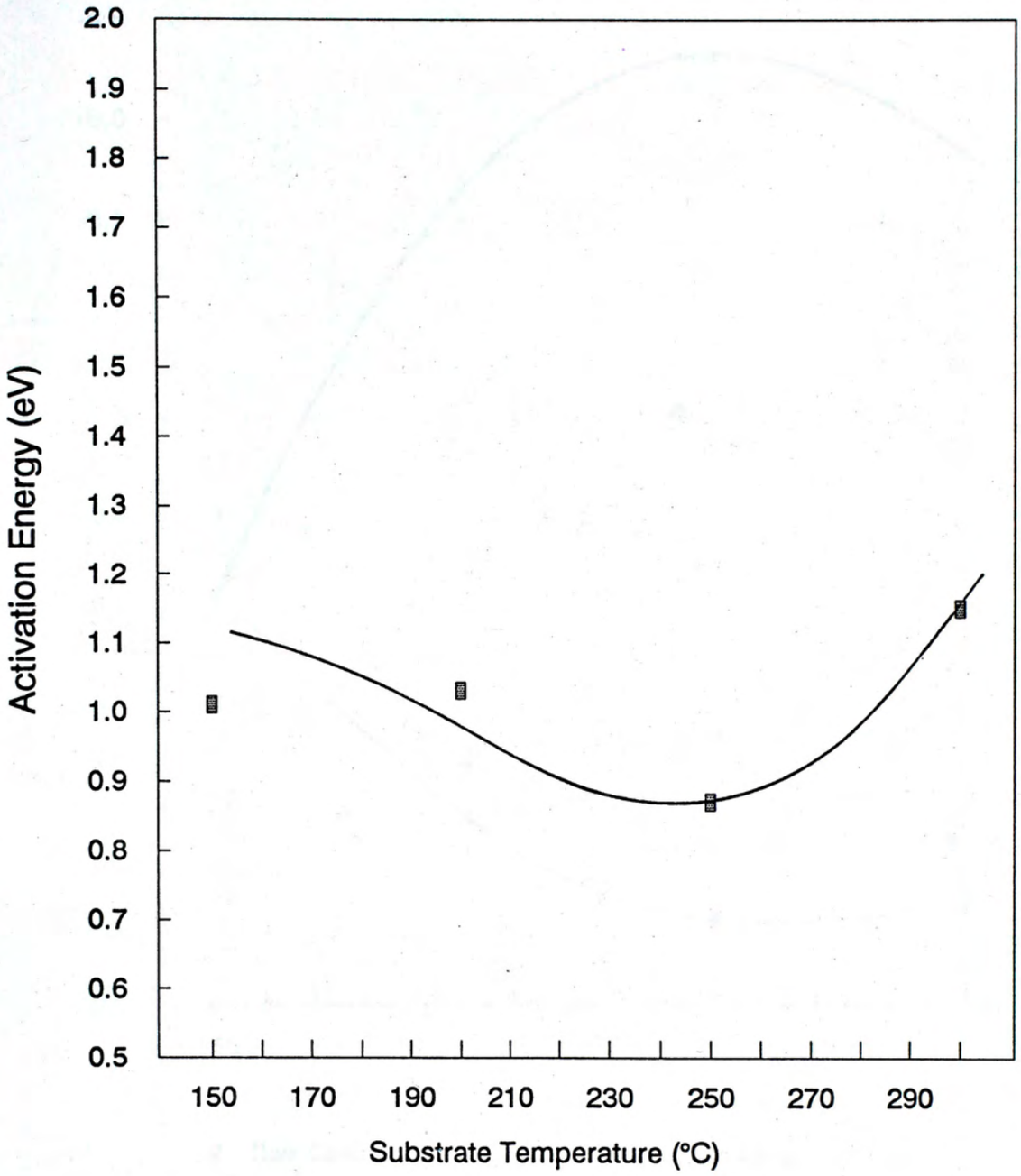

Figure 3-9b. A plot of activation energy against substrate temperature for extended states conduction in the temperature range 127 °C - 220 °C for reactively evaporated a-Si:H.

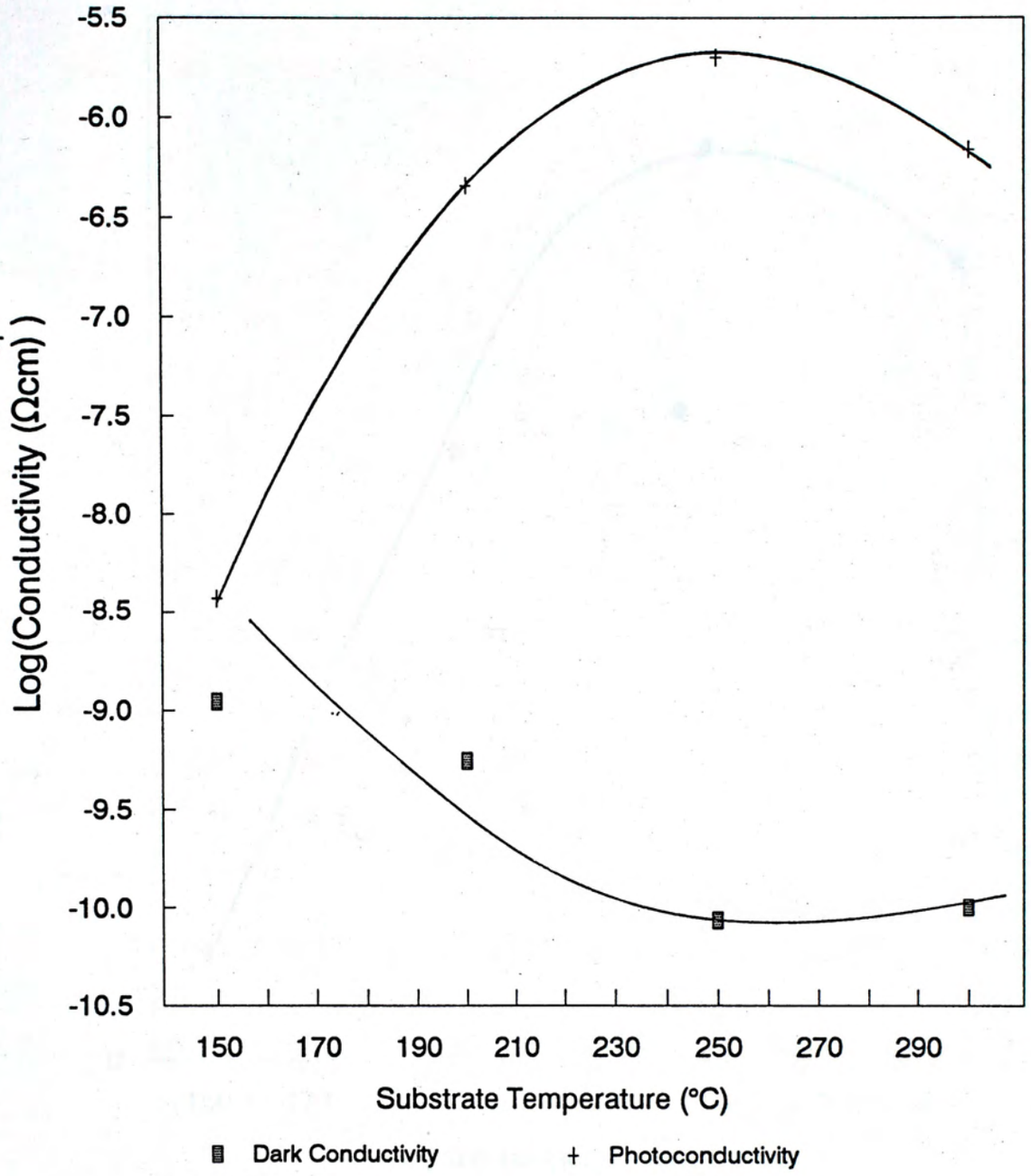

Figure 3-9c. A plot of room temperature conductivities against substrate temperature for reactively evaporated a-Si:H.
Photoconductivity was measured under AM1 illumination.

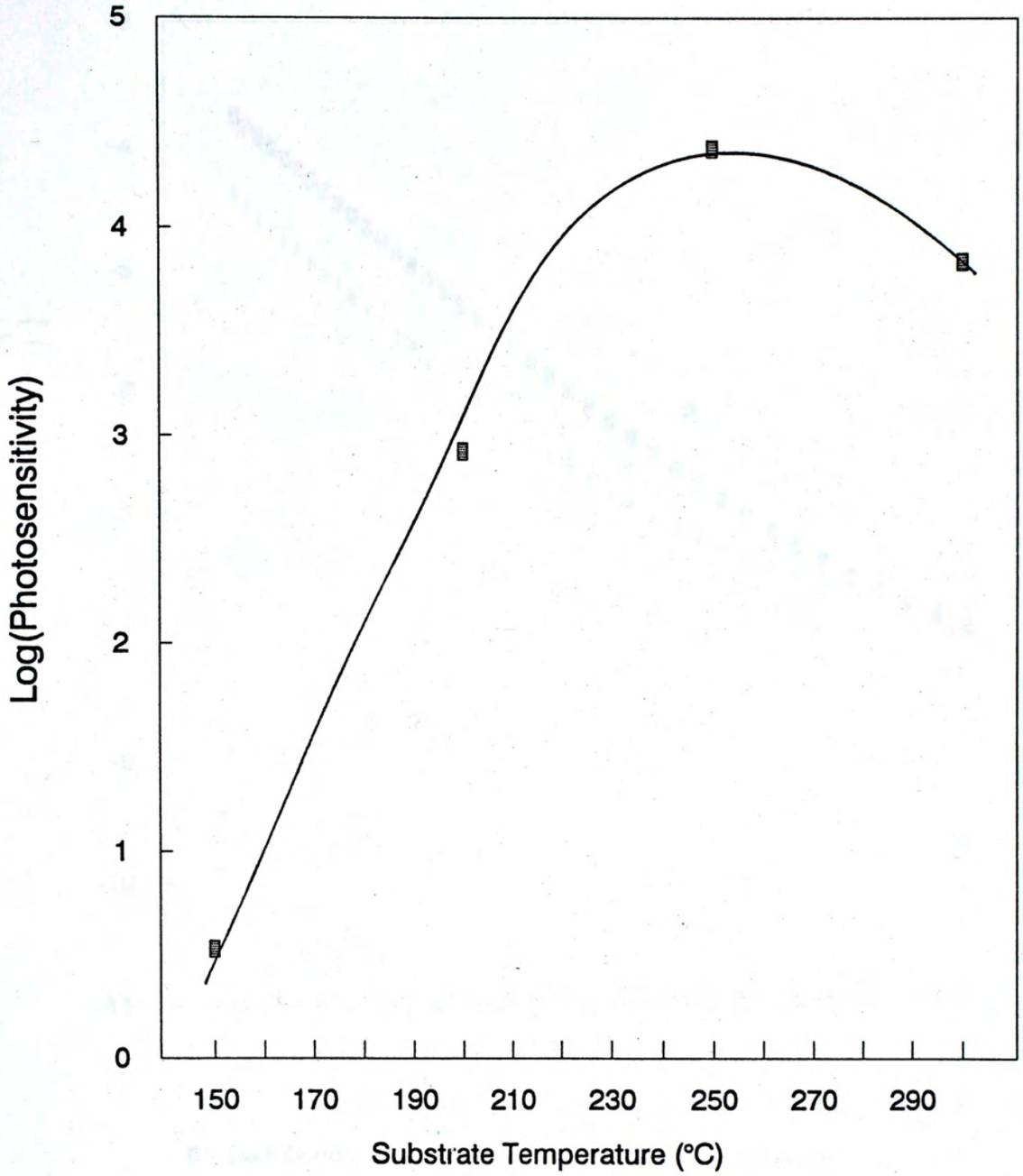

Figure 3-9d. A plot of room temperature photosensitivity under AM1 illumination against substrate temperature for reactively evaporated a-Si:H.

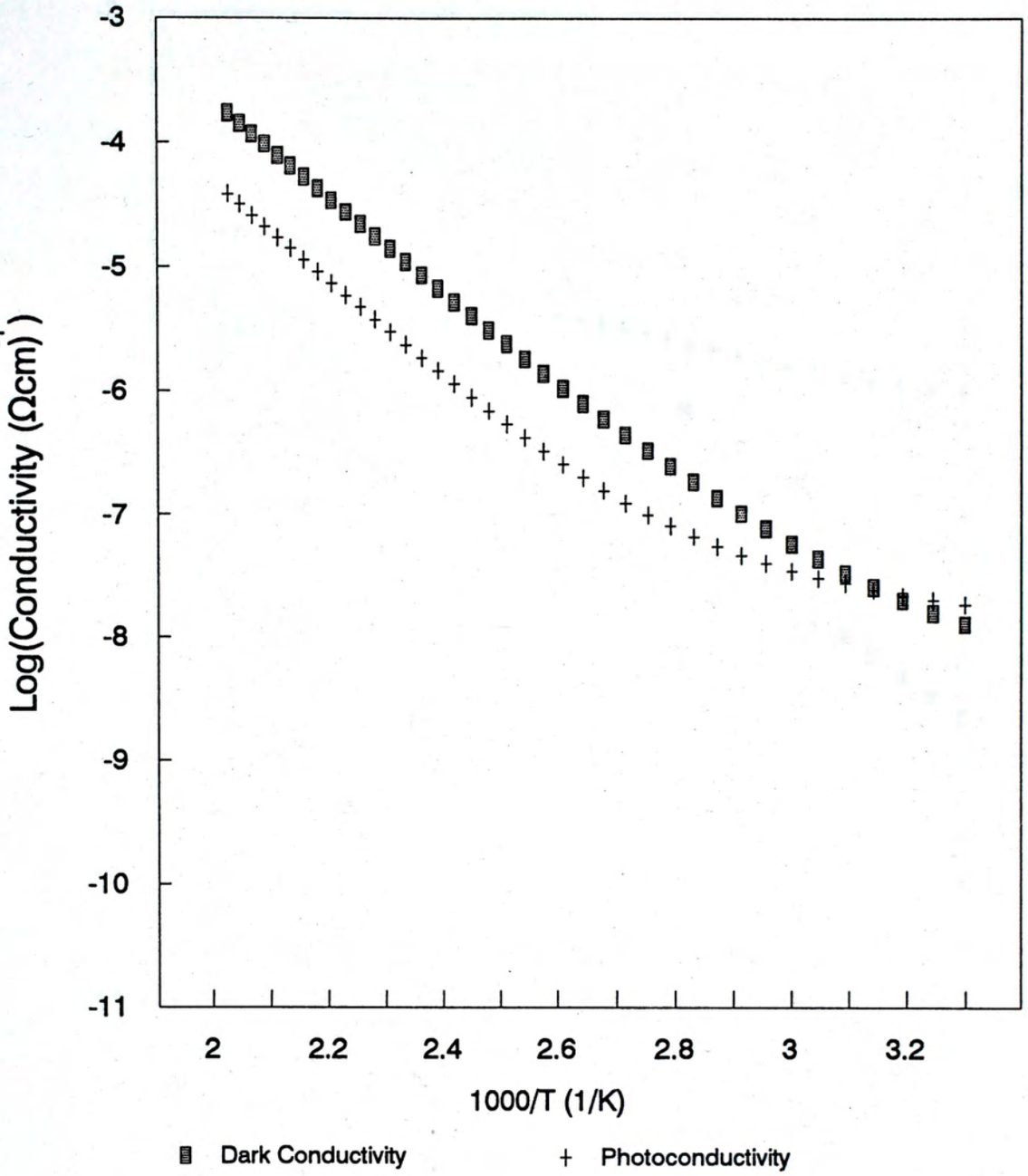

Figure 3-10a. A plot of temperature dependent conductivities for unhydrogenated a-Si deposited at Ts=250 °C. Photoconductivity was measured under AM1 illumination.

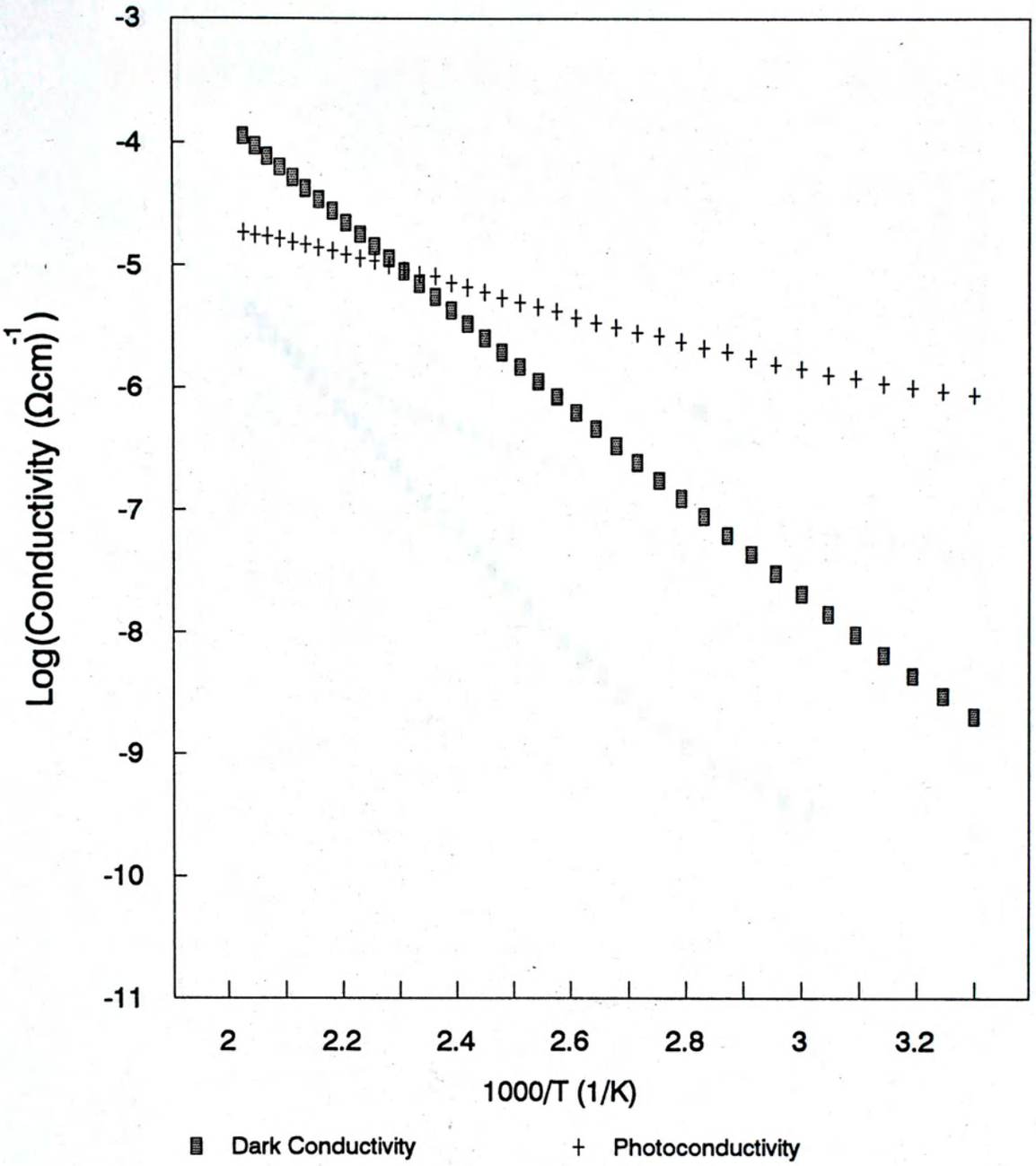

Figure 3-10b. A plot of temperature dependent conductivities for posthydrogenated a-Si:H deposited at Ts=250 °C. Photoconductivity was measured under AM1 illumination.

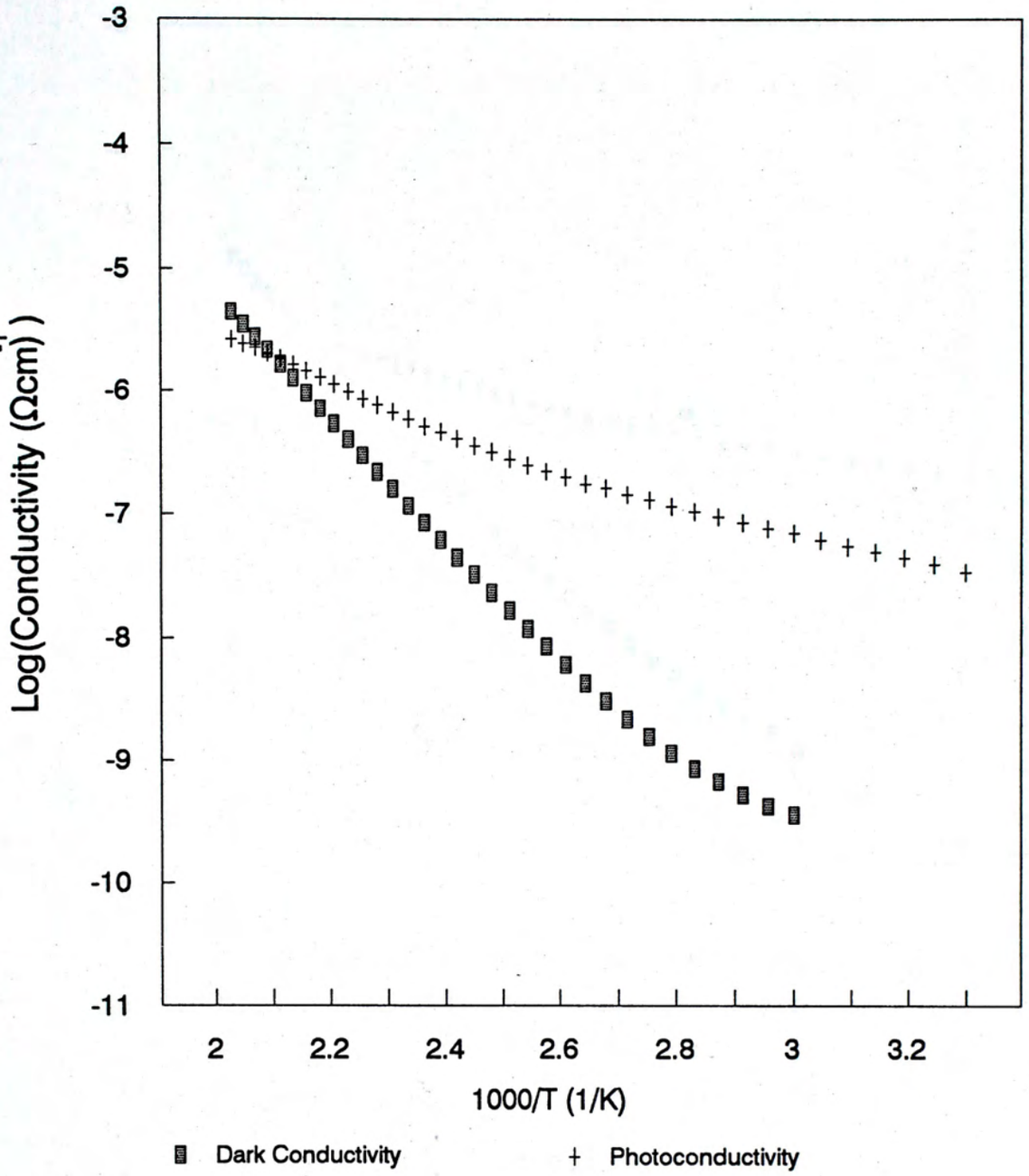

Figure 3-10c. A plot of temperature dependent conductivities for reactively evaporated a-Si:H deposited at Ts<150 ℃.
Photoconductivity was measured under AM1 illumination.

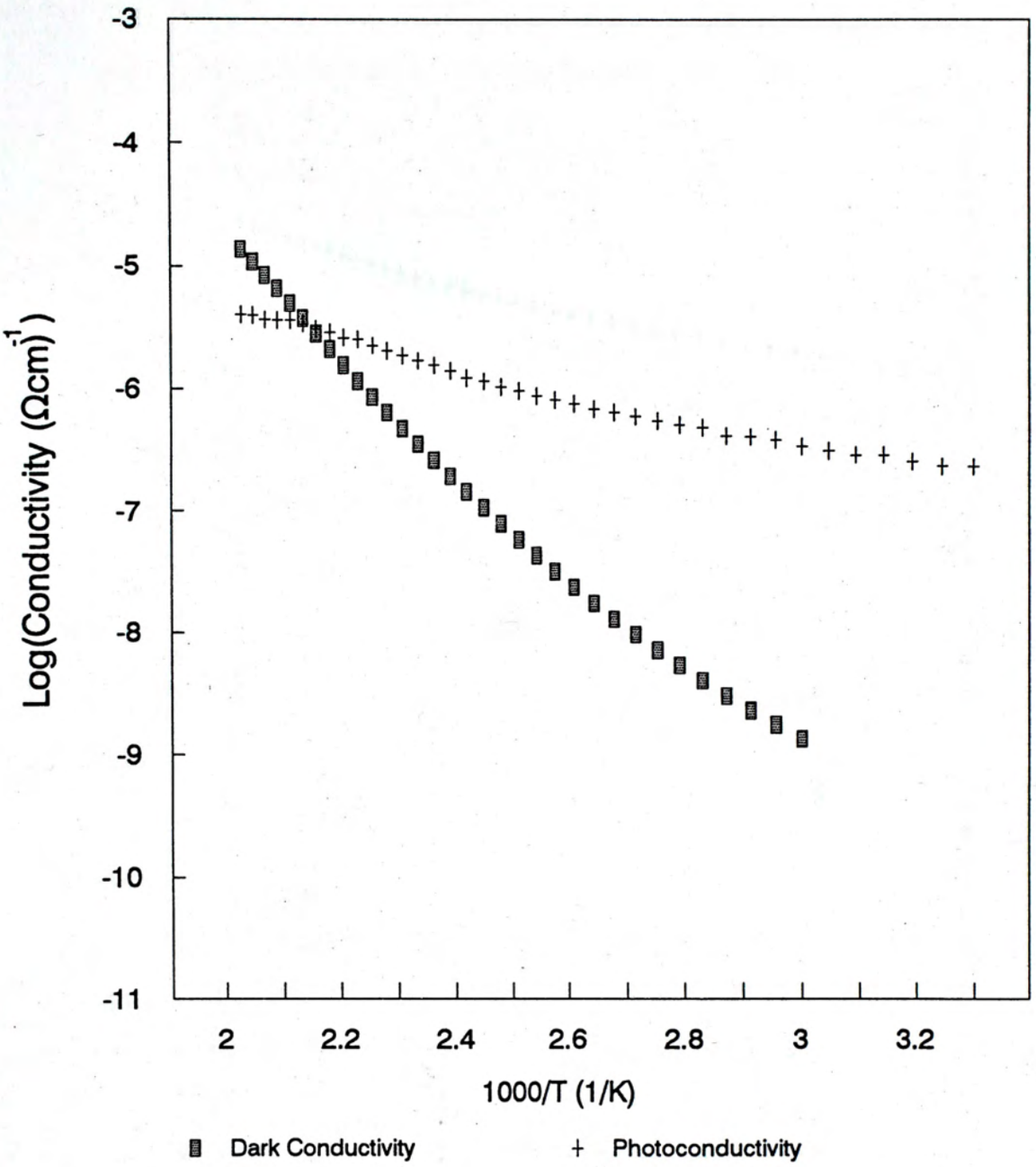

Figure 3-10d. A plot of temperature dependent conductivities for reactively evaporated a-Si:H deposited at Ts=200 °C.
Photoconductivity was measured under AM1 illumination.

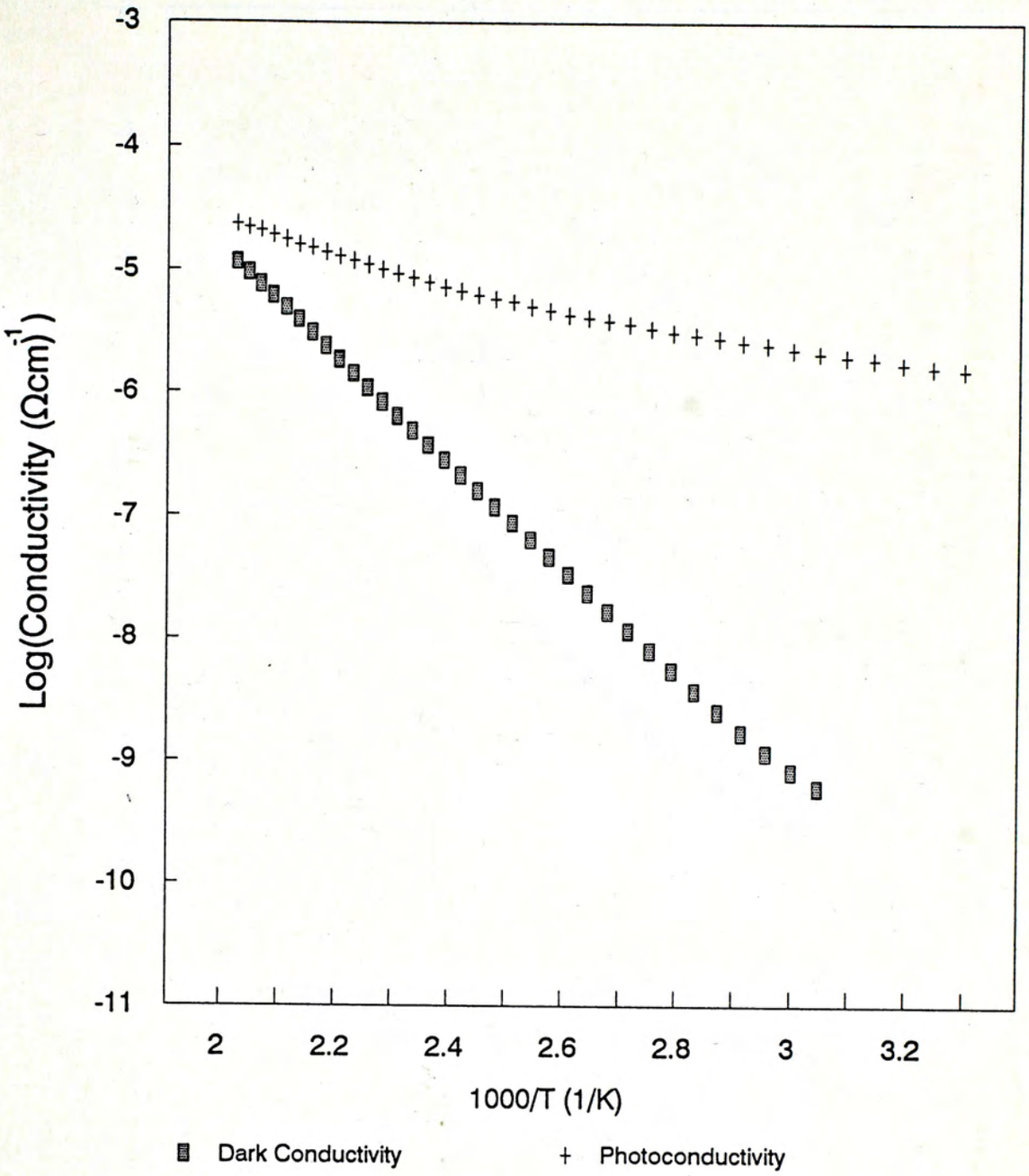

Figure 3-10e. A plot of temperature dependent conductivities for reactively evaporated a-Si:H deposited at Ts=250 °C. Photoconductivity was measured under AM1 illumination.

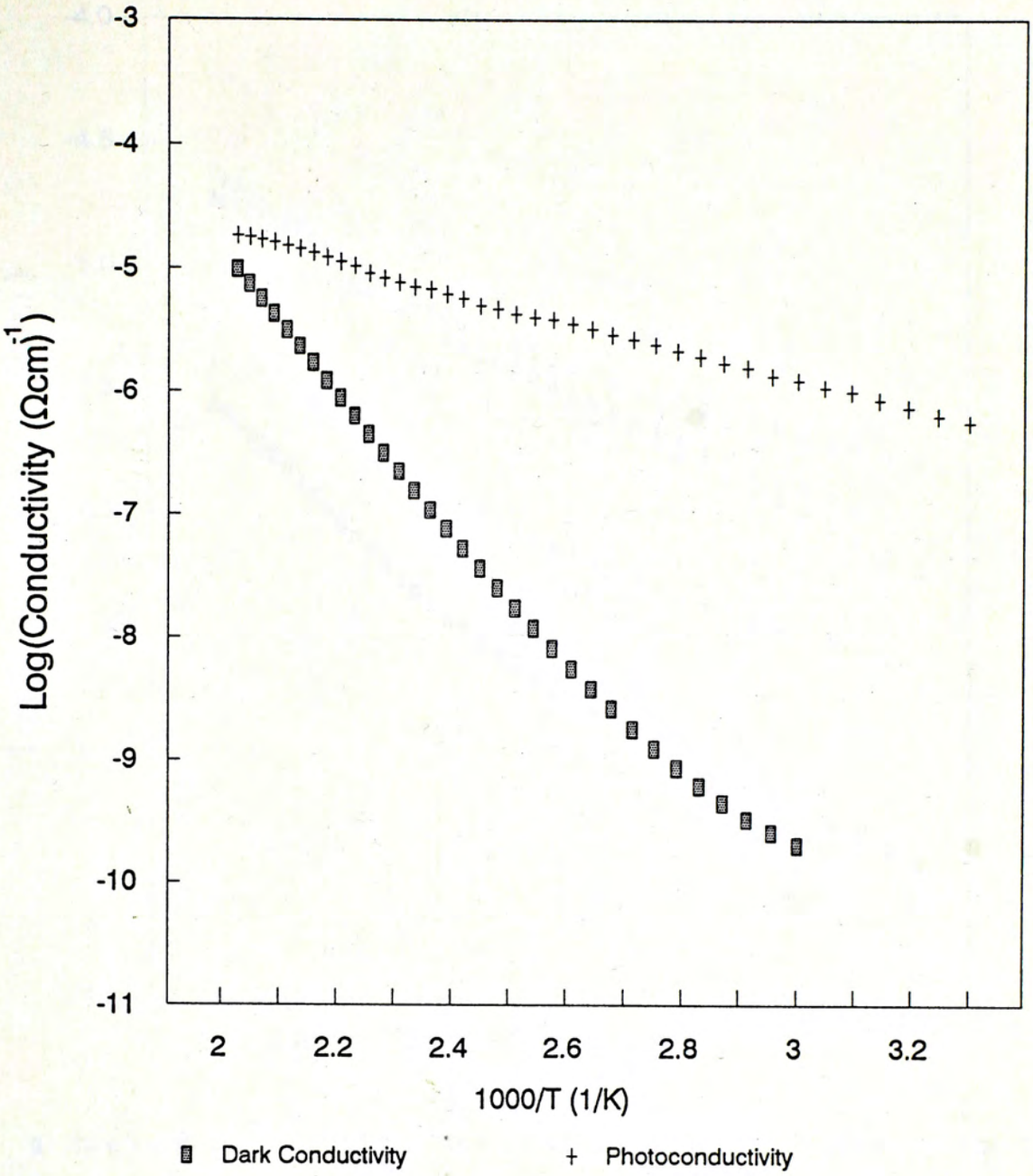

Figure 3-10f. A plot of temperature dependent conductivities for reactively evaporated a-Si:H deposited at Ts=300 °C. Photoconductivity was measured under AM1 illumination.

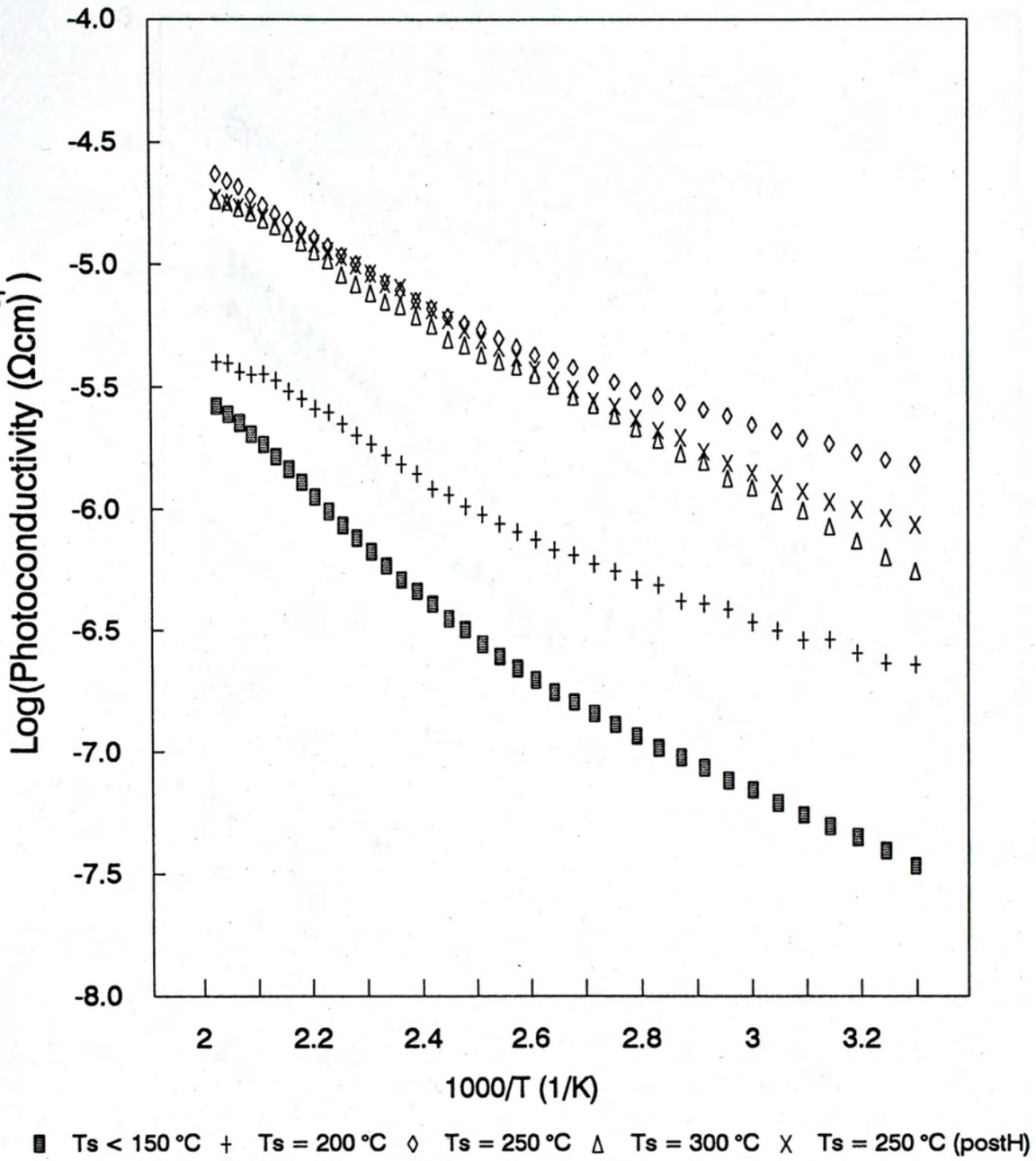

Figure 3-11a. A plot of temperature dependent photoconductivities for differently prepared a-Si.
Photoconductivity was measured under AM1 illumination.

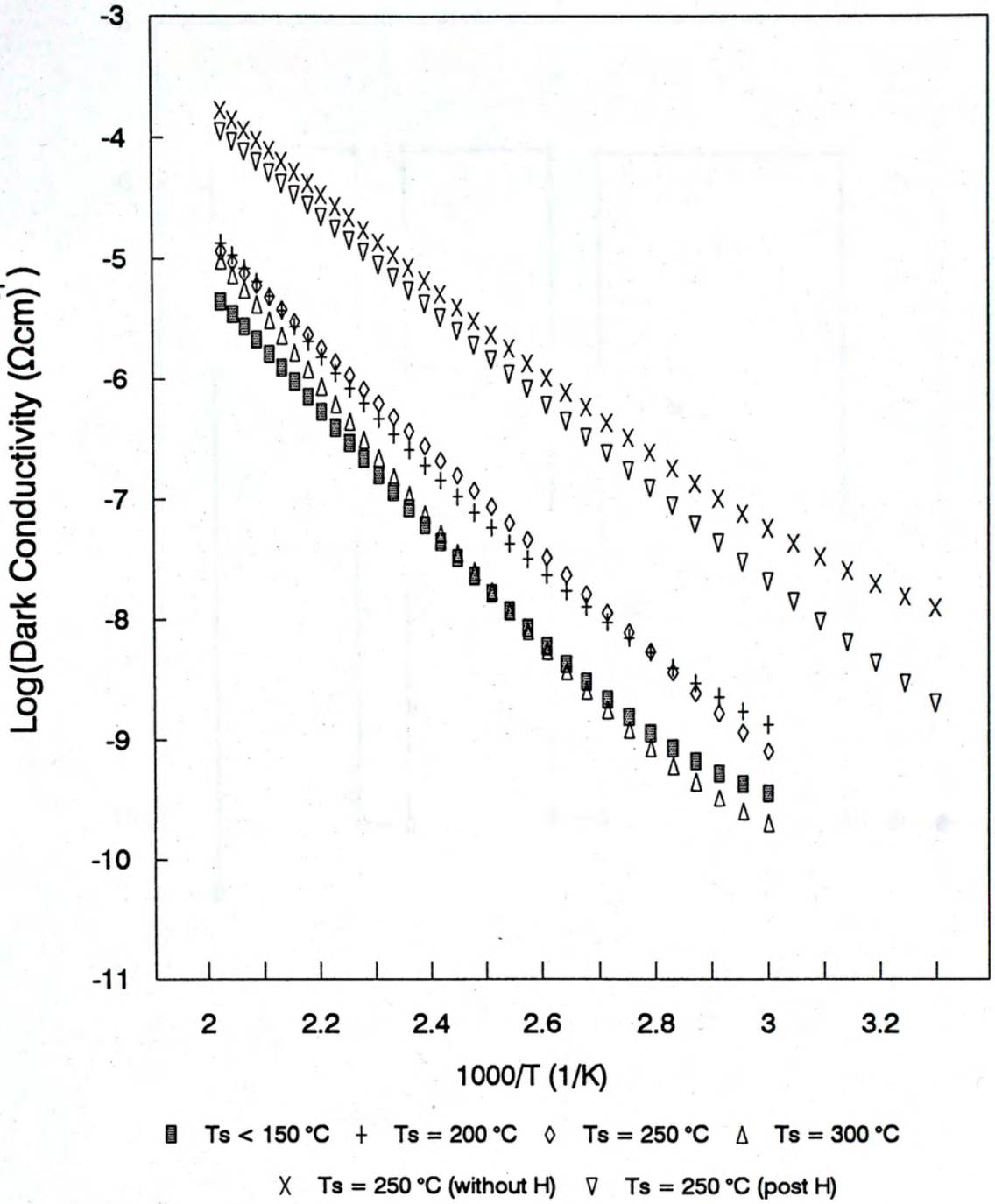

Figure 3-11b. A plot of temperature dependent dark conductivities for differently prepared a-Si.

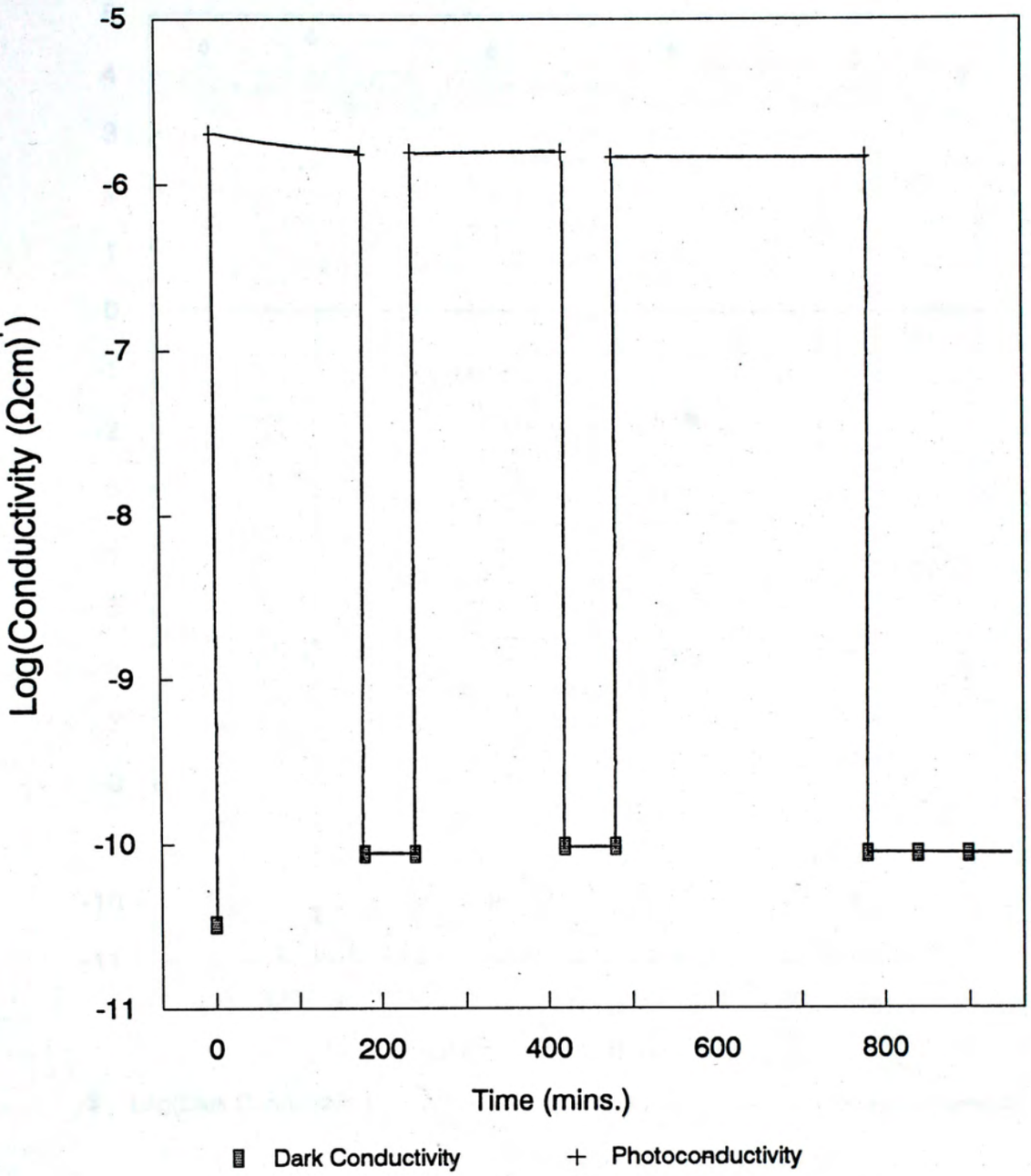

Figure 3-12. A measure of optical stability of reactively evaporated a-Si:H deposited at Ts=250 °C. Photoconductivity was measured under AM1 illumination.

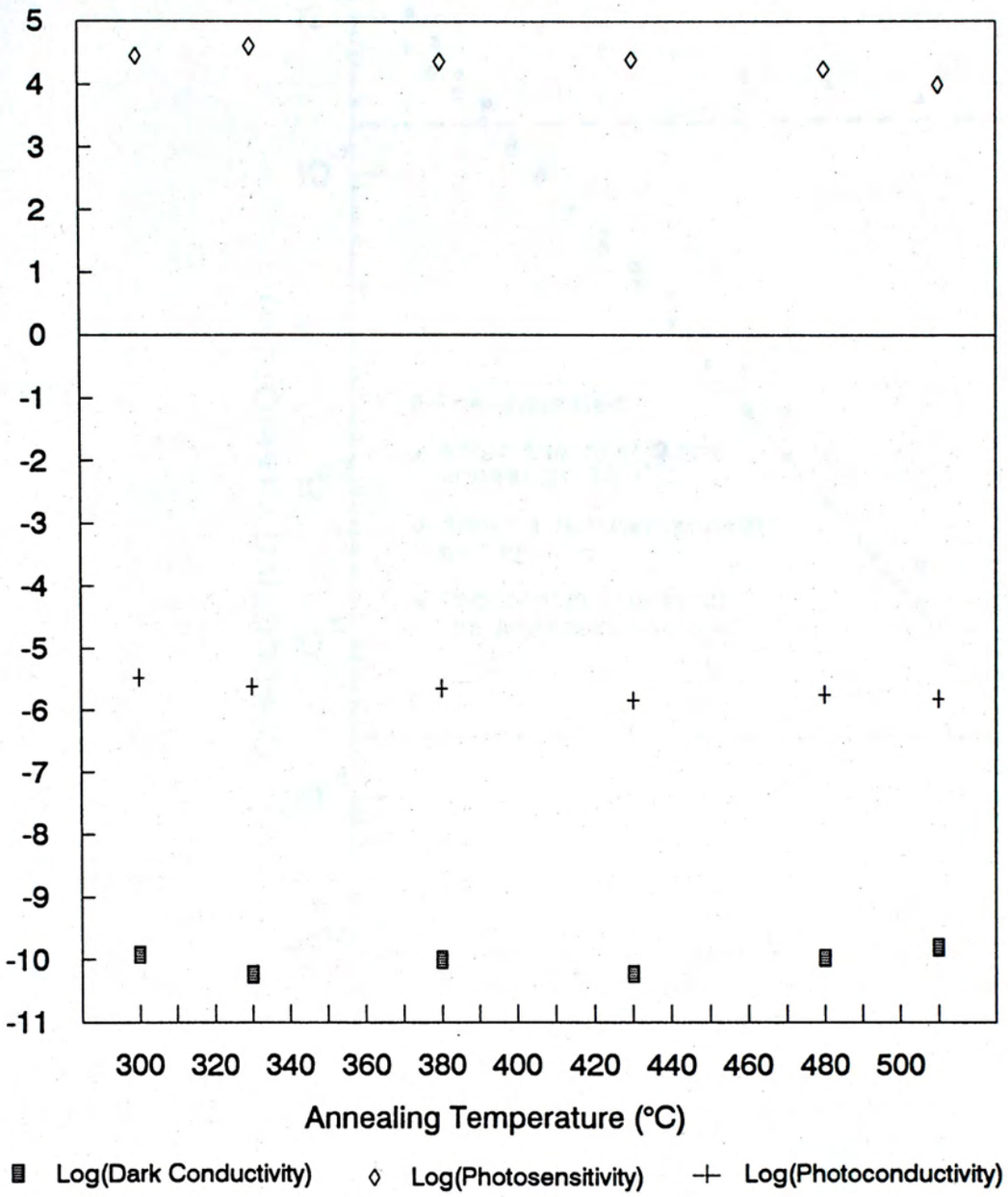

Figure 3-13. A measure of thermal stability of reactively evaporated a-Si:H deposited at Ts=250°C. Photoconductivity was measured under AM1 illumination.

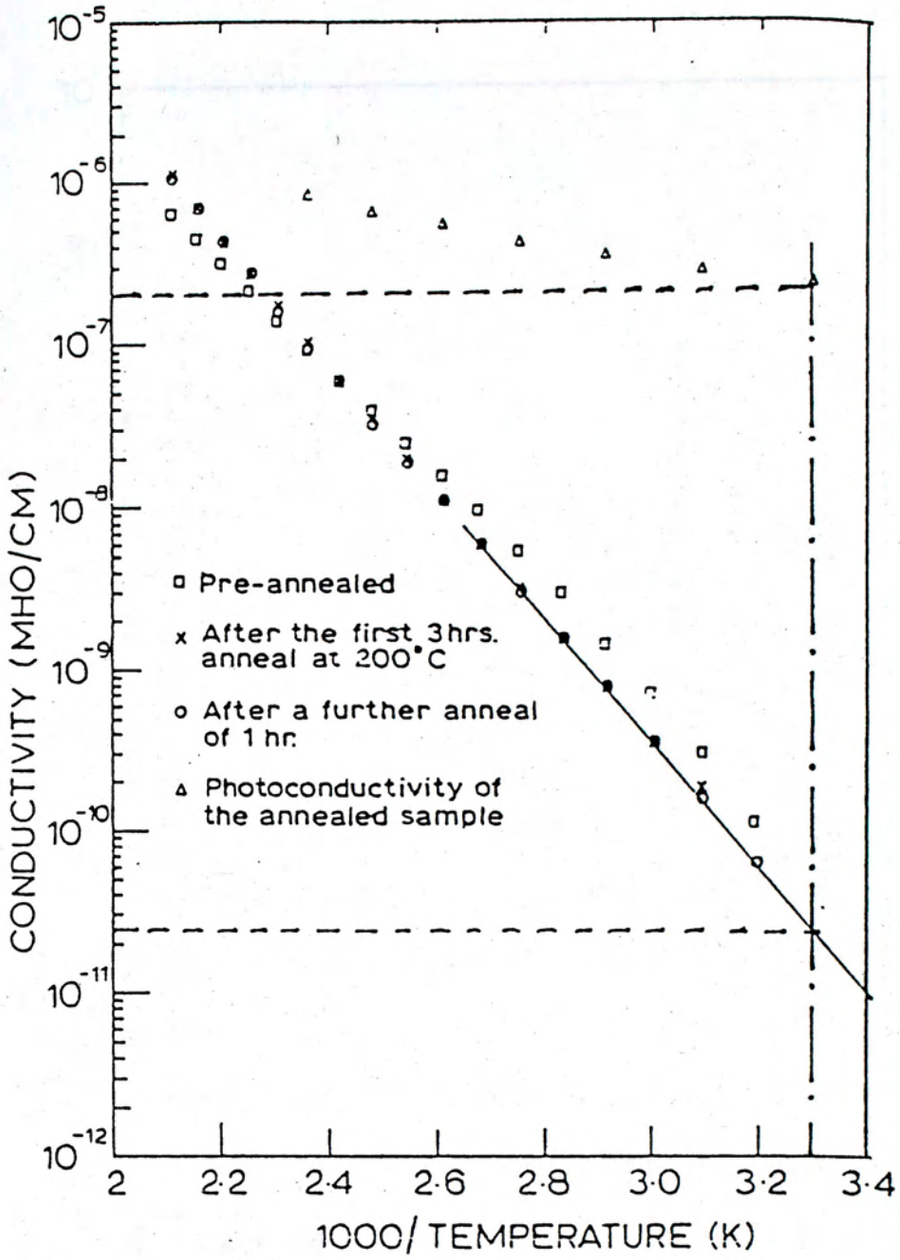

Figure 3-14. Conductivity/temperature plot showing thermal stability and photoconductivity for an intrinsic BARE film (J.C. Anderson et al., 1986).

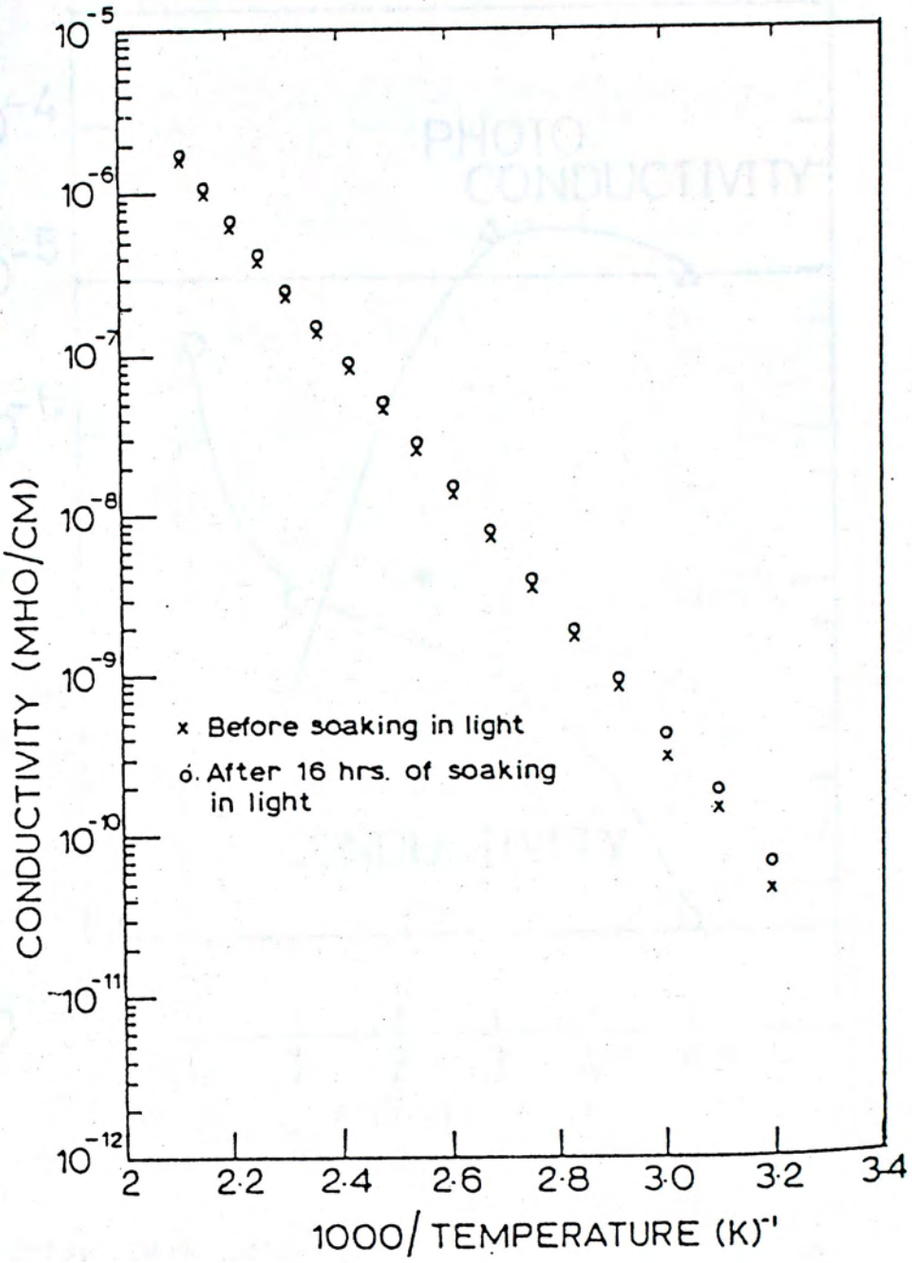

Figure 3-15. Conductivity/ temperature plot before and after irradiation in AM1 light fo 16 hr (J.C. Anderson et al., 1986).

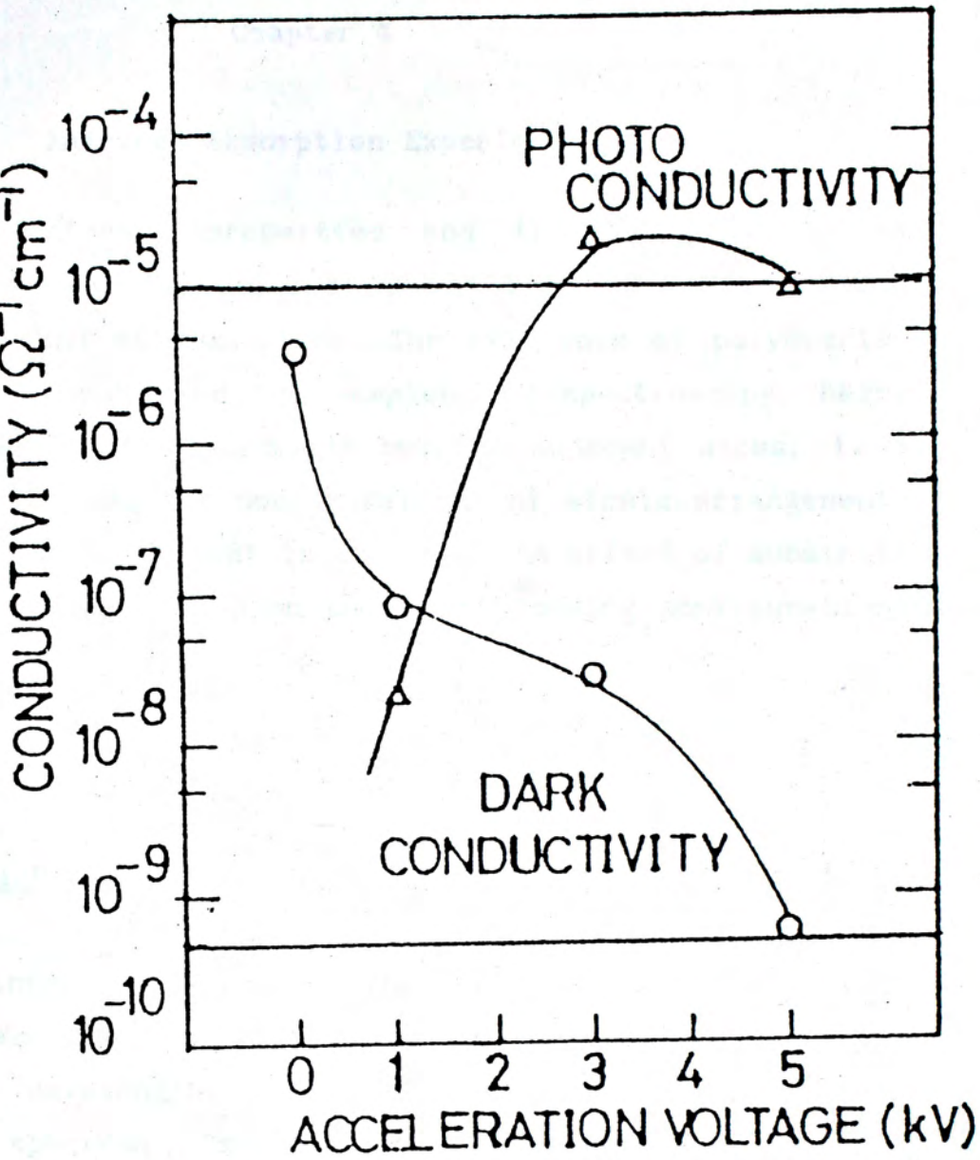

Figure 3-16. Dark conductivity and photoconductivity of the undoped films as a function of the acceleration voltage, Ts = 220 °C (I. Yamada et al., 1982).

Chapter 4

Infrared Absorption Experiment

The opto-electronic properties and thermal stability of a-Si:H are believed to be related to the bonding configurations between hydrogen and silicon atoms. The existence of polyhydride bondings is said to degrade the samples. IR spectroscopy, being sensitive to the vibrational modes between adjacent atoms, is a useful tool for probing the configurations of atomic arrangement. The purpose of this experiment is to study the effect of substrate temperature during deposition on the final bonding configurations of our a-Si:H films.

A) Introduction :

A.1 General Descriptions:

The infrared region of the electromagnetic radiation spectrum encompasses wave numbers from about 12,800 to 10 cm^{-1} or wavelengths from 0.78 to 1000 μm. Usually, the infrared spectrum is divided into near-, mid- and far-infrared radiation; rough limits of each region are shown in Table 4-1.

Region	Wavelength(λ) Range, μm	Wavenumber($\bar{\nu}$) Range, cm^{-1}
Near	0.78 to 2.5	12,800 to 4000
Middle	2.5 to 50	4000 to 200
Far	50 to 1000	200 to 10
Mostly used	2.5 to 15	4,000 to 670

Table 4-1

Generally, infrared radiation is not energetic enough to bring about electronic transitions like the ones with ultraviolet and visible radiation. So, absorption of infrared radiation in solids is largely confined to excitation of various vibrational states of atomic bonds, which requires much lower energy. In the case of a-Si:H, due to a difference

in electronegativity between silicon and hydrogen atom, a regular fluctuating dipole field is established when the atomic species vibrate. If an incoming I.R. radiation with frequency ν matches this fluctuating frequency, a net transfer of energy occurs that results in a change of vibrational amplitude of the atomic species, with subsequent absorption of the radiation.

A.2 Types of Atomic Vibrations :

Atomic vibrations fall into two basic categories, namely, stretching and bending. A stretching vibration involves a continuous change in the interatomic distance along the axis of the bond between two atoms. Bending vibrations are characterized by a change in the angle between two bonds and are of four types : scissoring, rocking, wagging and twisting. The various types of vibrations were shown schematically in Figure 4-1.

A.3 Infrared Spectroscopy of a-Si:H :

The presence of hydrogen in glow-discharge produced a-Si was firstly detected by both hydrogen evolution (A.Trisk et al. 1975) and IR absorption experiment (J. Knights et al. 1976). However, the evolution experiment gave no way about how hydrogen was incorporated into the parent lattice. The first identification of the atomic arrangements of bonded H-atoms in a-Si:H alloys were done by Brodsky et al.(1977). Further clarification through experiments and modelling was given by J.C. Knights, G. Lucovsky and R.J. Nemanich. Assignments of vibrational modes for a-Si:H are shown in Figure 4-2 and tabulated in Table 4-2. However, one should be cautioned that such assignments are not unique (P.J. Zanzucchi et al.,1977; Da-Wen Pang et al.,1986; F. Demichelis et al.,1985).

Group	Freguency (cm^{-1})	Assignment
SiH	2000	Stretching
	630	Bending
SiH_2	2090	Stretching
	880	Bend-scissors
	630	Rocking
$\{SiH_2\}_n$	2090-2100	Stretching
	890	Bend-scissors
	845	Wagging
	630	Rocking
SiH_3	2140	Stretching
	907	Symmetric Deformation
	862	Degenerate Deformation
	630	Rocking

Table 4-2. Assignments of the Principal IR Absorption Bands in a-Si:H to Local Structural Groups: SiH; SiH_2; $\{SiH_2\}_n$; SiH_3 (Lucovsky et al., 1979)

A.4 Effect of Substrate Temperture on Bonding Configuration :

As pointed out by many authors (e.g. G. Lucovsky, 1992), the local bonding arrangement varies systematically with the substrate temperature T_s, during film deposition (Figure 4-3, 4-4).

Films deposited at substrate temperatures <100°C contain bonded hydrogen predominantly in the polymerized or polyhydride bond arrangement represented by the structural formula, $\{SiH_2\}_n$, whereas films deposited at T_s >250°C contain predominantly monohydride or SiH groups (J.C. Knights et al. 1977). In 1989, G. Lucovsky et al. further pointed out that for different deposition methods, namely, glow-discharge, reactive magnetron sputtering and remote plasma-enhanced chemical vapour deposition, the distribution of hydrogen between monohydride and polyhydride groups is not uniquely determined by the substrate temperature, but also by the total amount of bonded hydrogen in the film (Figure 4-5, 4-6). So in order to investigate the effect of substrate

temperature, we have to keep other parameters except T_s fixed during deposition.

B) Experimental method:

Amorphous Si:H was deposited on boron-doped silicon wafers (10-20 Ωcm), 250 μm thick, orientation (110) cut into pieces of 1 cm × 2.5 cm. The substrate temperature, T_s, varies from 160°C to 300°C. The procedure for cleaning the substrates and deposition have been described in Chapter 2. α-step measurements have been performed to obtain the film thickness.

IR absorption spectra were taken by a double beam spectrometer (Unicam SP 1100ES) with wavenumbers ranging from 400 cm^{-1} to 2500 cm^{-1}. A schematic plot of the double-beam spectrometer is given in Figure 4-7. A piece of uncoated substrate was used as reference. The intensity of IR beams passing through the sample and the reference wafer was measured and their difference in intensity was recorded.

C) Results:

Figure 4-8 shows the two main absorption bands observed in our a-Si:H prepared at different substrate temperatures, T_s. The band labelled I and II were centred around 2040 cm^{-1} and 640 cm^{-1} respectively. The spectra between these two bands contained features varying in a less systematical way. This may be due to different surface morphologies existing among samples prepared at different T_s. For the present study, we focus on the above mentioned absorption bands. From Figure 4-8, it can be seen that as T_s was increased from 160°C to 250°C, the magnitude of absorption band II increased from an negligible amount to a maximum at T_s = 250°C. As T_s was further increased, this band began to diminish and eventually could not be detected at T_s = 300°C. For absorption band I, at T_s = 160°C, a broad absorption can be observed. This implies that more than one absorption band coexists under the envelope. As T_s was increased, the width of this band became narrower, accompanied by a decrease in magnitude.

Further increasing T_s to 300°C, this absorption band was beyond the limit of detection.

D) Discussions:

D.1 Identification of the two absorption bands:

Band I:

Band I absorption is associated with wavenumbers around 2000 - 2200 cm^{-1}. The width and magnitude of the absorption depended much on the substrate temperature. The assignment of IR frequency with a particular vibrational mode of a particular atomic group is an important task and has been done by many authors. Results tended to show that the assignment depended much on the local bonding environment and hence the particular deposition technique used (P.J. Zanzucchi et al 1977, Da-Wen Pang et al 1986).

For examples, F. Demichelis et al (1986) assigned 2000 - 2100 cm^{-1} to the stretching modes for magnetron sputtered a-Si. G. Lucovsky et al (1989) assigned 2000 cm^{-1} to the stretching mode of SiH, 2090 cm^{-1} to the stretching mode of SiH_2 and 2090 - 2100 cm^{-1} to the stretching mode of $\{Si_2H_n\}$ for reactive magnetron sputtered and remote plasma enhanced chemical vapor deposited a-Si. P.J. Anderson et al (1986) assigned 2000 cm^{-1} to the stretching mode of SiH and 2100 cm^{-1} to the stretching mode of SiH_2 for biased reactive evaporated a-Si. P.J. Zanzucchi et al (1979) assigned 2040 - 2050 cm^{-1} to the stretching mode of SiH for glow-discharge produced a-Si.

From the above reported data, one can assign 2000 - 2050 cm^{-1} to the stretching mode of SiH; 2050 - 2090 cm^{-1} to the stretching mode of SiH_2 and 2090 - 2100 cm^{-1} to the stretching mode of $\{SiH_2\}_n$. From our study, at least three kinds of atomic groups can be identified, though they are not necessarily present at all

substrate temperatures. The absorption at ≅ 2040 cm^{-1}, ≅ 2070 cm^{-1}, 2100 cm^{-1} can be identified as the stretching mode of SiH, SiH_2 and $\{SiH_2\}_n$ respectively, as described in the following section.

Band II:

Band II absorption corresponds to bond-bending vibrations with a wavenumber around 640 cm^{-1}. Again, the actual frequency seems to depend on the particular deposition technique used. Variation may be found within a range from 630 - 640 cm^{-1} (P.J. Zanzucchi et al 1977, Da-Wen Pang et al 1986, F.Demichelis et al 1985). Brodsky et al (1977) reported that 630 cm^{-1} was always a single band which could not be resolved into two or more components. However, several kinds of atomic groups can at the same time contribute to the absorption band, namely, the bending (or wagging) mode of SiH group, the rocking mode of SiH_2 group, $\{SiH_2\}_n$ group and SiH_3 group. Thus the stretching mode has to be taken together in order to determine which of them would prevail within the absorption band.

D.2 Effect of substrate temperature:

From Figure 4-8, the effect of increasing T_s is to decrease the width and magnitude of Band I. As mentioned earlierly, band I at low T_s should cover more than one absorption feature. In order to compare the gradual change in band I absorption along with different T_s and for the sake of preciseness, band I for each T_s was numerically fitted. To take the thickness variation of each sample into consideration, the IR transmission spectra has been converted into the corresponding absorption coefficient (Alpha) spectra according to the following formula:

$$\text{Alpha} = -\frac{\ln(\frac{I}{I_o})}{l} \qquad (4\text{-}1)$$

where I/I_o is the transmission percentage $\times$ 0.01

l is the thickness of the film.

The results are shown in Figure 4-9 to Figure 4-14.

For T_s = 160°C (Figure 4-9), Band I could be decomposed into three gaussian peaks. The peak centres are 2040 cm^{-1}, 2071 cm^{-1} and 2107 cm^{-1}, which can be identified to be the stretching mode of SiH group, SiH_2 group and $\{SiH_2\}_n$ group respectively. The area ratio of these three peaks were 80 : 6 : 14, showing that beside the monohydride and dihydride bondings a significant amount of hydrogen atoms are bonded in polymerized configuration within the silicon lattice.

For T_s = 200°C (Figure 4-10), band I could be decomposed into two gaussian peaks. The peak centres were 2041 cm^{-1} and 2074 cm^{-1}, and can be assigned to be the stretching mode of SiH group and SiH_2 group respectively. The area ratio of these two peaks were 94 : 6, showing that a significant amount of dihydride bondings present within the sample. Polyhydride groups no more exist.

For T_s = 250°C, 270°C and 290°C (Figure 4-11 - 4-13), band I could be fitted with a single gaussian peak with peak centre at $\cong$ 2041 cm^{-1}, corresponding to the stretching mode of SiH group. This implied that for $T_s \geq$ 250°C, hydrogen incorporated into the silicon lattice is in monohydride configuration only.

From the magnitude and width of band I, it can be deduced that at low T_s , large amount of hydrogen is

incorporated into the silicon lattice. As T_s increases, the band diminishes with a corresponding change from several bonding configurations into a predominant monohydride bonding configuration. Further increases in T_s made the incorporation of hydrogen difficult, As a result, band I disappears at T_s = 300°C.

Band II shows a more interesting change with increasing T_s. At T_s = 160°C, band II is negligible. However as T_s increases, its magnitude increased and reached a maximum at T_s = 250°C. From band I we know that at low T_s, larger amount of hydrogen is incorporated into the silicon lattice. So it is reasonable to assume that the large amount of hydrogen present suppresses the bending modes. It may be useful to compare this observation with those obtained by J.C. Anderson et al (1986), Shanks et al (1980) and W. Paul (1980). They found that the bend-scissors mode of SiH_2 was absent in spite of the fact that SiH_2 stretch mode at 2100 cm^{-1} was the dominant peak. Beyond T_s = 250°C, band II begins to diminish and becomes negligible at T_s = 300°C. This can be easily understood since at high T_s, the retention of hydrogen within the sample becomes difficult.

E) Conclusions:

The various atomic vibrational modes of different atomic groups were identified, and an optimum T_s for monohydride formation was found at $T_s \cong$ 250°C - 270°C, which is consistent with the conductivity measurements with an optimum photoconductivity and photosensitivity. It was also found that at low T_s polyhydrides exist in a significant amount, consistent with the findings of other authors. The absence of bending modes at low T_s may be due to the vast amount of hydrogen present which suppresses the changings of bond angles within the network and hence the bending modes.

Symmetric

Asymmetric

(a) Stretching vibrations

In-plane rocking

In-plane scissoring

Out-of-plane wagging

Out-of-plane twisting

(b) Bending vibrations

Figure 4-1. A schematic diagram showing the various types of atomic vibrations.

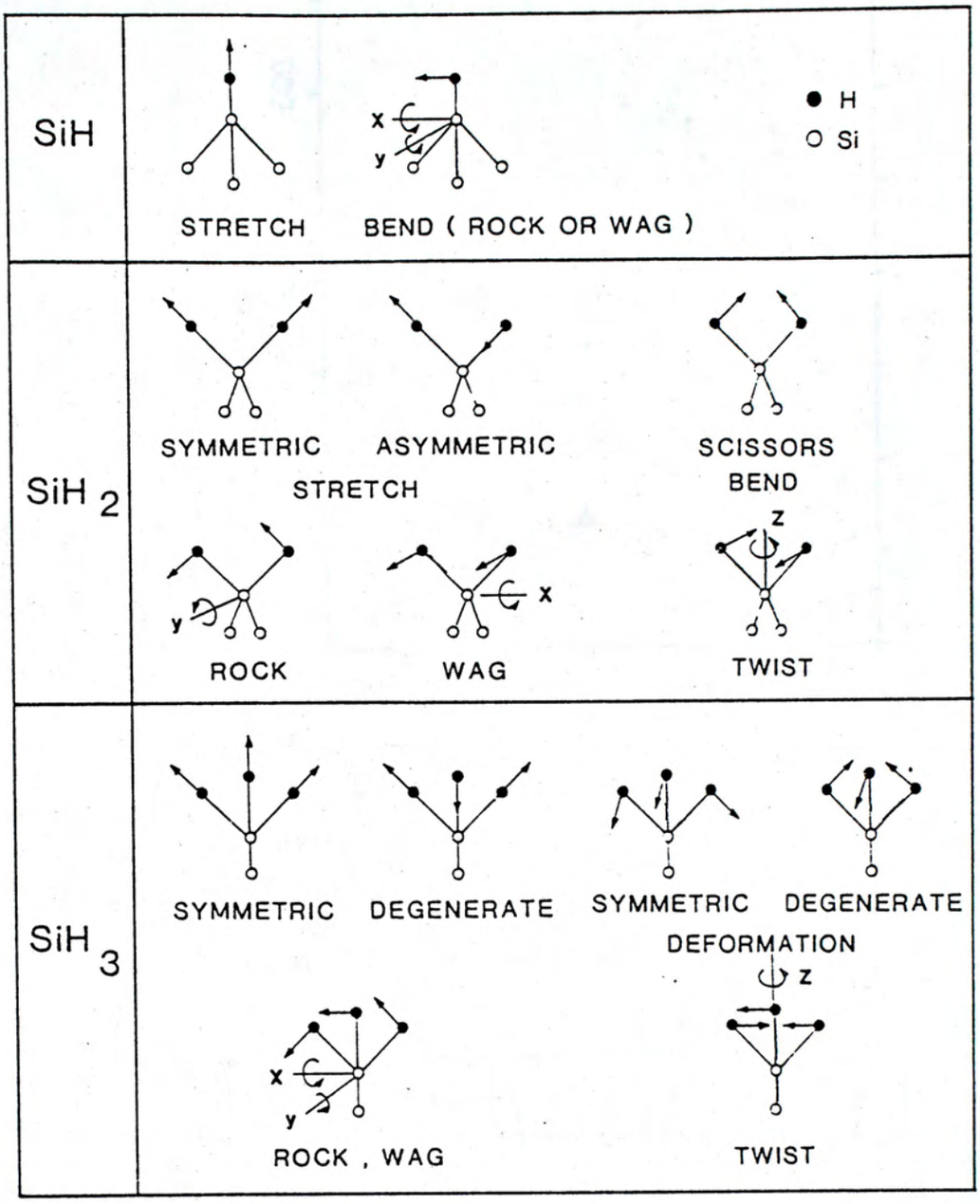

Figure 4-2. Local Si-H vibrations for SiH, SiH_2 and SiH_3 groups (Lucovsky et al., 1979).

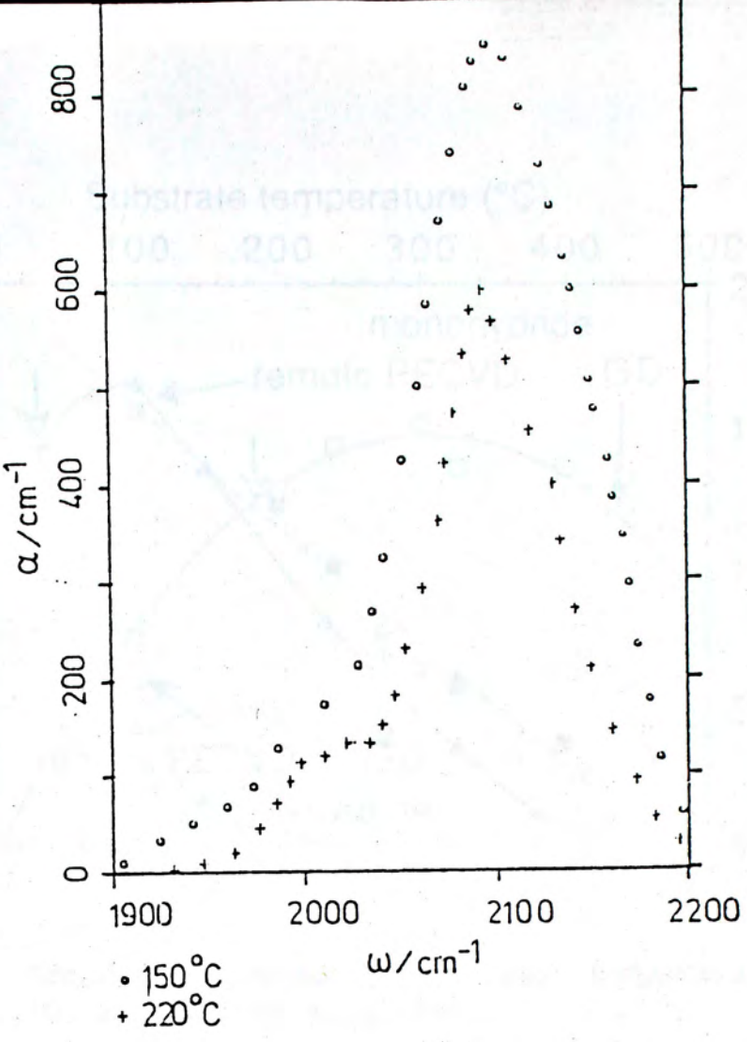

Figure 4-3. Infrared absorption spectra of two samples prepared at substrate temperatures of 150 and 220 °C (P. Dellafera et al., 1980).

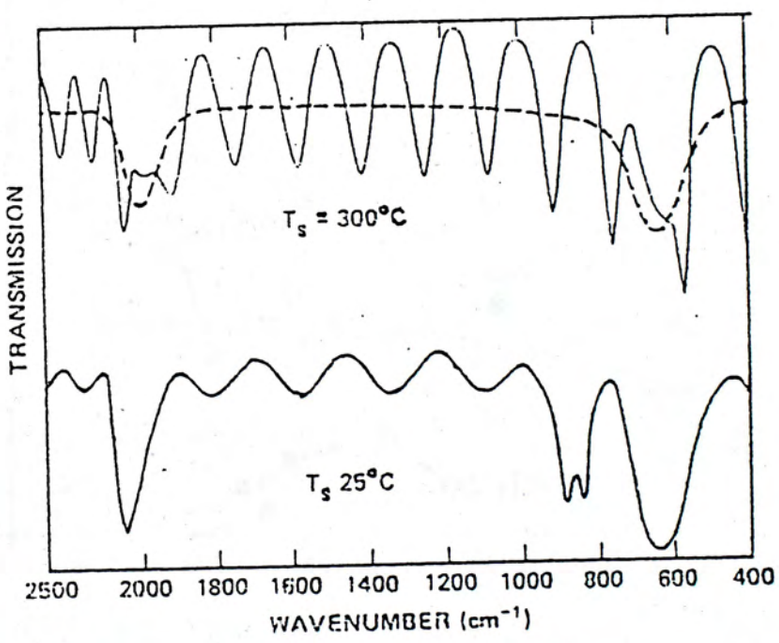

Figure 4-4. Infrared transmission spectra of a-Si:H films deposited at substrate temperatures of 25 and 300 °C. The dashed line in the upper trace represents the transmission with interference effects removed (J.C. Knights et al., 1977).

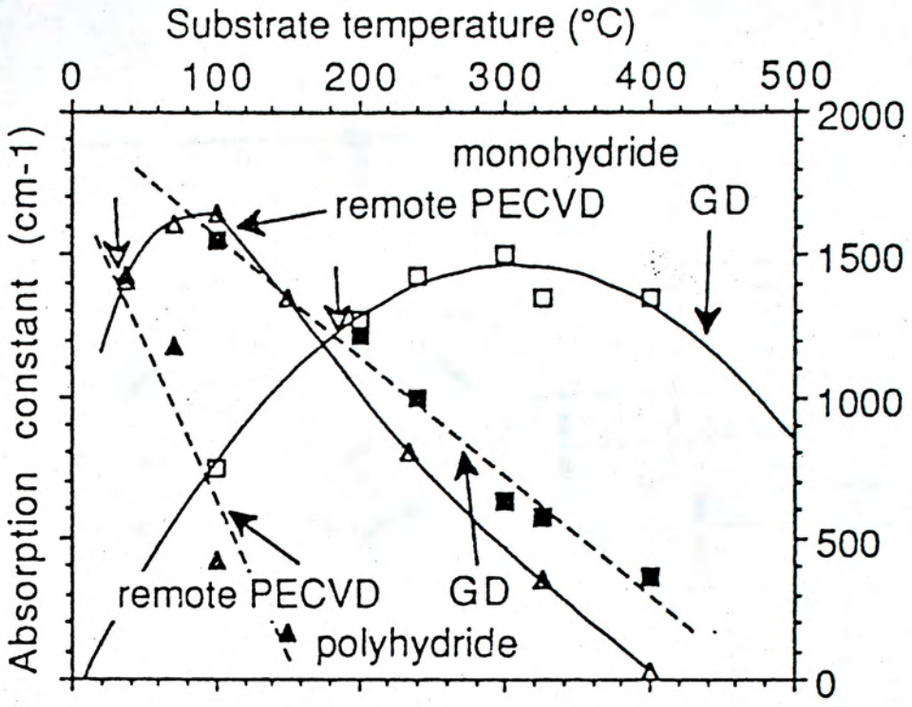

Figure 4-5. Absorption versus substrate temperature (G. Lucovsky et al., 1989).

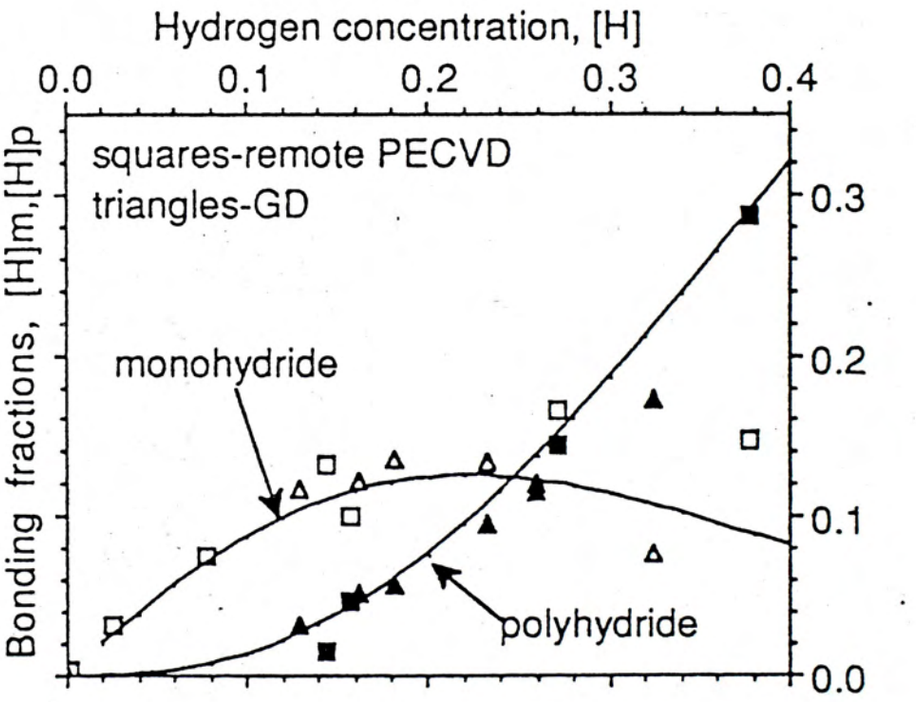

Figure 4-6. Bonding fraction versus [H] (G. Lucovsky et al., 1989).

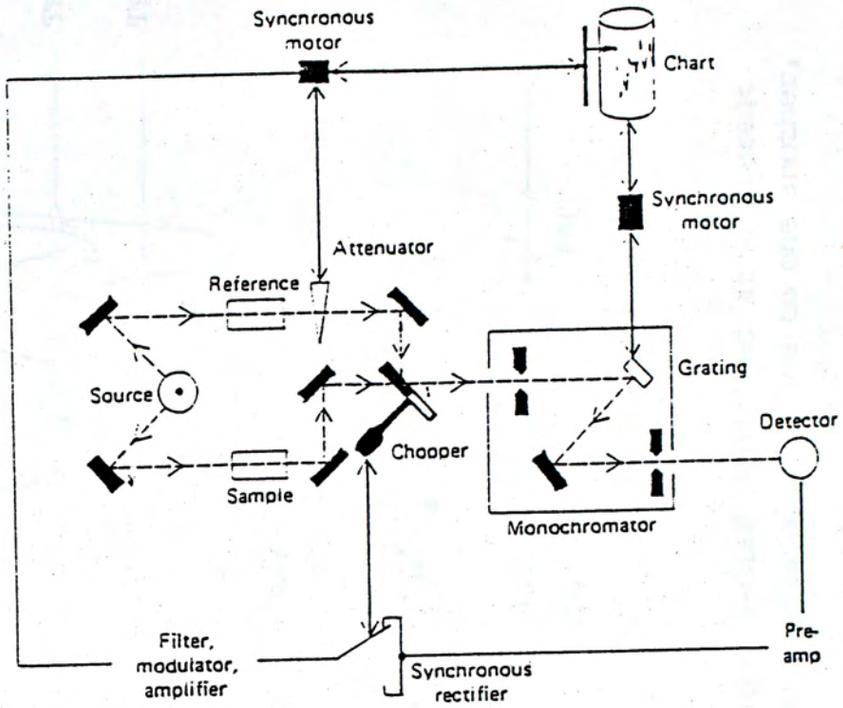

Figure 4-7. A schematic plot of a double beam spectrometer.

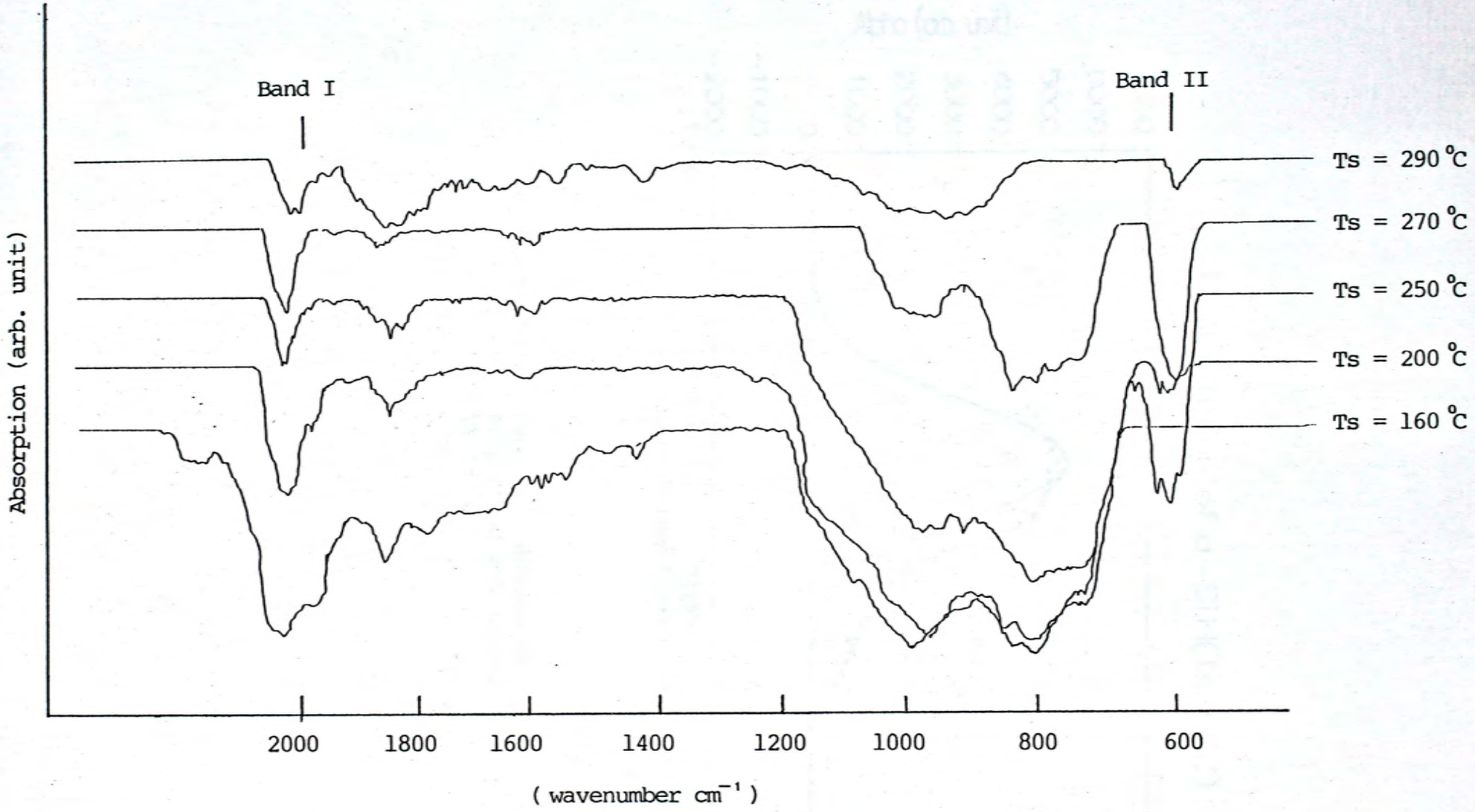

Figure 4-8. IR absorption spectra of reactively evaporated a-Si:H deposited at different substrate temperatures. The curves have been displaced relative to one another, but they are of the same scale.

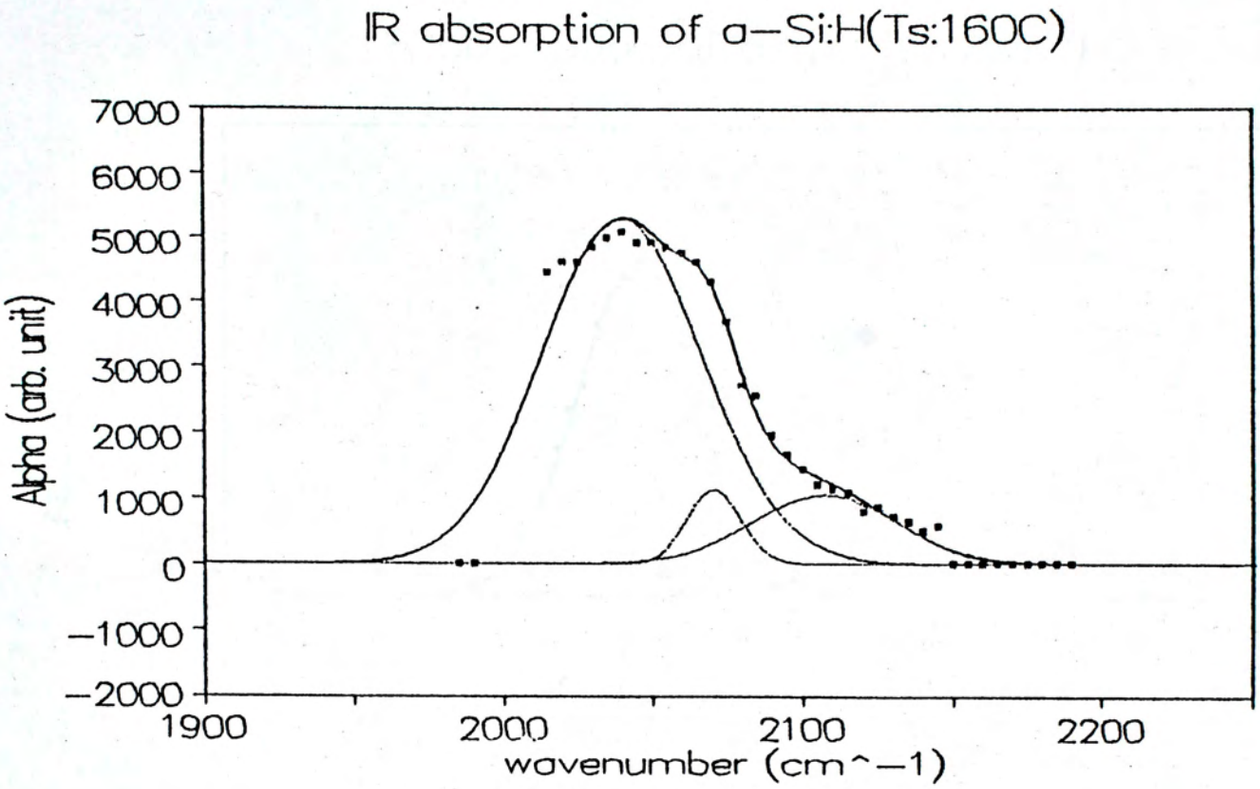

Figure 4-9. Band I absorption of reactively evaporated a-Si:H deposited at Ts=160°C.

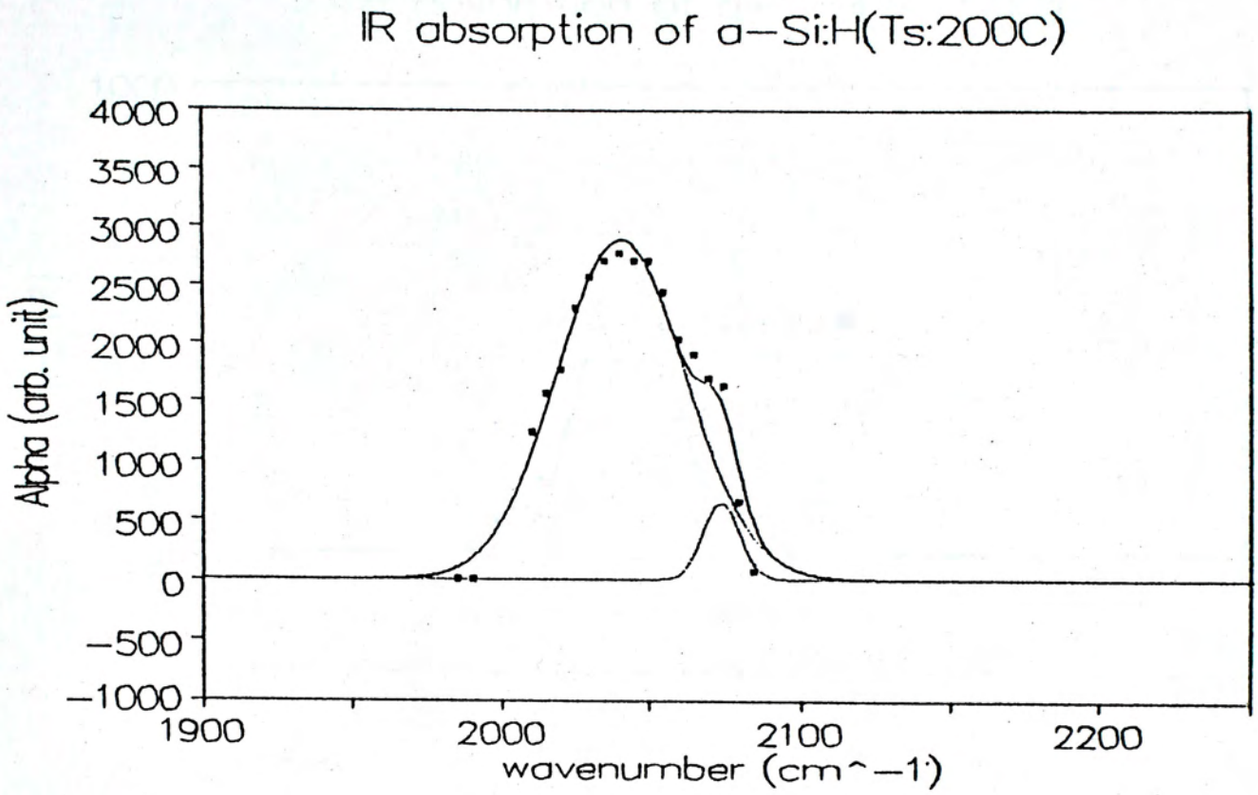

Figure 4-10. Band I absorption of reactively evaporated a-Si:H deposited at Ts=200°C.

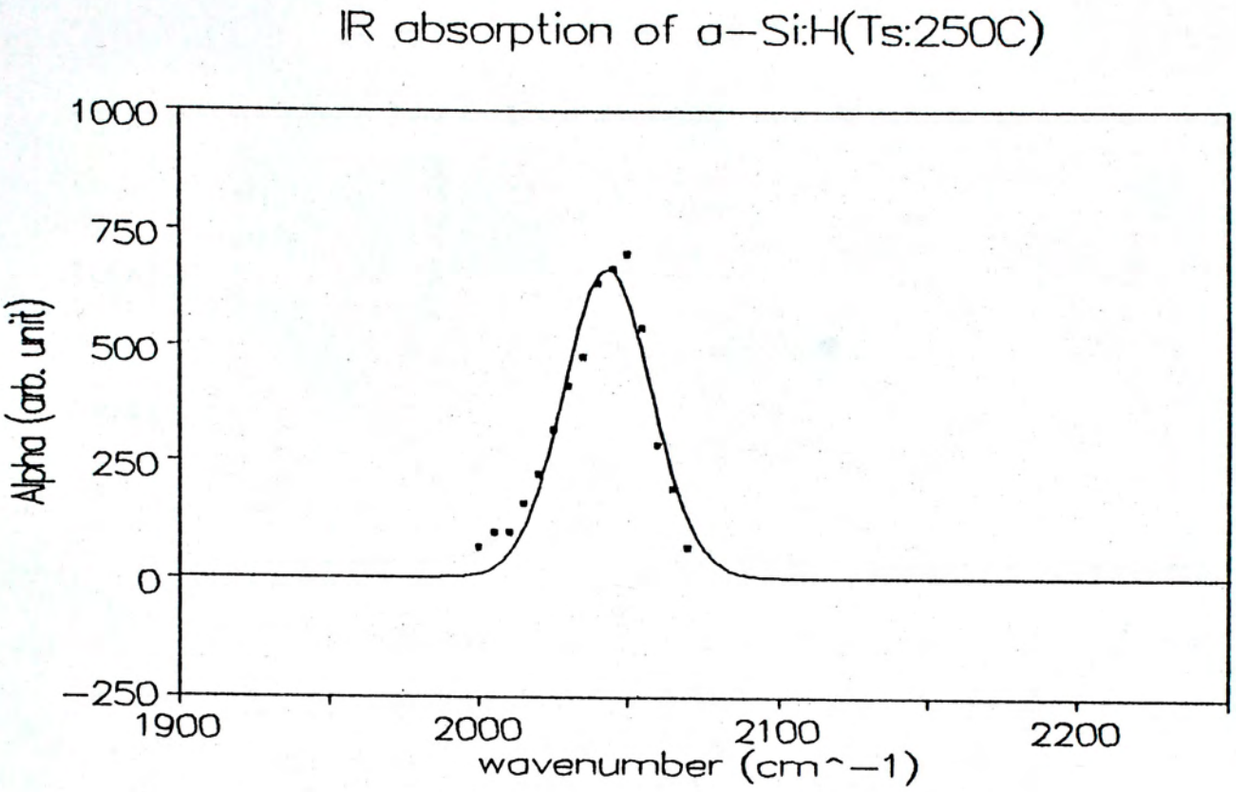

Figure 4-11. Band I absorption of reactively evaporated a-Si:H deposited at Ts=250 °C.

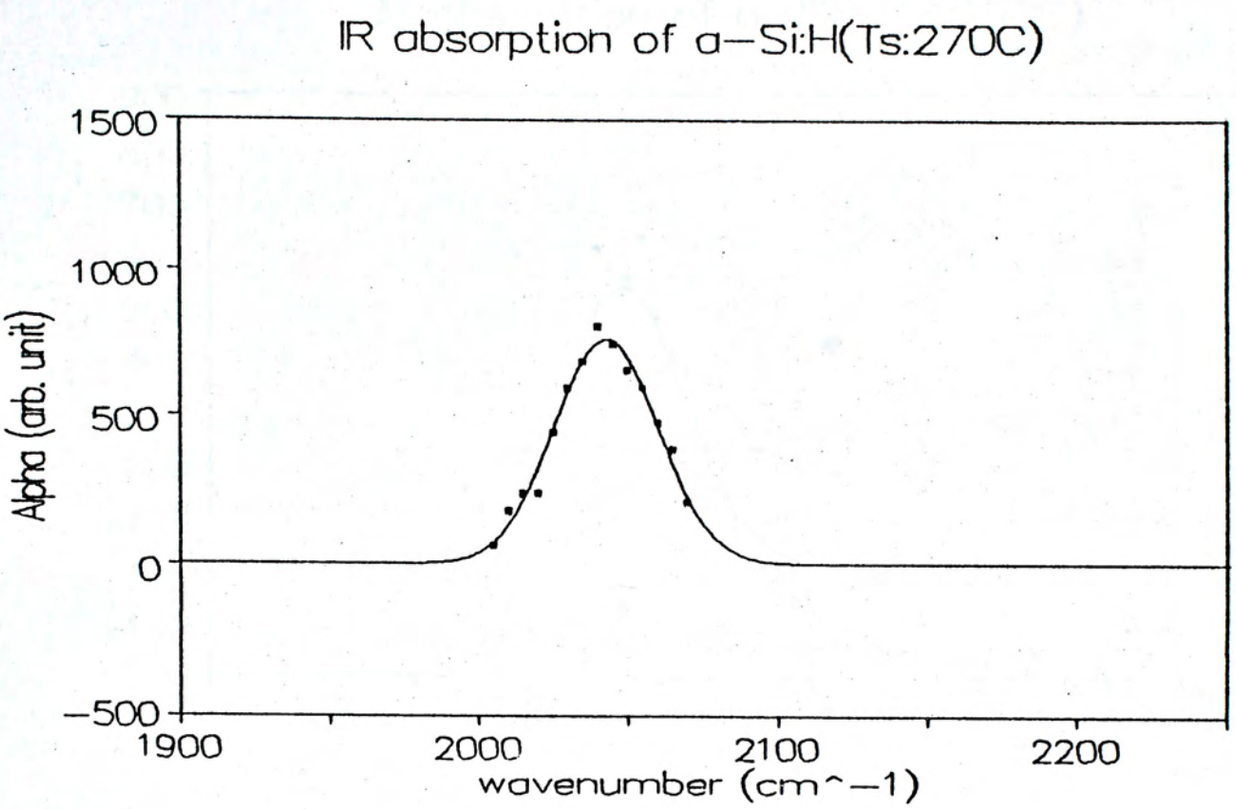

Figure 4-12. Band I absorption of reactively evapovated a-Si:H deposited at Ts=270°C.

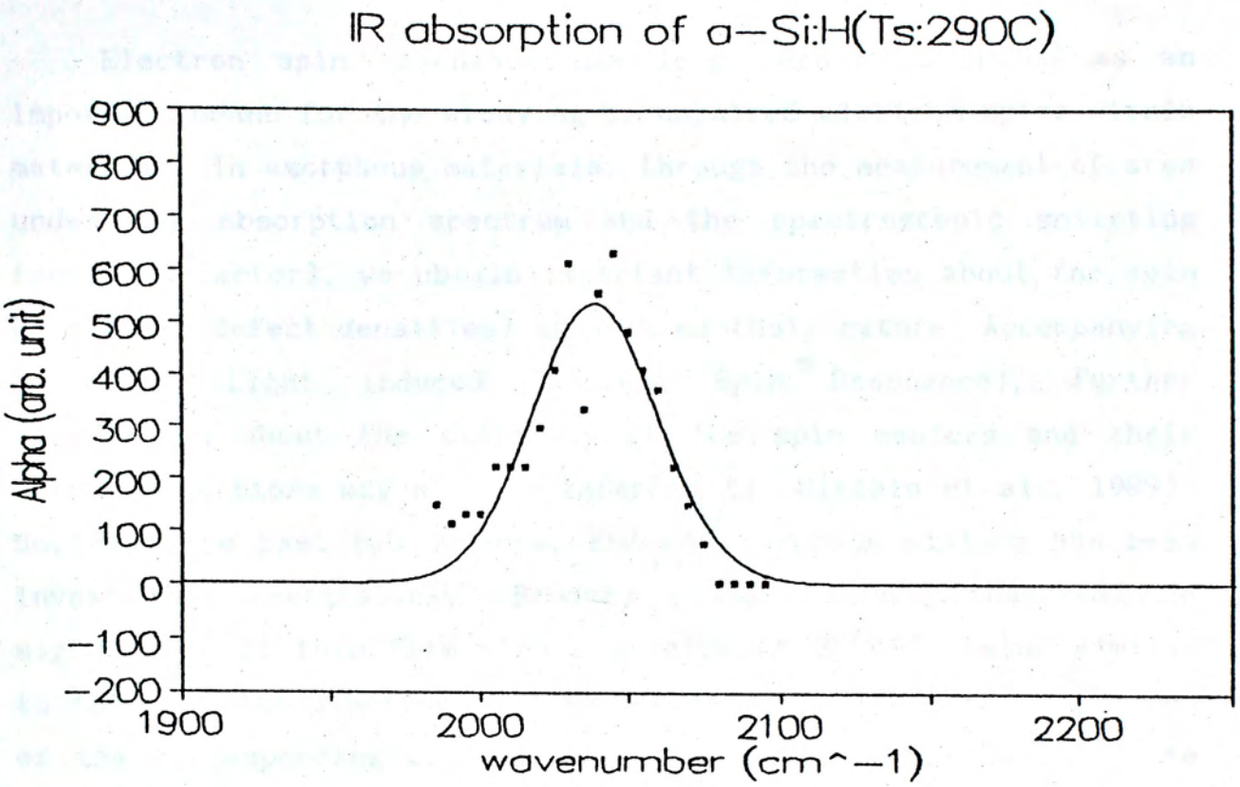

Figure 4-13. Band I absorption of reactively evaporated a-Si:H deposited at Ts=290 °C.

Chapter 5

Electron Spin Resonance Experiment

A) Introduction:

Electron spin resonance has long been established as an important means for the studying of unpaired electron spins within materials. In amorphous materials, through the measurement of area under the absorption spectrum and the spectroscopic splitting factor (g-factor), we obtain important information about the spin densities (defect densities) as well as their nature. Accompanying by LESR (Light induced Electron Spin Resonance), further information about the stability of the spin centers and their inter-transitions may also be inferred (J. Ristein et al., 1989). So, over the past two decades, ESR of amorphous silicon has been investigated extensively. Brodsky et al. (1969) observed ESR signal of a-Si thin film with a g-value of 2.0055, being similar to those of the electronic states observed in the surface regions of the corresponding crystalline forms (Table 5-1). Besides, the observed spin density was proportional to the film's thickness, allowing him to conclude that internal surfaces (micro voids) may exist in a-Si. Furthermore, he identified the 2.0055 spin signal as arising from dangling bonds, which upon annealing below the crystallization temperature decreased irreversibly, and so did both the electrical conductivity and optical absorption. This showed that dangling bonds had a vital control over the physical properties of a-Si. Later on, interests have been shifted to a-Si:H since its first successful fabrication. R.A. Street (1982) and H. Dersch (1983) studied the recombination process in a-Si:H. Both of them found a strong dependence of photoconductivity on spin density (Figure 5-1, 5-2). From the reduction of photoconductivity as the spin density increases, Street concluded that dangling bond acts as either trapping or recombination centres in a-Si:H. He experimentally observed that the origin of Staebler-Wronski effect comes being the increase in dangling bond density after the samples was put under prolonged illumination (Figure 5-3). Dersch et al. put forward a recombination model for a-Si:H, where he suggested that each

created electron-hole pair may be trapped in localized band tail states (Figure 5-4) and eventually recombined via defect states. On the contrary, Parker el al. (1986) showed that nearly all of the dangling bonds acted as traps rather than recombination centres. So the actual kinetics which hinder free charge carrier conduction in a-Si:H are still not clear and present many problems. This situation is worsened by the controversy in identifying the three well-documented defect-related ESR signals with g-values of approximately 2.0055, 2.013 and 2.0043 in a-Si:H. In undoped a-Si:H, g = 2.0055 is well known as arising from dangling bonds. Signals with g = 2.01 and 2.0043 can also be observed for p-type and n-type samples. Usually, they were ascribed as holes and electrons being trapped at the localized band tails (H. Dersch et al., 1981). However, Y Wu and A Stesmans (1985, 1987) found that both ESR signals with g = 2.012 and 2.0043 were also observed in pure a-Si and a-Si:H films sputtered at low deposition rates. Because of these observations, they argued that previous interpretation concerning the above two lines may be erroneous. Their argument followed closely the semi-quantitative analysis of the lowest-energy defects in tetrahedrally bonded amorphous semiconductors by David Adler (1978). According to Adler, upon *complete lattice relaxation,* the lowest-energy defect in amorphous silicon was the two-fold coordinated atom, T_2^0 (the superscript indicates the bearing charge while the subscript indicates the coordination number) (Figure 5-5), not the usual dangling bond T_3^0. Further he claimed that the reaction:

$$T_2^0 + T_3^0 \longrightarrow T_2^+ + T_3^- \qquad (5.1)$$

was exothermic by ≅ 2 eV. In the above equation, T_3^- is the *relaxed* negatively charged three-fold coordinated Si center. Hence, it was suggested from (5.1) that T_2^+ should be responsible for the ESR signal being observed in undoped a-Si. One should note that the above analysis is based on the assumption that the whole structure can be totally relaxed. However, as the defects prevailing in a-Si are mostly strain-induced because of the topologically

overstrained lattice, so the defect formation should depend sensitively on the details of the a-Si growth process. Complete relaxation might be hindered, thus allowing T_3^0 centers to coexist with $T_2^+ - T_3^-$ pairs. As a result, besides the T_2^+ signal, a T_3^0 signal may also be observed by ESR. The reason why usually only T_3^0 signal with $g \cong 2.0055$ has been observed is that reaction (5.1) may be prevented by a considerable strain-induced potential, hence hindering the relaxation process. With the above analysis, Wu et al. was ready to explain the gradually changing of g-value from 2.0047 to 2.0042 along with a gradual decrease in deposition rate from 0.6 Å/s to 0.28 Å/s for their undoped a-Si and a-Si:H films (Table 5-2, 5-3).

In the present study, both dark ESR and LESR were performed, and this chapter reports results with the following objectives in mind:

1) To study the electron spin density, ρ_s, for samples prepared by different procedures, namely, electron beam evaporated a-Si with T_s = 250°C, evaporated with T_s = 250°C and posthydrogenated at 450°C and reactively evaporated a-Si:H with T_s = 250°C;

2) To study the dependence of ρ_s on the substrate temperatures for reactively evaporated a-Si:H;

3) To identify the nature of defect states within the samples prepared by different procedure through an analysis of their g-values;

4) To study the defect transformation with LESR for reactively evaporated a-Si:H with T_s = 250°C;

Finally, a growth mechanism for our reactively evaporated a-Si:H is proposed, with which the absence of Staebler-Wronski effect within our samples is explained.

B) Theory:

The basic theory of ESR will be described phenomenogically by considering a system of non-interacting unpaired electrons. In real situations, the above non-interacting picture fails to explain some of the observations, such as linewidth narrowing and changes in lineshape with spin concentrations. Yet, it does provide the stepping stone for the understanding of electron spin resonance. The essential elements of ESR involves an absorption process and a relaxation process.

B.1) The absorption process:

Classically, an atom or molecule which contains unpaired electrons has non-zero angular momentum, and possesses a corresponding magnetic moment. If this magnetic dipole is situated in a uniform magnetic field $\mathbf{H} = H_o \mathbf{z}$, the magnetic moment will precess about the direction of H_o with an angular frequency ω_o given by (Figure 5-6):

$$\omega_o = g_L \left(\frac{e}{2mc}\right) H_o \qquad (5.2)$$

which is the classical Larmor precession frequency, g_L being the Lande' g-factor and for a free electron $g_L = 2$. However, for an electron placed in a lattice, its behaviour is modified by the environment and the g-factor may differ from the Lande' g-factor. The effective g-factor is known as the spectroscopic splitting g-factor.

If a circularly polarized oscillatory magnetic field is applied to the system so that it rotates about H_o in the same sense and with the same angular frequency as the precessing moment vector it will exert a couple on the dipole, causing it to reverse its direction with respect to H_o. This corresponds to an exchange of energy between the oscillatory

field and the magnetic system. It occurs only when the frequency of oscillation coincides with the Larmor precession frequency. ω_o is referred to as the resonant frequency.

Quantum-mechanically, for a free electron with spin 1/2 situated in $\mathbf{H} = H_o\,\mathbf{z}$, splitting of energy levels will be given by considering the Hamiltonian:

$$\begin{aligned}\mathcal{H} &= -\,\mu \circ H = -\,\mu_z H_o \\ &= -\,[-\beta\, g\, S_z\,]\, H_o \\ &= \beta\, g\, H_o\, S_z\end{aligned}$$

where β is the Bohr magneton $\equiv \frac{|e|\,\hbar}{2mc}$. The negative sign before β accounts for the negatively charged electrons. The eigen-values of S_z in this case are $m_s = 1/2$ and $-1/2$. Thus, the energies for the upper and lower level are $E(m_s=1/2) = \beta g H_o/2$ and $E(m_s=-1/2) = -\beta g H_o/2$ respectively. This implies a separation of energy $\Delta E = \beta g H_o$ (Figure 5-7).

So, an absorption occurs when the incoming photon with $\hbar\omega_o$ equals ΔE. Explicitly,

$$\hbar\omega_o = \frac{|e|\hbar}{2mc}\, gH_o$$

$$\Rightarrow \qquad \omega_o = \frac{ge}{2mc}\, H_o \qquad (5.3)$$

Note the result is the same as (5.1).

B.2) The relaxation process:

Consider macroscopically a system of N electrons with spin 1/2. We want to describe the different populations within the two energy levels. Assuming the number of electrons in the upper level be N_+, while the number for those in the lower level be N_- (Figure 5-8). Though the total amount of spins is N, the application of an alternating field

will iuduce transitions and will cause a change in both N_+ and N_-. By taking the transition rate probability being the same in both directions, we have:

$$\frac{dN_-}{dt} = N_+W - N_-W = W\,(N_+ - N_-) \qquad (5.4)$$

where W is the transition rate probability for both directions of transitions.

Rewriting (5.4):

$$\frac{dn}{dt} = -\,2\,W\,n \qquad (5.5)$$

where $n = N_+ - N_-$

$N = N_- + N_+$

$\therefore \quad N_+ = (N + n)/2$

$N_- = (N - n)/2$

The solution of (5.5) is $n = n(0)\,e^{-2Wt}$ (5.6)

where n(0) is the population difference at t = 0.

Obviously, from (5.6), the population difference will be zero as t becomes large enough. Hence the resonant absorption of energy from the alternating field will eventually stop and the resonance will disappear. This corresponds to the phenomenon of saturation. However, the above description is not yet complete. There is still another mechanism which induces transitions between the two energy levels, namely, by thermal process.

Assume the spin system is now allowed to be in thermal equilibrium (as it does in performing ESR experiment) with the lattice (which contains the spins) such that the spin temperature is the same as the lattice temperature and let it be T. The rate equation due to the thermal process is:

$$\frac{dN_-}{dt} = N_+ W_\downarrow - N_- W_\uparrow \qquad (5.7)$$

where $W_\downarrow$ is the transition rate probability for transition downward in energy;

$W_\uparrow$ is the transition rate probability for transition upward in energy.

At steady state, we have $\frac{dN_-}{dt} = 0$

$$\Rightarrow \quad \frac{N_+}{N_-} = \frac{W_\uparrow}{W_\downarrow} = e^{-g\beta H_o/kT} \qquad (5.8)$$

The ratio is governed by Boltzmann distribution law. So in general $W_\downarrow > W_\uparrow$, and it can be noticed that while the altenating magnetic field tends to equalize the populations between the two levels, the spin-lattice interaction, which is a heat transfer process, tends to relax electrons from the upper level back to the lower level.

Rewriting (5.7), we have:

$$\frac{dn}{dt} = N(W_\downarrow - W_\uparrow) - n(W_\downarrow + W_\uparrow) = \frac{n_o - n}{T_1} \qquad (5.9)$$

where $n_o = N\left(\frac{W_\downarrow - W_\uparrow}{W_\downarrow + W_\uparrow}\right)$, $\quad \frac{1}{T_1} = (W_\downarrow + W_\uparrow)$

The solution of (5.9) is:

$$n = n_o + Ae^{-t/T_1} \qquad (5.10)$$

where A is an integration constant;

n_o is the population difference at thermal equilibrium;

T_1 is the characteristic time for approaching thermal equilibrium and is called the " spin-lattice relaxation time".

Combining both transition mechanisms, we have:

$$\frac{dn}{dt} = -2Wn + \frac{n_o - n}{T_1} \qquad (5.11)$$

The solution of (5.11) is:

$$n(t) = \left(n(0) - \frac{n_o}{(1+2WT_1)} \right) e^{-(2W+1/T_1)t} + \frac{n_o}{(1+2WT_1)} \qquad (5.12)$$

where n(0) is the initial population difference at t = 0.

Taking the steady solution, $n = \frac{n_o}{(1+2WT_1)}$ (5.13)

From (5.13), as long as $2WT_1 << 1$, $n \cong n_o$, and the absorption of energy from the alternating field does not disturb the population much from their thermal equilibrium values.

Consider the power absorbed at steady state:

$$\frac{dE}{dt} = W\, n\, \hbar\omega = n_o \hbar\omega \frac{W}{(1+2WT_1)} \qquad (5.14)$$

Again, if $2WT_1 << 1$, the power absorbed is proportional to the transition rate probability, hence the square of the magnitude of the alternating magnetic field. However, once W is large enough so that $W \cong T_1/2$, the power absorbed levels off in spite of an increase in W. This effect is called saturation. On the other hand, T_1 also describes the life

time of an electron staying in the upper level, according to the Uncertainty principle $T_1 \Delta E \cong \hbar$, $\therefore \Delta\nu \propto 1/T_1$. So, the shorter the life time, the broader the measured line width. Indeed, in many cases very short values of T_1 occur at room temperature and the resulting line widths are so great as to make resonance unobservable. However, T_1 is usually sharply temperature dependent so that cooling the specimen to 20 K or 4 K increase T_1 sufficiently to solve the above problem.

C) Experimental Method:

The experiment was performed with an X band (frequency ≅ 9 GHz) electron resonance spectrometer (JOEL model: JES - FEBX). A static field of 3260 Gauss was superimposed by a sweeping field of ± 100 Gauss. Modulation width of 4 Gauss with modulation frequency 100 kHz was used. Microwave power was set at 5 mW. The measuring temperature was essentially at room temperature. The sample thickness ranged from 0.3 to 1 μm with a typical size of ≅ 3mm × 1 cm.

To obtain the spin density N_s, both the signal of the sample and that of a carbon standard with known total spins were recorded under the same condition. By performing a double integration, the area under both spectra were obtained. The total number of spin centers were then obtained from their integrated areas' ratio.

To measure the g-value, two methods were employed: 1) two of the six resonance lines of the marker (MgO) with g = 1.981 and 2.043 were read into the computer together with the signal line during data acquisition; 2) The whole spectrum was automatically plotted on a graph paper with the recording unit provided. Usually both of the above were done for comparison. To estimate the g-value, it can be done either graphically on the graph paper by measuring the relative separation between the signal line and the g = 1.981 marker signal, or numerically fitting of the spectrum by assuming a particular line shape. The latter was found to be useful when the spectrum has to be decomposed into more than one

component.

LESR was performed with essentially the same unit. However, the window of the cavity was uncovered (Figure 5-9a), and a 100 Watt quartz lamp (Philips PAR 38 Flood) was employed as a light source shinning through the cavity. Special care was taken to ensure the sample was facing towards the light source. The emission spectrum of the above light source is assumed to be the same as an ordinary quartz lamp, and the transmission spectrum of the sample tube (quartz with thickness $\leq$ 1 mm) is assumed to be that of an optical grade. Both spectra are shown in Figure 5-9b and 5-9c. So wavelengths from $\leq$ 1 μm to 3 μm should be able to reach the sample, corresponding to photon energies ranging from $\geq$ 1.2 eV to 0.4 eV. When performing LESR, the sample was allowed to be illuminated for 1 hour before the absorption spectrum was taken. During this duration, the resonator was cooled with compressed air to minimize any possibility of thermal excitations.

D) Results:

The electron spin density, ρ_s, for samples prepared by different procedures are tabulated in Table 5-4:

Methods:	ρ_s (cm^{-3})	g-value
E-beam evaporated T_s= 250°C	8×10^{18}	2.0055
Post-hydrgenated T_s= 250°C	5×10^{18}	2.0043
Reactively evaporated T_s< 150°C	6×10^{18}	2.0043
Reactively evaporated T_s= 200°C	4×10^{18}	2.0043
Reactively evaporated T_s= 250°C	3×10^{17}	2.0043

Table 5-4

From the above table, it can be seen that without the addition of hydrogen, the spin density was greater. Also, a shift of ESR active center from g = 2.0055 to g = 2.0043 was observed for hydrogenated samples. Furthermore, for the reactively evaporated samples, raising the substrate temperature from 100°C to 250°C leads to a decrease in the density of defects (Figure 5-10). This indicates that the substrate temperature has a pronounced effect on the density of defects in the samples.

When the electrical conductivities were plotted against spin density (Figure 5-11), it was observed that for $\rho_s > 10^{18}$ cm^{-3}, σ_p decreases rapidly as ρ_s increases, with a concomitant increase in σ_d. However, as ρ_s approaches 10^{17} cm^{-3}, both σ_p and σ_d tend towards a saturated value. This result is similar to those of Street (1982) and Dersh et al. (1988). In fact, Guha and Hack (1985) have pointed out that for high quality a-Si:H (i.e. $\rho_s \cong 10^{17}$ cm^{-3}), the photoconductivity was essentially independent of

ρ_s.

The 1st derivative of the absorption spectra from both ESR and LESR for reactively evaporated a-Si:H with T_s = 250°C are shown in Figure 5-12 and 5-13. It is shown that the spectrum taken by dark ESR (Figure 5-12) can be fitted by the derivative of a Gaussian line with a g-factor equal to 2.0043. This implies that a single type of ESR active centers was responsible for the line. On the other hand, the LESR spectrum is shown to be contributed by both a Lorentizian line with g = 2.0043 and a Gaussian line with g = 2.0055 (Figure 5-13 and 5-14). This implies that upon illlumination, the g-factor has been shifted to the side of 2.0055. This can be clearly seen from Figure 5-15. After performing double integrations, the areas under the absorption spectra were found to be 4285 units and 4435 units(or a ratio 1 : 1.04) for dark ESR and LESR respectively. So, it can be concluded that the total amount of ESR active defects was almost constant and yet a transformation between defect centres occured after illumination.

E) Discussions:

Firstly, for the reactively evaporated samples, an increase in the substrate temperature decreased ρ_s. However, from infrared absorption spectroscopy, it was found that at a lower substrate temperature, greater amount of hydrogen could be incorporated into the silicon lattice. It has been long believed that the role of hydrogen is to saturate isolated dangling bonds. From the above observation, two possibilities concerning the effect of substrate temperature may be infered: 1) the efficiency of defect passivation by atomic hydrogen was greater at a higher T_s ; 2) at a higher T_s, the number of intrinsic defects formed during film formation was lesser. While no information is at hand to discuss point 1, point 2 deserves a further elaboration. As the substrate temperature increases, the silicon atoms possess a greater surface mobility during the film growth process, and have more time to arrange themselves into a more complete and energetically

favourable configuration before being 'frozen out'. Hence less dangling bonds are formed. This can explain the result that ρ_s for films deposited at $T_s = 250^{\circ}C$ is an order of magnitude lower than that at $T_s \leq 150^{\circ}C$.

Secondly, σ_p shows saturation as ρ_s approached $10^{17} cm^{-3}$. This implies that some other spinless defects acting as either trapping or recombination centers may control the photoconducting behaviour. Otherwise σ_p should monotonically increases with decreasing ρ_s.

Thirdly, in view of the shift in g-factor when hydrogen atoms are incorporated into the silicon lattice (no matter the sample was post hydrogenated or reactively evaporated), the following growth mechanism is suggested:

When hydrogen atoms are added into the silicon network, they not only passivate *isolated* dangling bonds. Since hydrogen can only be singly coordinated and the silicon-hydrogen bond energy is about 3.4 eV larger than silicon-silicon bond energy (Adler 1978), the incoming hydrogen atom may break any *weak* Si-Si bonds (by a *weak* Si-Si bond, we mean that the bond length is other than the ideal value of 2.35 Å). The formation of weak bonds during film growth can be justified as amorphous materials are in general overstrained networks. The consequence of this weak-bond-attack is a relief in mechanical strains of the pure tetrahedral bonding (See Figure 5-16a - 5-16c). According to Adler, such a kind of strain relaxation enables the following reaction:

$$T_3^0 + T_2^0 \longrightarrow T_3^- + T_2^+ \quad \text{(exothermic by} \cong 2 \text{ eV)}$$

In the above equation only T_3^0 and T_2^+ are ESR active, so T_2^+ is assigned to be responsible for the g = 2.0043 ESR signal. The above reaction explains why an incorporation of hydrogen atoms changes the g-factor from 2.0055 to 2.0043. Note also that besides the T_2^+ defect states, there are T_3^- defects, whose presence may

also control the photoconducting behaviour of a-Si:H. One further notes that according to this growth mechanism, T_3^- - T_2^+ are nearest neighbour defects and are created in pairs.

With the above considerations, it is ready to explain the findings from LESR. When an electron was optically excited, the following transition may take place: an electron from a T_3^- center hops into a T_2^+ center, explicitly:

$$T_3^- \longrightarrow T_3^0 + e^-$$

$$T_2^+ + e^- \longrightarrow T_2^0$$

This explains why the power absorption spectrum of a-Si:H (T_s = 250°C) from LESR could be decomposed into two components with g = 2.0043 and g = 2.0055. Since this is only a transition process, no new defects are created. The area under both ESR and LESR spectra should remain nearly the same.

Finally, Staebler-Wronski effect is known to be a light induced degradation effect in glow-discharge produced a-Si:H. Several authors have accounted for its mechanism (e.g. Kazuo Merigaki, 1992 and the references there). An atomic configuration of glow discharge produced a-Si:H was shown in Figure 5-17. The essential steps for light induced defects creation were summarized as follows:

1) A weak Si-Si bond is broken and the SiH bond switches towards this weak bond to form two separate dangling bonds (Figure 5-18a);
2) The light induced dangling bonds may not yet be stabilized, The hydrogen may hop or tunnel into another site along the weak Si-Si bond and step 1 is repeated (Figure 5-18b);
3) Finally, the atomic configuration is stabilized, leaving two dangling bonds (Figure 5-18c).

The above argument is based on the presence of weak Si-Si

bonds. If this is so, the absence of S-W effect within our sample can be explained. As mentioned before, the growth mechanism of our reactively evaporated a-Si:H involves the attack of weak Si-Si bonds by atomic hydrogen, switching them into a more energetically favourable configuration. This reduces the presence of weak bonds in the resultant film to a great extent, hence the absence of S-W effect.

F) Conclusions:

A shift of g-factor from 2.0055 to 2.0043 was observed on the addition of hydrogen into the amorphous silicon lattice. This is explained by a switching of ESR active centers from T_3^0 to T_2^+. Besides, for reactively evaporated a-Si:H, an increase in T_s. decreases ρ_s, which is explained as an enhancement of atomic migration at higher T_s, resulting in a decrease of defect formation. Moreover, the shift of g-value of LESR from ESR for a-Si:H (T_s = 250°C) is explained as an optical transition between the two localized defects, T_3^- and T_2^+ centers. In addition, a growth mechanism is suggested for our reactively evaporated a-Si:H, with which the absence of Staebler-Wronski effect within our samples is explained.

Material	Amorphous films (77°K) (this work)			Other authors					
				Amorphous films		Crystalline surfaces		Neutron irradiated crystals	
	g value	Linewidth (G)	Density of spins[d] (cm^{-3})	*g* value	Linewidth (G)	*g* value	Linewidth (G)	*g* value	Linewidth (G)
Si	2.0055 ±0.0005	4.7	2×10^{20}	2.006 ±0.001[c]	15[c]	2.0055 ±0.002[a]	7-8[a]	2.0055[a]	16-20[a]
						2.0055[b]	5[b]		
Ge	2.021 ±0.001	39	1×10^{20}			2.023 ±0.003[a]	50[a]		
SiC	2.003 ±0.001	6	3×10^{20}			2.0027 ±0.002[a]	5.5[a]		

[a]G. K. Walters and T. L. Estle, J. Appl. Phys. 32, 1854 (1961).
[b]D. Haneman, Phys. Rev. 170, 705 (1968).
[c]Z. Z. Ditina, L. P. Strakhov, and H. H. Helms, Fiz. i Tekh. Poluprov. 2, 1199 (1968) [translation: Soviet Phys. -Semicond. 2, 1006 (1969)].
[d]The densities are estimated to be accurate within a factor of 2.

Table 5-1. The ESR results on amorphous films compared with the results from similar resonances in crystalline material (M.H. Brodsky et al., 1969).

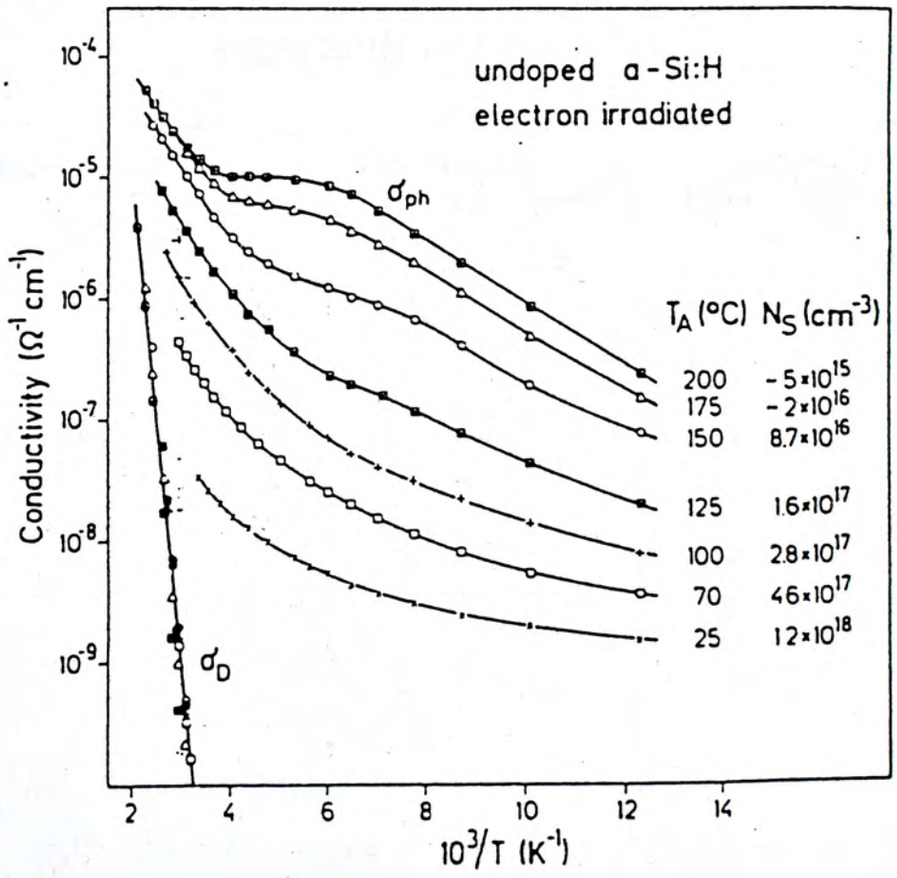

Figure 5-1. Photoconductivity and dark conductivity of electron-bombarded a-Si:H after different annealing temperatures (H. Dersch et al., 1983).

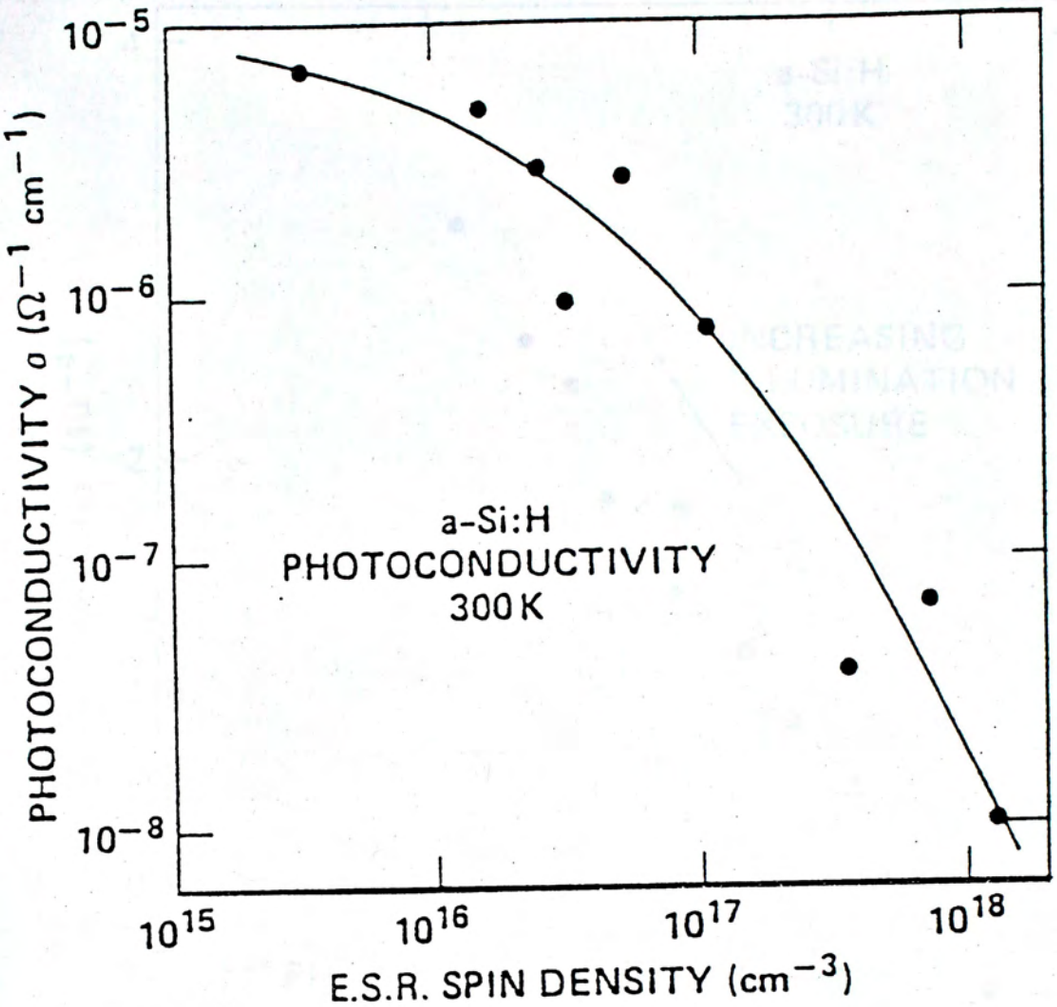

Figure 5-2. The photoconductivity for samples of different ESR spin density (R.A. Street, 1982).

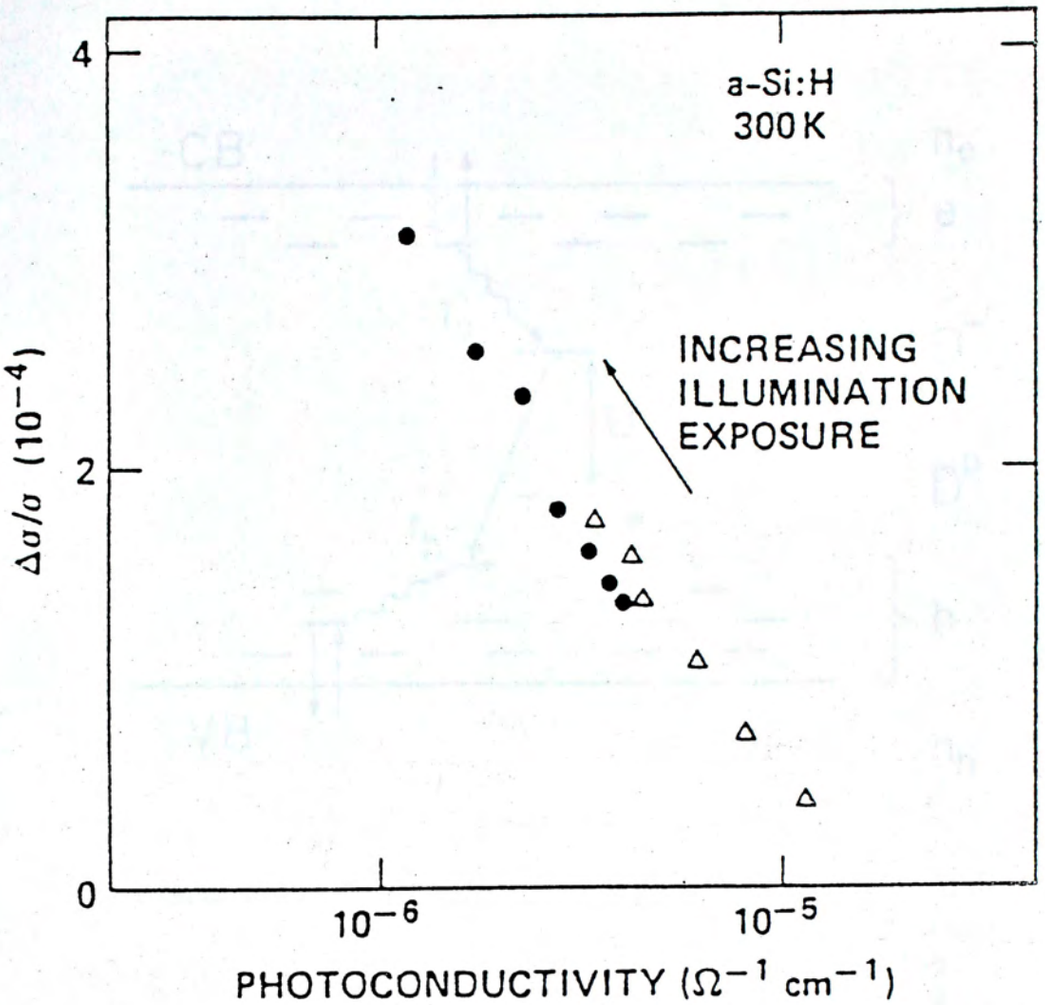

Figure 5-3. $\Delta\sigma/\sigma$ plotted versus the photoconductivity for two samples subject to prolonged exposure to white light.
$\Delta\sigma/\sigma$ is proportional to the density of bulk defects (R.A. Street, 1982).

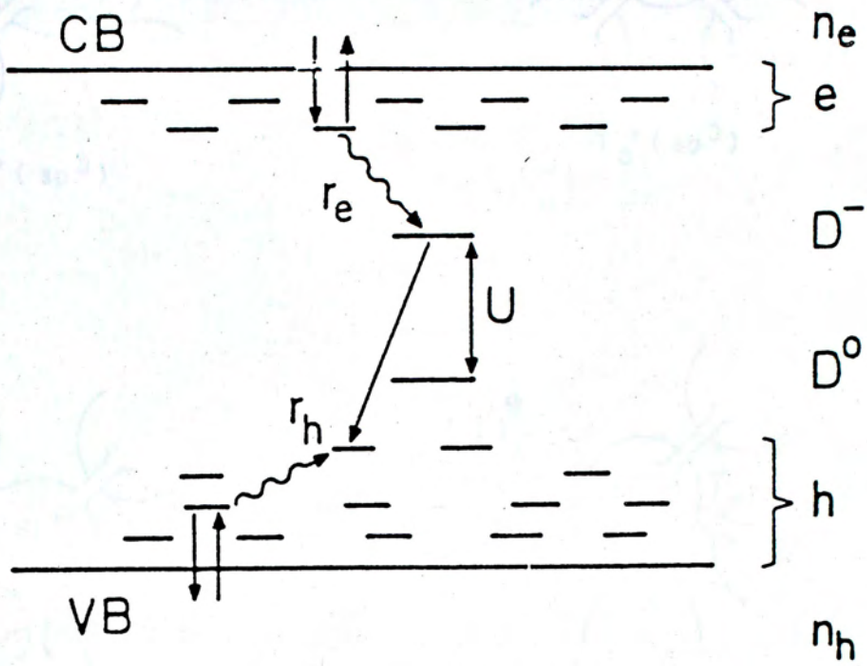

Figure 5-4. Recombination scheme for a-Si:H. wavy arrows indicate spin-dependent transitions (H. Dersch et al., 1983).

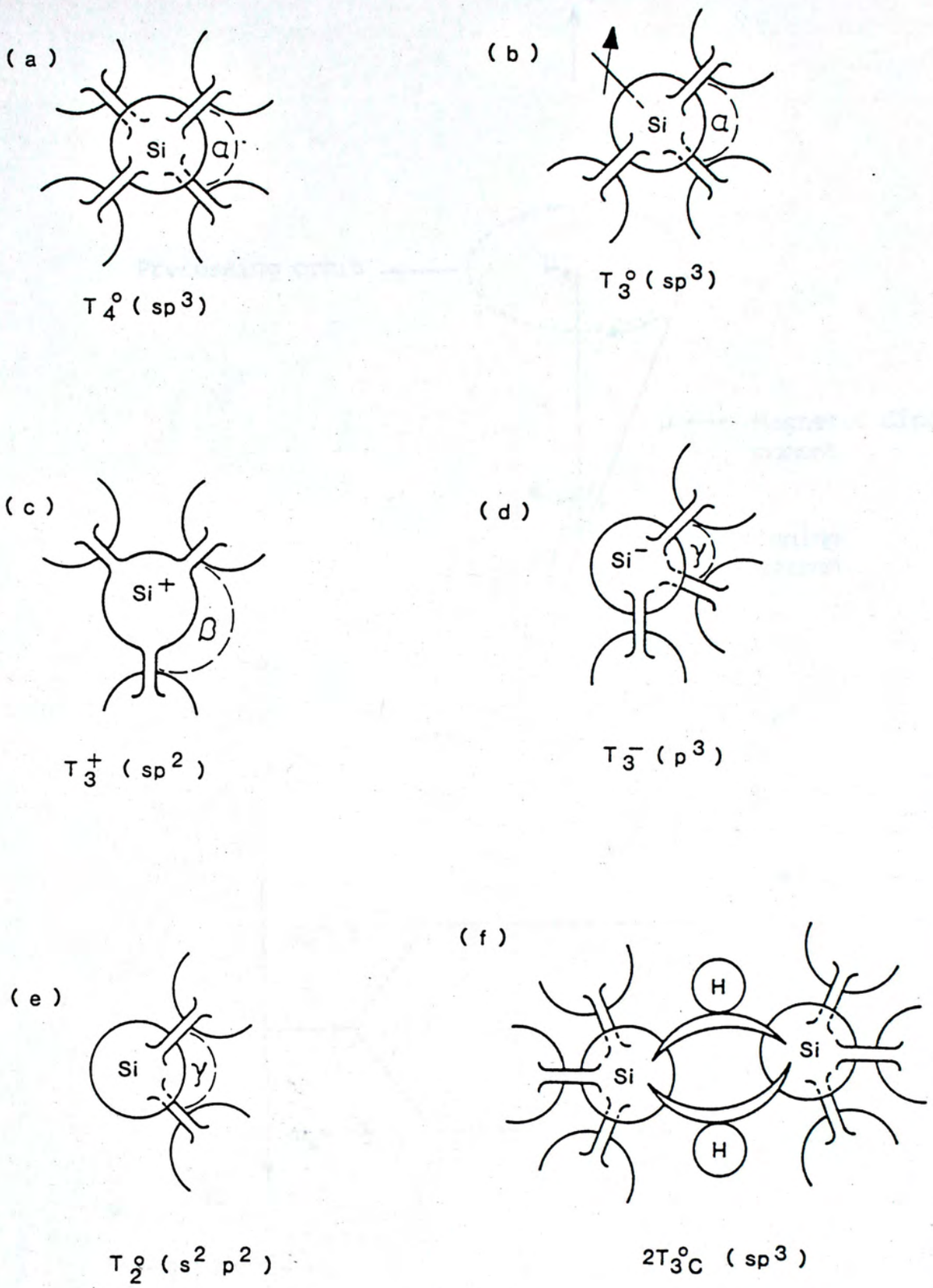

Figure 5-5. Sketches of the optimal local coordinations of a Si atom in several different configurations: (a) ground state, (b) neutral dangling bond, (c) positively charged dangling bond, (d) negatively charged dangling bond, (e) two-fold coordinated Si atom, (f) complex consisting of two three-center bonds with bridging H atoms. The bond angles identified are $\alpha = 109.5^\circ$, $\beta = 120^\circ$, $\gamma = 95^\circ$ (Adler, 1984).

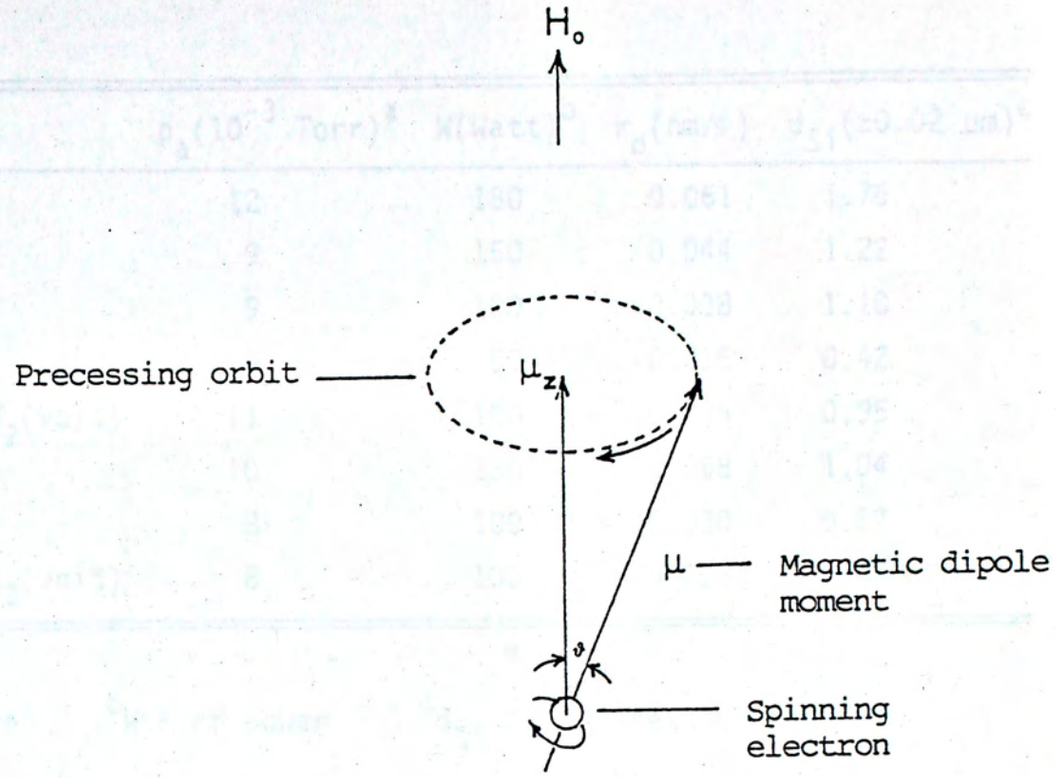

Figure 5-6.

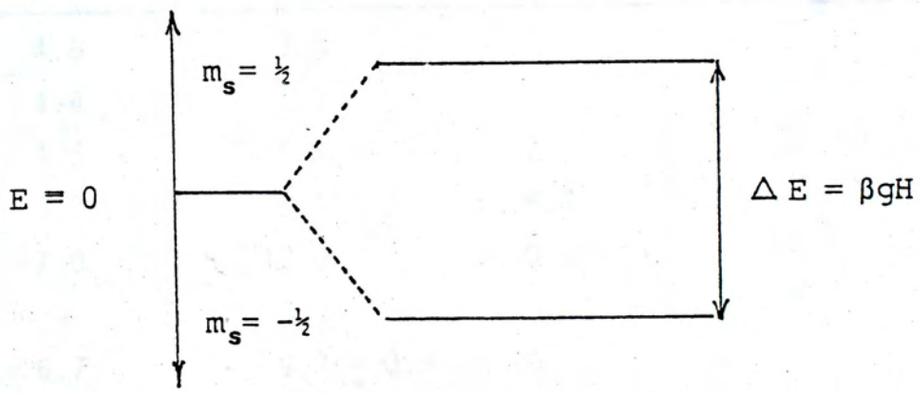

Figure 5-7.

Sample	Ambient	$p_a(10^{-3}$ Torr)[a]	W(Watt)[b]	r_d(nm/s)	d_{Si}(±0.02 μm)[c]
A1	Ar	12	180	0.061	1.76
A2	Ar	9	150	0.044	1.22
A3	Ar	9	100	0.038	1.10
A4	Ar	9	50	0.015	0.42
A5	97% Ar + 3% H_2(vol%)	11	100	0.035	0.95
B1	Ar	10	130	0.058	1.04
C1	Ar	8	100	0.030	0.52
C2	97% Ar + 3% H_2(vol%)	8	100	0.028	0.80

[a] p_a ≡ ambient pressure [b] W ≡ rf power [c] d_{Si} ≡ thickness of the film

Table 5-2. Characteristics of a-Si and a-Si:H films slowly sputtered onto quartz substrates at 300K (Y. Wu and A. Stesmans, 1987).

Sample	g (±0.0001)	ΔB_{pp}(9.0GHz) (±0.3G)	ΔB_{pp}(20.9GHz) (±0.3G)	N_S(±20%) ($10^{19}cm^{-3}$)
A1	2.0047	4.6	5.4	13
A2	2.0046	4.4	5.3	8
A3	2.0045	4.5	5.3	7
A4	2.0042	5.7	7.4	6.5
A5	2.0046	7.0	12.0	0.87
B1	2.0051	-	8.4	0.27
C1	2.0041	6.7	9.7 ± 0.5	10
C2	2.0042	6.4	11.3 ± 0.5	2.5

Table 5-3. ESR data obtained on slowly-deposited sputtered a-Si and a-Si:H (Y. Wu and A. Stesmans, 1987).

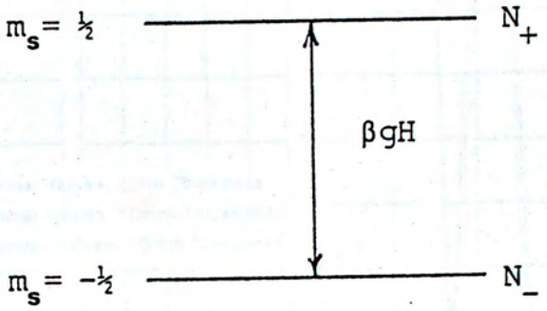

Figure 5-8.

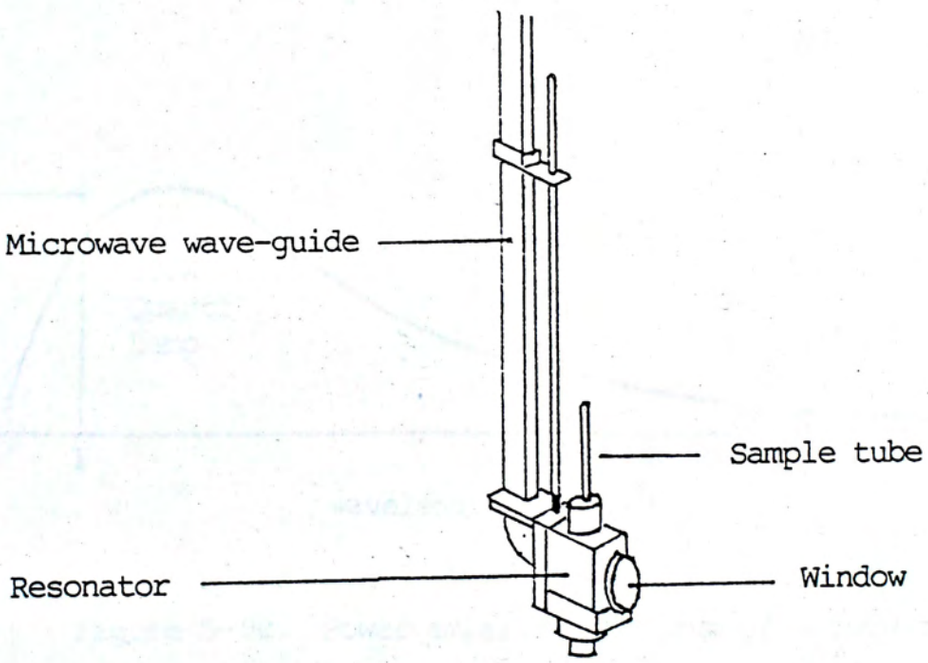

Figure 5-9a.

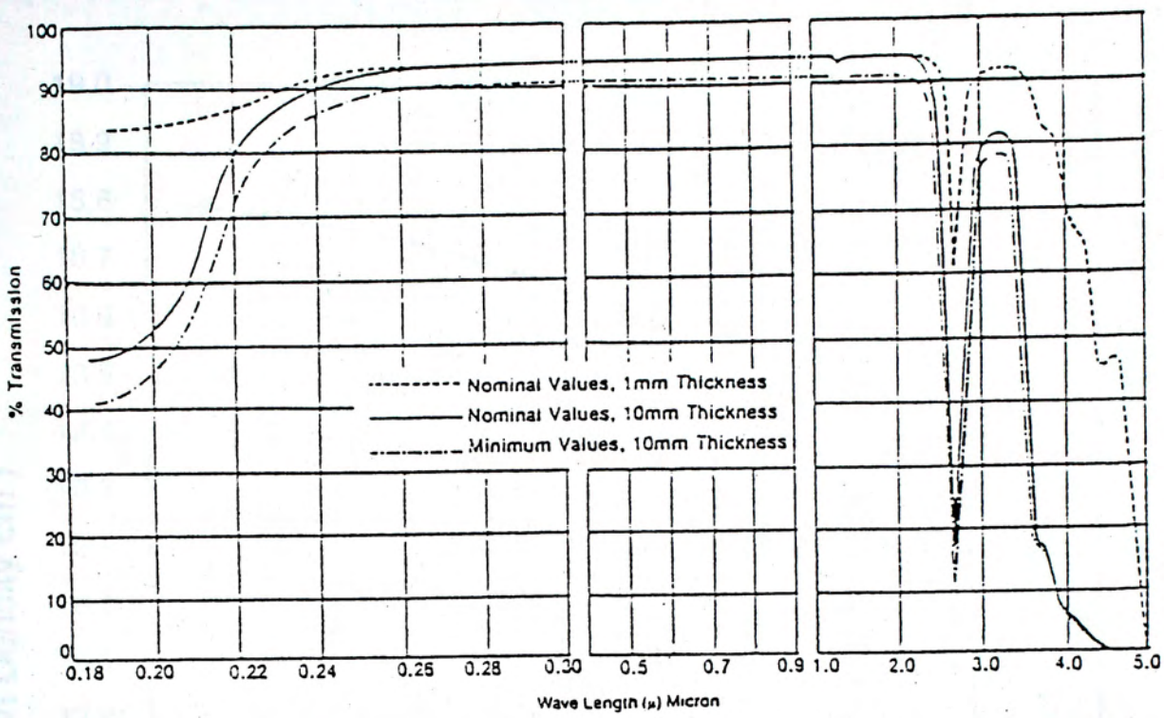

Figure 5-9b. Transmission spectra of optical grade quartz with various thicknesses.

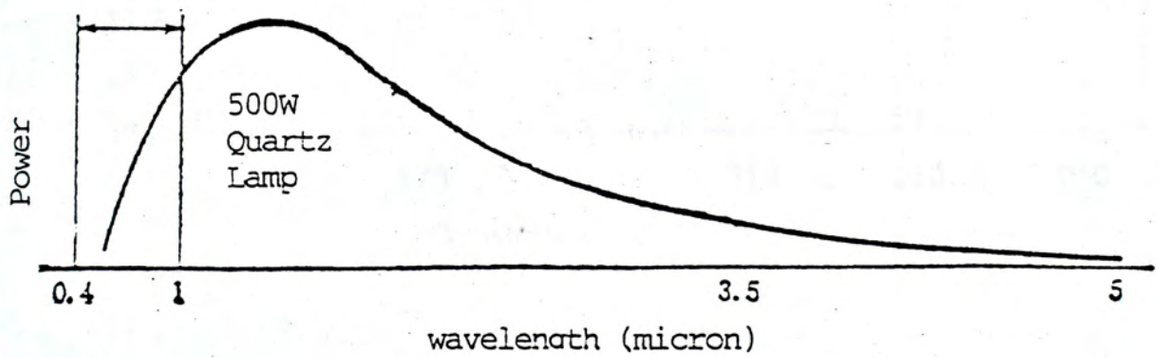

Figure 5-9c. Power emission spectrum of a 500W quartz lamp.

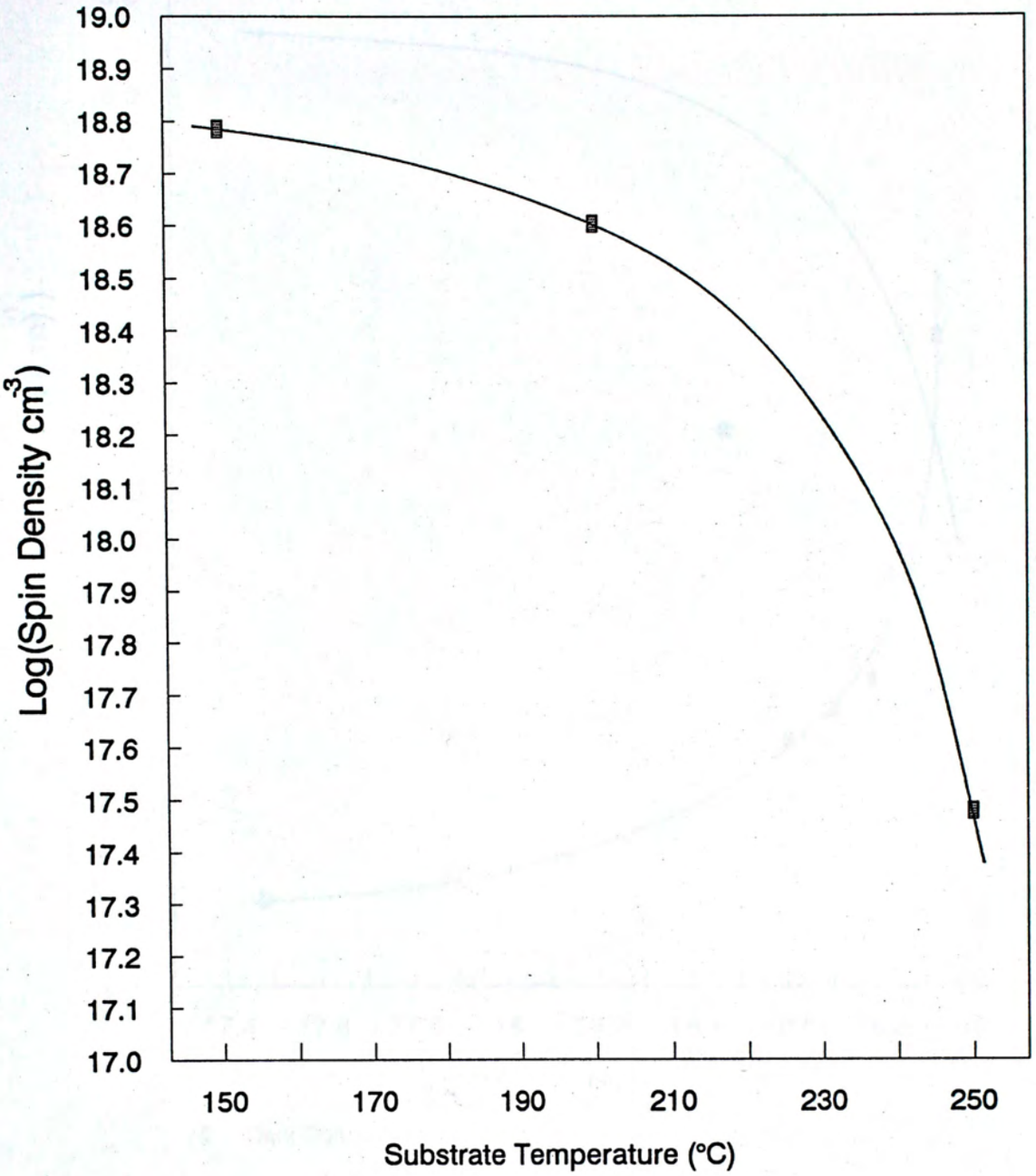

Figure 5-10. A plot of dark ESR spin density against substrate temperature for reactively evaporated a-Si:H. ESR was performed at room temperature.

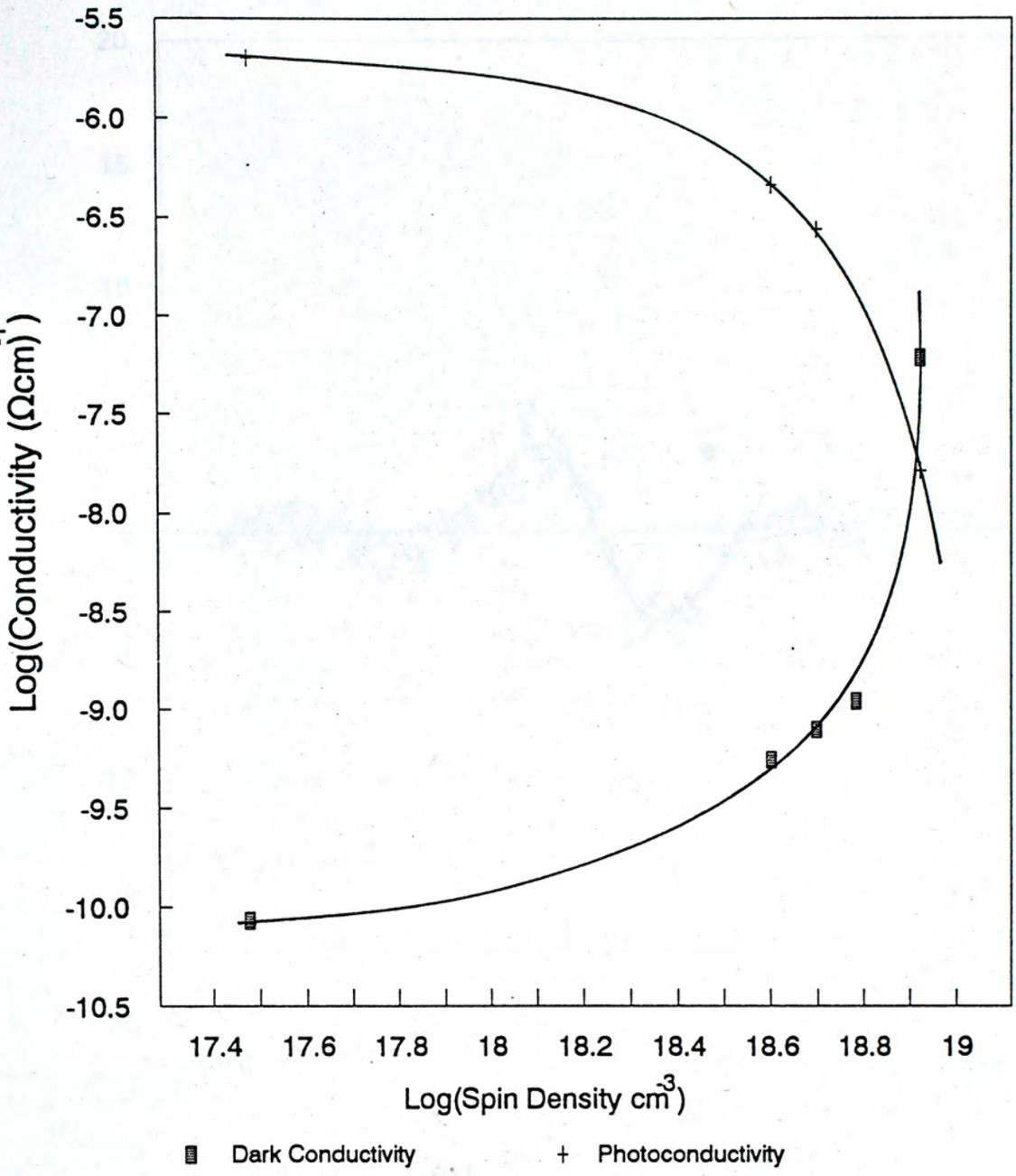

Figure 5-11. A plot of room temperature electrical conductivities against dark ESR spin density.
Photoconductivity was measured under AM1 illumination.
Dark ESR was performed at room temperature.

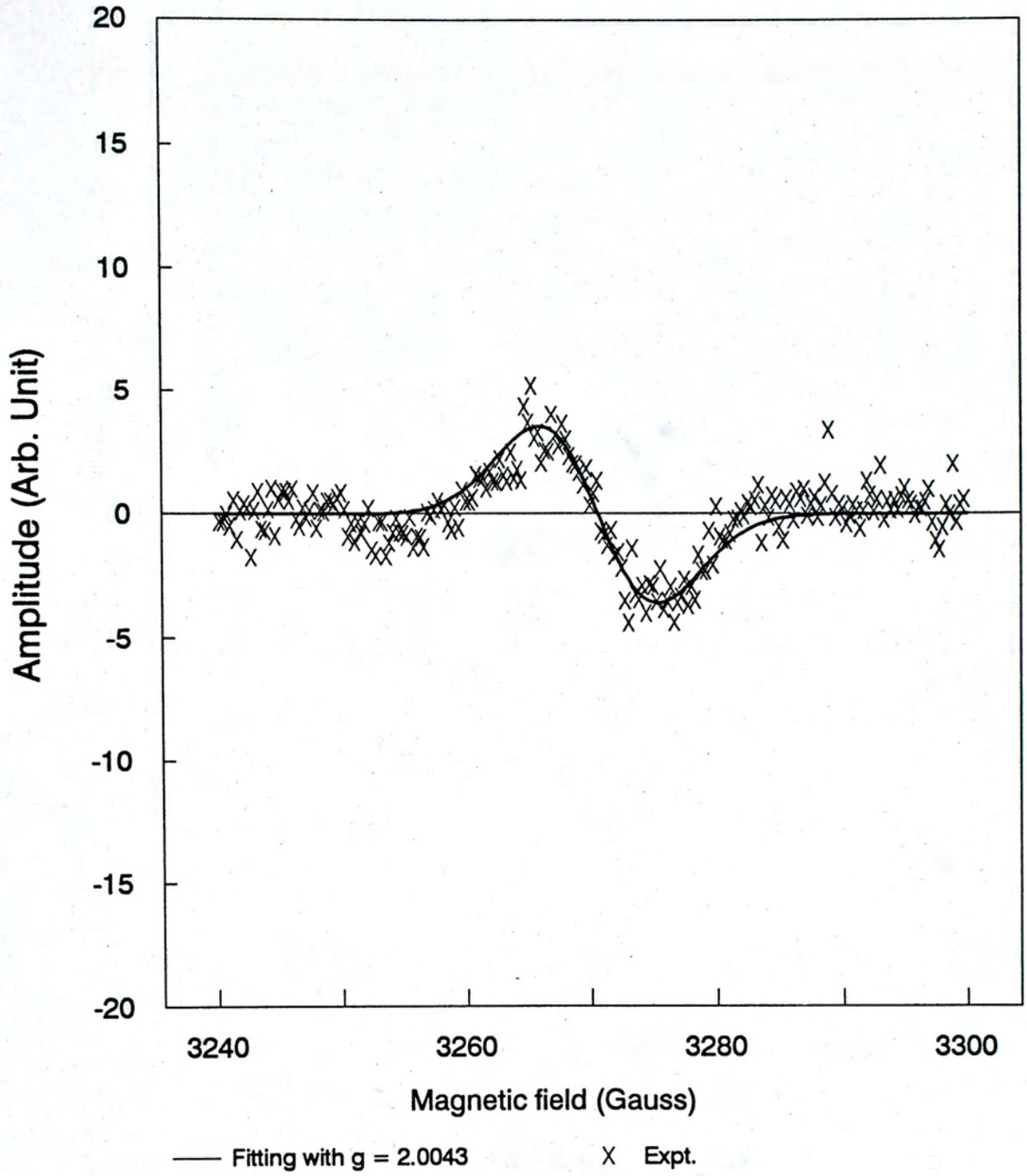

Figure 5-12. The first derivative of power absorption of dark ESR plotted against applied magnetic field. Dark ESR was performed at room temperature.

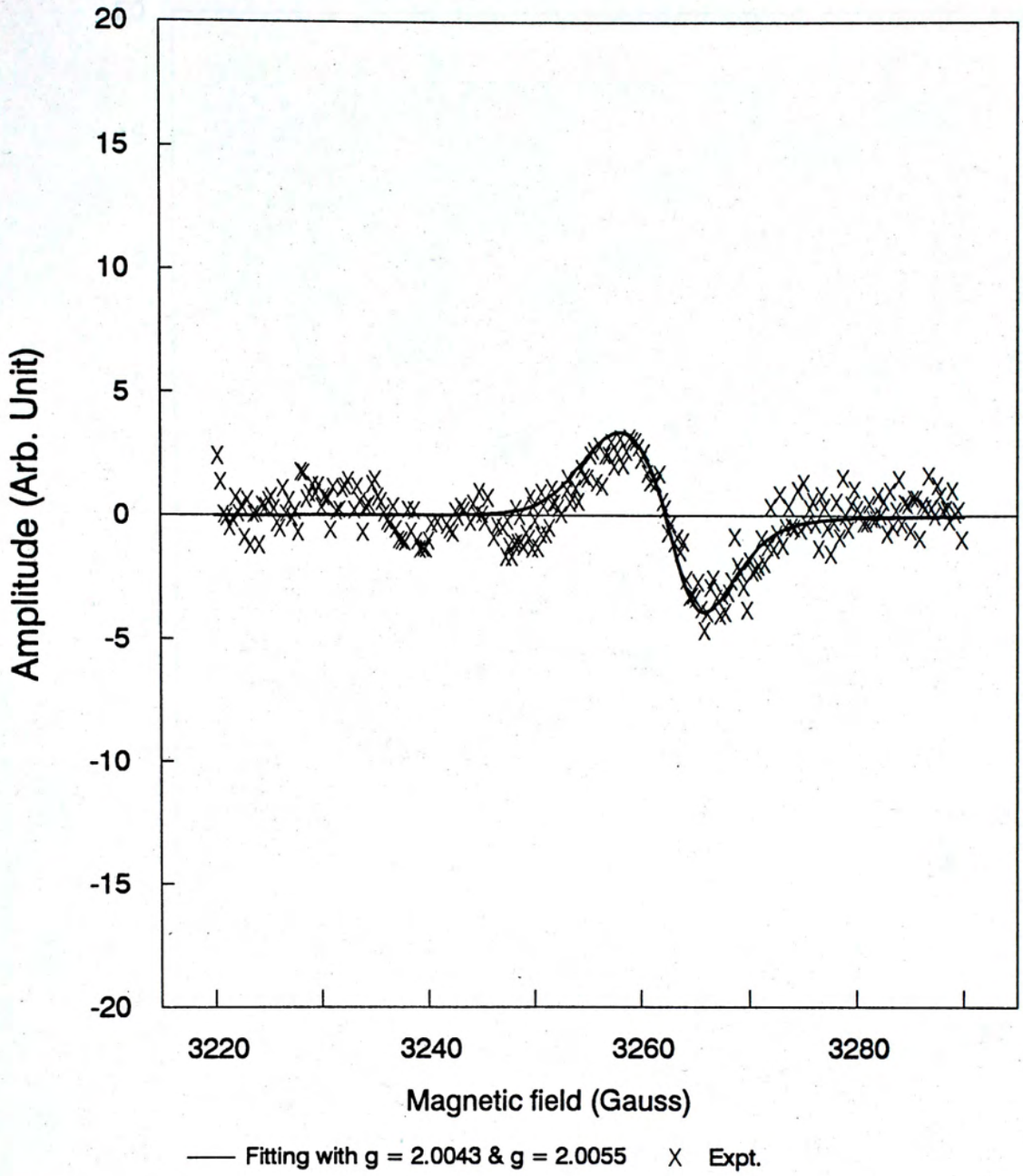

Figure 5-13. The first derivative of power absorption of LESR against applied magnetic field.
LESR was performed at room temperature and under 100W quartz lamp illumination.

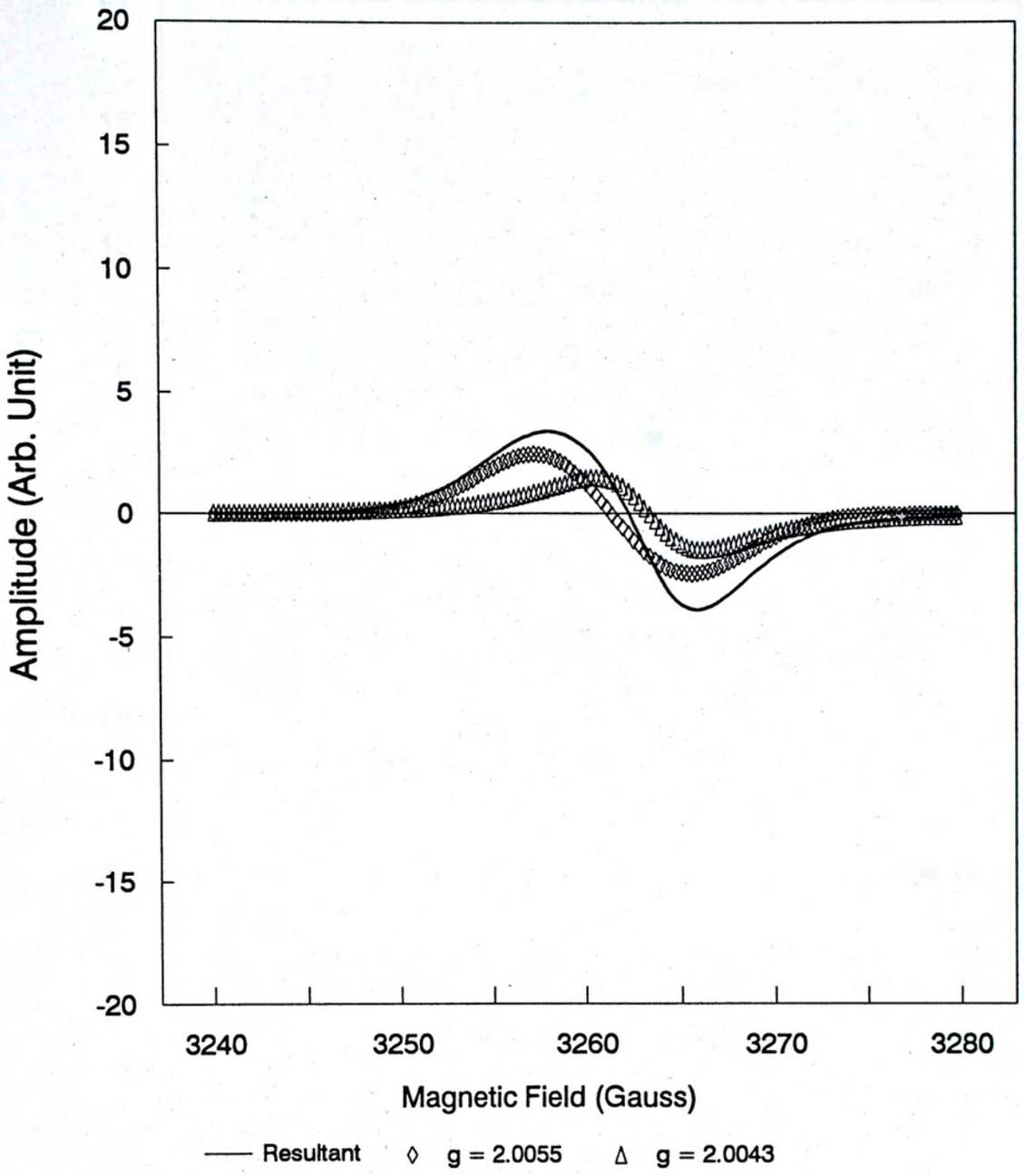

Figure 5-14. LESR absorption spectrum was decomposed into a Gaussian line with g=2.0055 and a Lorentizian line with g=2.0043.

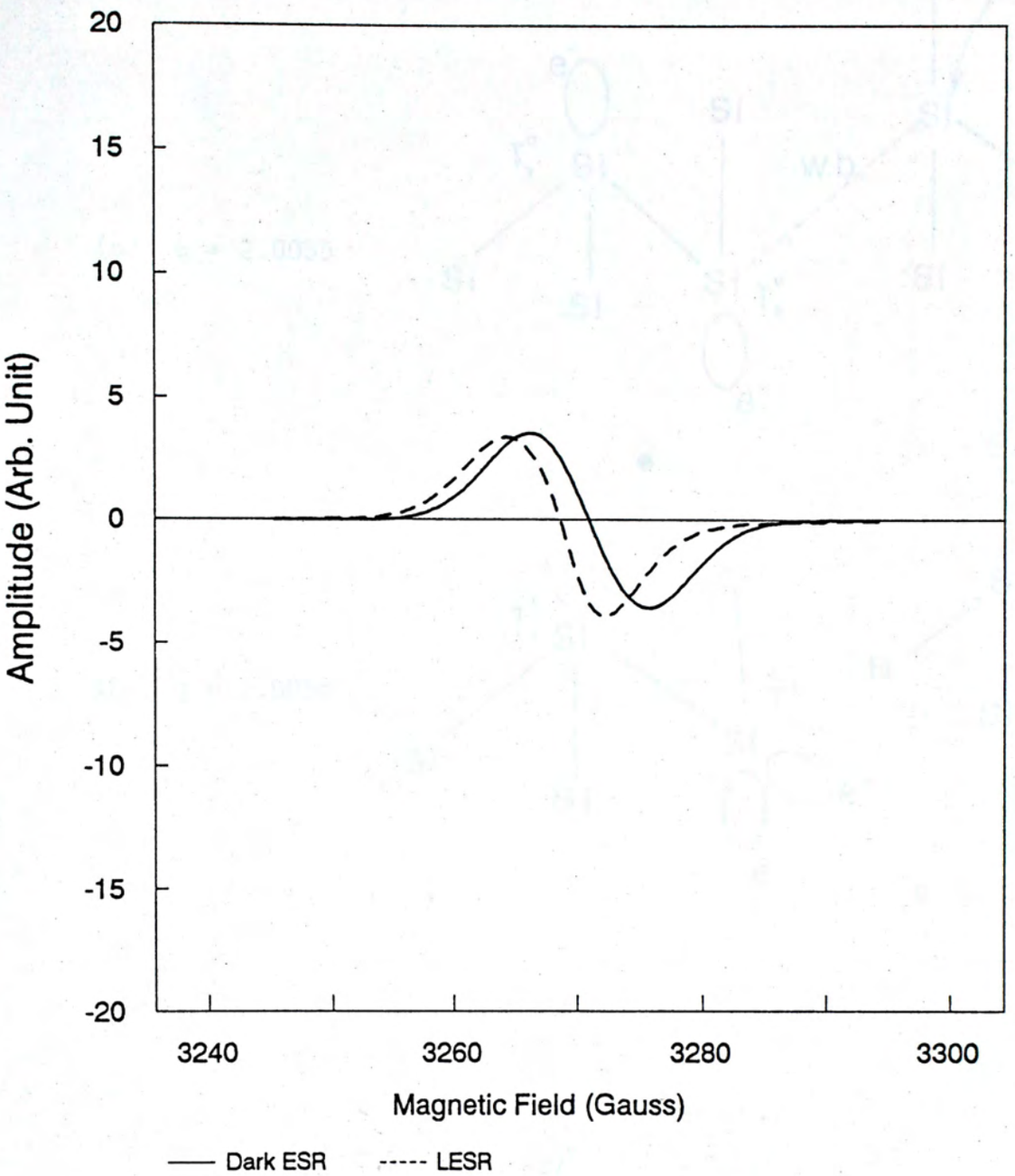

Figure 5-15. A comparison between dark ESR and LESR power absorption spectrum.
Both were done at room temperature.

(a) g = 2.0055

(b) g = 2.0055

(c) g = 2.0043

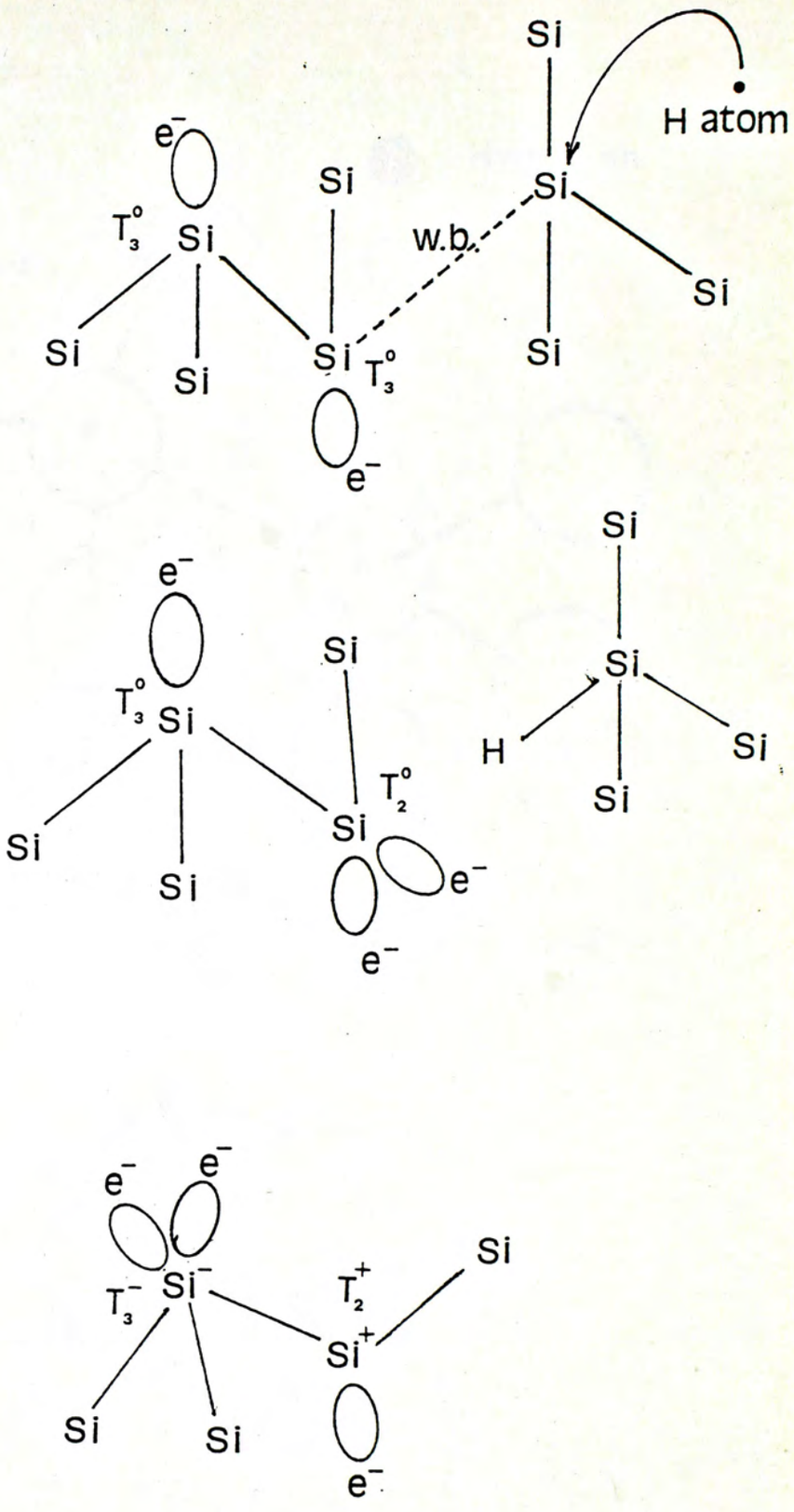

Figure 5-16 (a) - (c).

(a) An incoming H atom attacks the silicon atom with a weak bond.
(b) The formation of a spinless T_2^o center.
(c) According to Adler, T_2^+ defect is formed and the g-factor changes from 2.0055 to 2.0043.

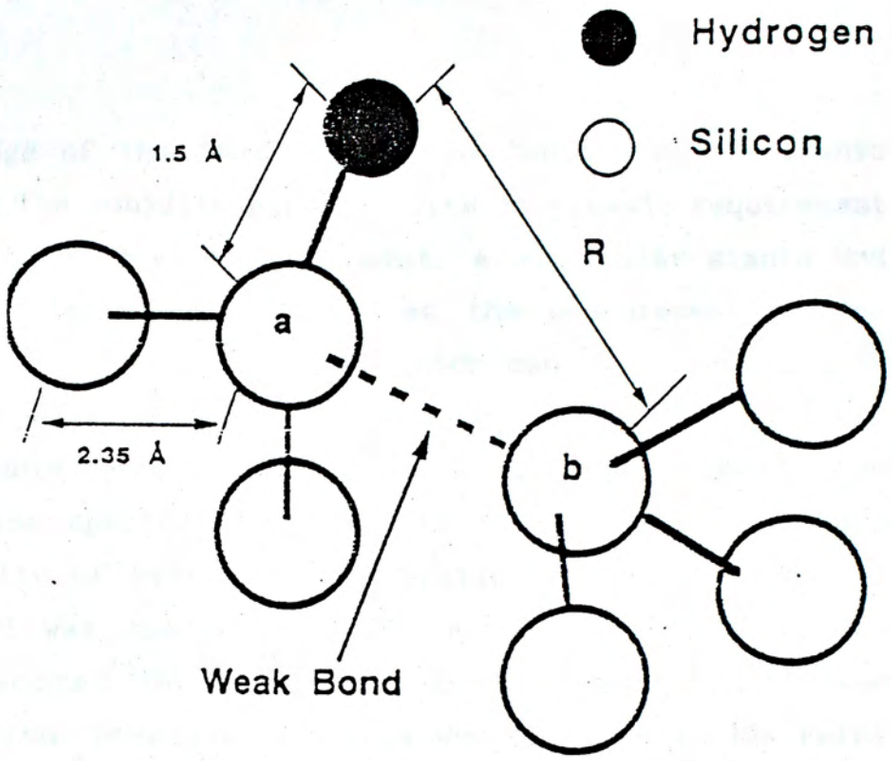

Figure 5-17. Atomic configuration around a weak Si-Si bond and a Si-H bond.

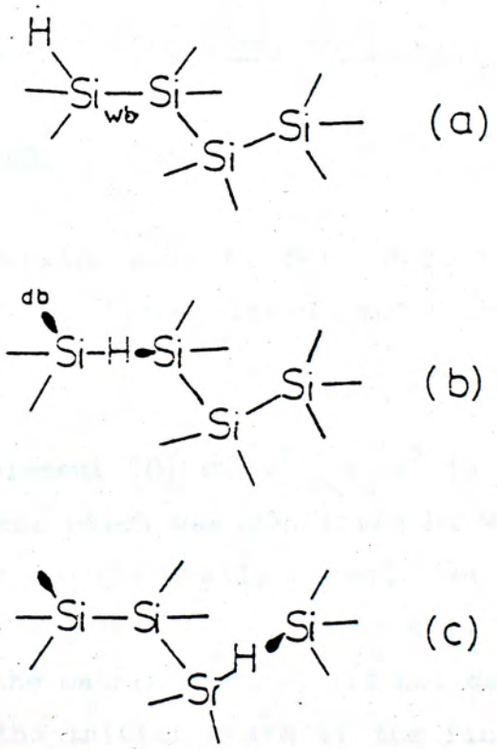

Figure 5-18. Atomic configurations corresponding to the initial step (before prolonged illumination) (a), the intermediate step (b) and the final step (c) during illumination (K. Morigaki, 1992).

Chapter 6

Optical Absorption Experiment

A) Introduction:

The knowledge of the density and distribution of electronic states, N(E), in the mobility gap of a-Si:H is a basic requirement both for research and device development. A particular simple and fast method to determine N(E) involves the measurement of the sub-band gap optical absorption $\alpha(h\nu)$ which can be performed by a combination of photothermal deflection spectroscopy (PDS) and conventional double beam spectroscopy. In this experiment, the optical absorption spectrum from visible to near infrared range and the uniformity of hydrogen incorporation of our a-Si:H film with T_s = 250°C was checked by PDS. Also, a band model was established to account for the optical transitions and hence the absorption spectrum. Numerical fittings were performed. The Fermi level and spin density obtained from fitted data agree reasonably well with those obtained from dark electrical conductivities and ESR measurements.

B) Theory on optical transitions within amorphous materials:

B.1 General descriptions:

Following the analysis made by N.F. Mott (1970), when dealing with optical transitions within amorphous materials, the following assumptions are made:

a) The matrix element $|D| \equiv \int \Psi_{E'}^{*} \frac{\partial}{\partial x} \Psi_{E} dx^3$ is independent of photon energies, which was confirmed by W.B. Jackson et al. (1985) who experimentally showed that the average dipole matrix element squared for a-Si:H is constant up to ≅ 3.4 eV and the matrix element did not depend on the localization of the initial state if the final state is delocalized;

b) The k-conservation selection rules* are relaxed. This assumption is made because at least at the band edges due to strong atomic scattering, $\Delta k/k \cong 1$ and thus k is not a good quantum number. On an E-k diagram such transitions may not be vertical. However no phonon is involved in the process. The only rule to be obeyed is the conservation of energy. So all states will be equiprobably participating in a transition as far as their energy difference equals the incoming photon;

(* $k' = k$ for direct transitions and $k' - k \pm q = 0$ for indirect transitions, where k', k are the wavevectors of electron after and before transitions, and q is the wavevector of a phonon . +(-) corresponds to emission(absorption) of a phonon during the process.)

c) The spectral dependence of the index of refraction (n = 3.6 - 4.4 in the range 0.8 - 2 eV) is neglected.

Under all these assumptions, starting from one electron approximation time dependent perturbation theory, it can be shown that the absorption coefficient $\alpha(h\nu)$ can be expressed by a convolution of density of states (N.F. Mott, 1970):

$$\alpha(\hbar\omega) = \frac{8\pi^2 e^2 \hbar^3 \Omega}{n_o c m^2 \hbar\omega} |D|^2 \int N(E) N'(E+\hbar\omega)\, dE \qquad (6.1)$$

where $N(E)$ and $N'(E+\hbar\omega)$ are the single particle density of states, corresponding to the initial occupied states and final unoccupied states respectively. As mentioned in assumption a) $N(E)$ and $N'(E+\hbar\omega)$ may be either extended or localized. However, if both final and initial states are localized, justification on the constancy of transition matrix element $|D|$ has to be made. Mott pointed out that the lacking of spatial overlapping of the localized electron wavefunctions may cut down $|D|$ to a small value. In other words the probability for such a kind of transition is very

small. On the other hand, Radha Ranganathan et al. (1987) found that for transitions between sets of localized states energy dependent optical matrix element has to be assumed in order to explain the presence of a weak maximum observed at $h\nu \cong 1.15$ eV in photoluminsence absorption spectrum of a-Si:H. From our LESR experiment (see Chapter 5), transitions between localized states has also to be assumed to explain a shift in g-value but there is no increase in magnitude of ESR signal when the sample was under illumination.

Finally, Mott (1971) expressed the matrix element for transition between extended states as:

$$|D| = \pi\left(\frac{a}{\Omega}\right)^{1/2}$$

where a is the average lattice spacing. According to assumption a), we shall take this $|D|$ for all kinds of transitions except those involving both initial and final states being localized. As a result, Eqt. (6.1) can be rewritten as:

$$\alpha(\hbar\omega) = \frac{2\pi^2 e^2 h^2 a}{n\ cm^2 \omega}\int N(E)N'(E+\hbar\omega)\ dE \qquad (6.2)$$

B.2) Band models for optical absorptions in an amorphous semiconductor:

A typical optical absorption spectrum was given in Figure 6-1. It shows that an absorption spectrum can be roughly divided into three regions. Though transitions of any kind may occur in all these regions, usually one single mechanism dominates in each of them. Accordingly, region A corresponds to electron transitions from occupied extended states of valence band to unoccupied extended states of conduction band. Region B corresponds to electron transitions from occupied localized states of valence band tail to unoccupied extended states of conduction band. Finally,

region C corresponds to electron transitions from occupied deep gap states within the mobility gap to unoccupied extended states of conduction band. During analyzing an absorption spectrum, a band model is often assumed. Though ad hoc hypothesis have to be made, it does help in interpreting experimental results.

B.2.1) The Tauc model:

In 1966, Tauc et al. (Tauc 1972, 1974) introduced a model which made quantitative predictions in quite good agreement with experimental results. The essential feature of the Tauc model is depicted in Figure 6-2.

where E_G: the optical gap;
E_G^M: the mobility gap;
E_C: the mobility edge for conduction band;
E_V: the mobility edge for valence band;
E_o: defining the width of localized tail states;
E_D: the position of gap states within the mobility gap.

The functions defining various states are as follows:
For extended states, a parabolic band shape was assumed:

$$N_{C,V}(E) = N_{C,V} (E - E_{C,V})^{1/2} \qquad (6.3)$$

For the tail states of valence band, an exponential shape was assumed:

$$N_{tail}(E) = N_V(\frac{3E_o^V}{2})^{1/2} \exp\left((E_V^M - E)/E_o\right) \qquad (6.4)$$

For the gap states within the mobility gap, a δ function was assumed:

$$N_G(E) = (\rho_D/2)\, \delta(E - E_d) \qquad (6.5)$$

where ρ_D is the volume density of "Si-like" deep states, such as dangling bonds.

Putting the corresponding density of states into Eqt (6.2), the absorption coefficient can be obtained for various transition mechanisms, namely:

For transitions between extended states:

$$\alpha(h\nu) = \frac{k_1}{h\nu} (E - E_g)^2 \quad ; E_g \equiv E_C - E_V \qquad (6.6)$$

where k_1 is a constant.

So a plot of $(\alpha(h\nu)\ h\nu)^{1/2}$ against E will yield a straight line in region A, and the abscissa intercept gives the optical gap width. The concept of optical gap in amorphous materials resembles that in crystalline semiconductors and is useful for understanding both electrical and optical properties of amorphous semiconductors.

For transitions between tail states and extended states of conduction band:

$$\alpha(h\nu) = \frac{k_2}{h\nu} \exp(\frac{E}{E_o}) \qquad (6.7)$$

where k_2 is a constant.

So, a plot of $\ln(h\nu\ \alpha(h\nu))$ against E will yield a straight line in region B, and the corresponding slope gives $1/E_o$. E_o is a parameter characterizing the width of exponential tail and is an important measure of the amount of thermal and structural disorder for amorphous semiconductors (B.A. Vaid et al.,1984). Minimizing E_o is an important target

to be achieved in fabricating a-Si:H thin films.

For transitions between deep gap states and extended states of conduction band:

$$\alpha(h\nu) = \frac{k_3}{h\nu} (E - E_D)^{1/2} \qquad (6.8)$$

where k_3 is a constant.

So a plot of $(h\nu\ \alpha(h\nu))^{1/2}$ against E will yield a straight line in region C, and the corresponding abscissa intercept gives the position of defect states within the mobility gap. As mentioned before, the transport properties of amorphous semiconductors are greatly affected by the amount of gap states present which always act as trapping centres for free charge carriers, hence degrading the electrical properties. Moreover, gap states are usually both optically and thermally unstable. To eliminate them is a basic goal in solar cell fabrication. One of the objectives in performing optical absorption experiment is to probe the gap states information.

B.2.2) Other band models:

Over the last decade, many band models were introduced. While the main features of extended states and tail states were retained, controversies concerning the nature and positions of gap states within the mobility gap arose. In this sub-section, some common models will be summarized for undoped a-Si:H.

a)(See Figure 6-3) In this model, an exponential tail, a Gaussian distribution of mid-gap states and a sharp conduction band edge were assumed. This model can be treated as an extension of the Tauc model and was used by Kočka et al. (1988) to fit their CPM (Constant Photocurrent

Method) data. Typical values for best fit were as follows: exponential VB and CB tails of characteristic energies E_{ev} = 60 and E_{ec} = 25 meV, Gaussian mid-gap states of f.w.h.m. 200 meV, centred at E_{mg} = 800 meV below the CB edge.

b)(See Figure 6-4) J.S. Payson et. al. (1984) argued that since optical absorptions were governed by a joint density of states, sub-band gap absorption measurements should not be sensitive enough to reveal fine structures of gap state distribution. Instead of using Gaussian function, they wrote the distribution function for gap states as a sum of two terms as:

$$N_v \exp\left(\frac{-E+E_g+\hbar\omega}{E_{ov}}\right) + N_m \exp\left(\frac{-E-E_g+\hbar\omega}{E_1}\right)$$

$$E_c \equiv 0$$

where E_{ov} is the slope of the valence band tail
E_1 is the slope of the mid gap states
N_m is the extrapolated value of the intercept of the mid-gap states at the optical edge.

They were able to show that comparable good fit could be obtained (Figure 6-5) with typical values of E_g = 1.7eV, N_m = 1.3×10^{17} $eV^{-1}cm^{-3}$, E_1 = 15 eV, $E_c - E_F$ = 0.5 eV and E_{ov} = 0.055 eV.

c)(See Figure 6-6). In the above models, the gap states were assumed to be neutrally charged. However, recent measurements indicated that for undoped a-Si:H a non-negligible fraction of defects were actually charged (Tatsuo Shimizu at al., 1989). Though the orgin of the charged defects are still not clear, they were used to fit photoconductivity data (G.Schumm et al., 1991). Best fit was obtained for N_D (defect density) = 6×10^{15} cm^{-3}, with the defect levels located at 1 eV and 0.6

eV below E_c.

d)(See Figure 6-7). Instead of only two correlated impurity bands, more general band model has been used to fit PDS measurement (N. Wyrsch, F. Finger et al.,1991). In this model neutral, positively charged and negatively charged defects were taken into consideration.

C) Experimental method:

The absorption coefficients have been obtained in two ways. For $\alpha < 10^4$ cm^{-1}, PDS was performed. For $\alpha \geq 10^4$ cm^{-1}, double beam spectrometer (Hitachi 220S spectrometer) was used.

Samples for PDS measurements were deposited on 3 mm × 10 mm 7059 Corning glass. The geometry during deposition was shown in Figure 6-8. Thickness of the samples measured by α-step was ≅ 1 μm. Each sample was then cut into two halves to check the uniformity of hydrogen incorporation. The samples were labelled as C1, C2, D1 and D2. Pieces with the same letter indicated they were from the same film.

Sample for double beam measurement was deposited on a 2.5 cm × 1 cm quartz substrate. Film's thickness was measured to be 0.3 μm. A piece of uncoated substrate acted as a reference and the difference between the signal beam and reference beam was recorded.

Since PDS experiment was performed by Dr. C.W. Ong at the University of Chicago, detail experimental procedure will not be given here. Nevertheless, the principle and theory of PDS can be found in Appendix A at the end of this chapter.

D) Results:

The absorption coefficient $\alpha(h\nu)$ from PDS for C1, C2, D1 and D2 were plotted on the same graph for comparison (Figure 6-9).

Firstly, it can be observed that all the samples gave essentially the same absorption spectrum, showing the uniformity of hydrogen incorporation in our a-Si:H films was good. Secondly, all the curves passes through 2×10^4 cm^{-1} at $h\nu$ = 2 eV, showing the standard feature of a-Si films. Finally, it is known that PDS signal depends on the thickness of the measuring sample (H. Cutins and M. Farre, 1988) (Figure 6-10). So, to compare the absorption spectra between our reactively evaporated a-Si:H and that from glow-discharge method, samples of comparable thickness have to be chosen. From Figure 6-10 and 6-12, it can be observed that two spectra for film thickness of 1 μm is highly comparable, even in the low $h\nu$ region. This implies that the density of defect states within our samples is of the same order as those in glow discharge samples.

The results from double beam spectrometer were shown in Figure 6-11. It can be seen that a peak existed at $\cong$ 1.5 eV which was due to constructive interference of the incident beam on the sample.

After combining with the absorption coefficients obtained from double beam spectrometer, the whole absorption spectrum from 0.4 -3.2 eV is shown in Figure 6-13. The spectrum can be roughly divided into three parts, namely, a slow varying region (A) at high $h\nu$s, a steep dropping region (B) between 1.6 - 2 eV, followed by a shoulder (C) at low $h\nu$s. By applying Eqt.(6.6), the optical band gap of our a-Si:H at T_s = 250 C was found to be $\cong$ 1.7 eV, which is comparable to that of high quality glow-discharge samples.

E) Analysis:

As mentioned in the introduction, optical absorption spectroscopy is particularly sensitive to sub-band gap absorption. When performing deconvolutions on joint density-of-states integral with appropriately assumed band model, we can estimate the position of Fermi level, locations and densities of gap states

within the mobility gap, as well as the tail width of valence band tail, size of optical gap and mobility gap. All these data are important for characterizing our a-Si:H samples.

From ESR experiment and following the argument of D. Adler (1978), Y. Wu and a.Stesmans (1985), there are two charged defect centres within the mobility gap, namely, the T_2^+ and T_3^- centres (where the subscript and superscript indicates the coordination number and bearing charge respectively). So the band model used to deconvolute our absorption spectrum should consist of these features within the gap.

E.1 Band model:

The band model used for analysis was shown schematically in Figure 6-14. Two Gaussian bands were used for charged defects. Their densities were taken to be the same so as to preserve charge neutrality.

The functional forms of the bands are as follows:

For extended states with a parabolic conduction band (Cohen et al., 1984)

$$N_c = A (E - E_c)^{1/2} \qquad (6.9)$$

Eqt.(6.9) implicitly neglects the localized states beyond the mobility edge E_c.

For extended states with a parabolic valence band (Cohen et al., 1984)

$$N_v = A (E_v - E + \frac{E_o}{2})^{1/2} \qquad (6.10)$$

where E_v is the mobility edge of valence band and E_o is the width of localized states beyond E_v.

For the exponential tail of valence band

$$N_v = A \left(\frac{E_o}{2}\right)^{1/2} e^{-\left(\frac{E-E_v}{E_o}\right)} \qquad (6.11)$$

$(E_o/2)^{1/2}$ is added in the pre-exponential factor to ensure continuity of density of states at $E = E_v$.

For the charged defect centres

$$G_{T_i} = G\, e^{-\left(\frac{E-E_{Gi}}{\delta E_{Gi}}\right)^2} \qquad (6.12)$$

where i = 2, 3 for T_2^+ and T_3^- centres respectively;

δE_{Gi} is the characteristic width of the band;

E_{Gi} is the position of the band within the gap.

E.2 Deconvolution of absorption spectrum:

Deconvolution was done by numerical fittings of parameters in the joint density of states integrals while assuming all states above the Fermi level were empty. Fast converging rate for integration with accuracy up to six significant figures was obtained by applying the Simpson's method.

1) α_1 - from extended states of valence band to extended states of conduction band:

$$\alpha_1 = \frac{kA^2}{h\nu} \int_{-(h\nu-E_g-E_o/2)}^{0} (-E+E_o/2)^{1/2} \, (h\nu+E-E_g-E_o/2)^{1/2} \, dE \qquad (6.13)$$

(See Figure 6-15a). For a photon energy $h\nu$, the highest energy for an electron to be excited from the valence band to the conduction band is just below E_v, hence the upper limit.

For the lower limit, consider an electron with energy which can be just excited above E_c by $h\nu$ (Figure 6-15b) and the result follows.

The fitting range of (6.13) is:

$h\nu-E_g-E_o/2 \geq 0 \Rightarrow h\nu \geq E_g + E_o/2$

2) α_2 - from valence band tail to extended states of conduction band:

For $h\nu \leq E_g + E_o/2$

$$\alpha_2 = \frac{kA^2}{h\nu} \left(\frac{E_o}{2} \right)^{1/2} \int_{E_g+E_o/2-h\nu}^{E_f} \exp(-E/E_o) \, (h\nu+E-E_g-E_o/2)^{1/2} \, dE \qquad (6.14a)$$

(See Figure 6-16a). For a photon energy $h\nu$, the highest energy of an electron which can be excited from the occupied states of band tail to the extended states of conduction band is just below E_f, hence the upper limit. For the lower limit, consider an electron with energy which can be just excited to above E_c by $h\nu$ (Figure 6-16b) and the result follows.

The fitting range of (6.14a) is:

$h\nu+E_f-E_g-E_o/2 \geq 0$ & $E_g+E_o/2-h\nu \geq 0$

$\Rightarrow$ $E_g+E_o/2-E_f \leq h\nu \leq E_g+E_o/2$

For $h\nu \geq E_g+E_o/2$

$$\alpha_2 = \frac{kA^2}{h\nu}\left(\frac{E_o}{2}\right)^{1/2}\int_0^{E_f}\exp(-E/E_o)\,(h\nu+E-E_g-E_o/2)^{1/2}\,dE \qquad (6.14b)$$

The upper limit is still E_f. However, to ensure excitations are still from the localized states of the tail, the lower limit has to be put as 0 (Figure 6-16c).

The fitting range of (6.14b) is:

$h\nu \geq E_g+E_o/2$

3) α_3- from extended states of valence band to T_2^+centre:

For $h\nu \leq E_g+E_o/2$

$$\alpha_3 = \frac{kAG}{h\nu}\int_{-(h\nu-E_f)}^{0}\exp-\left(\frac{E+h\nu-E_{G2}}{\delta E_{G2}}\right)^2(-E+E_o/2)^{1/2}\,dE \qquad (6.15a)$$

(See Figure 6-17a). For a photon energy $h\nu$, the highest energy of an electron to be excited from an extended states of valence band to an unoccupied state of T_2^+ centre is just below E_v, hence the upper limit. For the lower limit, consider an electron which can be just excited to above E_f by $h\nu$ (Figure 6-17b) and the result follows.

The fitting range of (6.15a) is:

$$h\nu \le E_g+E_o/2 \;\&\; h\nu-E_f \ge 0$$

$$\Rightarrow \quad E_f \le h\nu \le E_g+E_o/2$$

For $h\nu \ge E_g+E_o/2$

$$\alpha_3 = \frac{kAG}{h\nu} \int_{-(h\nu-E_f)}^{-(h\nu-E_g-E_o/2)} \exp -\left(\frac{E+h\nu-E_{G2}}{\delta E_{G2}} \right)^2 (-E+E_o/2)^{1/2}\, dE \qquad (6.15b)$$

The lower limit is still $-(h\nu-E_f)$. However, to ensure the excited electrons are within the localized states of T_2^+ centre, the upper limit has to be put as $-(h\nu-E_g-E_o/2)$ (Figure 6-17c).

The fitting range of (6.15b) is:

$h\nu \ge E_g+E_o/2$

4) α_4 - from T_3^- centre to extended states of conduction band:

For $h\nu \le E_g+E_o/2$

$$\alpha_4 = \frac{kAG}{h\nu} \int_{E+E_o/2-h\nu}^{E_f} \exp -\left(\frac{E-E_{G3}}{\delta E_{G3}} \right)^2 (h\nu+E-E_g-E_o/2)^{1/2}\, dE \qquad (6.16a)$$

(See Figure 6-18a). For a photon energy $h\nu$, the highest energy of an electron which can be excited from T_3^- centre to the extended state of conduction band is just below E_f, hence the upper limit. For the lower limit, consider and electron with an energy which can be just excited above E_c by $h\nu$ (Figure 6-18b) and the result follows.

The fitting range of (6.16a) is:

$h\nu \le E_g+E_o/2 \;\&\; E_f+h\nu-E_g-E_o/2 \ge 0$

$$\Rightarrow \quad E_g+E_o/2-E_f \le h\nu \le E_g+E_o/2$$

For $h\nu \ge E_g+E_o/2$

$$\alpha_4 = \frac{kAG}{h\nu} \int_0^{E_f} \exp -\left(\frac{E-E_{G3}}{\delta E_{G3}}\right)^2 (h\nu+E-E_g-E_o/2)^{1/2}\, dE \qquad (6.16b)$$

The upper limit is still E_f. However, to ensure the excited electrons are from T_3^- localized states, the lower limit has to be put as 0 (Figure 6-18c).

The fitting range of (6.16b) is:

$h\nu \ge E_g+E_o/2$

5) α_5 - from extended states of valence band to unoccupied states of valence band tail:

For $h\nu \le E_g+E_o/2$

$$\alpha_5 = \frac{kA^2}{h\nu} \left(\frac{E_o}{2}\right)^{1/2} \int_{-(h\nu-E_f)}^{0} \exp -\left(\frac{h\nu+E}{E_o}\right) (-E+E_o/2)^{1/2}\, dE$$

(6.17a)

(See Figure 6-19a). For a photon energy $h\nu$, the highest energy of an electron which can be excited from the extended states of valence band to the unoccupied states of the valence band tail is just below E_v, hence the upper limit. For the lower limit, consider an electron with an energy which can be just excited to above E_f by $h\nu$ (Figure 6-19b), and the result follows.

The fitting range of (6.17a) is:

$h\nu \le E_g+E_o/2$ & $h\nu-E_f \ge 0$

$$\Rightarrow \quad E_g+E_o/2 \ge h\nu \ge E_f$$

For $h\nu \geq E_g + E_o/2$

$$\alpha_5 = \frac{kA^2}{h\nu} \left(\frac{E_o}{2} \right)^{1/2} \int_{-(h\nu - E_f)}^{-(h\nu - E_g - E_o/2)} \exp - \left(\frac{h\nu + E}{E_o} \right) (-E + E_o/2)^{1/2} \, dE \qquad (6.17b)$$

The lower limit is still $-(h\nu - E_f)$. However, to ensure the excited electrons are still within the localized tail (just below E_c), the upper limit has to be put as $-(h\nu - E_g - E_o/2)$ (Figure 6-19c).

The fitting range of (6.17b) is :

$h\nu \geq E_g + E_o/2$

In the above equations, $k = \frac{\pi e^2 h^3 a}{n_o cm^2}$ and is taken to be the same as that of Wronski et al (1982), $k = 4 \times 10^{-38} (eV)^2 (cm)^5$ for their analysis of a-Si. "A" was taken to be $4 \times 10^{21} cm^{-3} eV^{-3/2}$. The order of magnitude was being typical for semiconductors. Besides, if we assumed the Fermi level to be pinned in the mid-way between the two Gaussian bands, we had $|E_f - E_{G2}| = |E_f - E_{G3}| = \Delta$. Finally, if we took each single particle state of T_2^+ centre effectively as an ESR active spin centre, we had the following:

$$\rho_s \cong G \int_{-\infty}^{+\infty} \exp - \left(\frac{E - E_G}{\delta E_G} \right)^2 dE$$

$$= 2G \int_{0}^{+\infty} \exp - \left(\frac{E - E_G}{\delta E_G} \right)^2 d(E - E_G)$$

$$= G \, \delta E_G \sqrt{\pi}$$

$$\therefore \quad G \cong \frac{\rho_s}{\delta E_G \sqrt{\pi}} \tag{6.18}$$

where ρ_s is the ESR spin density.

Since we have kept A and K to be fixed, the free parameters to be fitted were: E_o, E_g, E_f, δE_G, Δ and ρ_s. Although there were altogether six parameters to be fitted, usually each region (Figure 6-1) of the absorption spectrum can be used to fix two of them. Region A was highly sensitive to the value of the optical gap E_g, while region B can fix the value of E_o. Too small in the value of E_o may result in an underestimation on the absorption coefficients in region B. Region C was sensitive to both values of δE_G and Δ. During the fitting process, it was discovered that as the value of Δ increased, the absorption coefficients in region C decreased. Also, if a parameter is fixed in one region, its value usually has to be carried over to another region and a good example is E_f. However, no modification on its value is needed. This shows the self-consistency of the model assumed.

A numerically good fit has been shown in Figure 6-20 and the values of the parameters were as follows:

$\rho_s = 1.8\times10^{17}$ cm^{-3};
$E_o = 65$ meV;
$E_g = 1.7$ eV;
$E_f = 0.87$ eV from $E_v \Rightarrow 0.86$ eV from E_c;
$\delta E_G = 0.3$ eV;
$\Delta = 0.1$ eV;

F) Discussions:

Firstly, in view of the values of the parameters, the followings were observed:

1) The Fermi level was 0.87 eV from the mobility of valence band, implying $E_c - E_f \cong 0.86$ eV. This was in close agreement with the finding from dark electrical conductivities measurement which gave an activation energy of 0.866 eV for extended states conduction;

2) The optical band gap was found to be 1.7 eV, with an exponential tail width 65 meV. G.D. Cody et al.(1981) experimentally showed that for a-Si:H, an empirical relationship between E_g and E_o (Figure 6-21) could be established. He found that for E_o = 65 meV, E_g would be 1.7 eV, exactly the same as ours;

3) From dark ESR experiment, the spin density for a-Si:H deposited at T_s = 250°C was approximately $3\times10^{17}cm^{-3}$, which was in close agreement with the fitted ρ_s: $1.8\times10^{17}cm^{-3}$. This showed that T_2^+ centre was highly possible to be the candidate responsible for the ESR signal;

4) The characteristic width, δE_G, was found to be 0.3 eV and the separation between the Gaussian peaks was 0.2 eV. Their presence pinned the Fermi level nearly at the mid-gap.

Secondly, comparing the optical properties of our a-Si:H film at T_s= 250°C with those from the BARE process (J.C. Anderson et al., 1986) and glow-discharge produced (H. Curtins and M.favre, 1988), the followings were obtained:

1) The optical gap of the BARE films were in the range 1.55 - 1.67 eV, slightly lower than ours and those from glow discharge samples (1.6 - 1.7eV);

2) The minimum absorption for sub-band gap radiations for BARE film was $\leq 10^3$ cm^{-1} (Figure 6-22), while that of ours and glow-discharge produced were of order 10^0 cm^{-1}. This implies a value of nearly three order of magnitude higher than ours.

Finally, when each transition mechanism was separately plotted (Figure 6-23) against the photon energies, the followings were observed:

1) For $h\nu \geq 1.8$ eV, band to band transitions dominated, but its contribution dropped quickly for $h\nu < 1.8$ eV. This could be easily explained. As $h\nu$ approaching 1.7 eV, less and less electrons were available for excitations (due to the parabolic band shape). No contribution was made by this transition for $h\nu < 1.7$ eV, since no extended state electrons from valence band was available;

2) Due to the functional form assumed, the tail to band transitions gave a straight line in the range $1 \leq h\nu \leq 1.7$ eV. Once $h\nu$ larger than 1.7 eV, the absorption due to this mechanism began to saturate, which resulted in a levelling off in its absorption curve for $h\nu \geq 1.8$ eV;

3) For the gap states transitions (T_3^- centre to conduction band and valence band to T_2^+ centre), two curves were found to be overlapping each other. This should not be taken as the general case. It results from the facts that the Fermi level was pinned nearly at the mid-gap while the two Gaussian bands were of the same shape and the two Gaussian peaks were equally away from the Fermi level. This transition mechanism dominated in the range $0.9 \leq h\nu \leq 1.4$ eV and its corresponding absorption began to saturate for $h\nu \geq 1.4$ eV;

4) Valence band to unoccupied tail states transition was found to be weak for the whole range of $h\nu$s. This was expected since the tail states have a width of only 65 meV and their density decay exponentially with energy. So, not many unoccupied states beyond E_f were available for the

transitions, hence weak absorption.

G) Conclusions:

The parameters for the band model assumed for our a-Si:H with T_s = 250°C was taken by deconvolution of an optical spectrum which was resulted from both PDS and double beam spectroscopy. Numerical fittings gave an optical gap of 1.7 eV, an exponential tail of 65 meV, a mobility gap of 1.73 eV, an ESR active spin density of $1.8\times10^{17}cm^{-3}$, a characteristic width of 0.3 eV for both T_2^+ and T_3^- Gaussian peaks, a separation of 0.2 eV between the two Gaussian peaks, a Fermi level of 0.86 eV below E_c. All the above findings were consistent with a high quality a-Si:H material with low gap state defects. In particular, the position of Fermi level and spin density were found to agree reasonably well with other experiments. The relationship between optical gap and the width of exponential tail established by Cody et al.was found to be also obeyed by our sample. To conclude, the optical properties of our a-Si:H samples were highly comparable to those of glow-discharge samples and were much better than those of BARE samples.

Appendix A:

A.1 An outline on theoretical and experimental aspects of PDS:

A set up for transverse PDS has been plotted schematically in Figure 6-24. Detail treatments on both theoretical and experimental aspects of PDS have been given by W.B. Jackson et al. in 1981. The followings just give a brief description on the subject.

When a sample is irradiated by a light flux, there is a conversion of the absorbed light into thermal energy, resulting in heating of the sample. If the impinging beam is modulated, the sample surface exhibits a modulated surface temperature. The periodically heated sample surface is a heat source for the surrounding medium, which exhibits a periodic temperature gradient near the sample surface. This periodic temperature gradient gives rise to a refractive index gradient suitable for periodically deflecting a probe beam propagating along the surface of the solid.

The amplitude of this periodic deflection is given by (see Figure 6-25):

$$\theta = \frac{l}{n} \left[\frac{dn}{dT} \right] < \frac{dT(x,t)}{dx} > \qquad (6.19)$$

where l is the interaction path length between the probe beam and the temperature gradient $\frac{dT}{dx}$ and n is the refractive index of the medium. The brackets in Eq.(6.19) denote a spatial average over the path length.

In order to estimate the surface temperature of a sample, we have to solve the heat diffusion equation in all the regions where heat can propagate. Consider Figure 6-26, the sample is irradiated by a modulated light beam whose intensity at the frequency $\omega/2\pi$ is I_o. Thus the heat

diffusion equations can be written in the three regions shown i.e. the transparent fluid (f), sample (s) and the transparent backing (b):

$$\frac{\partial^2 T_f}{\partial x^2} = \frac{1}{D_f}\frac{\partial T_f}{\partial t} \qquad 0 < x < l_f \qquad (6.20)$$

$$\frac{\partial^2 T_s}{\partial x^2} = \frac{1}{D_s}\frac{\partial T_s}{\partial t} - A\exp(\alpha x)\, e^{j\omega t} \qquad -1 < x < 0 \qquad (6.21)$$

$$\frac{\partial^2 T_b}{\partial x^2} = \frac{1}{D_b}\frac{\partial T_b}{\partial t} \qquad -1-l_b < x < -1 \qquad (6.22)$$

where T_i (i = f,s,b) is the modulated temperature in the region (i) and D_i is the thermal diffusivity.

The term $A\exp(\alpha x)\exp(j\omega t)$ represents the modulated heat source due to the light absorbed by the sample, α being the optical absorption coefficient. In Eqt. (6.21)

$$A = \frac{\alpha I_o \eta}{2 k_s}$$

where η is the optical to thermal energy conversion efficiency by non-radiative de-excitations. The general solutions of Eqs. (6.20), (6.21) and (6.22) are given by:

region I: $$T_f(x,t) = T_s \exp(-\sigma_f x + j\omega t) \qquad (6.23)$$

region II: $$T_s(x,t) = [\, U\exp(\sigma_s x) + V\exp(-\sigma_s x) - E\exp(\alpha x)\,]\exp(j\omega t) \qquad (6.24)$$

regionIII: $$T_b(x,t) = W\exp[\,\sigma_b(x+1) + j\omega t\,] \qquad (6.25)$$

where T_s, U, V, E and W are complex constants; $\sigma_i = (1+j)\mu_i$ where μ_i is the thermal diffusion length; $\mu_i = \sqrt{D_i / \pi f}$ in region (i).

These constants are found by applying the following boundary conditions:

$$T_s|_{x=0} = T_f|_{x=0} \; ; \quad k_s\left(\frac{\partial T_s}{\partial x}\right)|_{x=0} = k_f\left(\frac{\partial T_f}{\partial x}\right)|_{x=0}$$

$$T_b|_{x=0} = T_s|_{x=0} \; ; \quad k_s\left(\frac{\partial T_s}{\partial x}\right)|_{x=0} = k_b\left(\frac{\partial T_b}{\partial x}\right)|_{x=0}$$

where k_i is the thermal conductivity of medium (i). Once $T_s(x,t)$ is known, the deflection amplitude θ is given by Eqt. (6.19)

It can be shown that for a sample deposited on a transparent backing, the deflection amplitude θ and hence the signal S from the position sensor can be written as :

$$S \propto 1 - e^{-\alpha d} \qquad (6.26)$$

where S : voltage signal from position sensor

α : absorption coefficient of sample in cm^{-1}

d : thickness of sample in cm

Or explicitly:

$$S(\lambda) = A\, I_o(\lambda)\, (\, 1 - e^{-\alpha(\lambda)d}\,) \qquad (6.27)$$

where A is a geometric factor

$I_o(\lambda)$ is the incident light intensity of wavelength λ

To determine A, we have to find a λ_{short} such that as λ tends to λ_{short}, $\alpha((\lambda) >> 1$; or $e^{-\alpha(\lambda_{short})d}$ tends to zero. Thus:

$$S(\lambda_{short}) = A\, I_o(\lambda_{short}) \qquad (6.28)$$

From (6.10), it is clear that A can be obtained from the linear portion of the plot $S(\lambda)$ vs. $I_o(\lambda)$.

So, we have:

$$S(\lambda) = \frac{S(\lambda_{short})}{I_o(\lambda_{short})} I_o(\lambda) \left(1 - e^{-\alpha(\lambda) d} \right) \qquad (6.29)$$

And the absorption coefficient can be found to be :

$$\alpha(\lambda) = -\frac{1}{d} \mathrm{Ln}\left(1 - \frac{S(\lambda) I_o(\lambda_{short})}{S(\lambda_{short}) I_o(\lambda)} \right) \qquad (6.30)$$

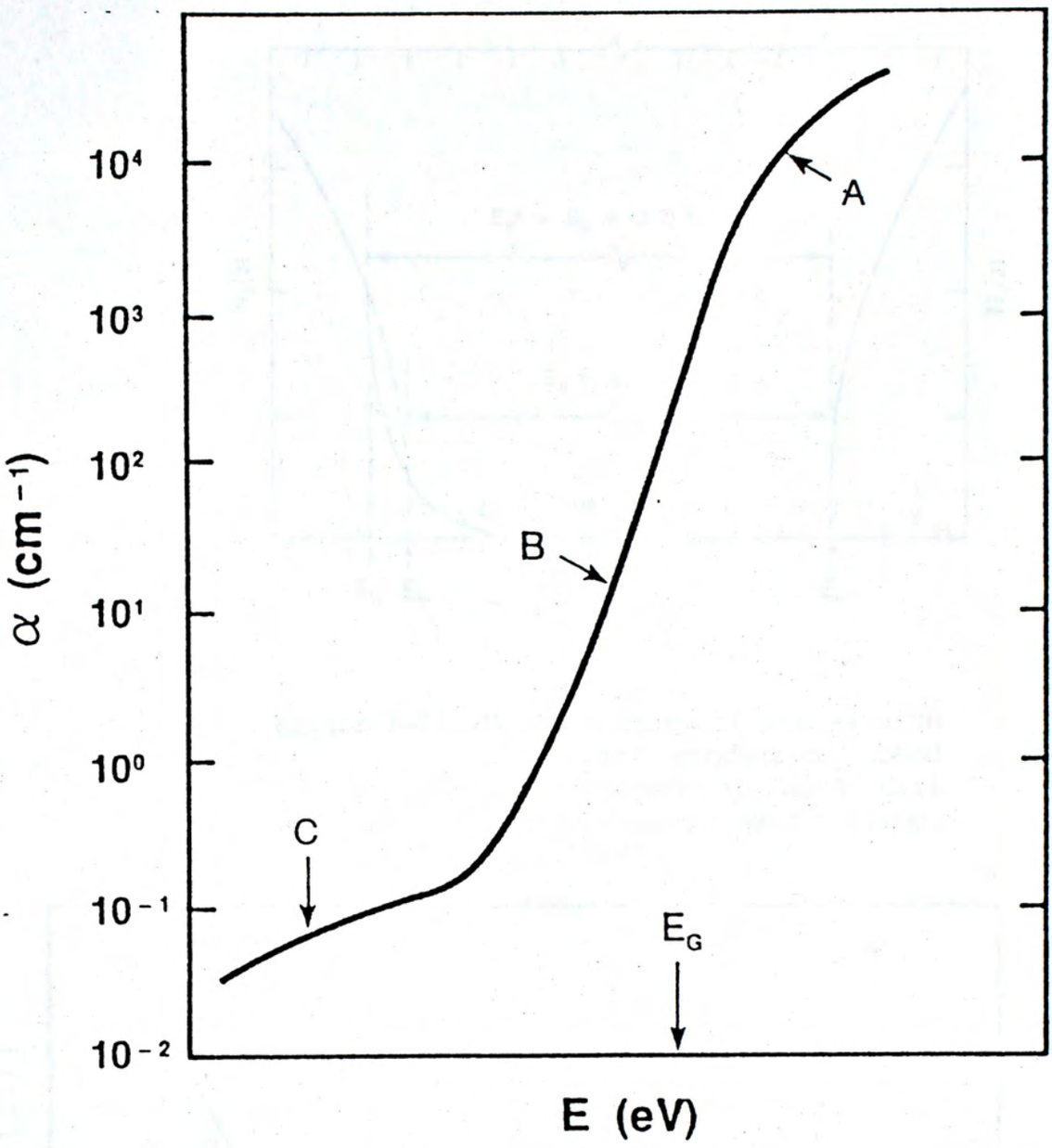

Figure 6-1. An idealized absorption edge of amorphous semiconductor (Tauc, 1970).

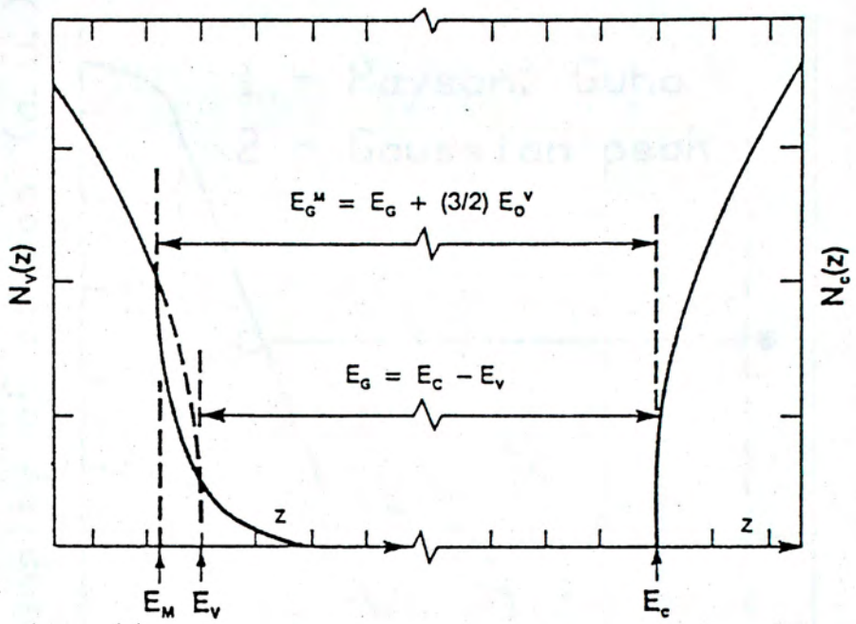

Figure 6-2. Model density of states with parabolic conduction band and exponential band tail for valence band (Tauc, 1972,1974).

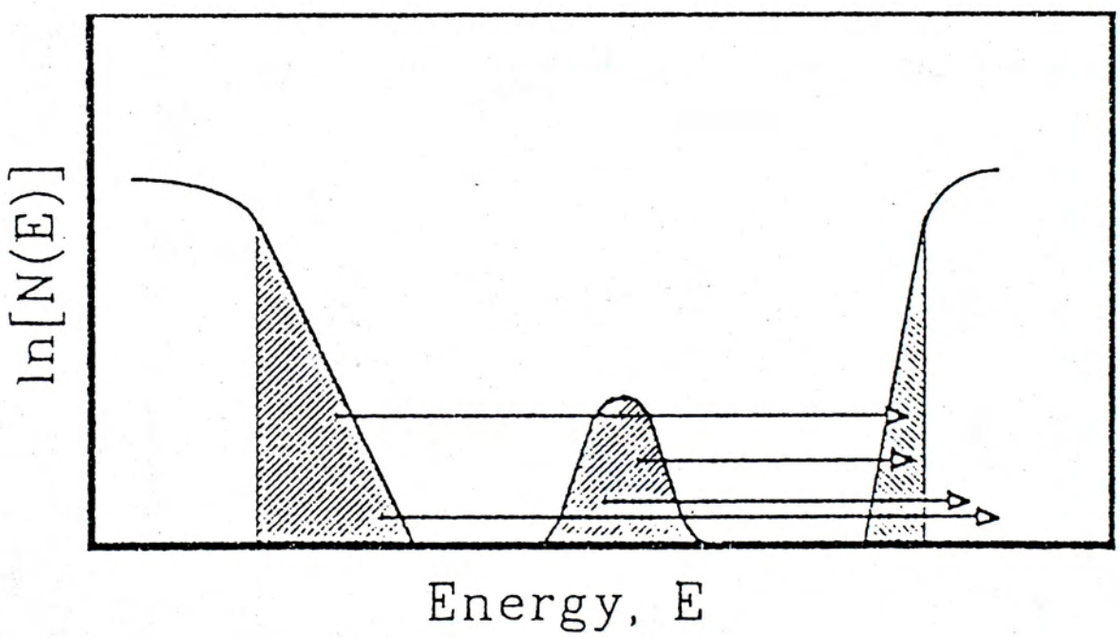

Figure 6-3.

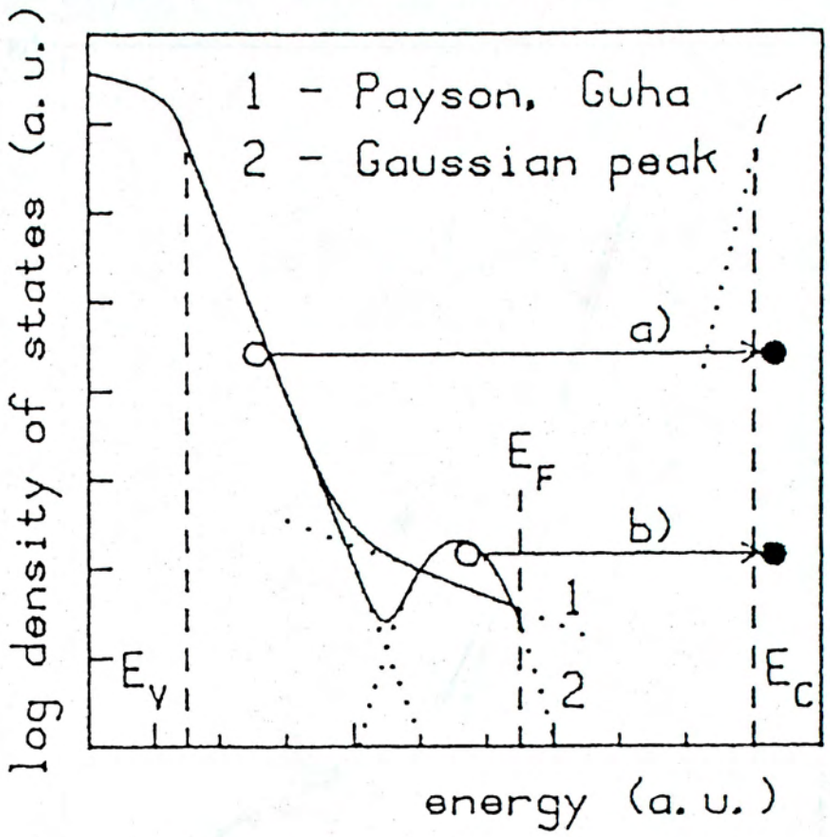

Figure 6-4. Schematic picture of DOS as illustration of deconvolution suggested by Payson and Guha (1985).

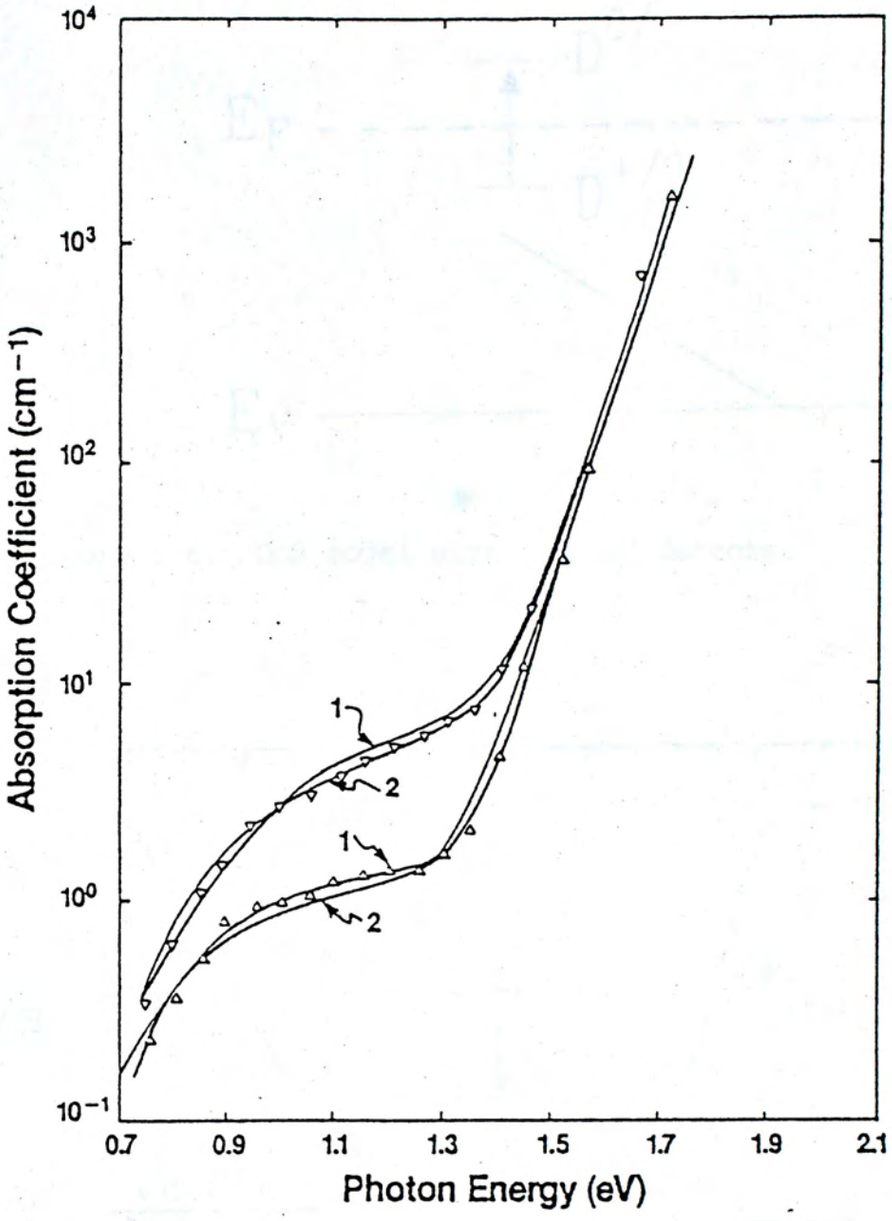

Figure 6-5. Absorption spectrum for two undoped a-Si:H. 1 and 2 refer, respectively, to the fits obtined using exponential and peak mid-gap distribution (J.S. Payson and S. Guha, 1984).

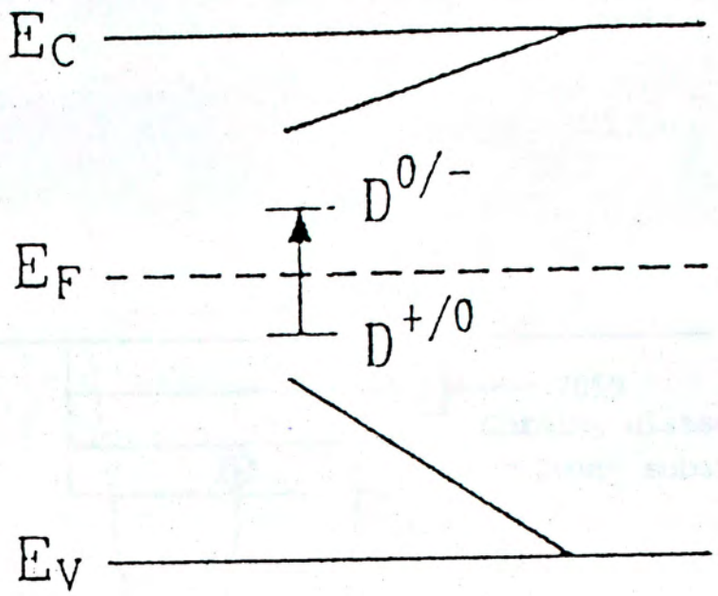

Figure 6-6. DOS model with charged defects.

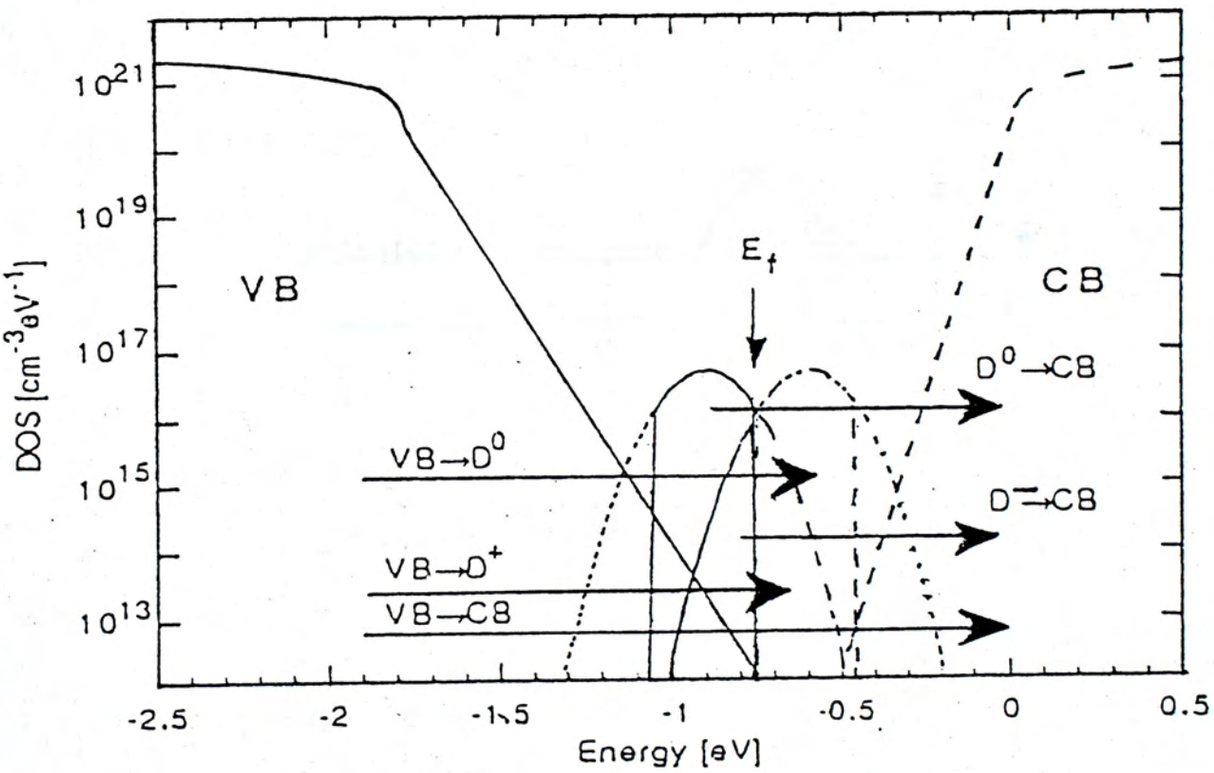

Figure 6-7. Possible transitions in a-Si:H with various types of defects within the mobility gap (N. Wyrsch et al., 1991).

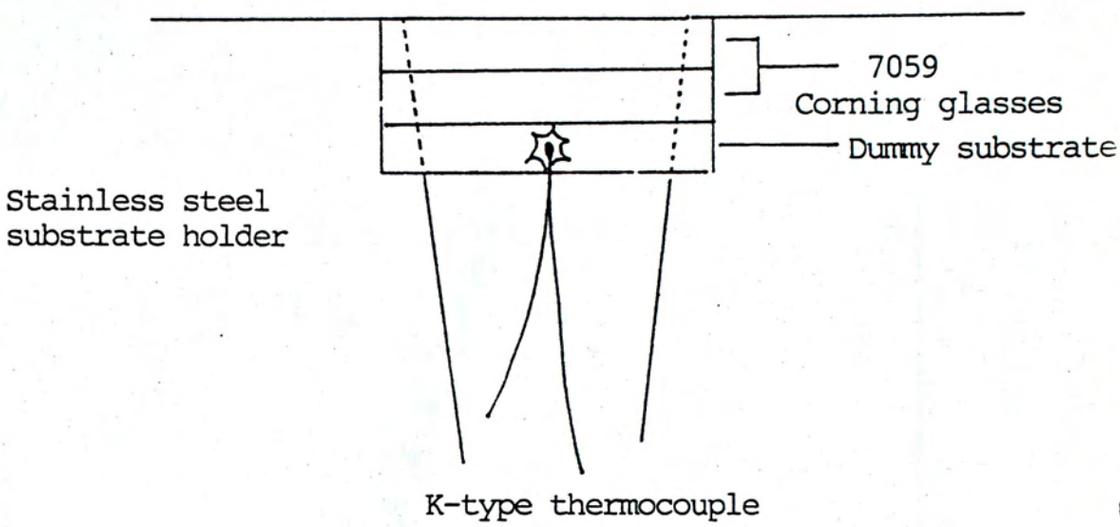

(Top view)

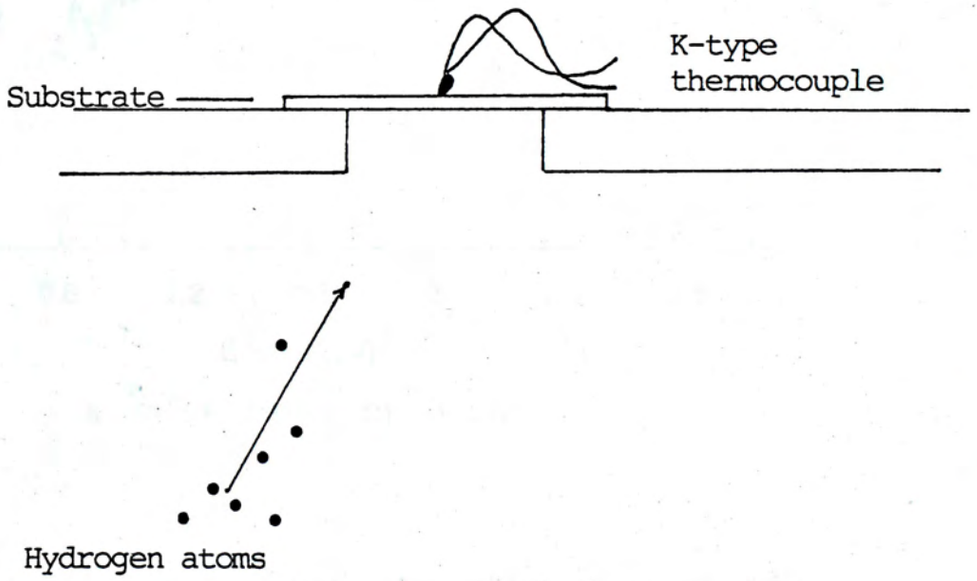

(Side view)

Figure 6-8.

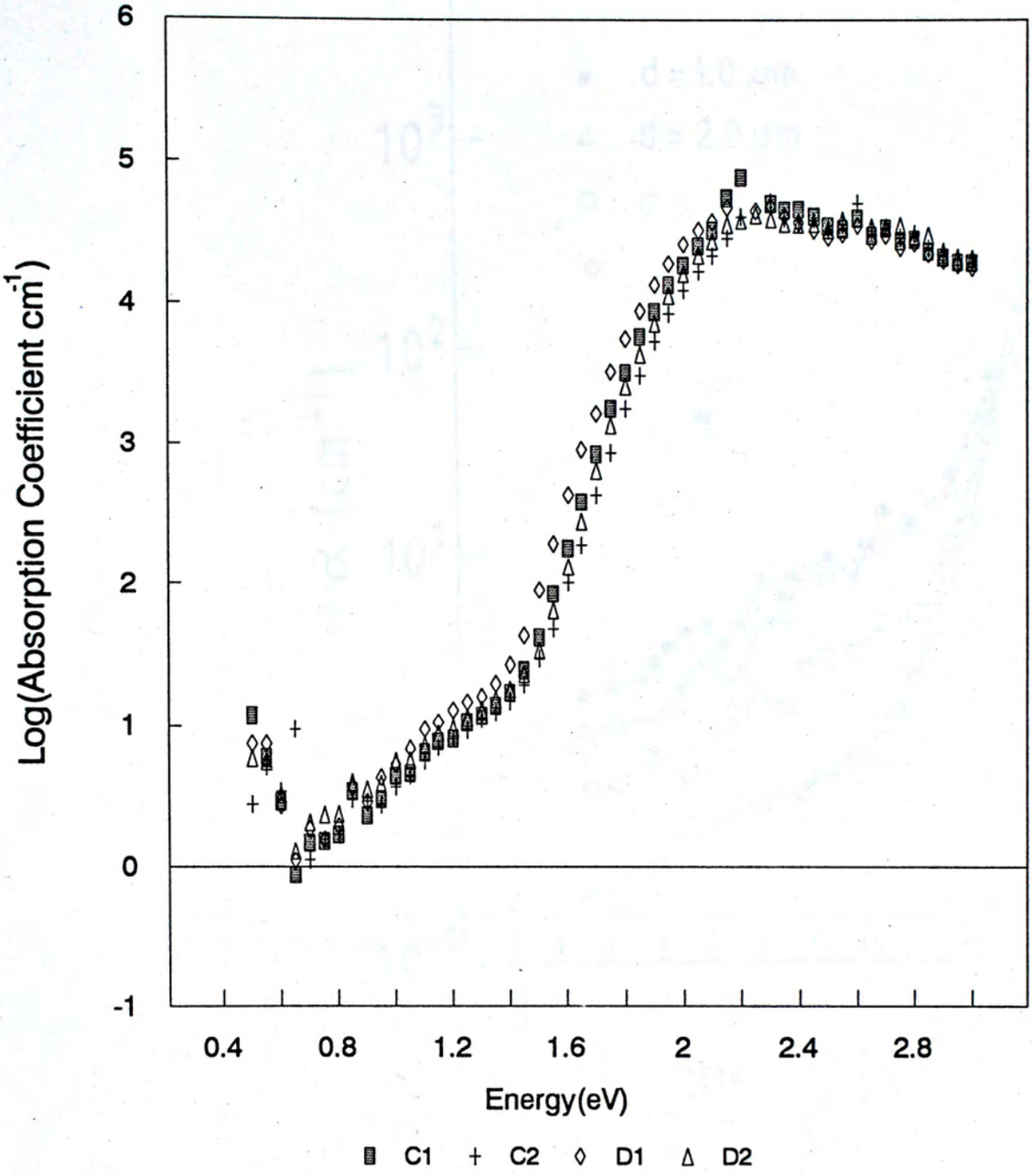

Figure 6-9. The optical absorption spectra of sample C1, C2, D1 and D2.
The spectra were obtained from PDS.

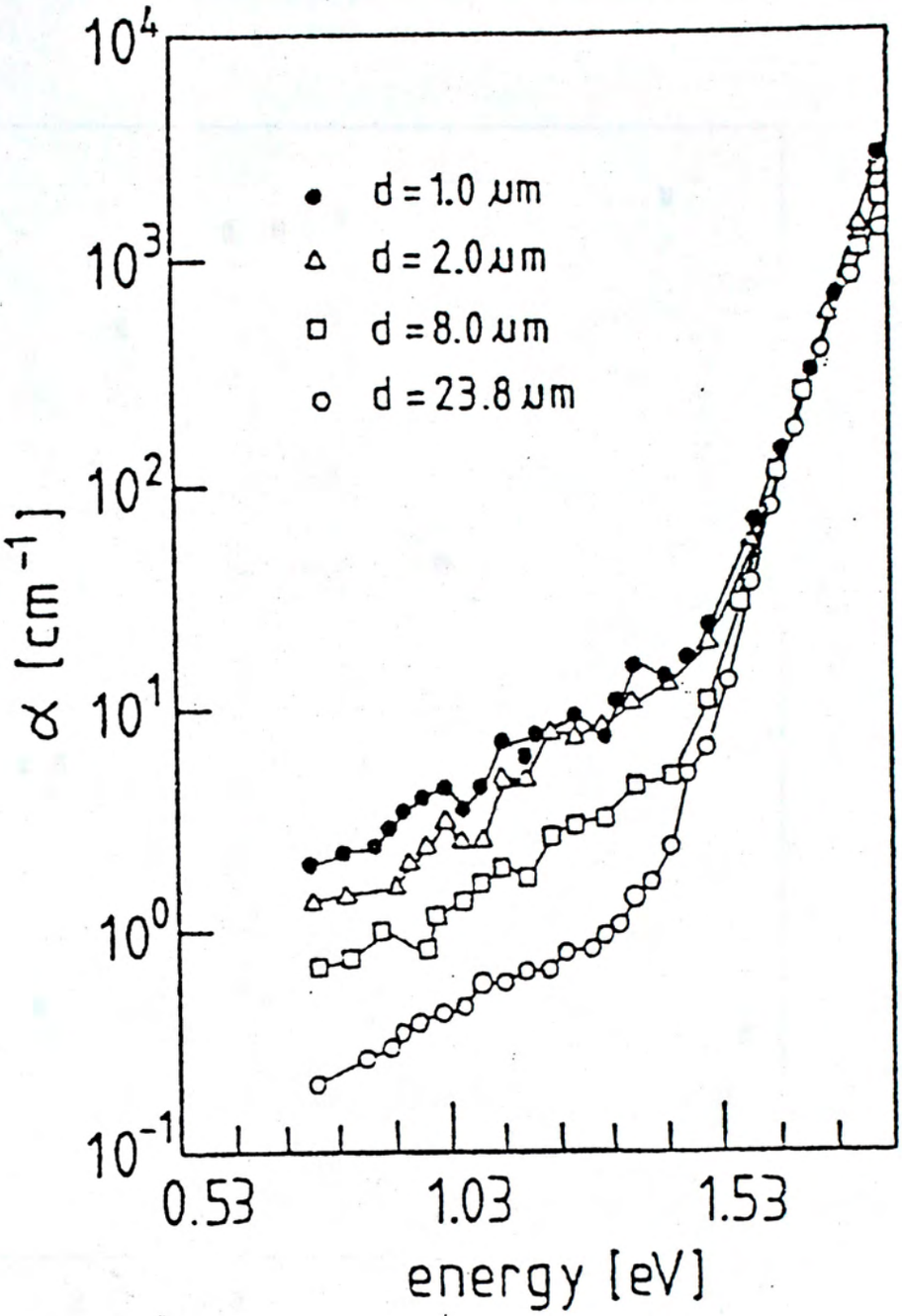

Figure 6-10. Thickness dependent of PDS sub-bandgap absorption spectra for a series of a-a-Si:H films by glow-discharge technique (H. Curtins and M. Favre, 1988).

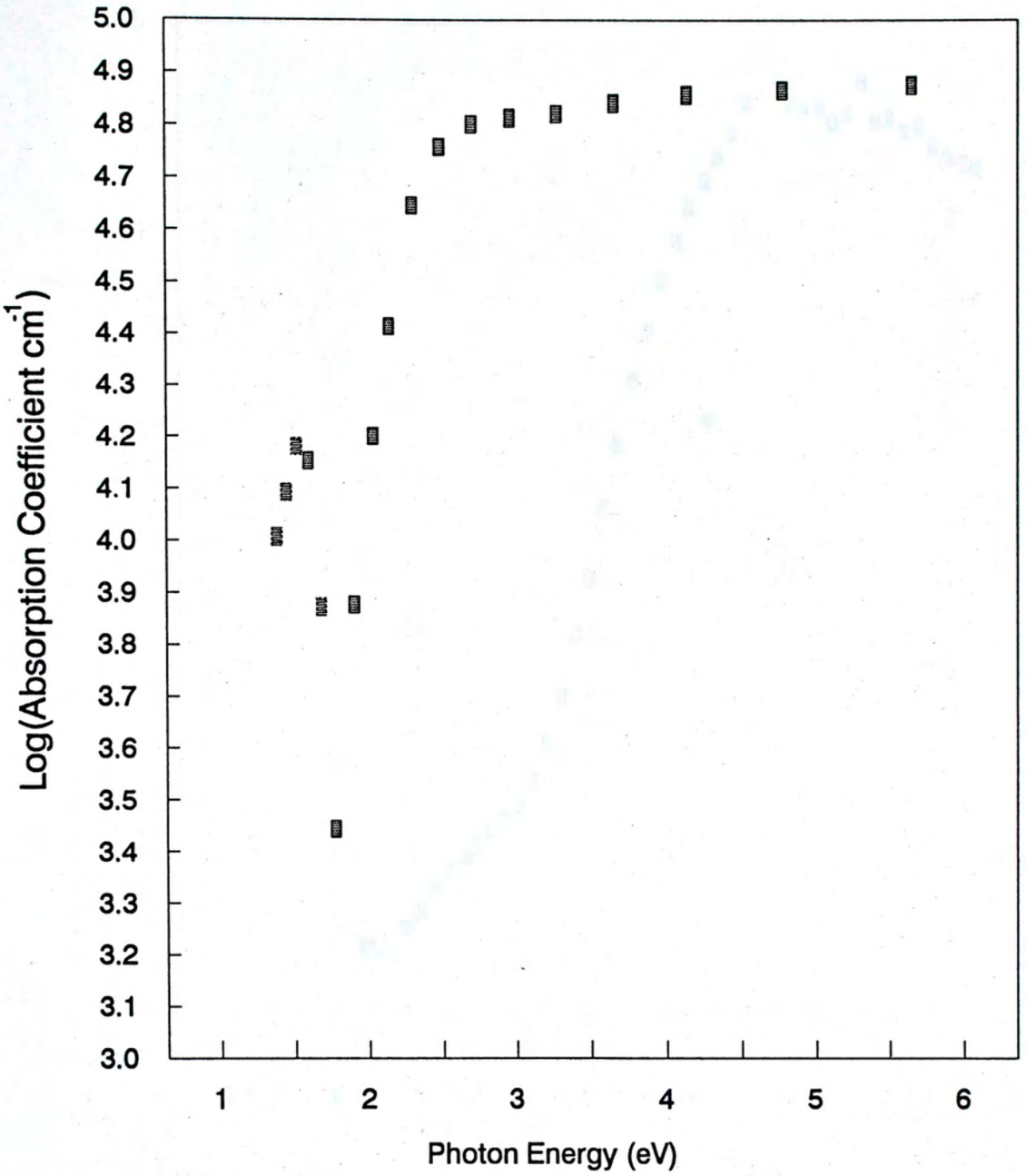

Figure 6-11. The optical absorption spectrum of reactively evaporated a-Si:H deposited at Ts=250°C.
The spectrum was obtained from a double beam spectrometer.

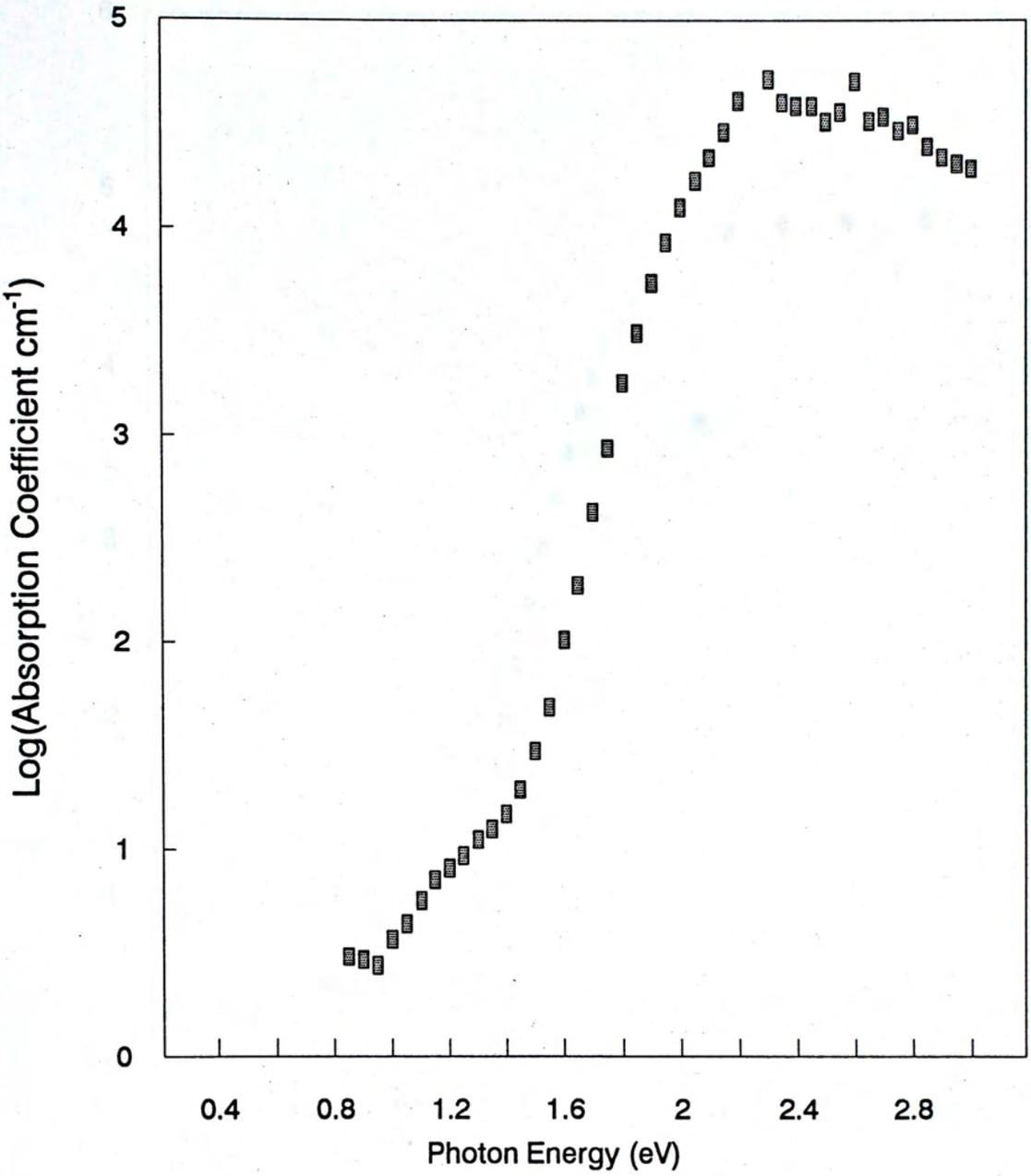

Figure 6-12. Optical absorption spectrum of C2 sample obtained from PDS experiment.

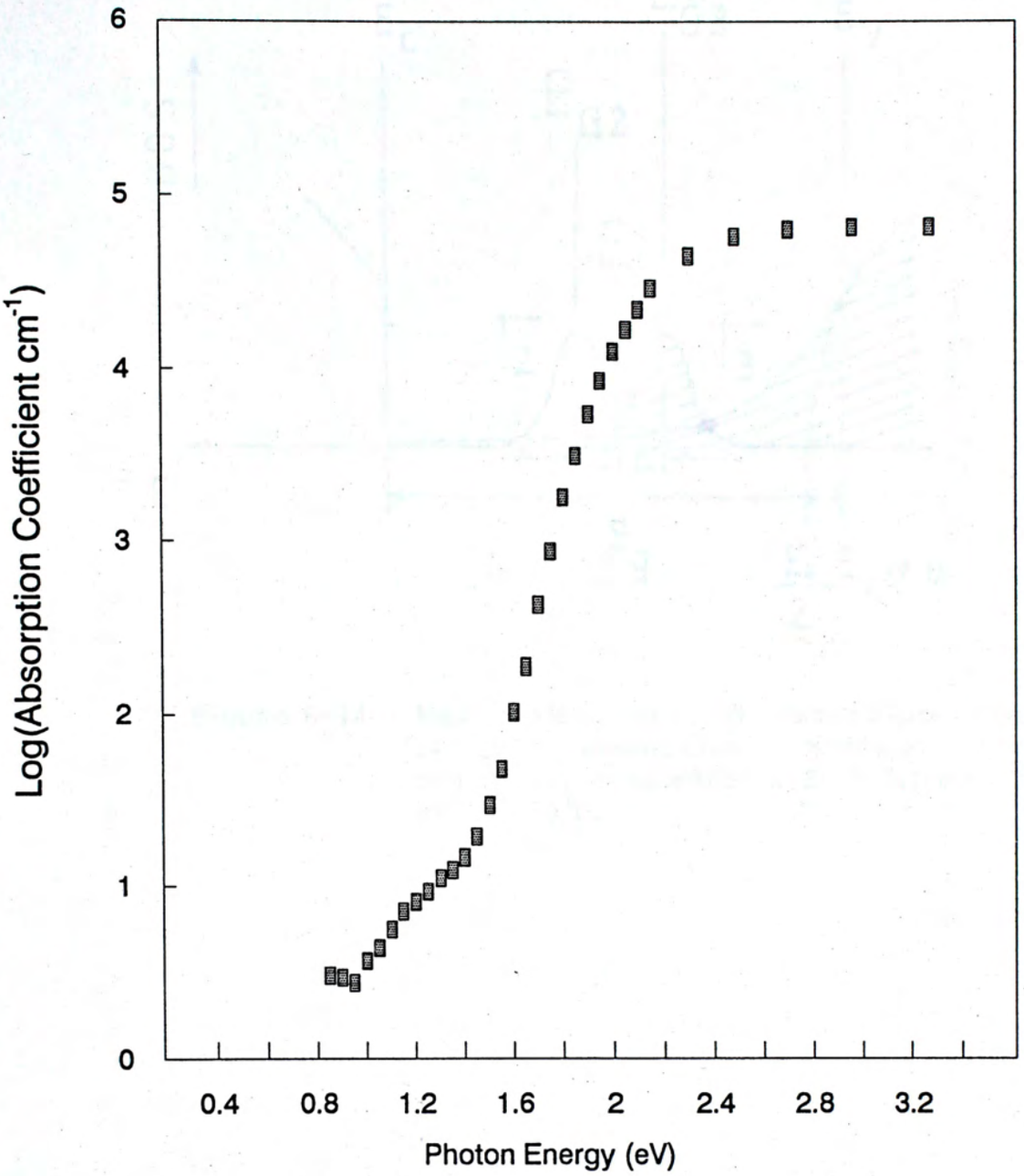

Figure 6-13. Optical absorption spectrum of C2 sample obtained by combining the spectra from PDS and double beam spectroscopy.

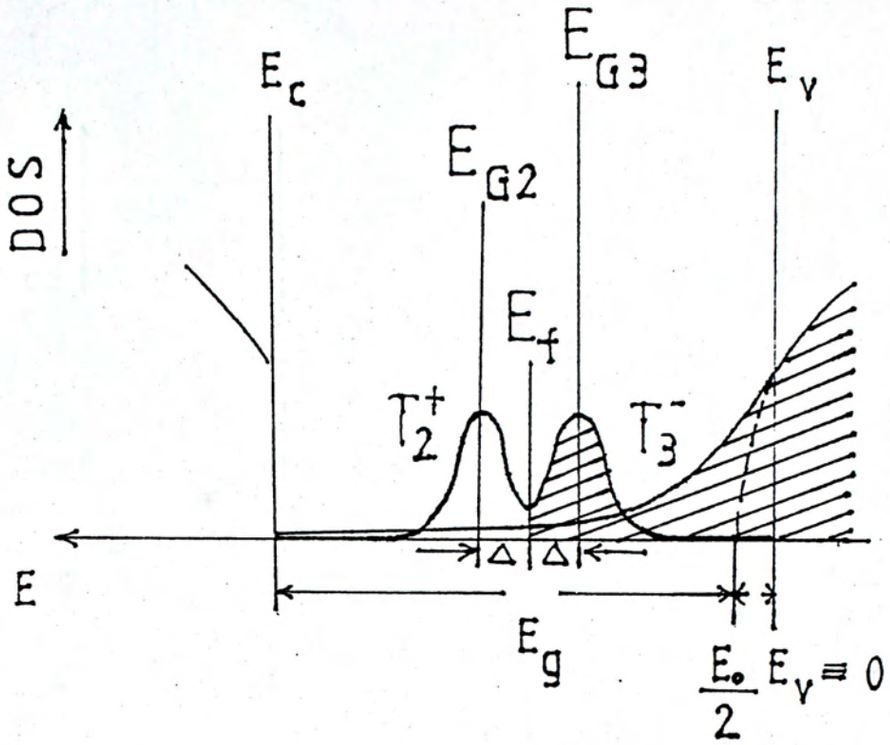

Figure 6-14. Band model used to deconvolute the optical absorption spectrum for reactively evaporated a-Si:H deposited at Ts=250 °C.

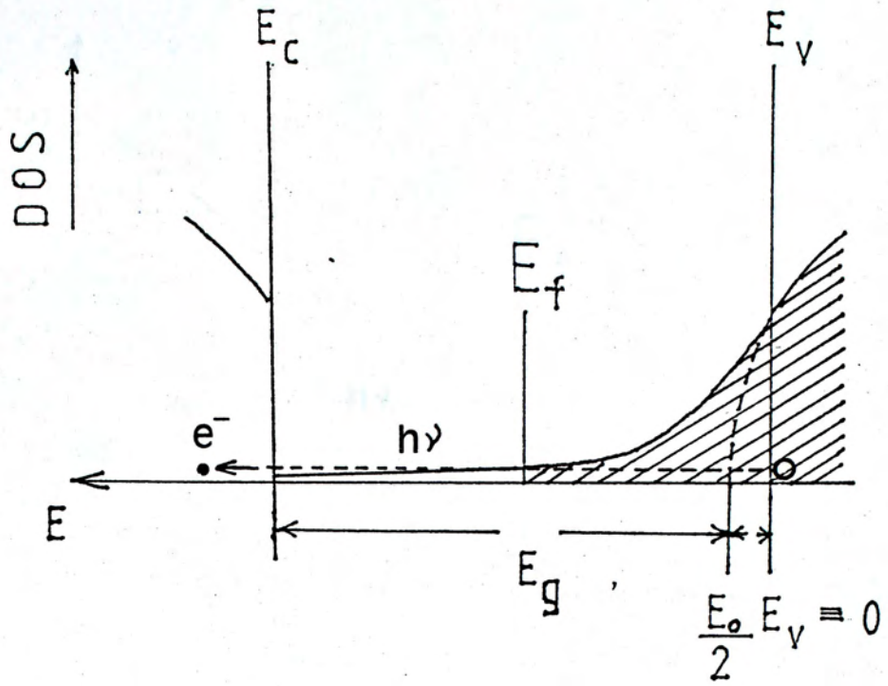

Figure 6-15a.

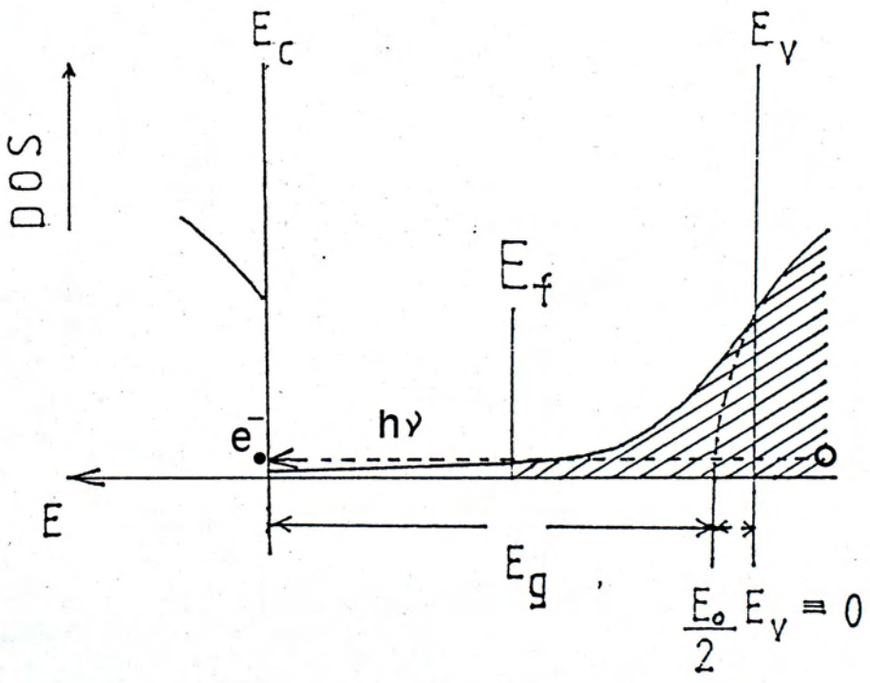

Figure 6-15b.

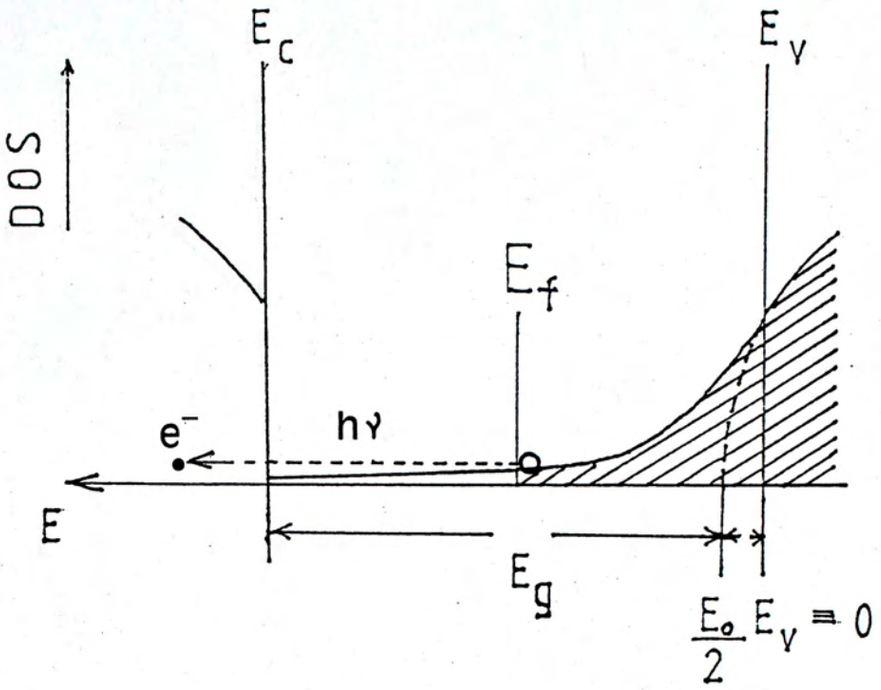

Figure 6-16a.

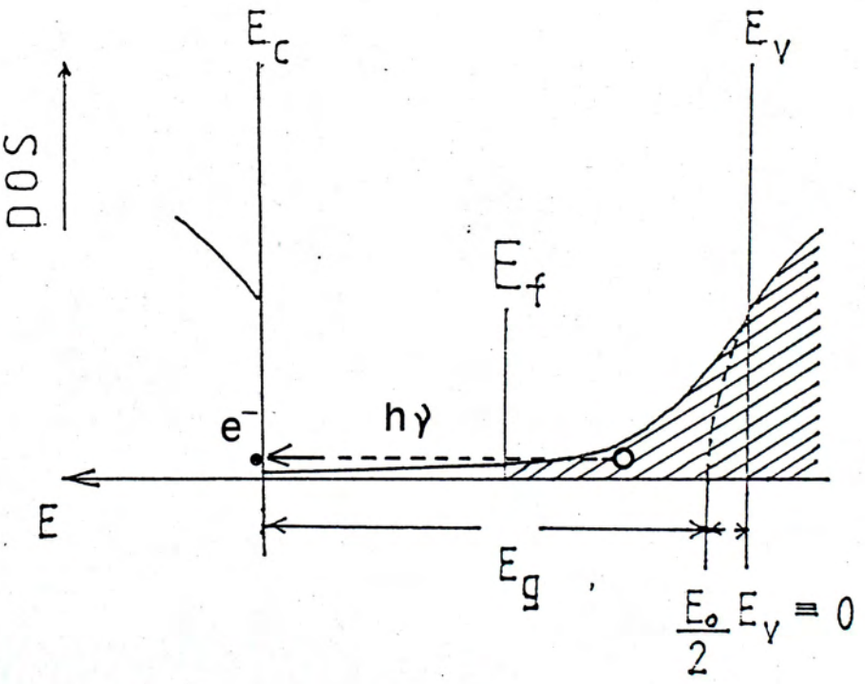

Figure 6-16b.

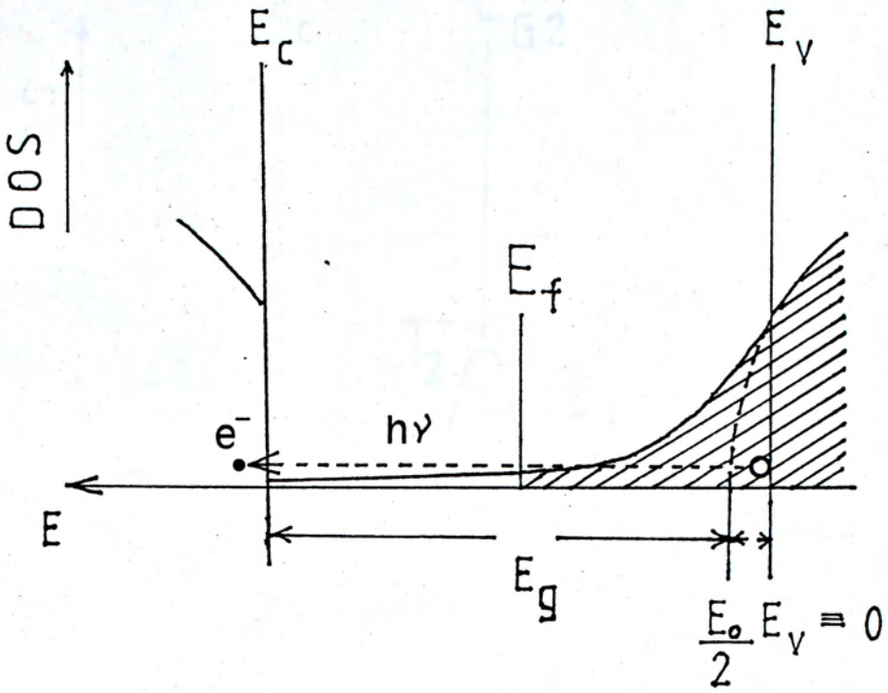

Figure 6-16c.

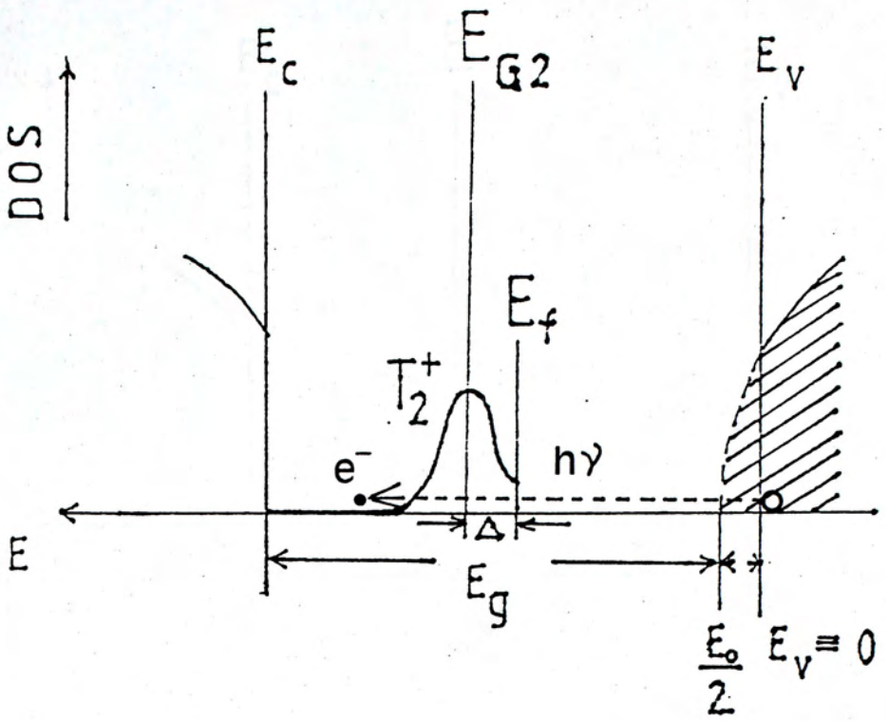

Figure 6-17a.

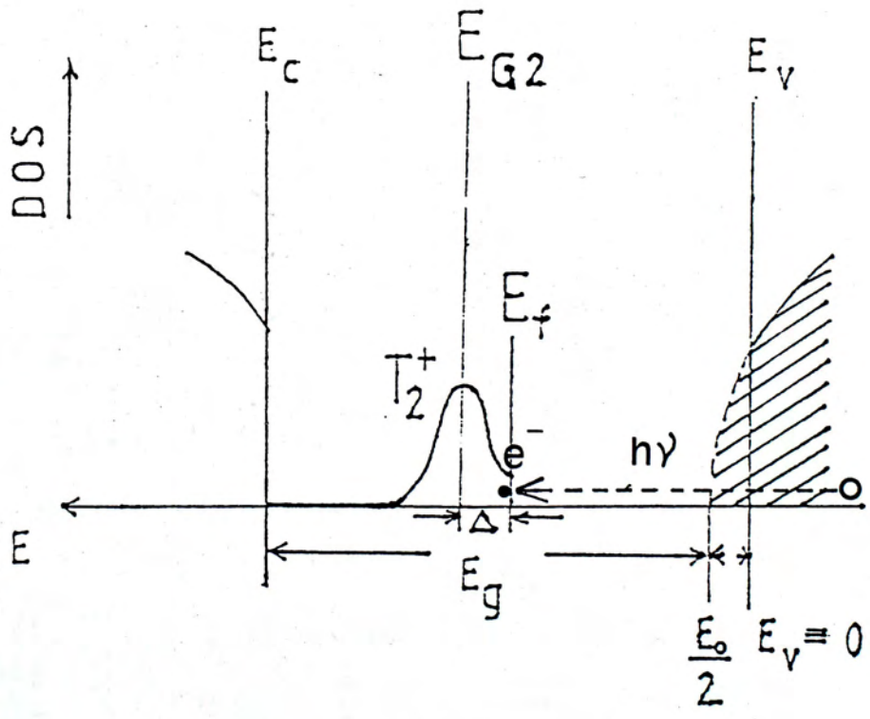

Figure 6-17b.

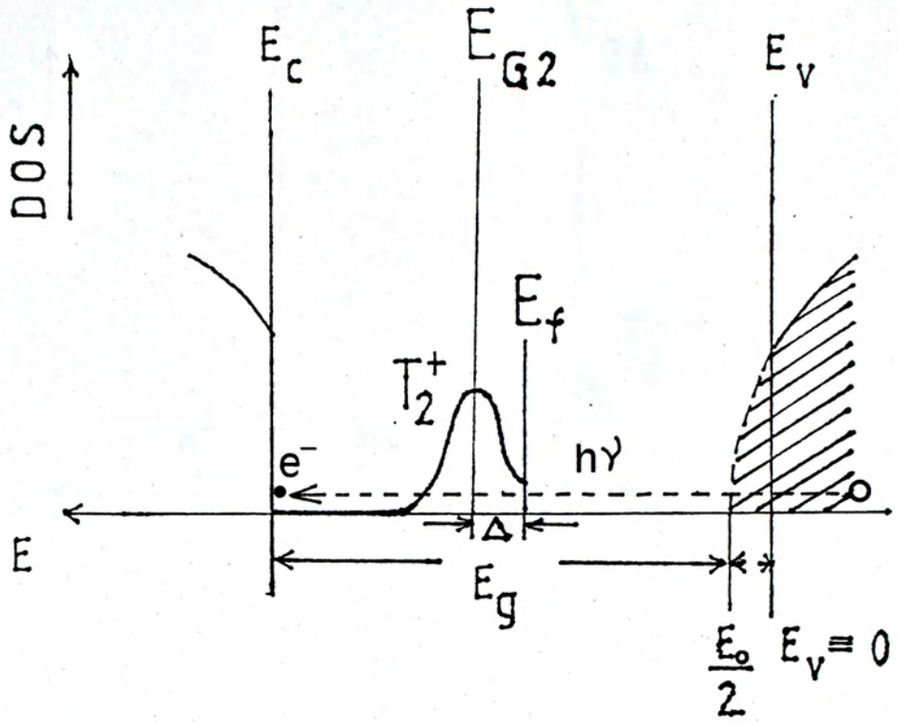

Figure 6-17c.

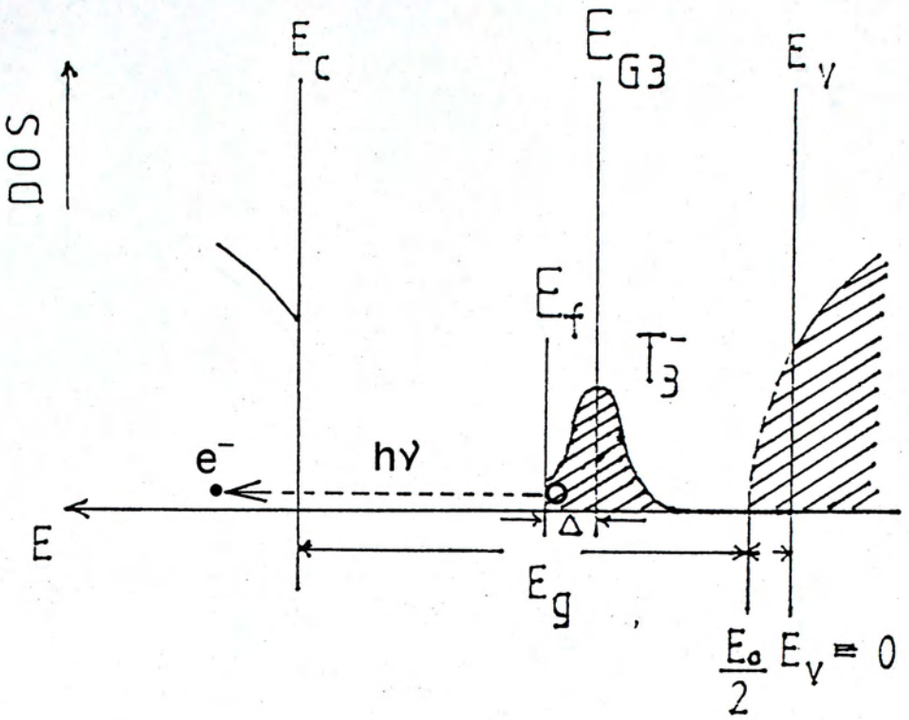

Figure 6-18a.

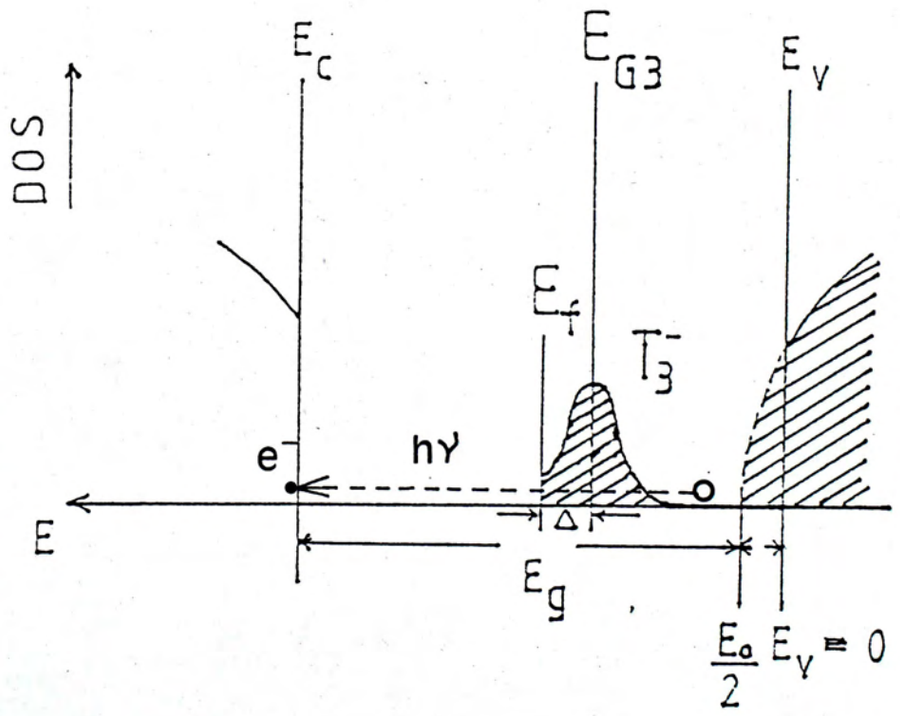

Figure 6-18b.

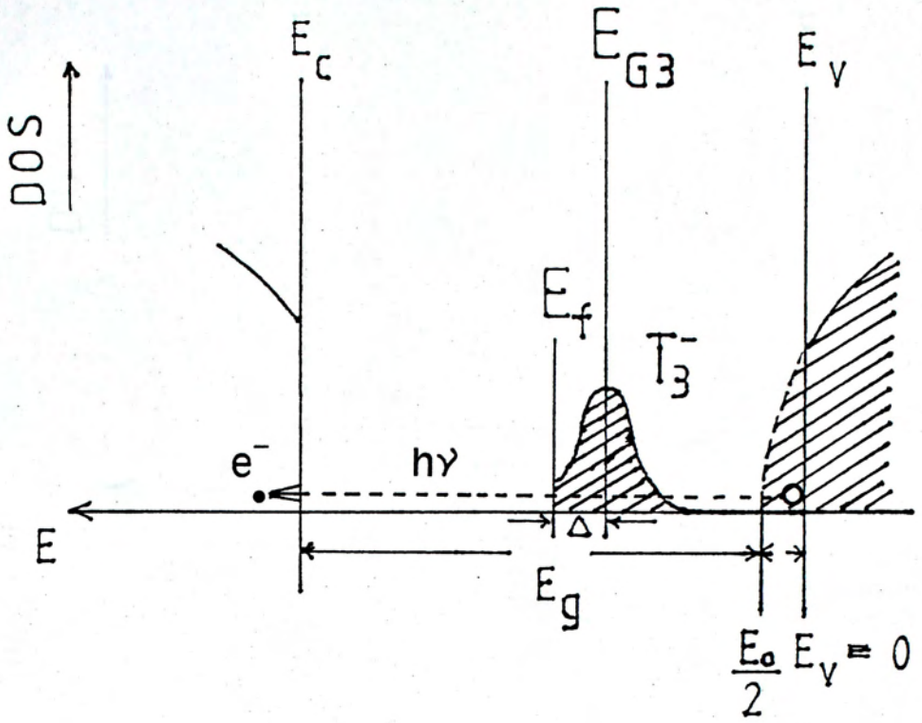

Figure 6-18c.

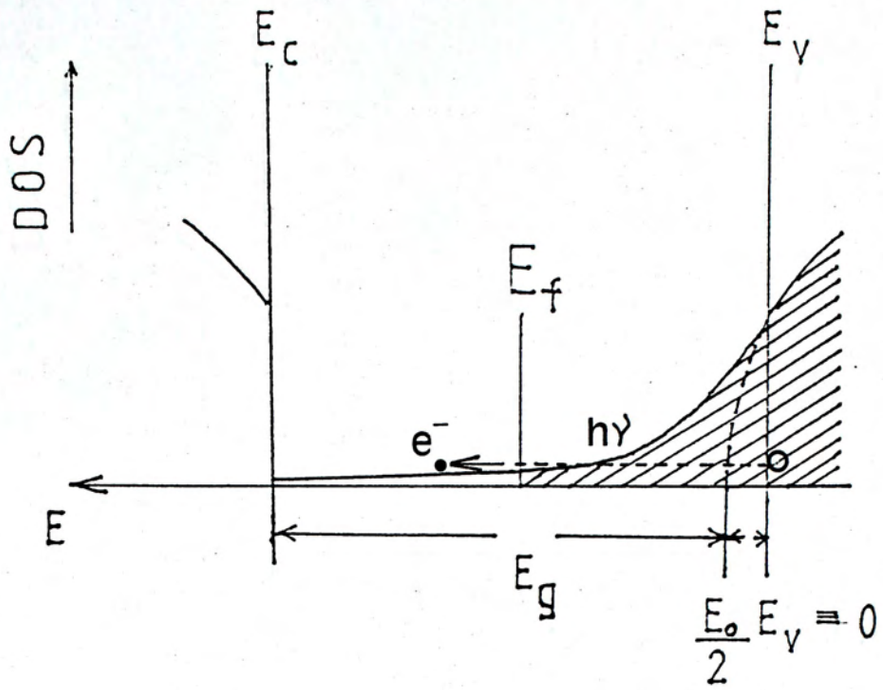

Figure 6-19a.

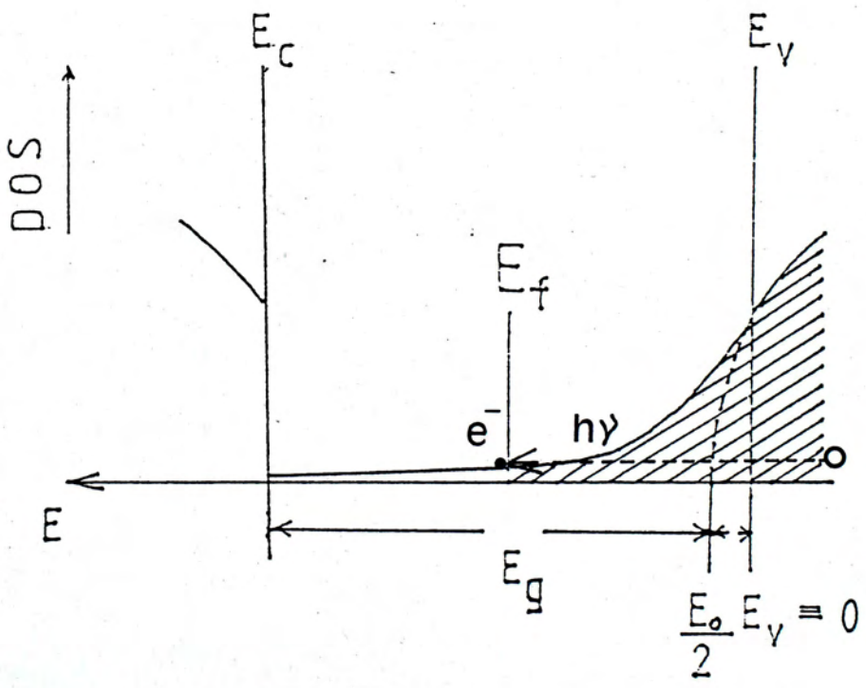

Figure 6-19b.

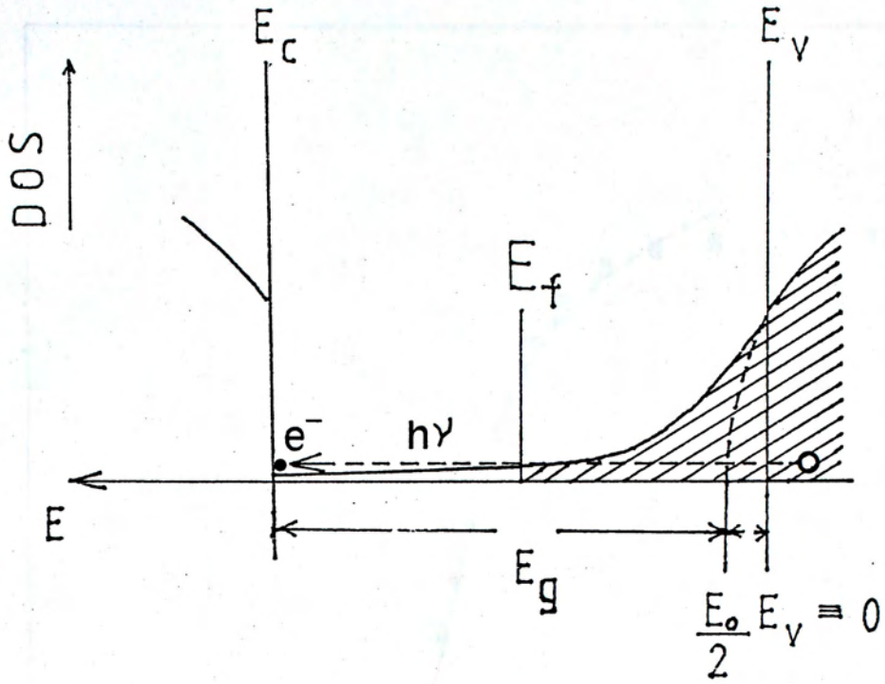

Figure 6-19c.

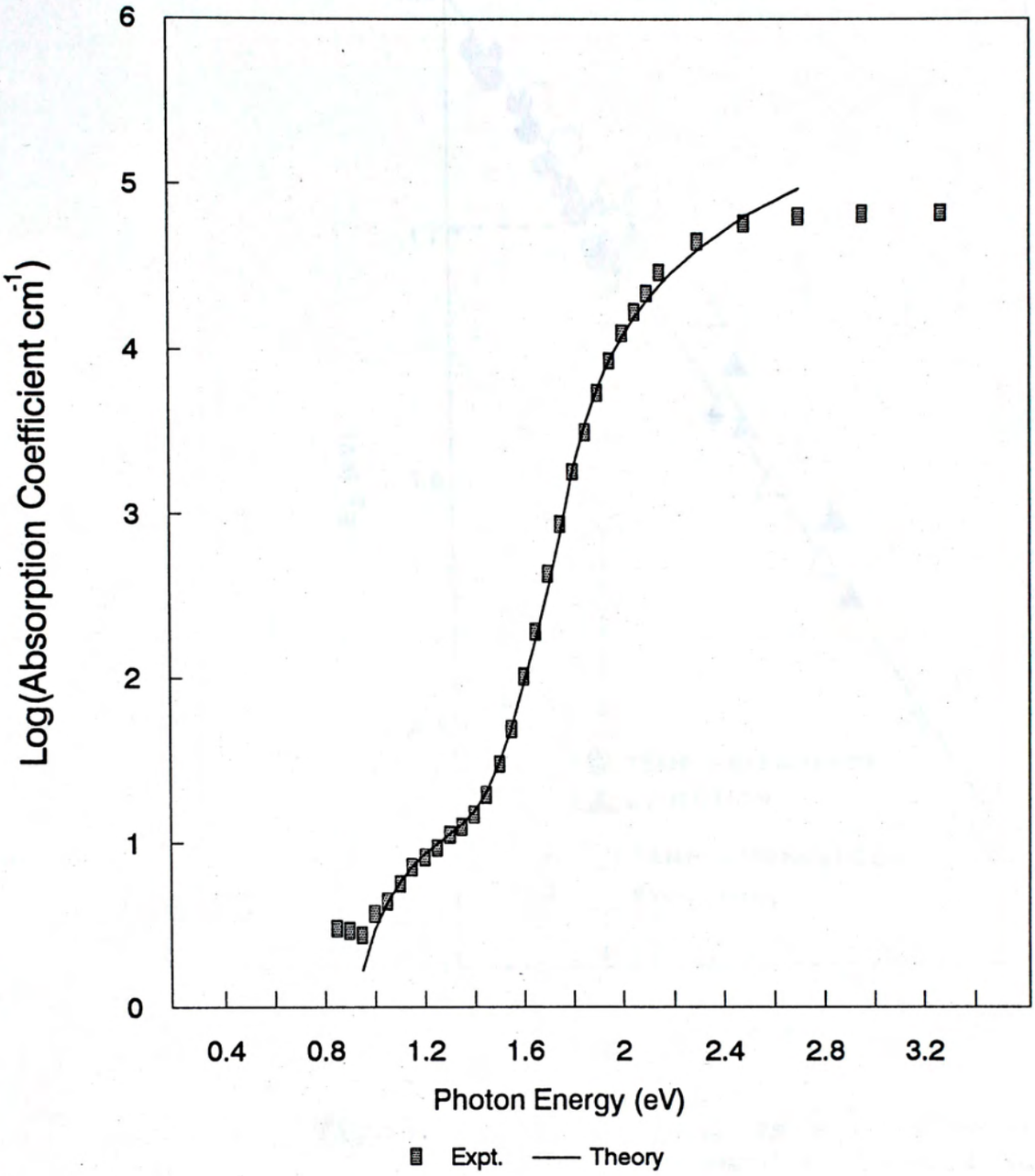

Figure 6-20. The optical absorption spectrum of C2 sample.
The solid line was obtained by a deconvolution of an assumed band model described in section E.1.

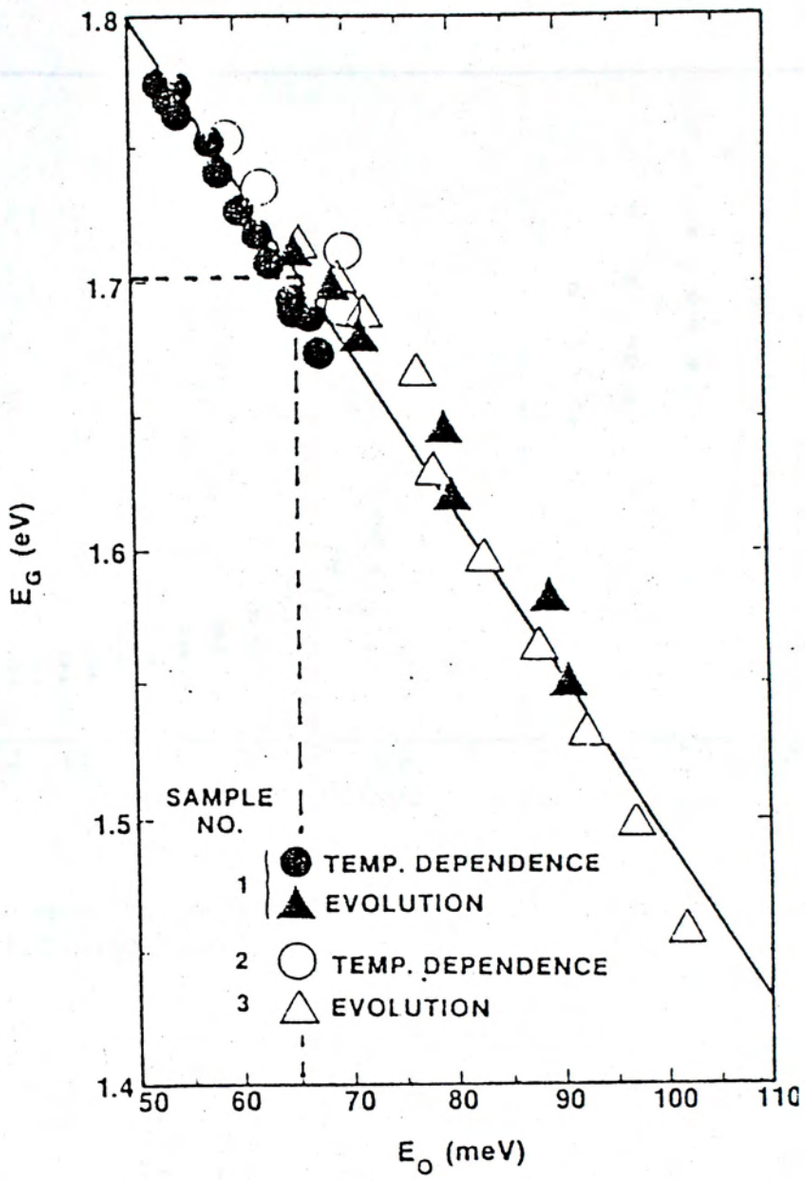

Figure 6-21. Optical gap as a function of E_o for three samples of a-Si:H (G.D. Cody et al., 1981).

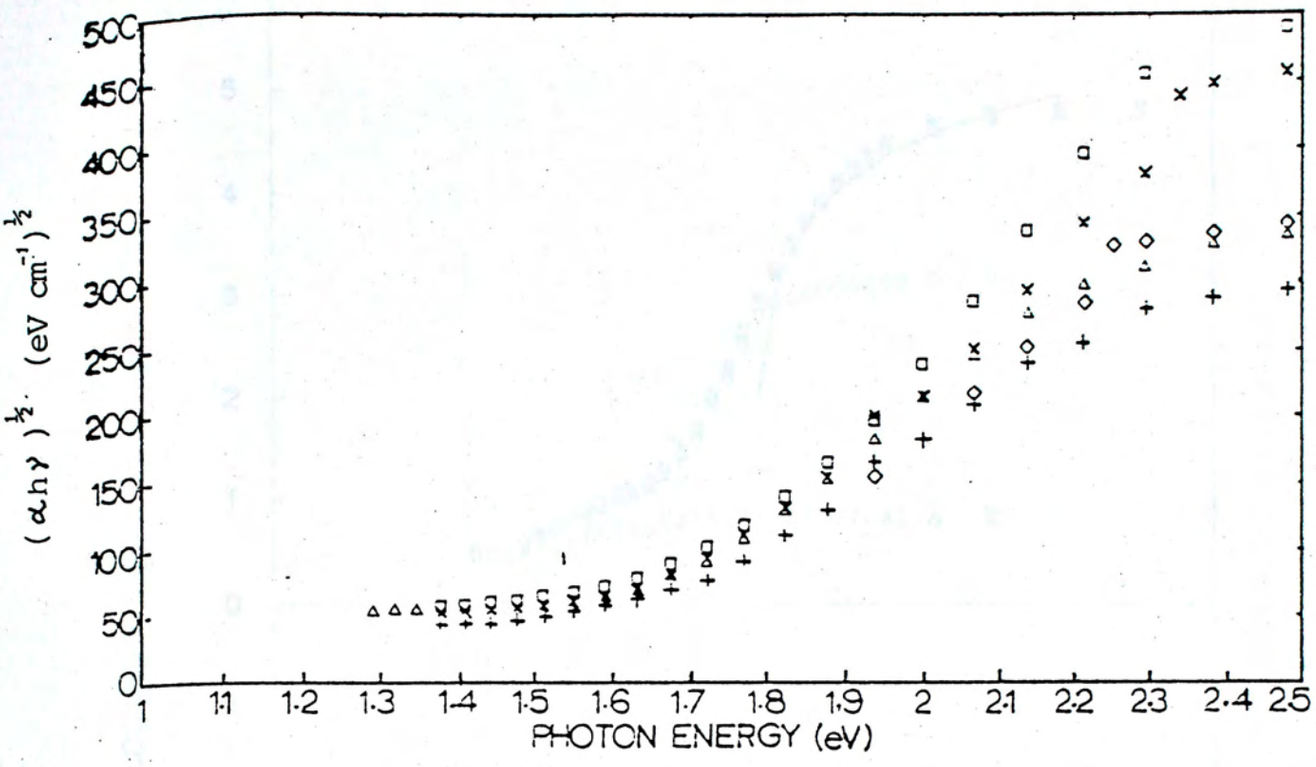

Figure 6-22. Optical absorption for a family of intrinsic BARE films (J.C. Anderson et al., 1986).

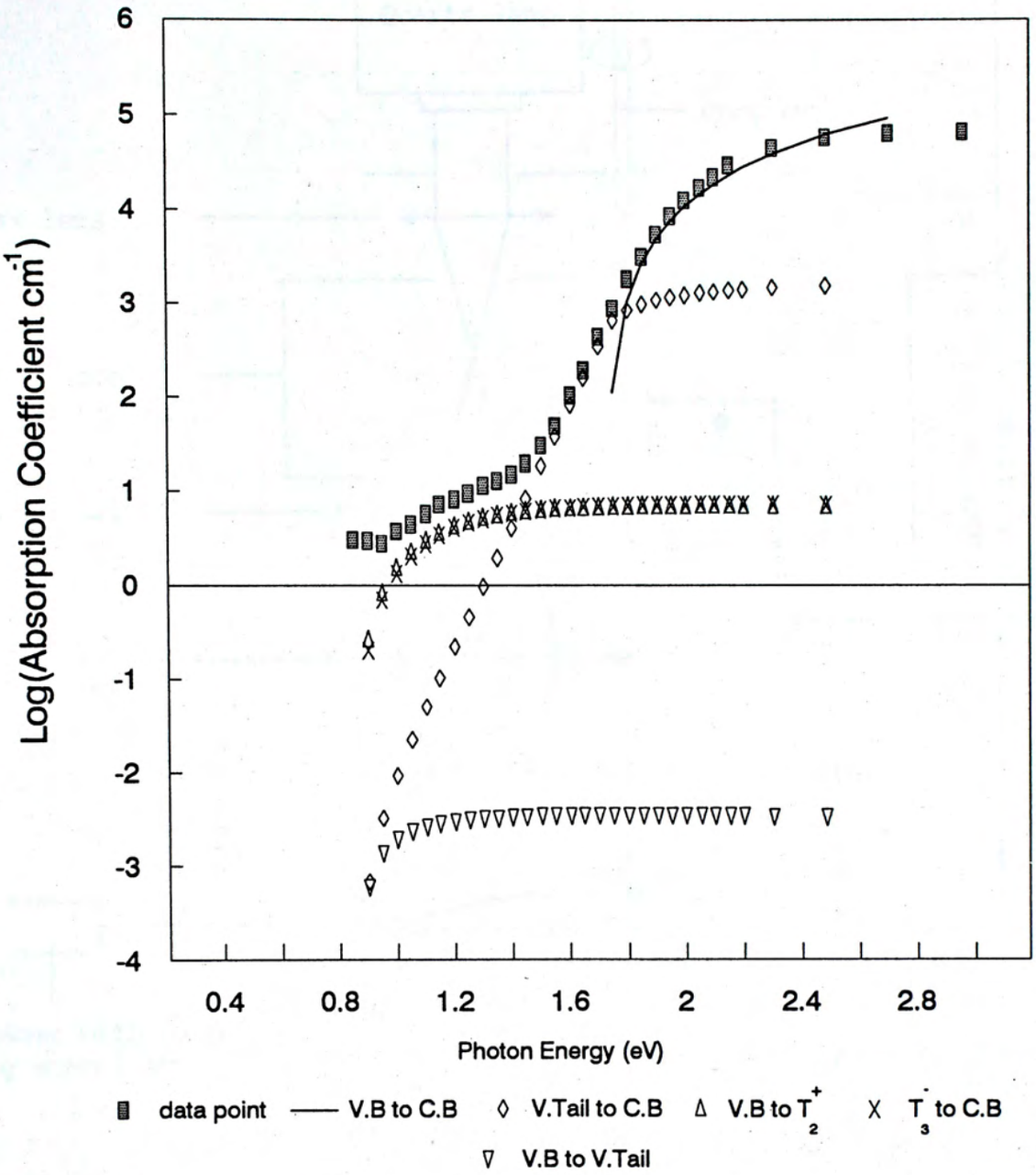

Figure 6-23. A plot of absorption spectra for different transition mechanisms.
V.B. : occupied valence band;
C.B. : unoccupied conduction band;
V.Tail : valence band tail;
T_2^+ : T_2^+ center;
T_3^- : T_3^- center.

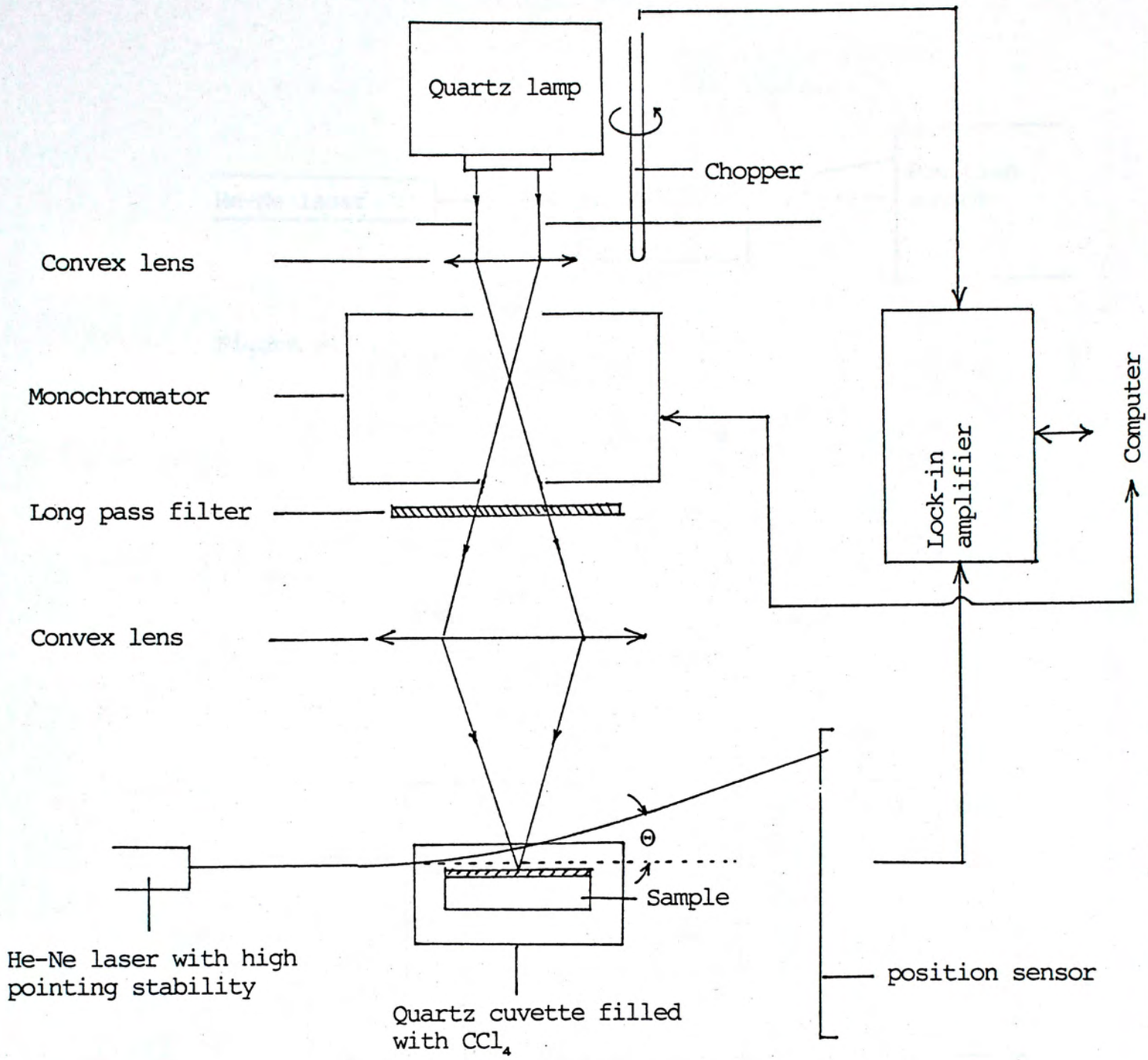

Figure 6-24. A schematic diagram showing the experimental set-up for transverse PDS.

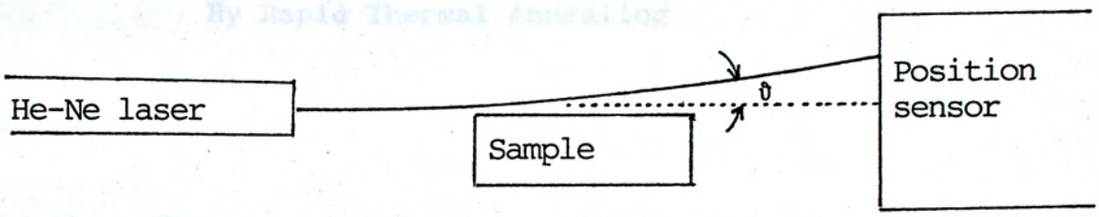

Figure 6-25.

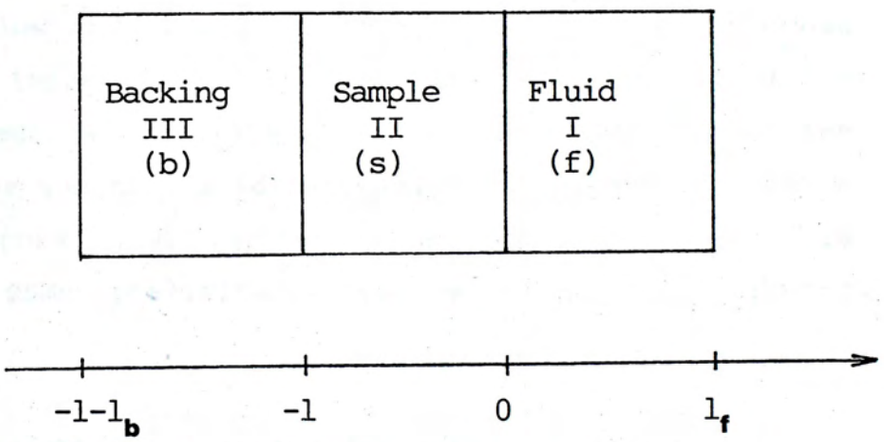

Figure 6-26. Geometry of a one dimensional system.

Chapter 7

Recrystallization of Amorphous Germanium By Rapid Thermal Annealing

A) Introduction:

Rapid thermal processing furnace allows one to have a short duration (≅ 10 s) of thermal pulse at a high but controllable temperature. Within the furnace, heat transfer is predominantly by radiation (Fred Roozboom et al., 1990). This is different from conventional furnaces in which conduction and convection dominate the heating processing. As a result, the efficiency of power absorption depends on the optical properties of the samples themselves. The above point plus the short rise time and rapid cooling rate characteristics, minimize the impurity effect from the glass substrate (such as diffusion of ions) on the sample when performing high temperature annealing. Since the short duration of the thermal pulse can be accurately controlled by electronics, it allows one to follow any crystallization or grain growth process closely with a temperature well beyond the crystallization temperature without evaporating the sample away from the substrate. So it is worthwhile to re-examine the behaviour of a-Ge under both isochronal and isothermal annealing by RTP. This chapter reports some preliminary results with the following objectives:

1) To study amorphous germanium deposited at different T_s:
   - i) by isochronal annealing with different durations of thermal pulses;
   - ii) by isothermal annealing with different annealing temperatures;
   - iii) by X-ray diffraction of fully crystallized samples;
   - iv) by following the crystallization process at one temperature, namely 610°C, with fifteen-second thermal pulse. Between each step, X-ray experiment was performed.

2) For reactively evaporated amorphous hydrogenated germanium deposited at different T_s, isochronal annealings were performed to investigate whether the lattice reconstruction of a-Ge:H during annealing due to the incorporation of hydrogen should be different from that of a-Ge.

B) Theory:

B.1 Recrystallization of Amorphous Germanium:

A schematic diagram and experimental results showing the change in resistivity against annealing temperature are shown in Figure 7-1 and 7-2 (K.P. Chik and S.H.Fung, 1977). According to these authors, the recrystallization of germanium can be divided into two stages, namely, a precrystallization stage and a main crystallization stage. The precrystallization stage is being ambient sensitive. It has been argued that due to the incorporation of residue oxygen during film growth process in a conventional high vacuum system, subsequent annealing enhanced the reaction of forming GeO within the germanium matrix. The effect of the formation of GeO are two-fold. Firstly, it makes the rearrangement of Ge atoms become difficult, hence delaying the crystallization process. Secondly, GeO formation removes states in the band gap (passivation of dangling bonds), hence increasing the film's resistivity. However, due to the vast difference in bond energies between Ge-Ge (2.8 eV) and Ge-O (6.8 eV), Ge-O as a whole may eventually break away from the Ge matrix at a high enough temperature. This process can regenerate dangling bonds in the germanium network, leading to a drop in resistivity due to hopping conduction. The above viewpoints have been confirmed in amorphous silicon (K.P. Chik et al., 1980) (see Figure 7-3 and 7-4), where the regeneration of dangling bonds was checked by ESR experiments, and the nearest neighbour hopping conduction could also be inferred from electrical conductivity

measurements. Following the precrystallization stage comes the main crystallization stage. It is characterized by a sudden drop in resistivity over several orders of magnitude.

B.2) Nucleation and Growth - Isothermal Transformation:

(Christian, 1975)

Before going into the theory, several parameters have to be defined:

V : the total volume of the assembly;

V^{α} : the total volume of α phase;

V^{β} : The total volume of β phase;

N.B. $V^{\alpha} + V^{\beta} = V$ (7.1)

I_{ν} : nucleation rate per unit volume at a particular time;

γ_i : growth rate along the i^{th} direction. $i = 1,2,3$ for three arbitrary set of orthogonal axes in space.

The isothermal transformation is taken to be from the α phase to the β phase, and the relations among these parameters are as follows:

For a time between τ and $\tau + d\tau$, the volume V_{τ} of a β region is :

$$V_{\tau} = \eta\, \gamma_1\, \gamma_2\, \gamma_3\, (t - \tau)^3 \qquad t > \tau \qquad (7.2)$$
$$V_{\tau} = 0 \qquad t < \tau$$

where τ can be viewed as the incubation time (i.e. time needed for nucleation). η is a geometrical factor.

Consider during an initial stage of transformation, $V^{\beta} << V^{\alpha}$ and $V^{\alpha} \cong V$. The nuclei are widely spaced, and the interference of neighbouring nuclei is negligible. Since the total number of nuclei formed between τ and $\tau + d\tau$ is

$V^{\alpha} I_{\nu} d\tau$, the total volume of transformed β region can be written as :

$$V^{\beta} = \int_{t_o}^{t} V_{\tau} V^{\alpha} I_{\nu} d\tau \qquad t_o : \text{incubation time}$$

$$= \int_{t_o}^{t} V^{\alpha} \eta \gamma_1 \gamma_2 \gamma_3 (t-\tau)^3 I_{\nu} d\tau$$

$$= \int_{t_o}^{t} \eta V \gamma_1 \gamma_2 \gamma_3 (t-\tau)^3 I_{\nu} d\tau \qquad (7.3)$$

In particular, if the growth rate is isotropic, $\gamma_1 = \gamma_2 = \gamma_3 = \gamma$ (the transformed region will be spherical), and if I_{ν} is constant for all τ, Eqt. (7.3) can be rewritten as:

$$V^{\beta} = \frac{4}{3} \pi \gamma^3 V I_{\nu} \int_{t_o}^{t} (t-\tau)^3 d\tau$$

$$= \frac{\pi V I_{\nu} \gamma^3}{3} (t - t_o)^4$$

Or

$$\frac{V^{\beta}}{V} \equiv \xi = \frac{\pi V I_{\nu} \gamma^3}{3} (t - t_o)^4 \qquad (7.4)$$

So, the transformed volume fraction will be a power law in time. The rate of transformation according to this equation rises rapidly in the initial stages. However, at a later time, we must consider the mutual interference of regions growing from separate nuclei. In all solid transformations, when two β phase regions impinge on each other, the two regions will develop a common interface, over which growth ceases, although it continues normally elsewhere. To take the impingement into account is purely a geometrical problem. Notwithstanding, we can take another approach by observing that between τ and $\tau + d\tau$, the actual

volume transformed into β phase is:

$$
\begin{aligned}
dV^{\beta} &= V_{\tau}\, I_{\nu}\, V^{\alpha}\, d\tau \\
&= V_{\tau}\, I_{\nu}\, (V - V^{\beta})\, d\tau \\
&= V\, V_{\tau}\, I_{\nu}\, (1 - V^{\beta}/V)\, d\tau \\
&= [(V^{\alpha} + V^{\beta})\, V_{\tau}\, I_{\nu}\, d\tau]\, (1 - V^{\beta}/V) \\
&\equiv dV_{e}^{\beta}\, (1 - V^{\beta}/V) \qquad (7.5)
\end{aligned}
$$

dV_{e}^{β} is the increment in extended volume of transformed material between τ and $\tau + d\tau$.

Since $dV_{e}^{\beta} = V\, V_{\tau}\, I_{\nu}\, d\tau$

$$V_{e}^{\beta} = \eta\, V \int_{t_o}^{t} \gamma_1 \gamma_2 \gamma_3\, I_{\nu}\, (t-\tau)^3\, d\tau \qquad (7.6)$$

The meaning of extended volume deserves a further discussion. V_{e}^{β} differs from the actual transformed volume V^{β} in two ways. Firstly, nuclei are imagined to exist in regions which have already been transformed into β phase. Secondly, two or more β regions may grow through one another (see Figure 7-5, 7-6). So some of the transformed volume are counted more than once. In fact, V_{e}^{β} may be larger than the real volume of the whole assembly V. In the original words of Christian, " the significance of V_{e}^{β} is that it is simply related to the kinetic of growth, which may thus be separated from the geometrical problem of impingement.". To put it in other words, the actual increment dV^{β} can be expressed in terms of dV_{e}^{β} without explicitly considering the geometrical impingement.

From Eqt. (7.5), we have:

$$V_e^{\beta} = - V \ln(1 - V^{\beta}/V) \qquad (7.7)$$

Putting (7.7) into (7.6), we have:

$$- \ln\left(1 - \frac{V^{\beta}}{V} \right) = \eta \int_{t_o}^{t} \gamma_1 \gamma_2 \gamma_3 \, I_{\nu} \, (t-\tau)^3 \, d\tau$$

Or

$$\xi = 1 - \exp\left(- \eta \int_{t_o}^{t} \gamma_1 \gamma_2 \gamma_3 \, I_{\nu} \, (t-\tau)^3 \, d\tau \right) \qquad (7.8)$$

Again, if the constancy of I_{ν} and isotropic growth rate are assumed, Eqt. (7.8) can be rewritten as:

$$\xi = 1 - \exp\left[-(\pi/3) \, \gamma^3 \, I_{\nu} \, (t - t_o)^4 \right] \qquad (7.9)$$

So, when the crystallization process is followed, the crystallized volume fraction obtained from X-ray analysis under different time intervals of isothermal annealing can be used to verify Eqt. (7.8).

B.3) The Structure of Polycrystalline Aggregates By X-Ray Analysis: (Cullity 1959)

B.3.1) Grain Size:

The finite grain size D of a polycrystalline structure is usually evaluated from the Scherrer formula:

$$D(hkl) = \frac{K\lambda}{B \cos\theta} \qquad (7.10)$$

where K : Scherrer constant;

λ : wavelength of incident wavelength;

B : line boardening due to finite grain size only;

θ : angular position that satisfies the Bragg condition.

B can be evaluated by the following equation:

$$B^2 = B_M^2 - B_S^2 \qquad (7.11)$$

where B_M is the measured integral breadth (peak area/ peak height);

B_S is the diffraction linewidth of a standard.

(7.11) is the consequence of the assumption that the diffraction line has the shape of a Gaussian curve.

Accordingly, Eqt.(7.10) gives the mean extension of the crystallites in the direction perpendicular to the (hkl) plane. However, since the individual grains are often nonuniformly strained, this gives a further broadening of the diffraction line. In fact, a strong presumption on the absence of mechanical stress is implied when applying Eqt.(7.10), which is not always true (Figure 7-7).

Whether strains are uniformly or non-uniformly present within the sample, the diffraction line profile is changed accordingly. Figure 7-8 shows a portion of unstrained grain and its corresponding diffraction line. When there is a uniform tensile strain, there is no change in the line profile except that there is a shift of diffraction angle to a lower value (Figure 7-9). However, if the strain is non-uniform, the diffraction line will be boardened. Actually, the observed line profile envelopes a number of diffraction lines which correspond to different lattice spacings.

The presence of strains always complicates the analysis

of diffraction pattern. The application of Eqt.(7.8) for calculating the grain size always leads to an under-estimation. To separate the effect between grain size and strain on line boardening, more sophisticated methods have to be used, for examples, the methods described by Warren-Averbach (1950) or Smith (1960).

C) Experimental Set-ups:

C.1) The Rapid Thermal Processing Unit:

C.1.1) General Description:

(See Figure 7-10). The rapid thermal processing unit mainly consists of six 1250 W, 220-230 V halogen lamps (Philips 6358R P2/12) which are symmetrically mounted within a water cooled cylindrical stainless steel chamber with an inner diameter ≅ 52 mm. A cylindrical quartz tube with an outer diameter ≅ 18 mm is employed as the processing chamber. The temperature of the furnace is monitored by a K type thermocouple, which has been already pasted on a dummy a-Ge sample with ceramic cement (Omega). (The use of ceramic cement to paste the thermocouple on a dummy sample has been used in system calibration in industrial RTP systems (F. Roozboom, 1990)). The thermovoltage is fed into a temperature controller (Shimaden S-R 18) which in turn controls the power output of three power regulators (Shimaden). Each of them is responsible for the power supply for two halogen lamps. Besides, an electronic circuit (P.C. Wong, 1992) acting as a time control unit is built, so that the processing time can be accurately controlled. Moreover, during the period of processing, dry nitrogen gas obtained by passing normal grade nitrogen gas (99.9% purity) through a series of copper coils immersed in liquid nitrogen was introduced into the quartz chamber in order to provide an inert environment. Pressure within the quartz chamber is ensured to be slightly larger than one atmospheric pressure by employing a pressure release

valve at the open end of the quartz tubing. Furthermore, a flow meter (Fisher & Porter Ltd.) is used to monitor the flow rate of nitrogen gas both during the processing and cooling period in order to obtain a good reproducibility of the thermal annealing cycle. A typical run of the RTP furnace is shown in Figure 7-11.

C.1.2) Details on Design and operation:

The details of each component and their operations are divided into several parts and discussed in the followings.

Firstly, the essential components of the sample holder are composed of a quartz boat and a long ceramic rod. Thermocouple is embodied in the ceramic rod, and finally pasted on a dummy a-Ge sample with ceramic cement. The stainless steel cap of the sample holder is provided with a gas outlet which has been connected with a pressure release valve in order to maintain the N_2 gas pressure within the quartz chamber slightly higher than one atmospheric pressure.

Secondly, the whole furnace has been mounted on a movable trolley. During the annealing cycle, it is pulled to a position where the quartz boat is approximately in the middle of the furnace. However, once the annealing cycle is finished, it is pushed back to its starting place so that the sample is out of the furnace. This enhances the cooling rate. Moreover, during the cooling cycle, the flow rate of nitrogen gas is allowed to reach a maximum of 6 l/min. This gives an initial cooling rate over 30°C/s (from 1000°C).

Thirdly, the thermovoltage from the K-type thermocouple is used as a control feedback, and the temperature controller employs a PID algorithm to control the power output of the three regulators. Since the optimum PID settings are different for different annealing temperatures,

in particular for temperature below 500°C, overshooting usually occurs and the time needed to reach equilibrium is very long. In such cases, less number of the halogen lamps will be used in the heating process by simply disconnecting them from the power supply. Also, the optimum PID values for different temperatures have been tabulated for later references.

Finally, for the time control unit, a complete circuit can be found in Appendix A at the end of this chapter. Its operating principle is as follows:

1) When the power switch is at the 'ON' position, a 24 V_{ac} relay will be switched on, hence connecting each phase from the three-phase mains to one of the three power regulators. However, there is no power output to the lamps yet as the power regulators needed to wait for the control signals from the temperature controller.

2) Also, a 12 V_{ac} from a step-down transformer, after being fully rectified, acts as a series of fundamental clock pulses and is fed into the logic circuit for timing. The logic circuit performs two functions: a) it can be pre-set to any time interval between 0 to 9999 seconds; b) once it is triggered to start, it automatically counts down to 0 with a time-out signal sending out.

3) When the 'Run' button is pressed, a 9 V_{dc} relay will be switched on, connecting the signal output line of the temperature controller and the signal input line of the power regulators, and at the same time, the electronic timer is triggered to count down. Within the pre-set time interval, the temperature controller obtains feedbacks from the thermocouple and control the output of the power regulators according to the PID algorithm. Once the timer reaches 0, the time-out signal sent out from the logic circuit triggers the release of the 9 V_{dc} relay, hence

disconnecting the signal lines between the temperature controller and the power regulators and all the lamps will be shut off.

C.2) The Conventional Furnace:

The experimental set-up of the conventional furnace used in the present study is shown in Figure 7-12. The furnace mounted on a movable trolley is resistively heated by a heating wire and is under the control of a temperature controller accompanied with a power regulator (Shimaden). The sample holder is made of copper with a hole drilled to embed a K-type thermocouple, whose thermovoltage signal can be monitored with a DVM (Thurlby 1905a). During the annealing process, the quartz chamber is filled with normal grade (99.9%) nitrogen gas, which has been purified by passing through a cold-trap prior to its being admitted in the chamber. In the experiment, the furnace had to be firstly heated to 10°C higher than the desired annealing temperature. Then the trolley was pulled so that the sample holder is enclosed by the furnace. A typical time of about 10 minutes has to be waited before the sample holder reaches the desired annealing temperature.

C.3) The X-ray Diffractometer:

The X-ray diffractometer used is a 4-circle diffractometer, which is composed of a $\theta/2\theta$ goniometer and a Eulerian cradle (Huber 424 and 511.1); each circle has a step size of 0.0001° with positioning reproducible to within 2 arcsec. Using a flat graphite crystal monochromator, unresolved Cu K_α radiation from a fine-focus X-ray tube (40 kV, 20 mA) is selected and a beam is formed by a 0.5 mm collimator. The receiving slits for the detector are set at 1mm (horizontal) × 2mm (vertical), and NaI(Tl) scintillation counter has been employed as the detector. The cylindrical detector head is clamped to the 2θ arm by means of a bolt. In

the present study, θ-2θ scans have been performed for differently prepared samples, and the only alignment procedure to be done was to ensure the polycrystalline sample to be placed at the center of the θ-2θ circle (see Figure 7-13, 7-14).

C.4 Electrical Conductivity Measurements:

The circuit diagram and experimental set-up for measuring electrical conductivity is shown in Figure 7-15 and 7-16 respectively.

An electrometer (model 617. Keithley Instruments) with an input impedance of 10^{16} Ω was used to measure the voltage drop across a standard resistor with a value of either 10^{8} Ω, 10^{5} Ω or 10^{4} Ω. Then the conductivity can be calculated according to the following formula:

$$\sigma = \frac{l}{w\ t}\ \frac{V}{(\varepsilon - V)\ R_s} \qquad (7.12)$$

where l : gap width in mm;
w : strip width in mm;
t : film's thickness in cm;
V : voltage dropped across the standard resistor in V;
ε : total voltage supplied in V;
R_s : resistance of the standard resistance in Ω.

Two knife edges with a fixed separation of 5.75 mm were used as electrodes and were pressed on the sample. This procedure avoided coating metal electrodes onto the film, as the electrode materials can affect the crystallization of the amorphous films at the annealing temperatures (K.P. Chik et al., 1975). All the measurements were done under room conditions.

the present study, θ-2θ scans have been performed for differently prepared samples, and the only alignment procedure to be done was to ensure the polycrystalline sample to be placed at the center of the θ-2θ circle (see Figure 7-13, 7-14).

C.4 Electrical Conductivity Measurements:

The circuit diagram and experimental set-up for measuring electrical conductivity is shown in Figure 7-15 and 7-16 respectively.

An electrometer (model 617. Keithley Instruments) with an input impedance of 10^{16} Ω was used to measure the voltage drop across a standard resistor with a value of either 10^{8} Ω, 10^{5} Ω or 10^{4} Ω. Then the conductivity can be calculated according to the following formula:

$$\sigma = \frac{l}{w\ t}\ \frac{V}{(\varepsilon - V)} \qquad (7.12)$$

where l : gap width in mm;
w : strip width in mm;
t : film's thickness in cm;
V : voltage dropped across the standard resistor in V;
ε : total voltage supplied in V;
R_s : resistance of the standard resistance in Ω.

Two knife edges with a fixed separation of 5.75 mm were used as electrodes and were pressed on the sample. This procedure avoided coating metal electrodes onto the film, as the electrode materials can affect the crystallization of the amorphous films at the annealing temperatures (K.P. Chik et al., 1975). All the measurements were done under room conditions.

D) Experimental Methods:

For the sake of clarity, the experiments done on each kind of samples will be described in a reasonable length here.

D.1 The Samples:

Amorphous germanium thin films were either electron beam evaporated or reactively evaporated with hydrogen onto 3x25 mm^2 Corning 7059 glasses with substrate temperatures, T_s, ranging from 100°C to 300°C, thicknesses of which are ≅ 0.5 μm, measured by Alpha Step. The coating rate for electron beam evaporated samples was ≅ 2 Å/s, while that for reactively evaporated samples was 0.5 Å/s. (For the details of sample preparation, please refer to chapter 2).

D.2) The Experiments:

For amorphous germanium deposited at different T_s:

i) a-Ge with T_s = 100°C, 150°C and 210°C were isochronally annealed from 300°C to 650°C, with thermal pulse durations of 30 s and 15 s . Between each annealing step, their resistivity were measured according to section C.4;

ii) a-Ge with T_s = 100°C, 150°C and 210°C were isothermally annealed with annealing temperature T_a ≅ 550°C, 570°C, 590°C and 720°C respectively. The time interval between each annealing step was 30 s for T_a ≅ 550°C, 570°C and 590°C. For T_a ≅ 720°C, the annealing time was 15 s. Electrical conductivity measurements were performed on each sample between each annealing step according to section C.4;

iii) For samples annealed at T_a = 720°C, X-ray diffraction experiments were performed to obtain the integral breadths and relative intensities of the crystal planes (111),

(220) and (311). Sample with T_s = 150°C were also isothermally annealed at 500°C and 600°C for 5 hours in a conventional furnace described in section C.2 for comparison;

iV) For samples with T_s = 150°C, the main crystallization stage was followed closely with a 15 s, 610°C thermal pulse. Between each annealing step, electrical resistivity measurement was performed according to C.4 and X-ray diffraction experiment was performed to obtain the change in diffraction intensity, and 2θ position for (111) crystal plane.

For reactively evaporated a-Ge:H, isochronal annealings were performed on samples with T_s = 140°C, 150°C and 170°C. The annealing temperatures ranged from 100°C to 610°C, with an annealing time of 30 s at each step.

E) Results and Discussions:

The results of the experiments will be presented in the same order as described in section D.2.

From Figure 7-17, it can be seen that the precrystallization stage for both a-Ge deposited at T_s = 150°C and 210°C, can only be weakly identified under an annealing time interval of 30s. This result is same as that found by Tolunay et al. (1990). They found that as the substrate temperature was increased, a-Ge would crystallize without showing the precrystallization stage upon isochronal annealing (Figure 7-19). However, when the pulse duration was shortened to 15 s, the pre-crystallization stage for sample with T_s = 150°C became apparent again (Figure 7-18). This shows the ability of RTP to refine small structural changes in a-Ge matrix. According to Chik et al. (1979), the precrystallization stage is a consequence of desorption of Ge-O from the a-Ge matrix. The desorption process should be both temperature and annealing time dependent. For a sample with an

elevated T_s, the time used in traditional annealing may be long enough to finish both the process of desorption and recrystallization, hence resulting in an absence of the precrystallization stage. Also, it is worth noting that for films deposited at different T_s, their final resistivity after complete crystallization was different. This implies a subtle difference in structure for samples deposited at different T_s. The above statement is further supported by the isothermal annealing behaviour of the samples. Figure 7-20 shows the isothermal annealing curves for samples annealed at $T_a \cong 550^{\circ}C$, with pulse duration of 30 s. It can be observed that sample with the lowest T_s took the longest time to be fully crystallized. As mentioned in section B.1, annealing enhanced the formation of Ge-O within the germanium matrix, and this in turn hindered the rearrangement of Ge atoms, resulting in a delay of crystallization. If this is so, samples with lower T_s should have absorbed more residue oxygen from the high vacuum chamber during the film growth process than those with higher T_s. Moreover, it has been pointed out that amorphous germanium would crystallize around 300°C - 450°C (K.P. Chik et al., 1975). When the annealing temperatures were well beyond this range, crystallization could take place in a very short period of time. From Figure 7-21 and 7-22, when the annealing temperature were 570°C and 590°C, crystallization was practically complete in the first 30 s. If the annealing temperature was further increased to 720°C (Figure 7-23), the crystallization was completed in the first 15 s. Besides, at such a high annealing temperature, germanium will very likely be evaporated away from the substrate, if the processing time is too long. Actually, one sample (T_s = 150°C) after 5 hours annealing at 600°C in a conventional furnace, only the glass substrate was left behind. Finally , it can be observed from these four figures that samples with the higher T_s, the lower was resistivity after complete crystallization.

Amorphous germanium with T_s = 100°C, 150°C and 210°C have been rapid thermal annealed to $\cong$ 720°C. X-ray analysis on these samples revealed their internal textures. On analysis, the

diffraction intensity of (111) reflections was taken to be 100. Then the intensities among other crystal reflections were calculated relative to (111) reflection intensity (i.e. the total area of the diffraction peak/ total time to accumulate the peak). The results for the above mentioned samples, together with the relative intensities of (111), (220) and (311) crystal reflections obtained from the powdered pattern of germanium crystal, are shown in Figure 7-24. It can be seen that the relative intensities for all the samples deviate from the powdered pattern of germanium crystal, which assumes a random orientation of crystal planes. This implies that a preferred orientation in <111> direction can be obtained from recrystallization of amorphous germanium deposited on glass substrate. The relative intensities of (111), (220), and (311) planes of sample with T_s = 150°C, crystallized by annealing in a conventional furnace at 500°C for 5 hours were also shown on the same graph for comparison. Within experimental errors, it can be concluded that all of them are essentially the same. This indicates that the final crystal orientation deposited on amorphous substrate does not depend on the deposition temperature and the annealing method. The preferred orientation in <111> direction can be understood as one of the natural way to stack up an assembly of atoms from a disorder state on a 'smooth' surface in FCC close packing form (See Figure 7-25).

Also, according to Scherrer formula (Eqt.7.10), the final grain size is inversely proportional to the line boardening due to finite grain size, which is revealed in the integral line breadth of the corresponding diffraction peak. Form Figure 7-26, it can be seen that as the substrate temperature increased, the integral line breadth for <111> and <220> direction decreased, while the breadth along <311> direction increased parallel with T_s. From the relative intensities of the corresponding crystal reflections (Figure 7-24), it is known that crystals exist predominantly in <111> orientation, then followed by the <220> crystal orientation. The <311> crystal orientation makes the least contribution. So it is reasonable to assume that any physical property of the

recrystallized germainum film should be to a larger extent controlled by crystals with either <111> or <220> crystal orientation. If this is the case, the difference in final resistivies exists among sample with different T_s can be ascribed to their different grain sizes after complete crystallization. The larger the final grain size, the lower is the electrical resistivity after complete crystallization. However, all the above arguments are based on the crucial assumption that the resultant films are all strain free, as required by the Scherrer formula. Obviously, this assumption has to be justified experimentally. Warren-Averbach (1950) described a method to seperate the broadening effect between finite grain size and non-uniform strains by making use of higher order diffractions. However, with the present X-ray source (40 kV, 20 mA), the intensities of high order diffractions are usually too weak for any quantitative analysis (Warren's method needs to perform a Fourier transform on the diffraction line profile). So up to this stage, nothing about the strains within our samples is known to our best knowledge, and a definite conclusion concerning the grain size effect on samples' resistivities seems not appropriate, not until more experimental and theorectical work has been done. On the other hand, with X-ray diffraction, we monitored the crystallization process of a-Ge with T_s = 150°C, which is rapid thermally annealed by 15 s of 610°C thermal pulse at each step. Since grains were predominantly oriented in <111> direction, diffraction experiments were performed on (111) plane. From Bragg condition,

$$2\, d \sin\theta = n\, \lambda \qquad \Rightarrow d \propto 1/\sin\theta$$

So, by measuring the 2θ position after each step of annealing, one can trace any changes in the lattice constant which in turn is a measure on the change of uniform strain within the samples. From Figure 7-27, within the error of profile fittings, the 2θ position are found to remain constant at an initial stage of annealing. Then after a certain time T, the 2θ position began to decrease and approached that of bulk material. This implies that the lattice constant was relaxed back to the value of bulk

material for <111> crystal orientation. Although the exact time T is not well defined, uniform strains are seen to relax upon annealing.

The change in diffraction intensity (total diffraction peak area/total time taken to accumulate the peak) and the corresponding change in electrical resistivity are shown in Figure 7-28. It can be observed that as the diffraction intensity increased, the electrical resistivity decreased, and they both approached a constant value after six steps of thermal annealing. Here we define the crystalline fraction as follows:

$$f_{cry} \equiv \frac{\text{Diffraction intensity at a particular annealing step}}{\text{Diffraction intensity after complete recrystallization}}$$

The physical meaning of f_{cry} is the volume fraction of crystalline phase that exists within the sample. A plot of f_{cry} against annealing time is shown in Figure 7-29. From both Figure 7-28 and 7-29, it can be seen that electrical measurements may not be sensitive enough to reveal the internal structure of a-Ge upon annealing, as it can be seen that the resistivity of the sample began to drop only after the crystalline fraction reached a value of 0.77. From section B.2, it is seen that under an isothermal condition, the crystalline fraction f_{cry} obtained from a transformation from amorphous phase to crystalline phase can be written as:

$$f_{cry} = 1 - \exp\left(- \eta \int_{t_o}^{t} \gamma_1 \gamma_2 \gamma_3 \, I_\nu \, (t-\tau)^3 \, d\tau \right) \qquad (7.13)$$

where η : a geometrical factor;

γ_i: growth rate along the i^{th} direction of a 3-dimension orthogonal axes;

I_ν : nucleation rate per unit volume;

t_o: incubation time.

Assuming that I_ν is essentially constant, we have:

$$f_{cry} = 1 - e^{-k(t-t_o)^4} \qquad (7.14)$$

where $k = \eta/4\ (\gamma_1\gamma_2\gamma_3\ I_\nu)$

It should be noted that there is no assumption on the isotropy of growth rates. F.Edelman et al. (1992) pointed out that γ_i and I_ν have a thermally activated characteristic, so they are essentially constant under isothermal conditions.

Rewritting (7.14),

$$[-\ln(1 - f_{cry})]^{1/4} = k^{1/4}\ (t - t_o) \qquad (7.15)$$

Therefore, a plot of $[-\ln(1 - f_{cry})]^{1/4}$ against t should yield a straight line. The result has been shown in Figure 7-30. The value of k and t_o were found to be 1.48×10^{-8} s^{-4} and - 53 s respectively. One of the possible explanations for such a negative t_o is that there were already crystal nuclei present within the sample during the film growth process, especially when the substrate temperature is elevated. It has been observed that for a-Ge film deposited at T_s = 300°C, the resultant film was already in a polycrystalline structure. If one believes that the transformation from amorphous phase to crystalline phase is a continuous phenonmenon along with an increase in substrate temperature, it may be reasonable to assume that nanocrystalline structure or even microcrystalline structure were already embedded in the amorphous phase when T_s= 150°C. Of course, the validity of above arguments should be subjected to later experiments (e.g. Raman analysis).

The isochronal annealing behaviour of a-Ge:H for T_s = 140°C, 150°C and 170°C are shown in Figure 7-31. The isochronal annealing behaviour of a-Ge with T_s = 150°C is also shown for comparison. Firstly, it can be seen that for reactively evaporated a-Ge:H, the

higher was T_s, the lower was the resistivity. This can be understood that one of the function of hydrogen incorporation is to saturate any dangling bonds. This is equivalent to the sweeping out of gap states within the mobility gap. As T_s was increased, less hydrogen could be retained in the germanium lattice, hence a lowering in resistivity. Secondly, the isochronal behaviour for electron beam evaporated a-Ge and reactively evaporated a-Ge:H are seen to be very different. The whole isochronal annealing curve for reactively evaporated samples can be roughly divided into 4 regions (Figure 7-32).

Region A corresponds to a monotonically decrease in resistivity along with an increase in annealing temperature. This can be attributed to the desorption of loosely bounded hydrogen within the Ge matrix, hence resulting in a drop in resistivity.

Region B and C correspond to lattice reconstruction and different forms of hydride desorptions. The initial rise in resistivity in both region can be attributed to an annealing initiated lattice reconstruction, part of the defects being annealed away under this action, resulting in a rise in resistivity. However, as a certain temperature (corresponding to the peak position) was reached, hydrides with different bonding configurations began to desorb from the matrix. This regenerated dangling bonds and caused a drop in resistivity. The desorption temperature for region B and C were found to be around $\cong 250^{\circ}C$ and $\cong 400^{\circ}C$ respectively.

Finally comes region D. From Figure 7-31, it can be seen that samples with different T_s reached their peak positions at different annealing temperatures, being lower for a sample with a lower T_s. This can be understood that for films with a higher T_s, the incorporated hydrogen should be thermally stable up to a higher annealing temperature. The peak positions for a-Ge:H with T_s = 140°C, 150°C and 170°C were found to be $\cong$ 540°C, 560°C and 600°C respectively. Once the annealing temperature was increased beyond these peaks, desorption of hydrogen occurred, which was

characterized by a drop of resistivity. The main crystallization stages were seen to follow immediately and the resistivities for all samples dropped several orders of magnitude. It may be useful to compare the above observations with the gas evolution spectrum of glow-discharge produced a-Ge:H, deposited on 7059 Corning Glass at T_s = 250°C (W. Paul et al. 1990) (Figure 7-33), where three peaks can also be found at temperature ≅ 300°C, ≅ 450°C and ≅ 650°C respectively. They were all attributed to the desorptions of hydrogen from the Ge matrix. Their desorption temperatures were all ≅ 50°C higher than those obtained from Figure 7-31. This may be due to the different deposition method and substrate temperature used.

F) Conclusions:

Firstly, the isochronal annealing and isothermal annealing behaviours of a-Ge deposited at T_s = 100°C, 150°C and 210°C were investigated by rapid thermal annealing method. It was found that sample deposited at different T_s, turned out to have different final resistivities after their complete crystallization. This observation motivated us to perform the X-ray diffraction experiments.

Secondly, from X-ray diffraction experiment, it was found that a-Ge deposited at T_s = 300°C was already in polycrystalline structure. For samples with lower substrate temperatures, it was found that a-Ge deposited on amorphous substrate, when fully crystallized, showed a preferred orientation in <111> direction, being independent of the substrate temperatures and annealing methods. Besides, the integral line breadths for samples rapid thermally annealed at ≅ 720°C were obtained. However, results were not conclusive enough to explain the differences in final resistivities for samples with different substrate temperatures.

Thirdly, the change in crystalline fraction f_{cry} was monitored by measuring the diffraction intensity of (111) plane after each annealing step (at T_a ≅ 610°C, 15 s interval) for sample

deposited at T_s = 150°C. It was found that electrical measurement was not sensitive enough to reveal fine changes in internal structure of a-Ge upon annealing, though the resistivity data showed a consistent trend with f_{cry}, and both of them approached a constant value after the sample has been fully crystallized. Attempts in using a nucleation and growth theory to interpret the change in f_{cry} leads one to suspect that crystalline nuclei are already present in a-Ge deposited at an elevated temperature. Nevertheless, more experiments have to be done to justify this argument.

Finally, the isochronal annealing behaviour of reactively evaporated a-Ge:H deposited at different T_s, namely, 140°C, 150°C and 170°C, were investigated. A plot of resistivity against annealing temperature for these three samples revealed three pesks. Since same number of peaks occur roughly at same temperatures found by previously reported hydrogen gas evolution experiments, they are ascribed to be due to the desorption of hydrides of different form with subsquent lattice reconstructions upon annealing.

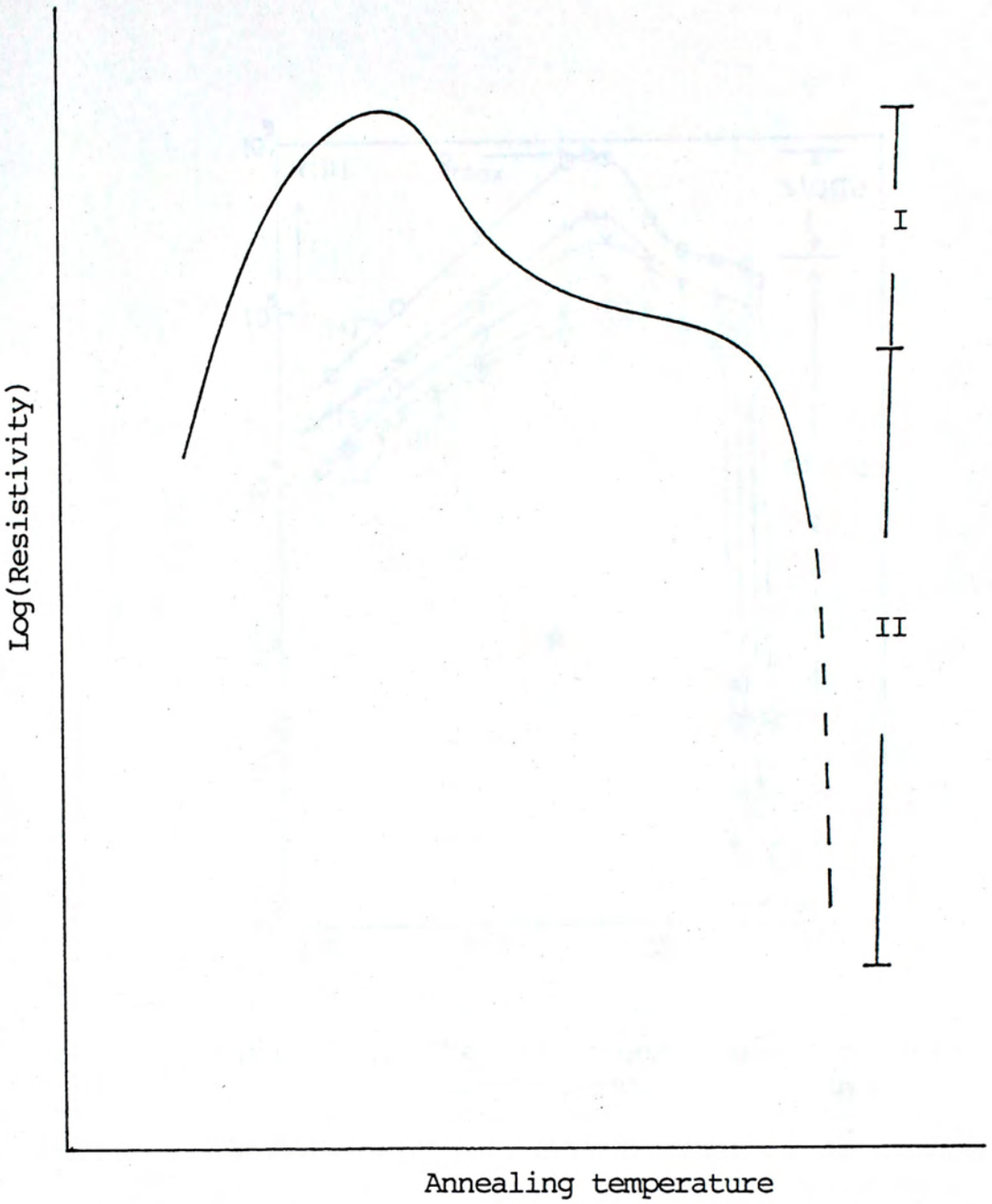

Figure 7-1. A schematic plot of isochronal annealing of a-Ge. I corresponds to the pre-crystallization stage while II coresponds to the main crystallization stage.

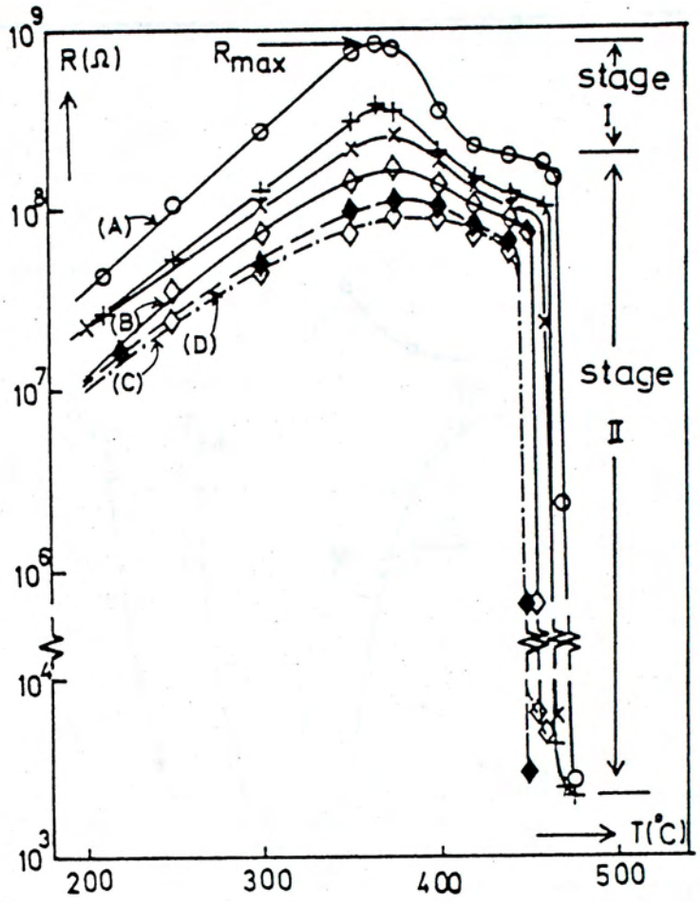

Figure 7-2. The isochronal annealing of room-temperature resistance of a-Ge films (K.P. Chik and S.H. Fung, 1977).

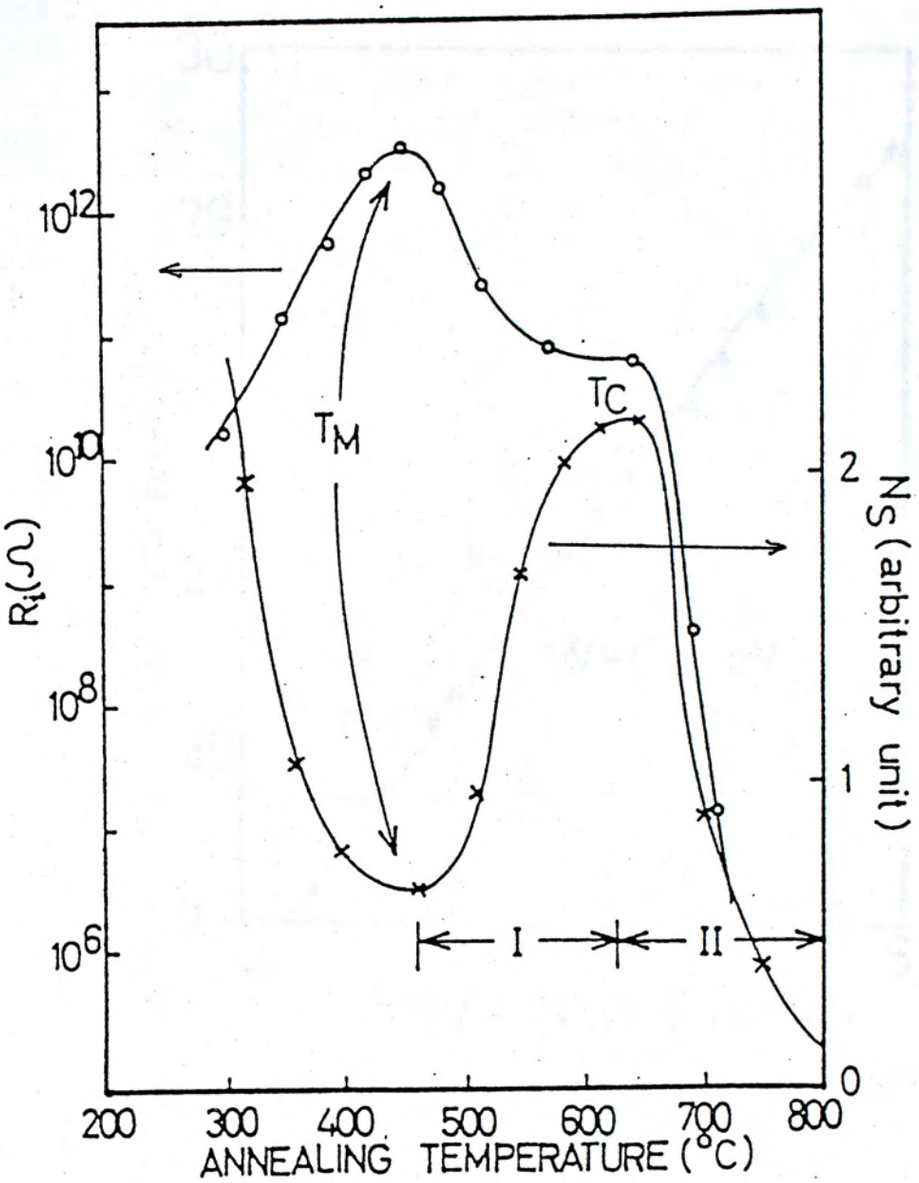

Figure 7-3. Isochronal annealing of film resistance at room temperature and ESR signal Ns of a-Si deposited on quartz substrate in a vaccum of $3*10^{-7}$ Torr (K.P. Chik et al., 1980).

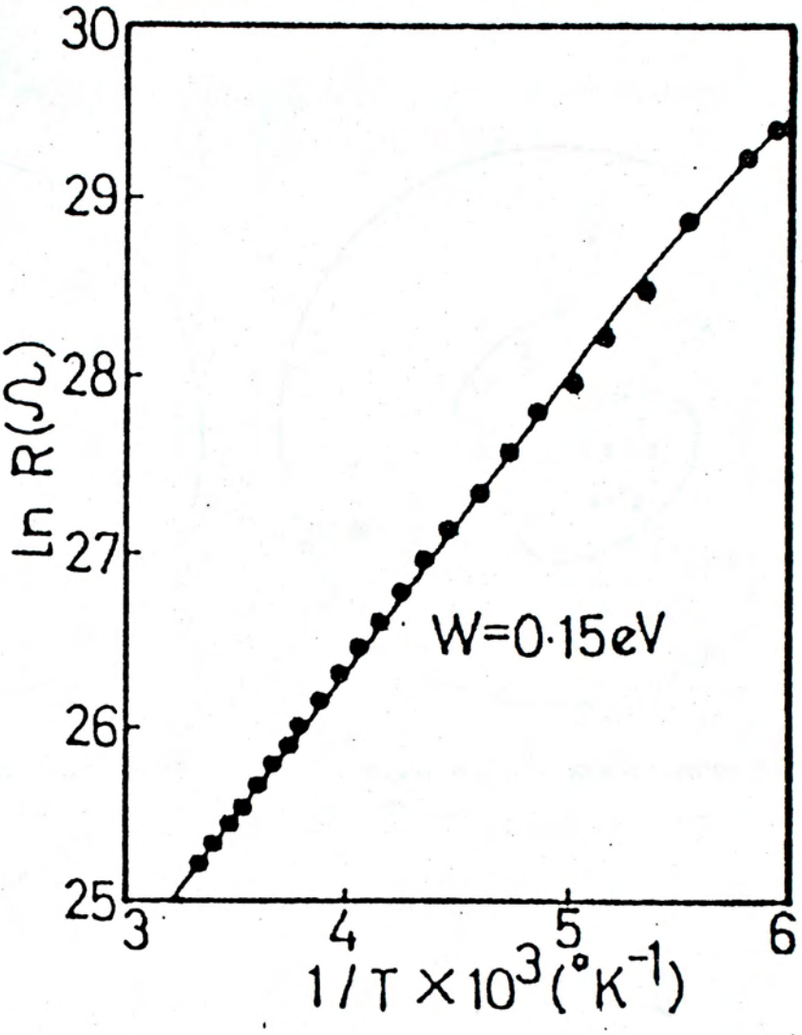

Figure 7-4. Nearest neighbour hopping conduction of a-Si.

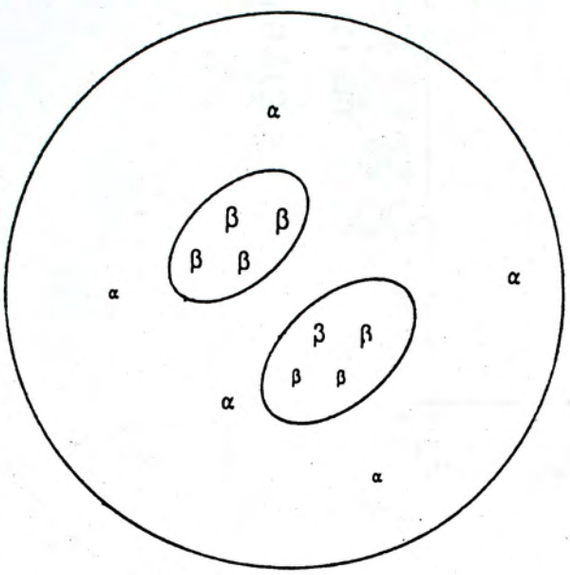

Two β regions embeded in α phase, but they are not yet touching each other.

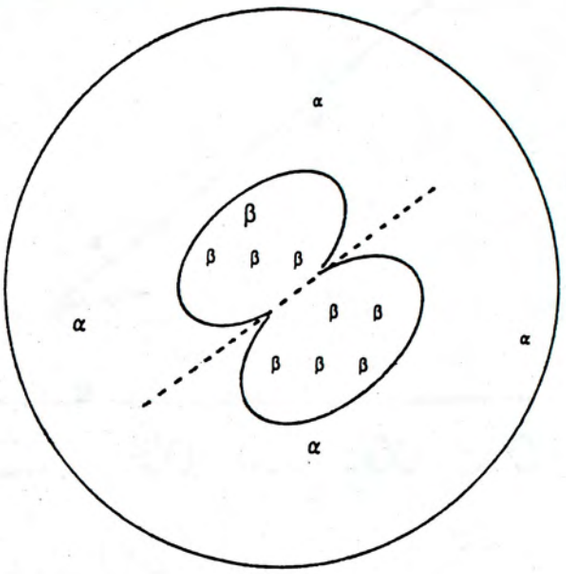

At a time t, a common interface develops.

Figure 7-5.

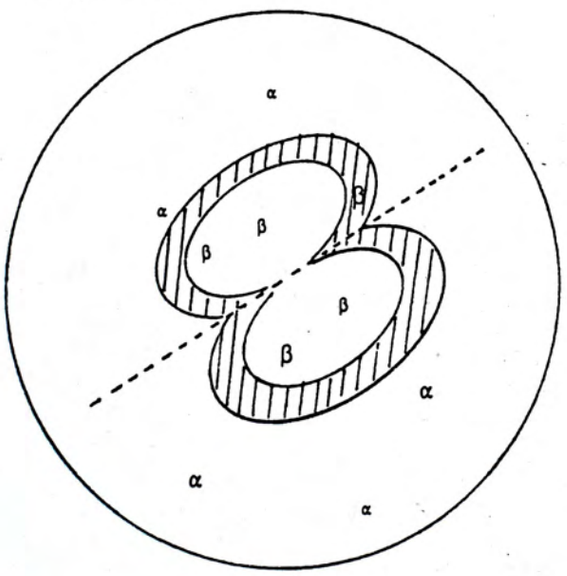

After a time dt, the real surface transformed into β region dS^{β} is shown as the shaded region.

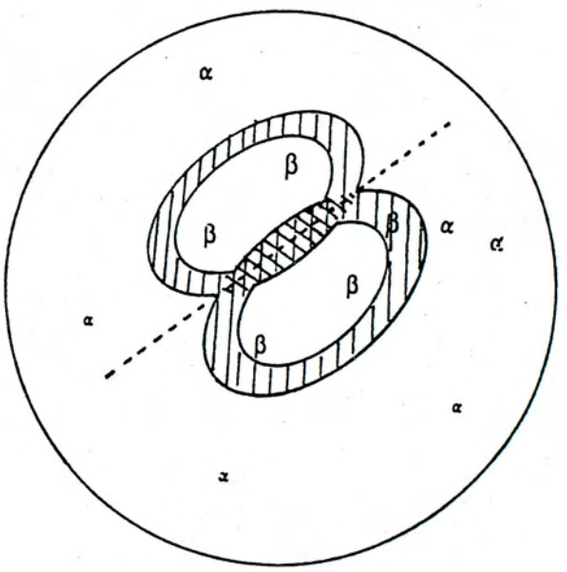

After a time dt, the extended surface dS_e^{β} increased is shown as the shaded region. The grided region corresponds to surface which has been counted more than once.

Figure 7-6.

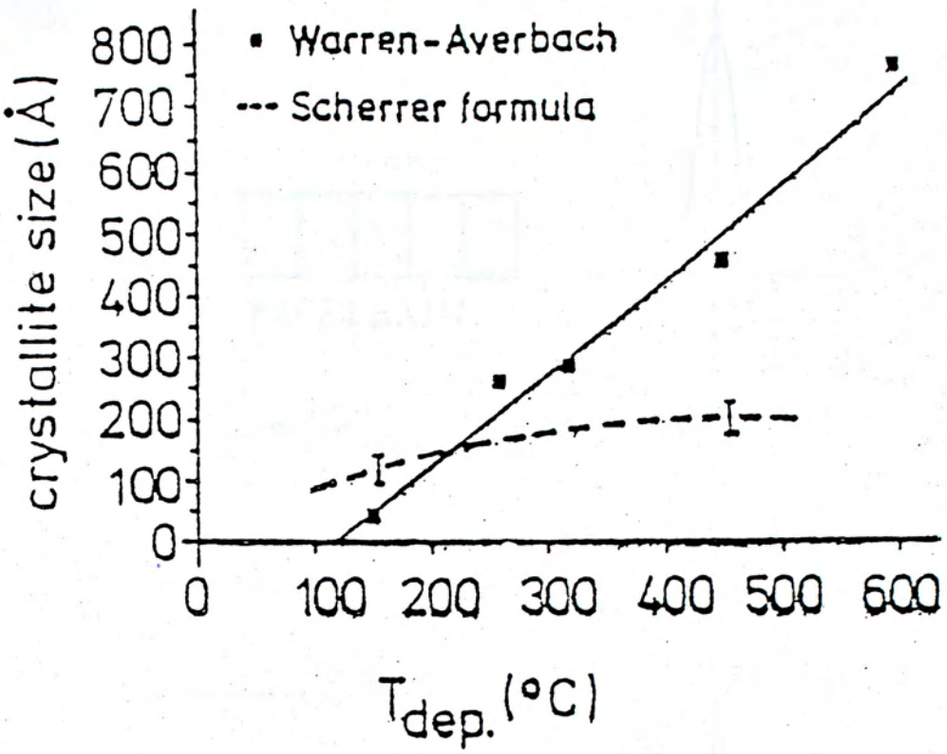

Figure 7-7. Crystallite size of nc-Si deposited at floating substrate potential by chemical transport of silicon in hydrogen plasma. Broken line: Data from Scherrer formula; Full line: More accurate data obtained from the Warren-Averbach analysis (S. Veprek et al, 1991).

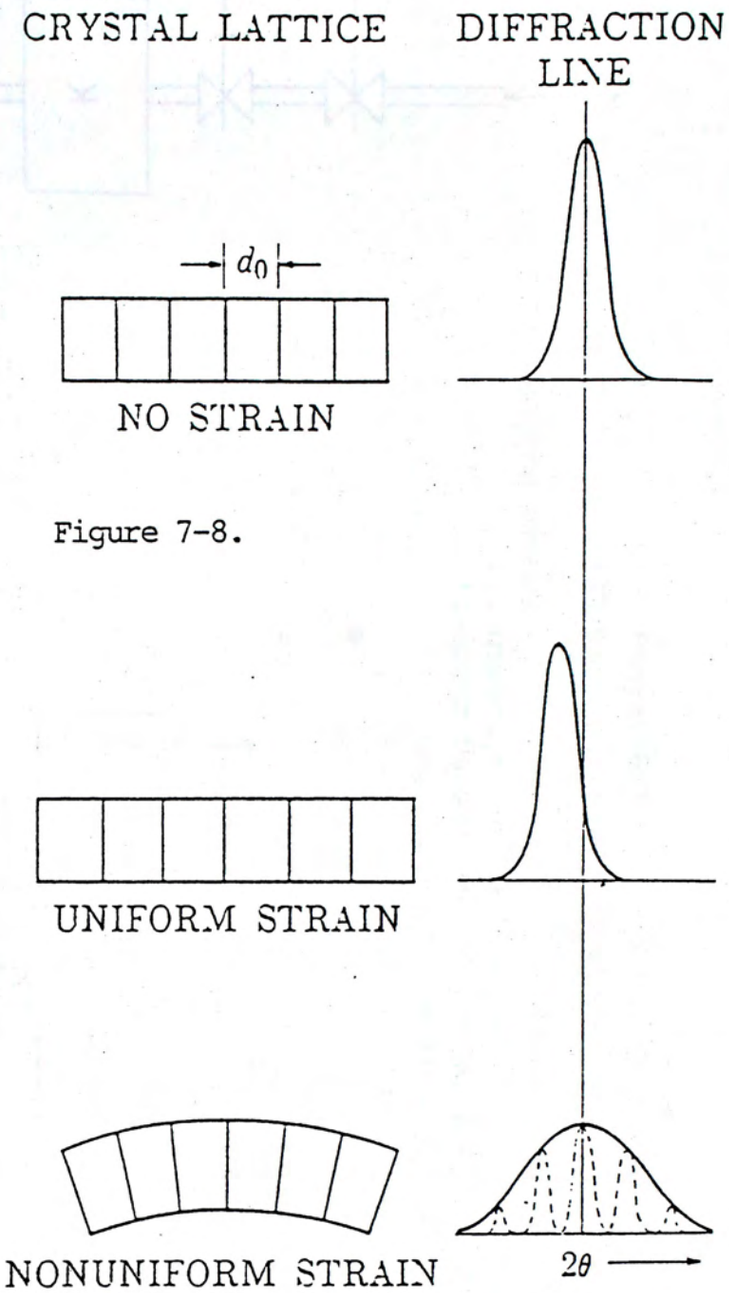

Figure 7-8.

Figure 7-9. Effect of lattice st rain on Debye-line width and position.

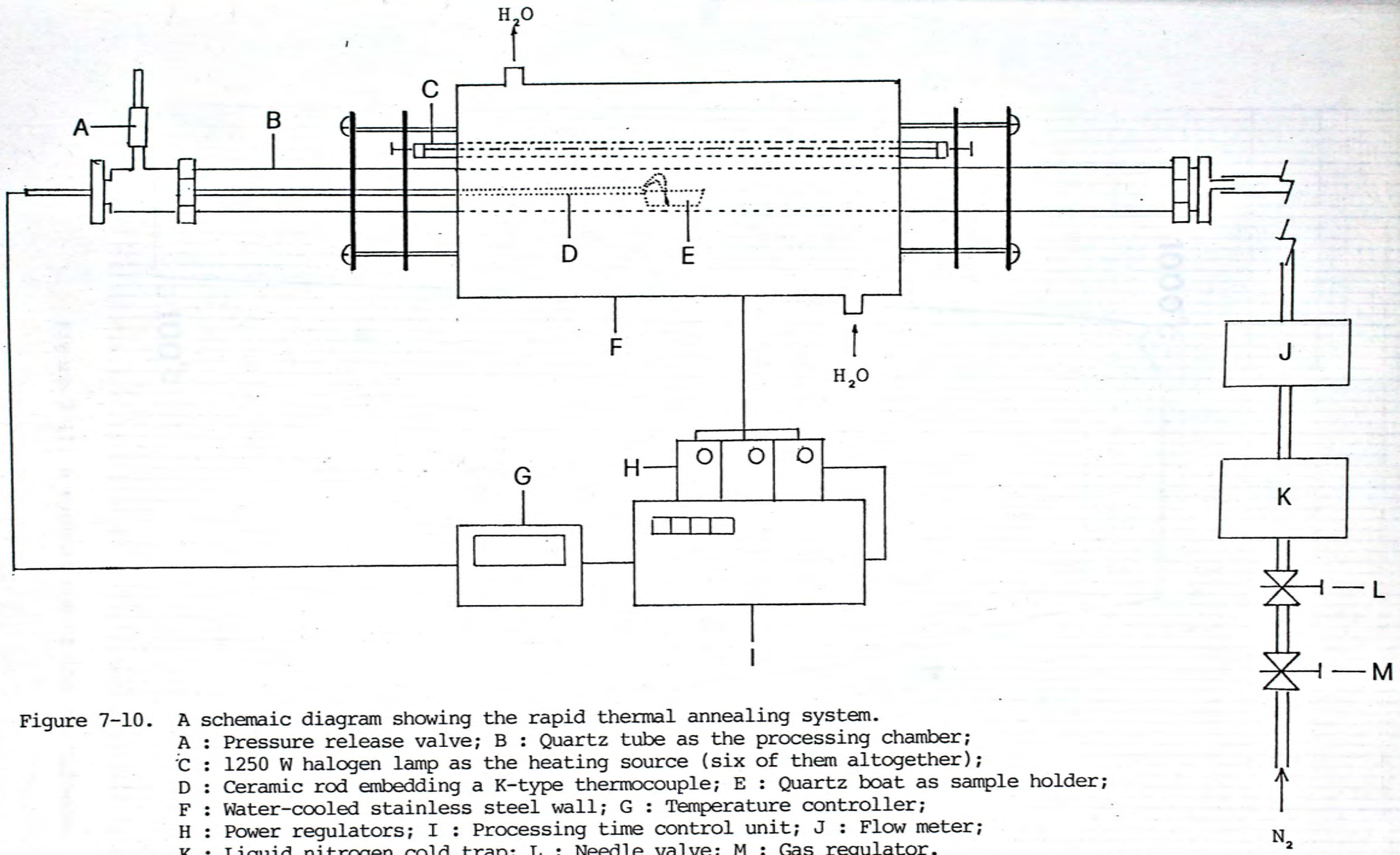

Figure 7-10. A schemaic diagram showing the rapid thermal annealing system.
A : Pressure release valve; B : Quartz tube as the processing chamber;
C : 1250 W halogen lamp as the heating source (six of them altogether);
D : Ceramic rod embedding a K-type thermocouple; E : Quartz boat as sample holder;
F : Water-cooled stainless steel wall; G : Temperature controller;
H : Power regulators; I : Processing time control unit; J : Flow meter;
K : Liquid nitrogen cold trap; L : Needle valve; M : Gas regulator.

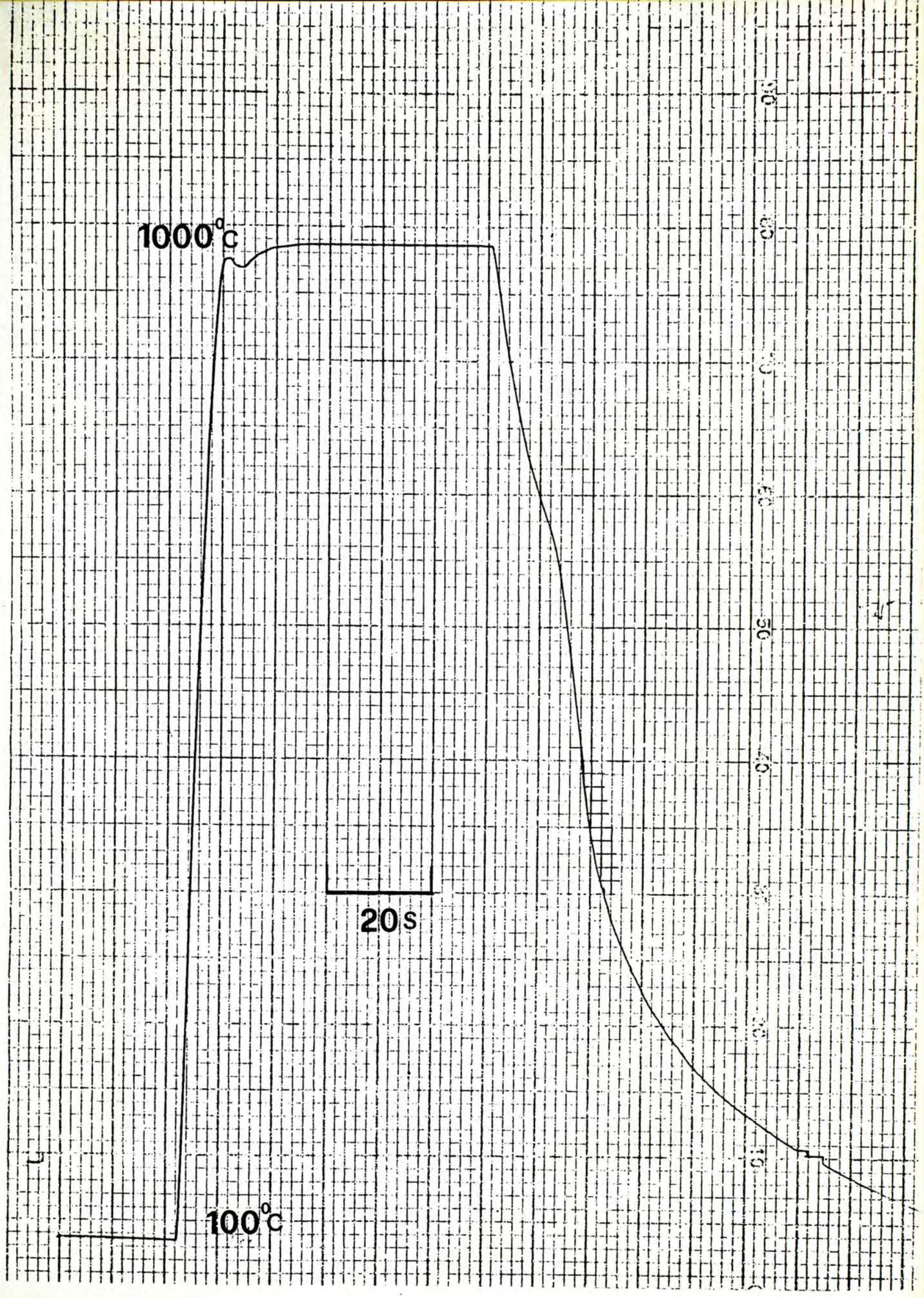

Figure 7-11. A typical run of the RTP furnace.

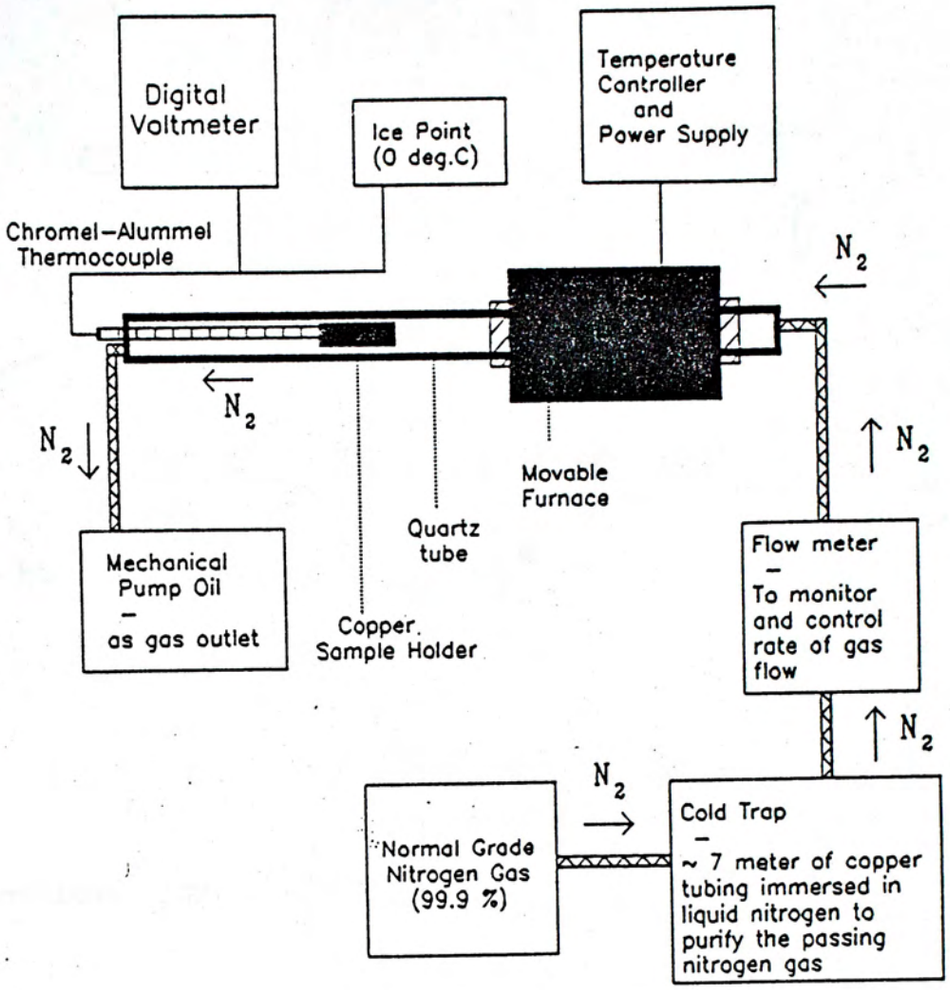

Figure 7-12. Annealing system with a conventional furnace (C.Y. Tang, 1991).

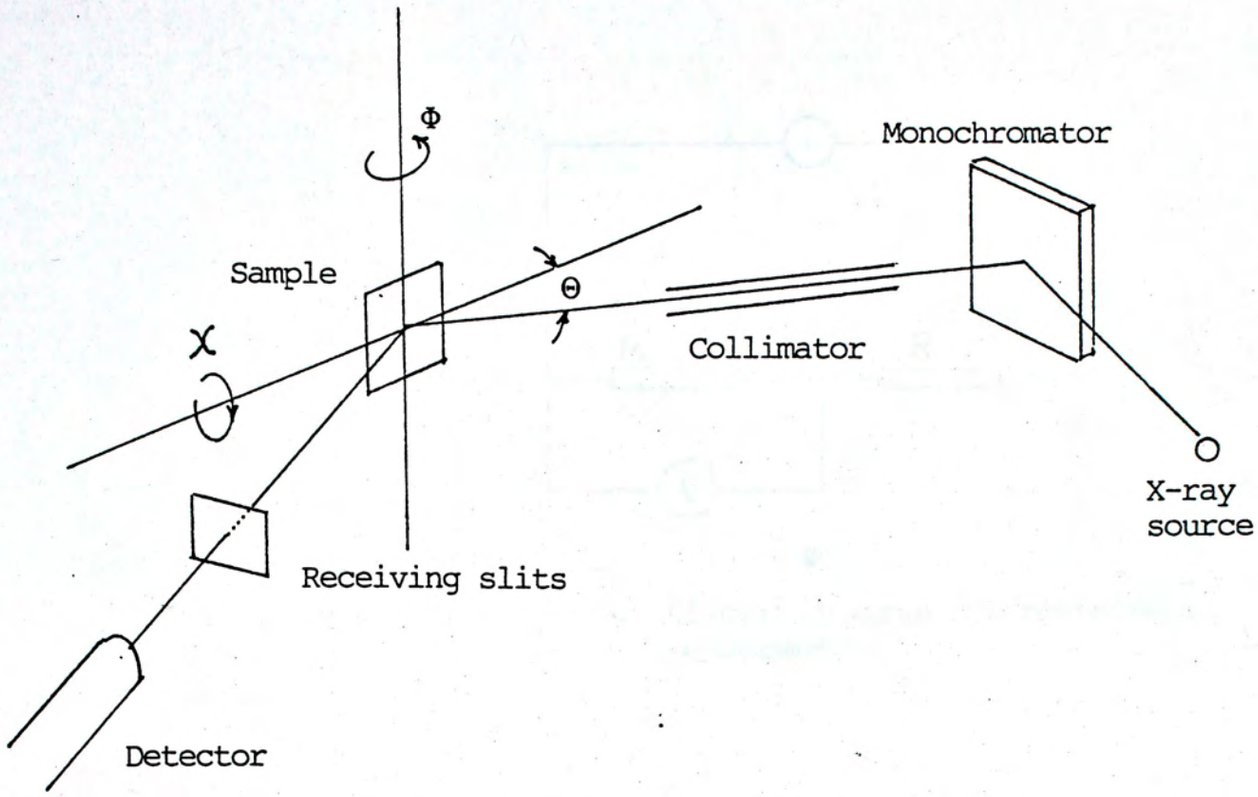

Figure 7-13. A 4-circle diffractometer.

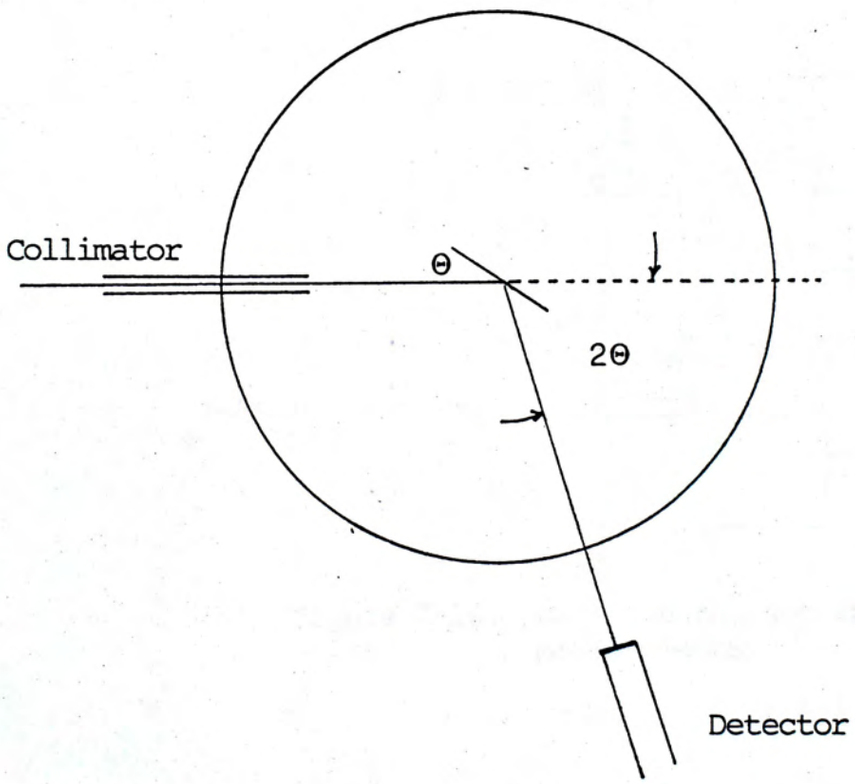

Figure 7-14.

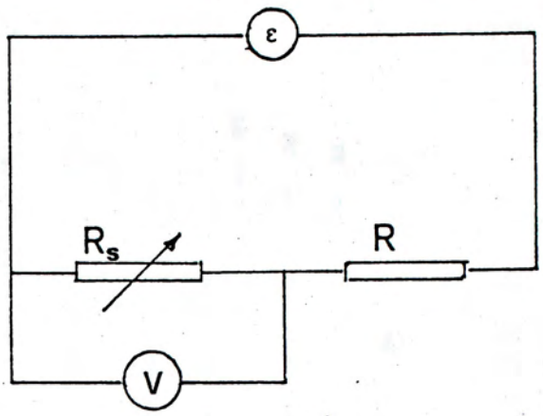

Figure 7-15. Circuit diagram for resistivity measurements.

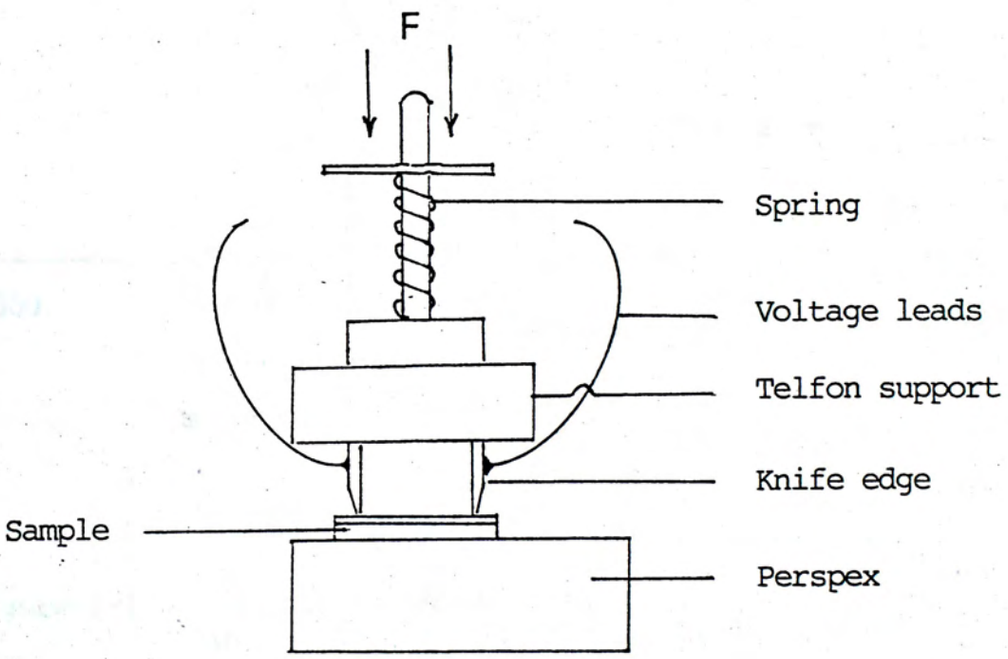

Figure 7-16. Experimental set-up for resistivity measurements.

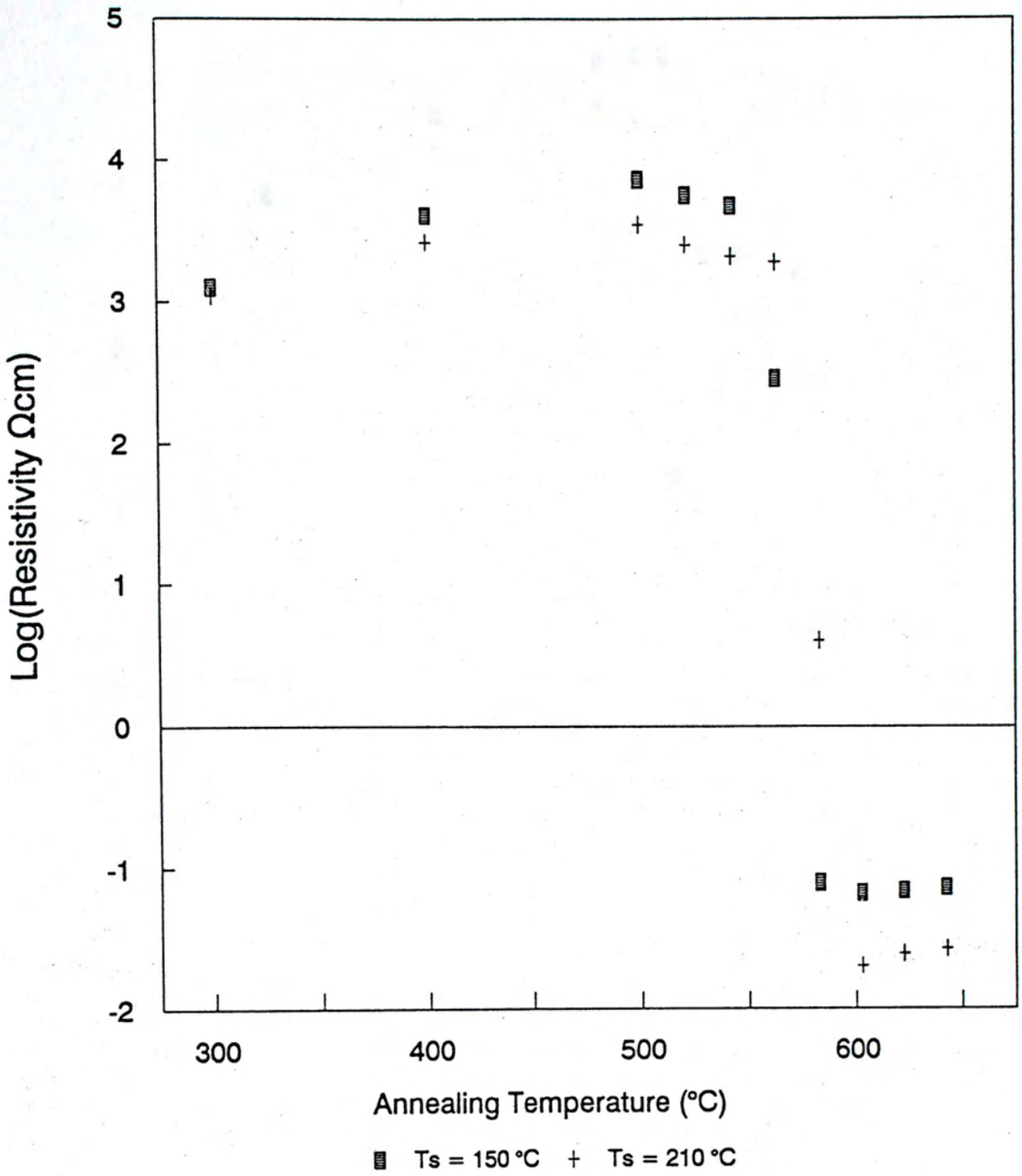

Figure 7-17. Isochronal annealing of a-Ge by RTA with a thermal pulse duration of 30s.

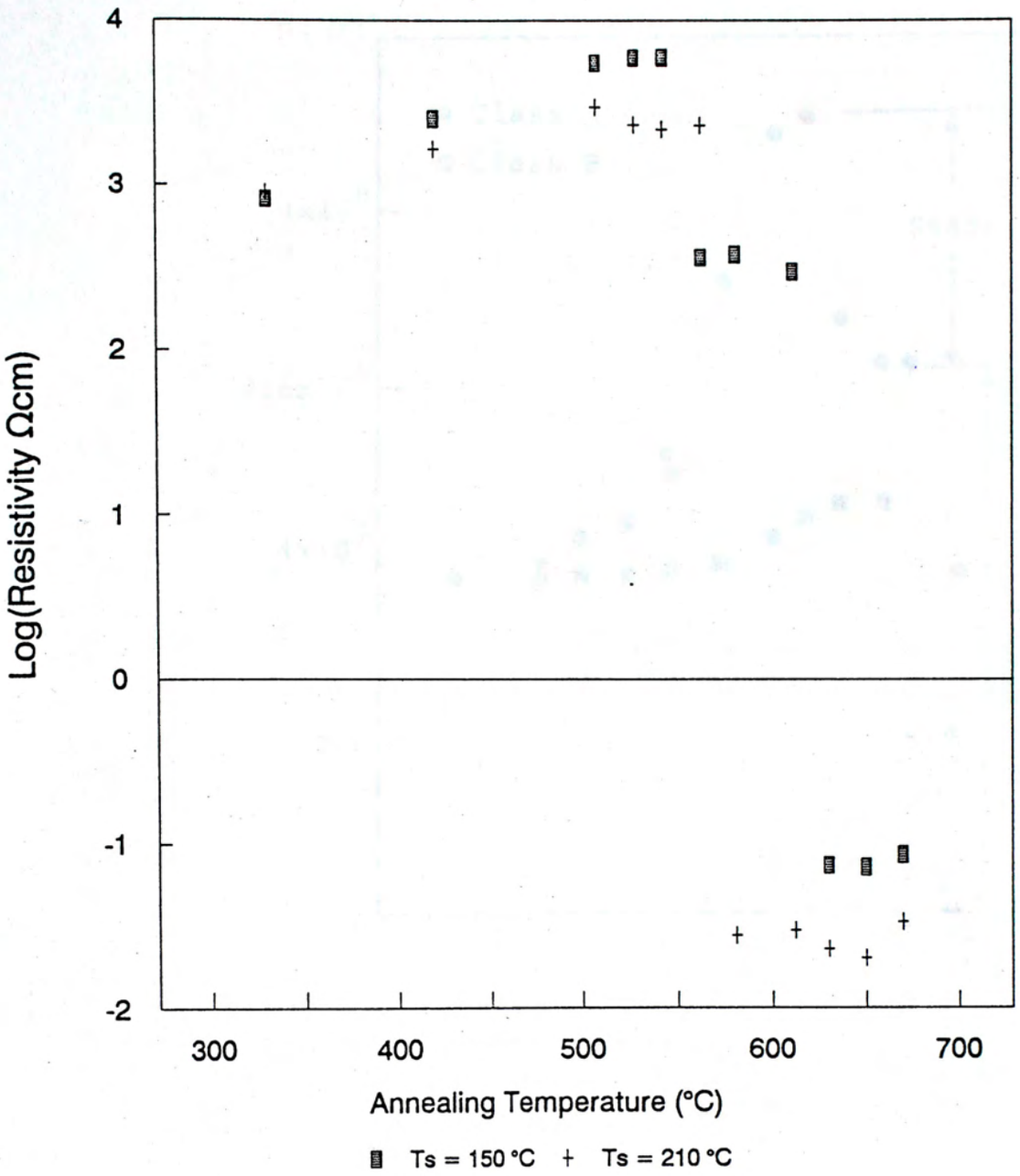

Figure 7-18. Isochronal annealing of a-Ge by RTA with a thermal pulse duration of 15s.

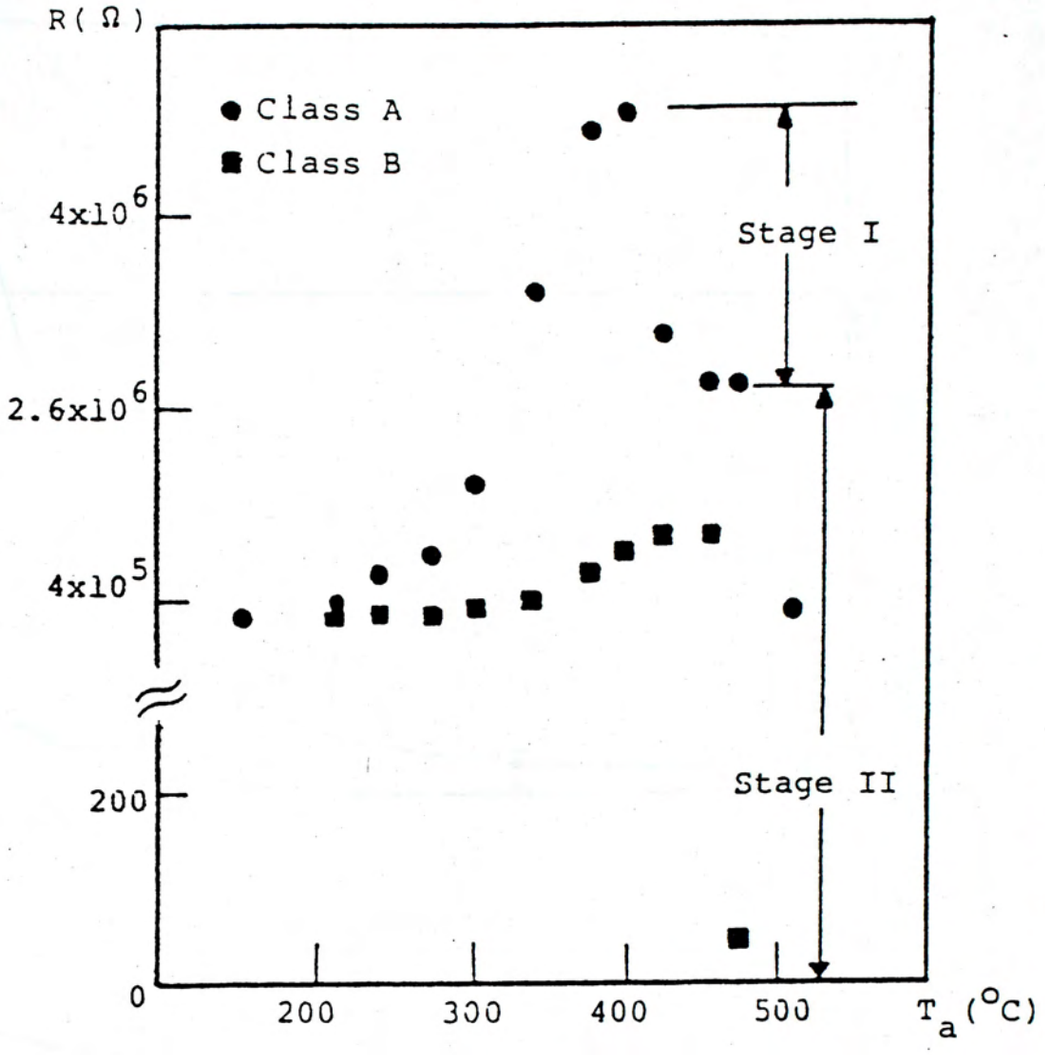

Figure 7-19. Room temperature resistance of a-Ge as function of annealing temperature (H. Tolunay, 1990).

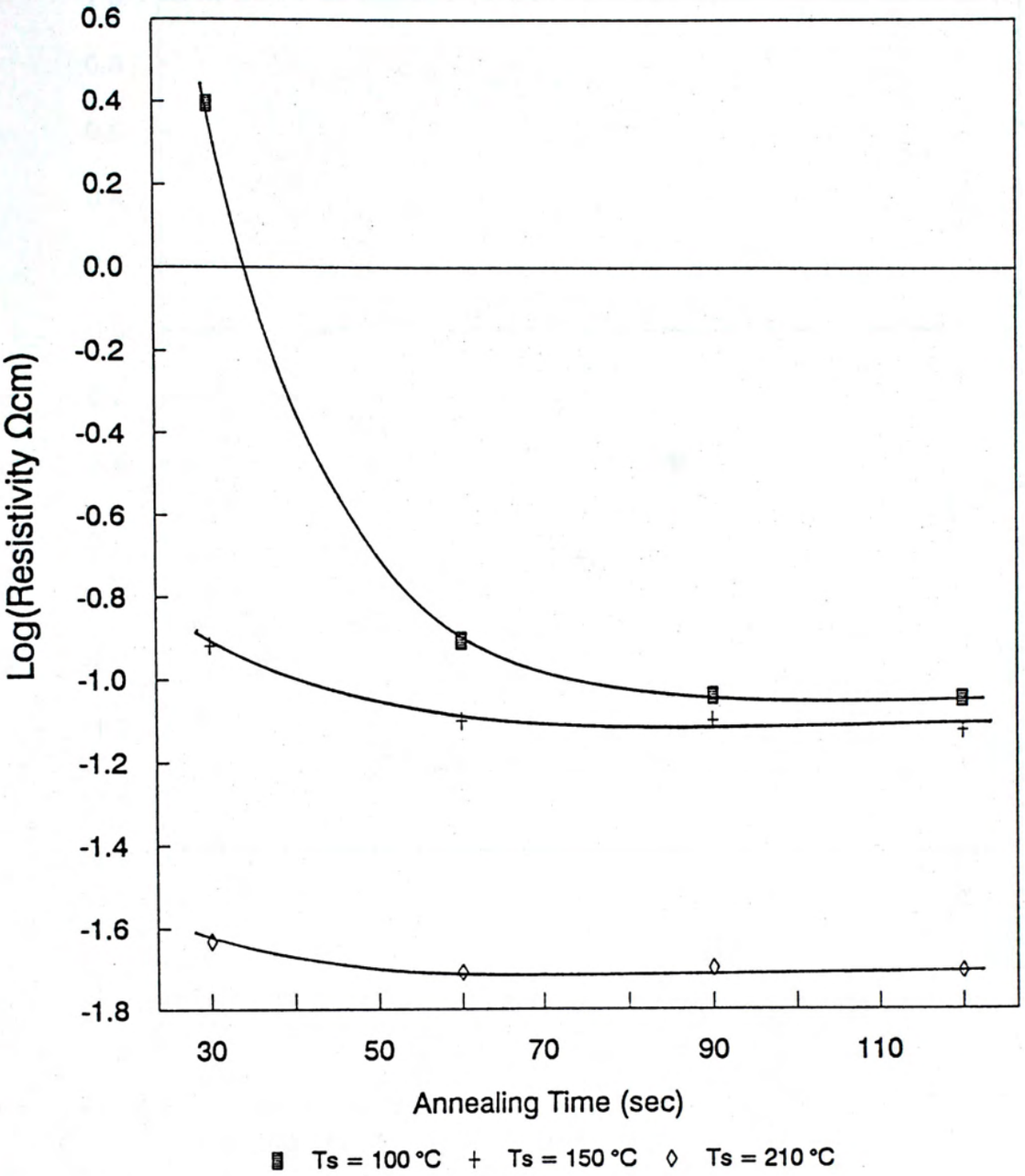

Figure 7-20. A-Ge isothermally annealed at 550 C by RTA with a thermal pulse duration of 30s.

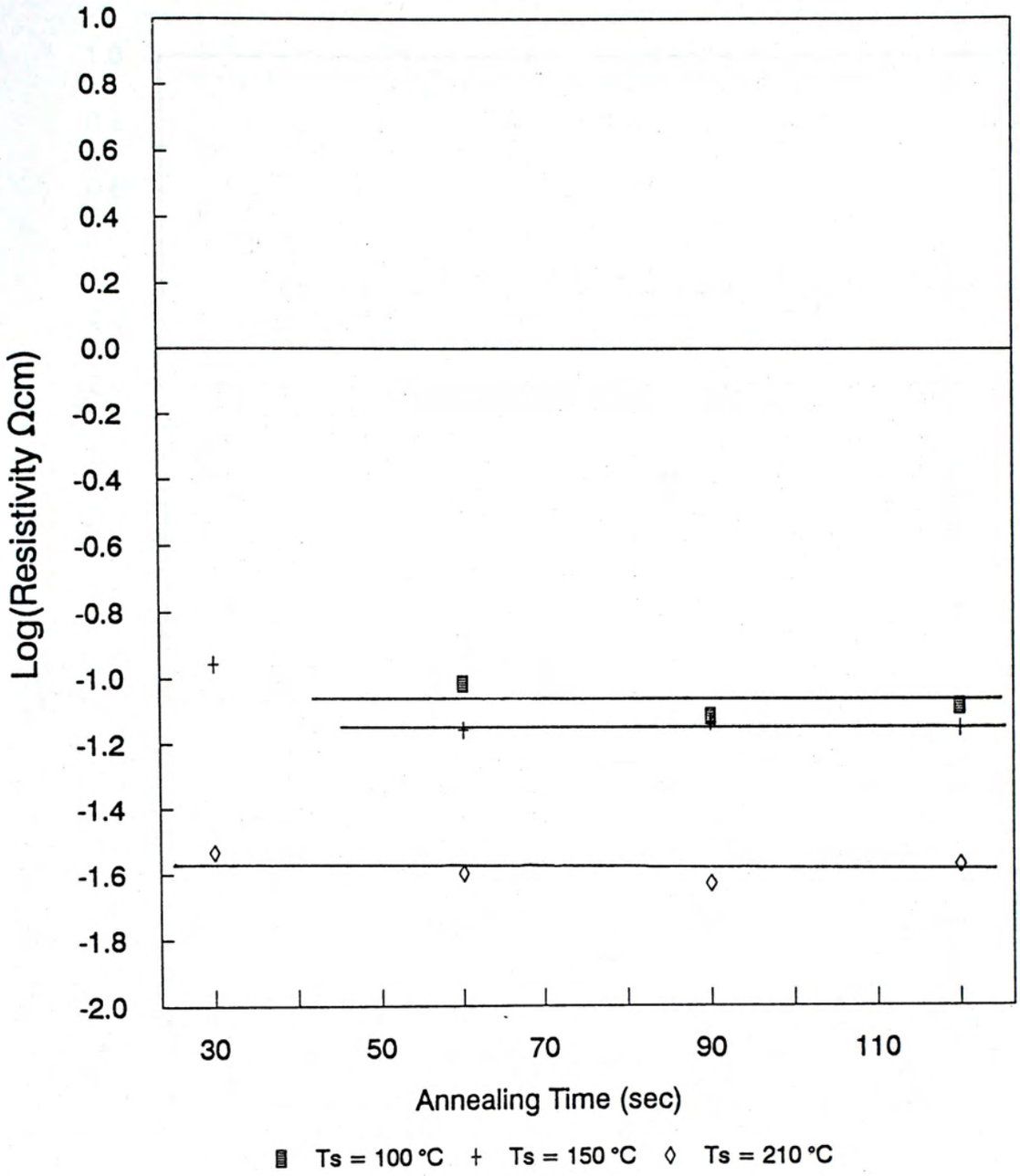

Figure 7-21. A-Ge isothermally annealed at 570 °C by RTA with a thermal pulse duration of 30s.

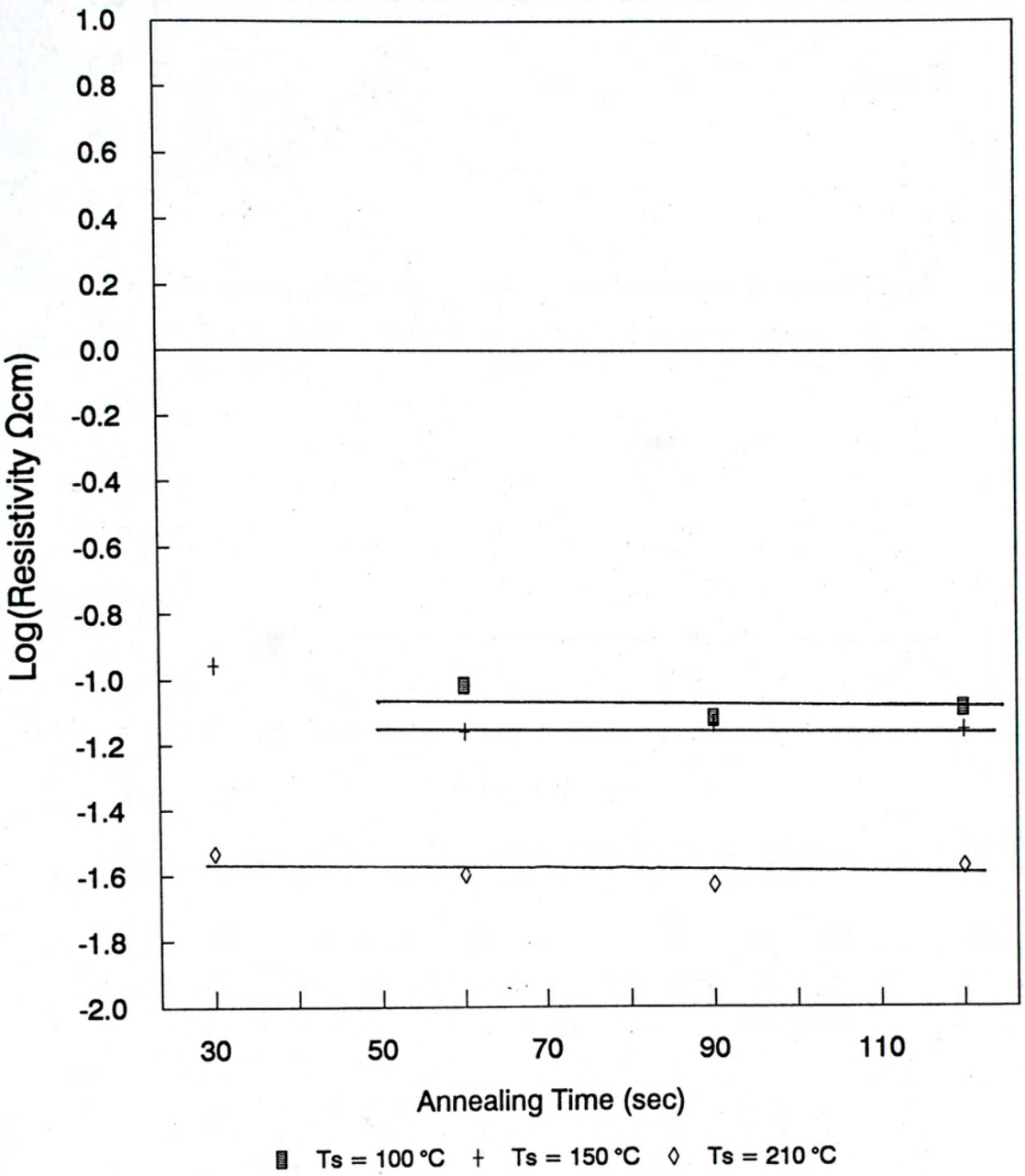

Figure 7-22. A-Ge isothermally annealed at 590 °C by RTA with a thermal pulse duration of 30s.

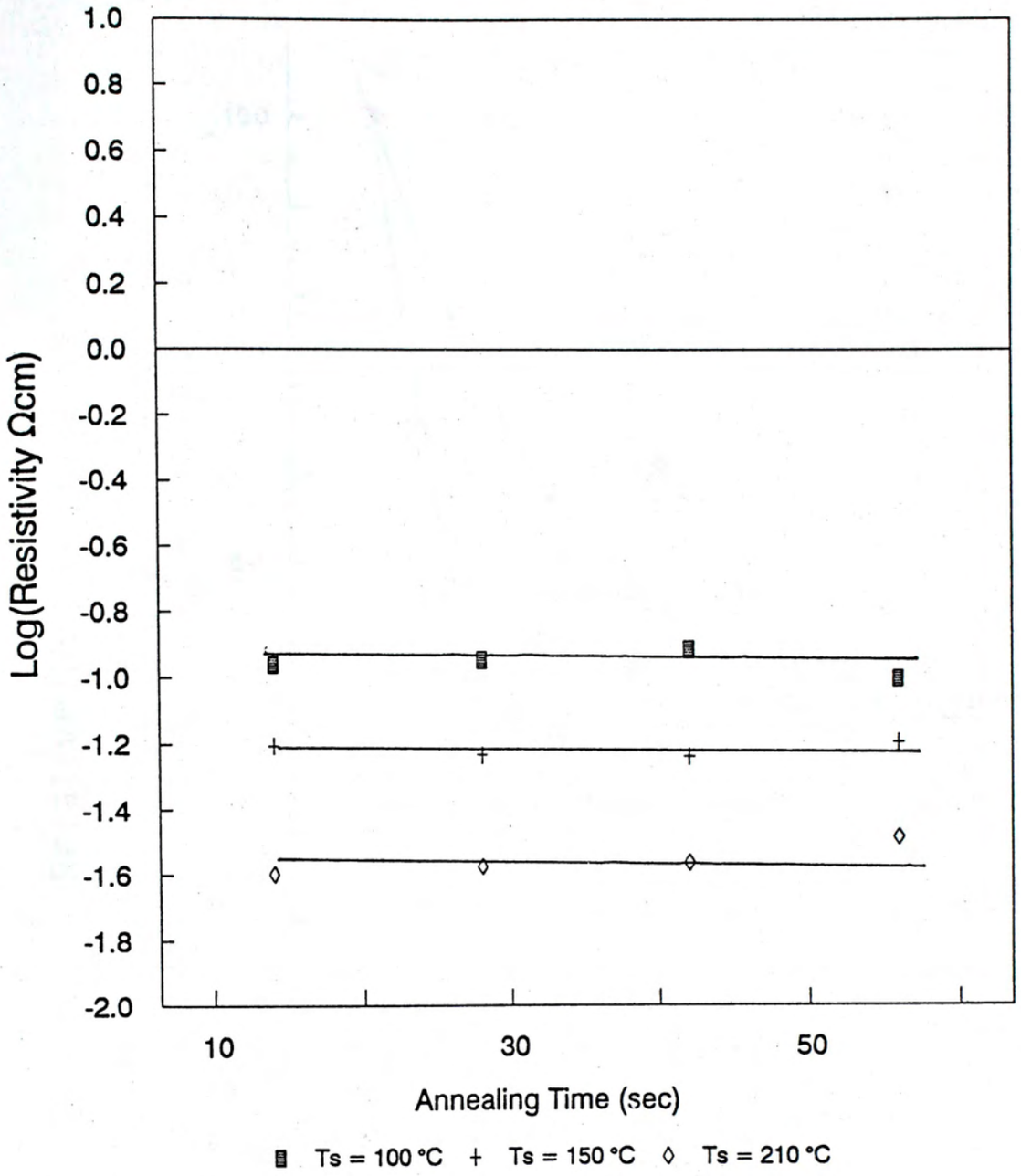

Figure 7-23. A-Ge isothermally annealed at 720 °C by RTA with a thermal pulse duration of 15s.

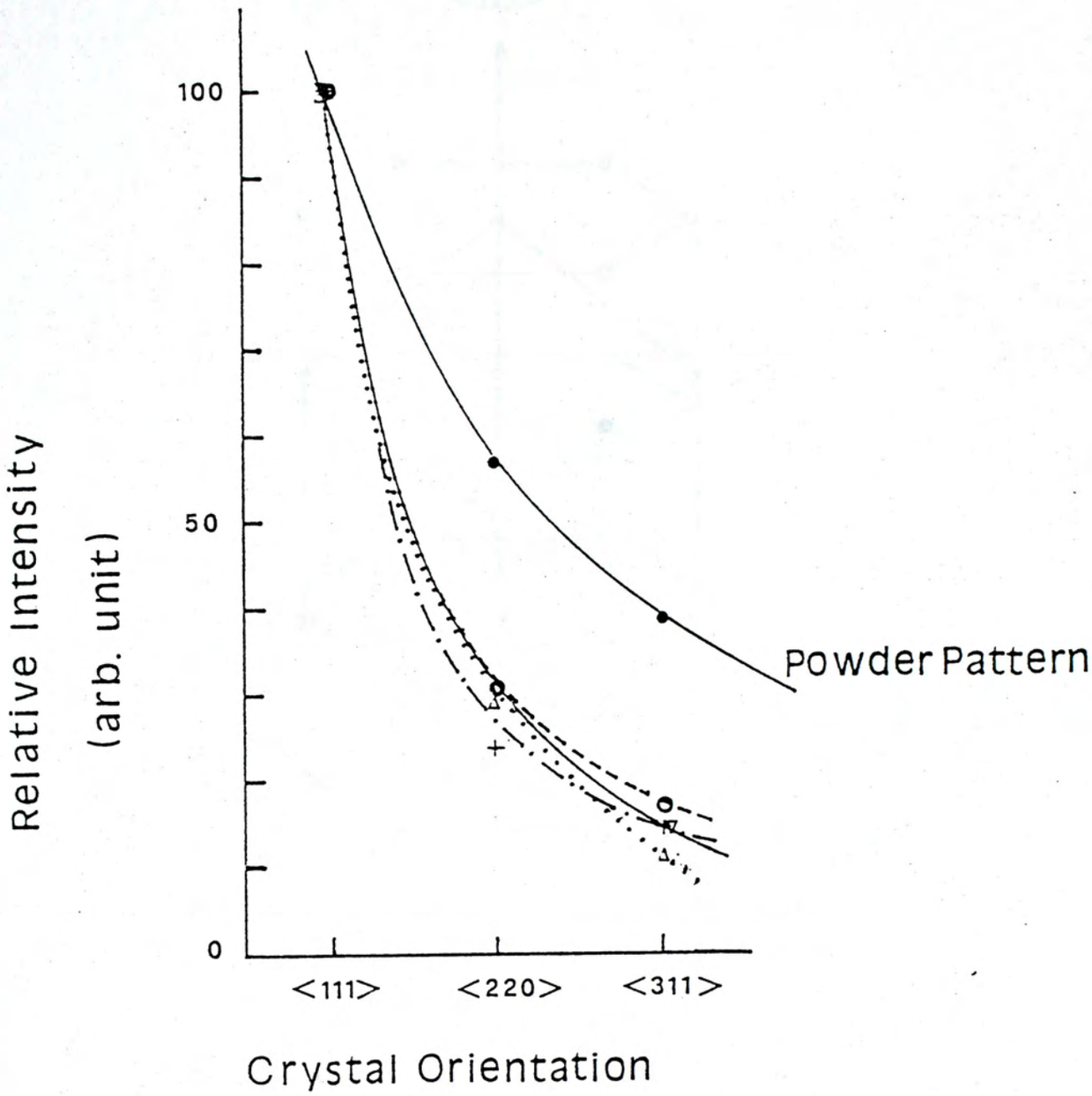

Figure 7-24. Relative intensity of different crystal orientations.

--o--o-- : a-Ge with Ts=150°C, RTA at 720°C
—▽—▽— : a-Ge with Ts=210°C, RTA at 720°C
····△····△···· : a-Ge with Ts=100°C, RTA at 720°C
—·+—·+—· : a-Ge with Ts=150°C, annealed at 500°C by a conventional furnace.

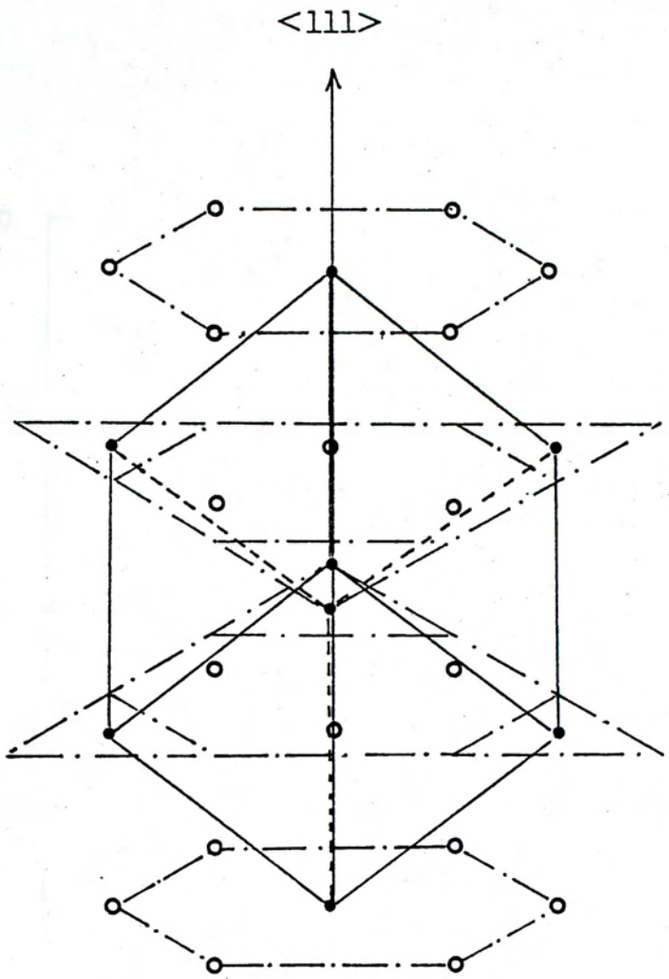

Figure 7-25. FCC close packing structure.

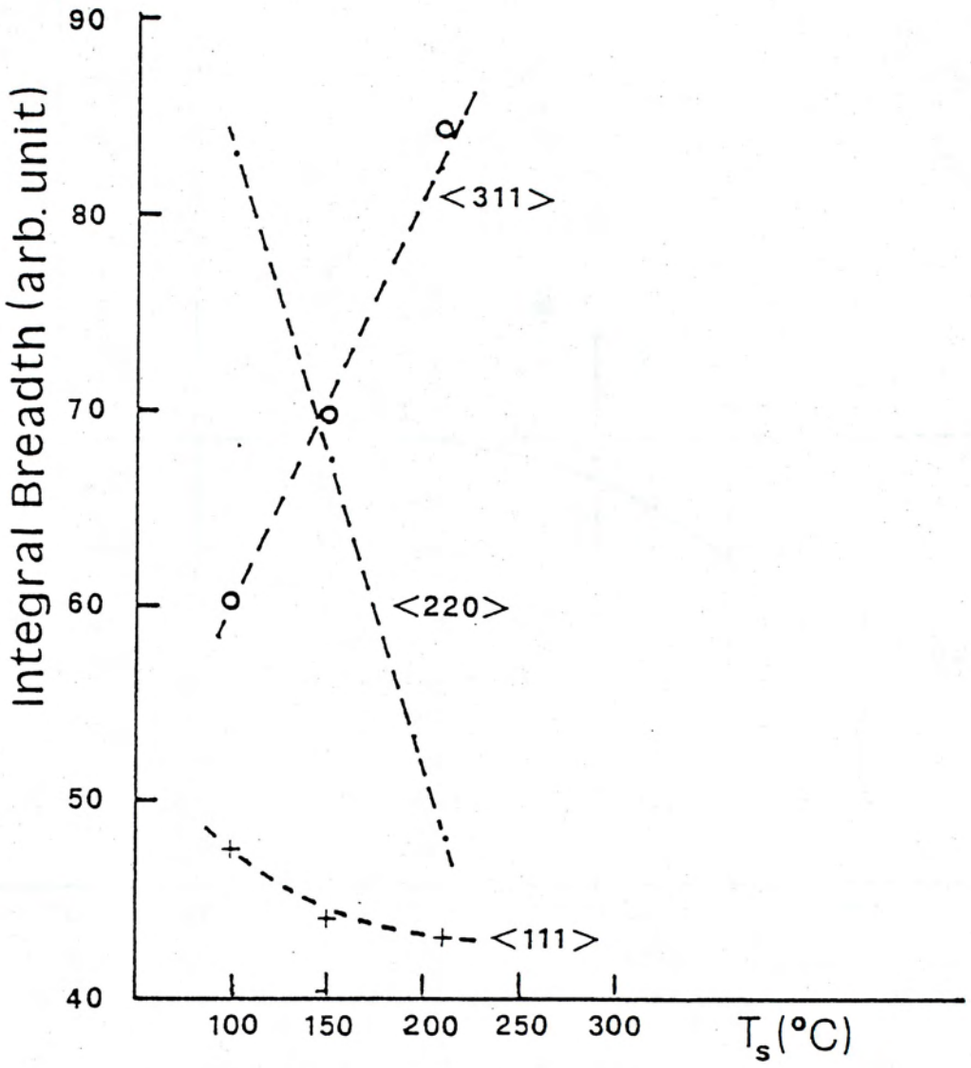

Figure 7-26. A plot of integral breadth against substrate temperature for different crystal orientations.

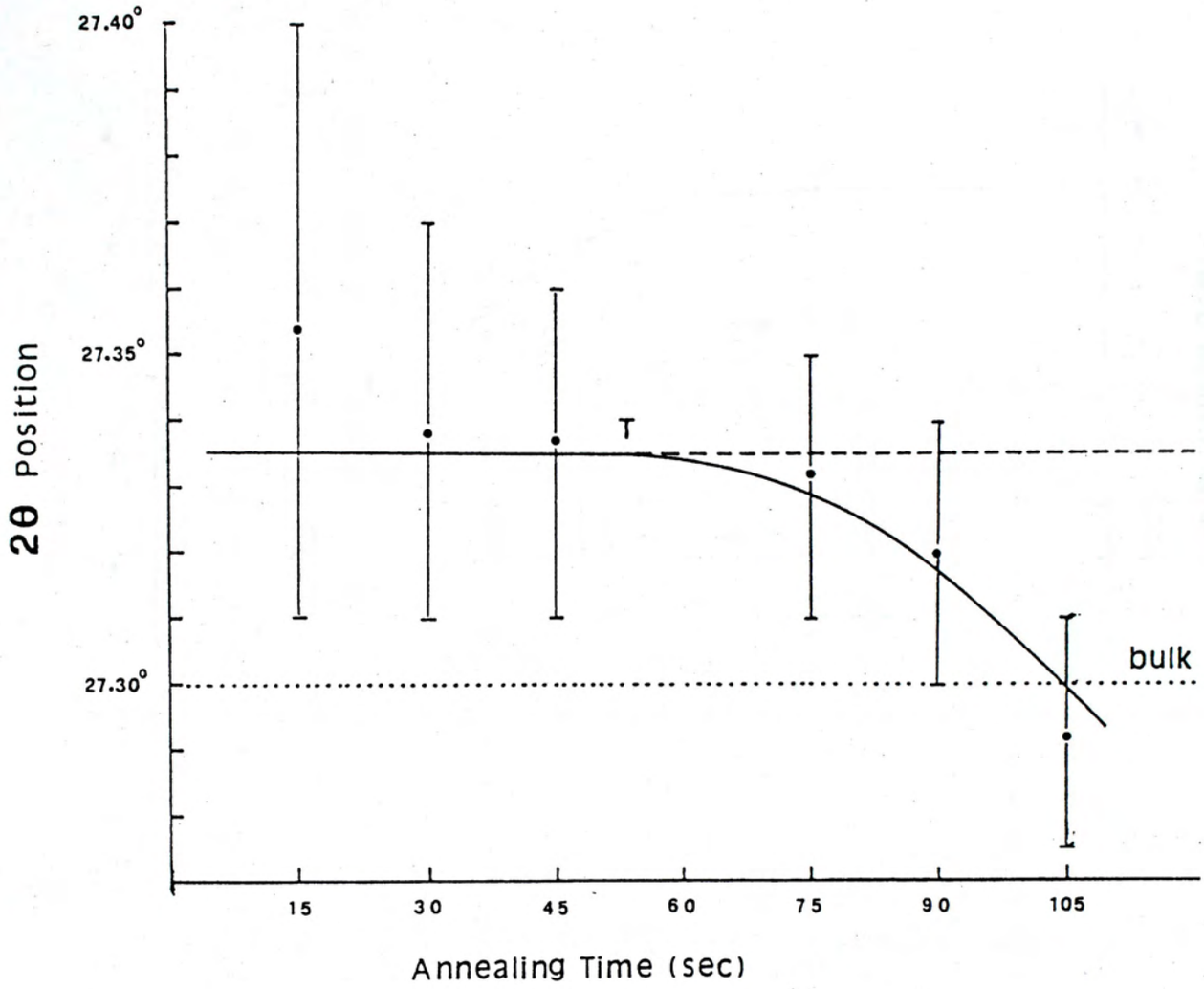

Figure 7-27. A plot of 2θ position of <111> reflection against annealing time. The sample was a-Ge with Ts=150 °C, isothermally annealed at 610°C by RTA with a thermal pulse duration of 15s.

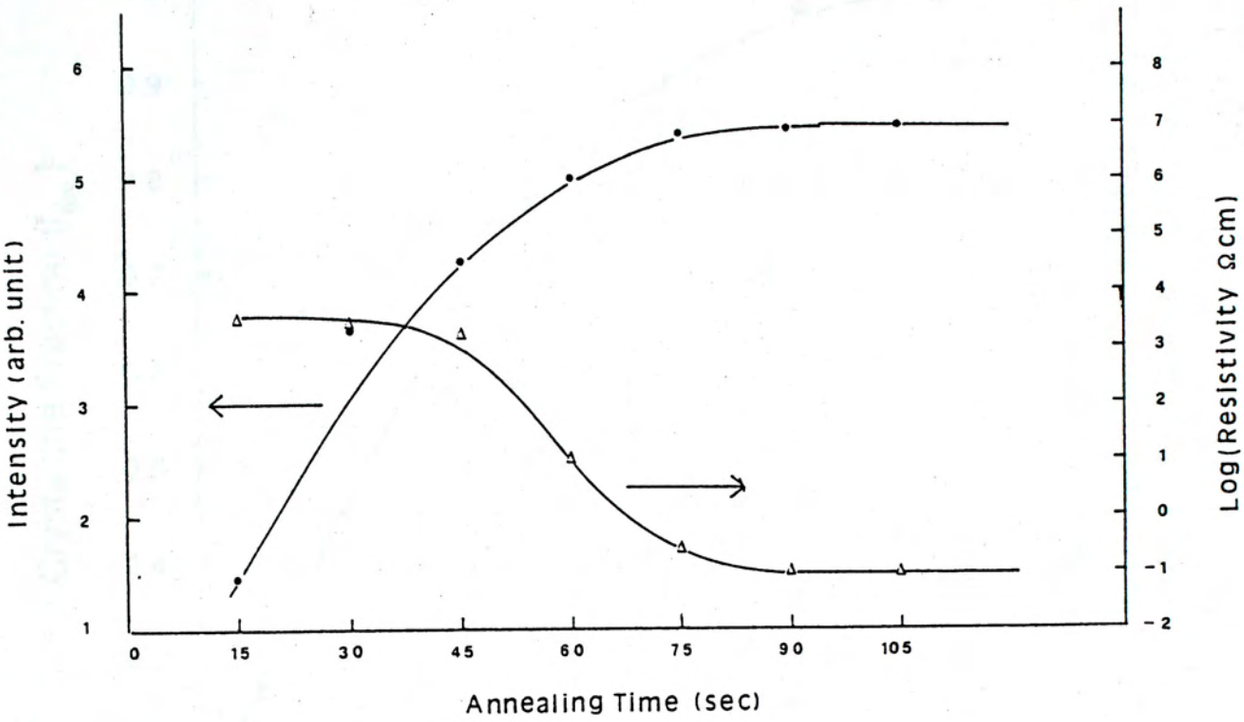

Figure 7-28. A plot of diffraction intensity and resistivity against annealing time. The sample was a-Ge with Ts=150 °C isothermally annealed at 610 °C by RTA with a thermal pulse duration of 15s.

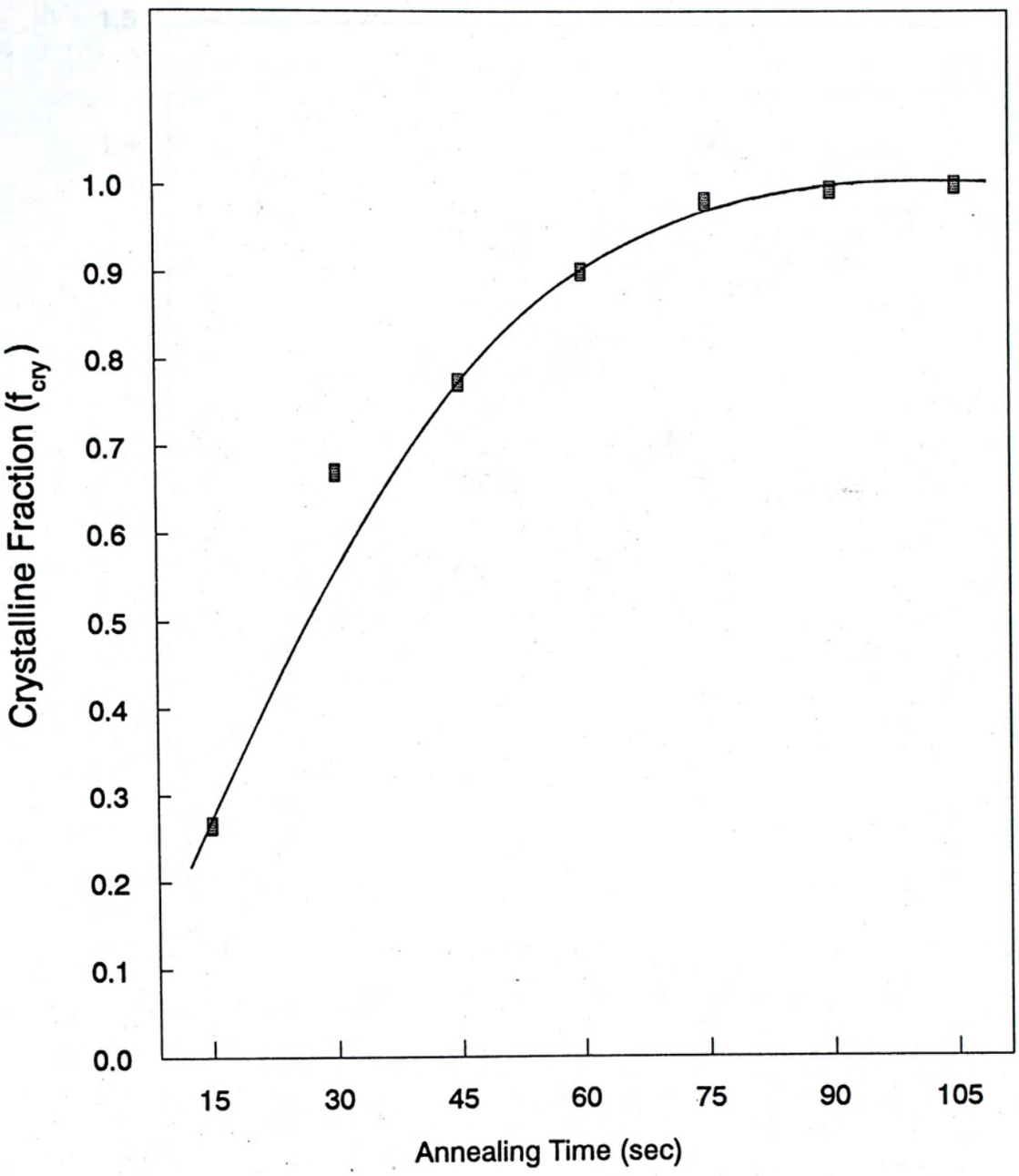

Figure 7-29. A plot of crystalline fraction against annealing time.
The sample was a-Ge with Ts=150 °C isothermally annealed at 610 °C by RTA with a thermal pulse duration of 15s.

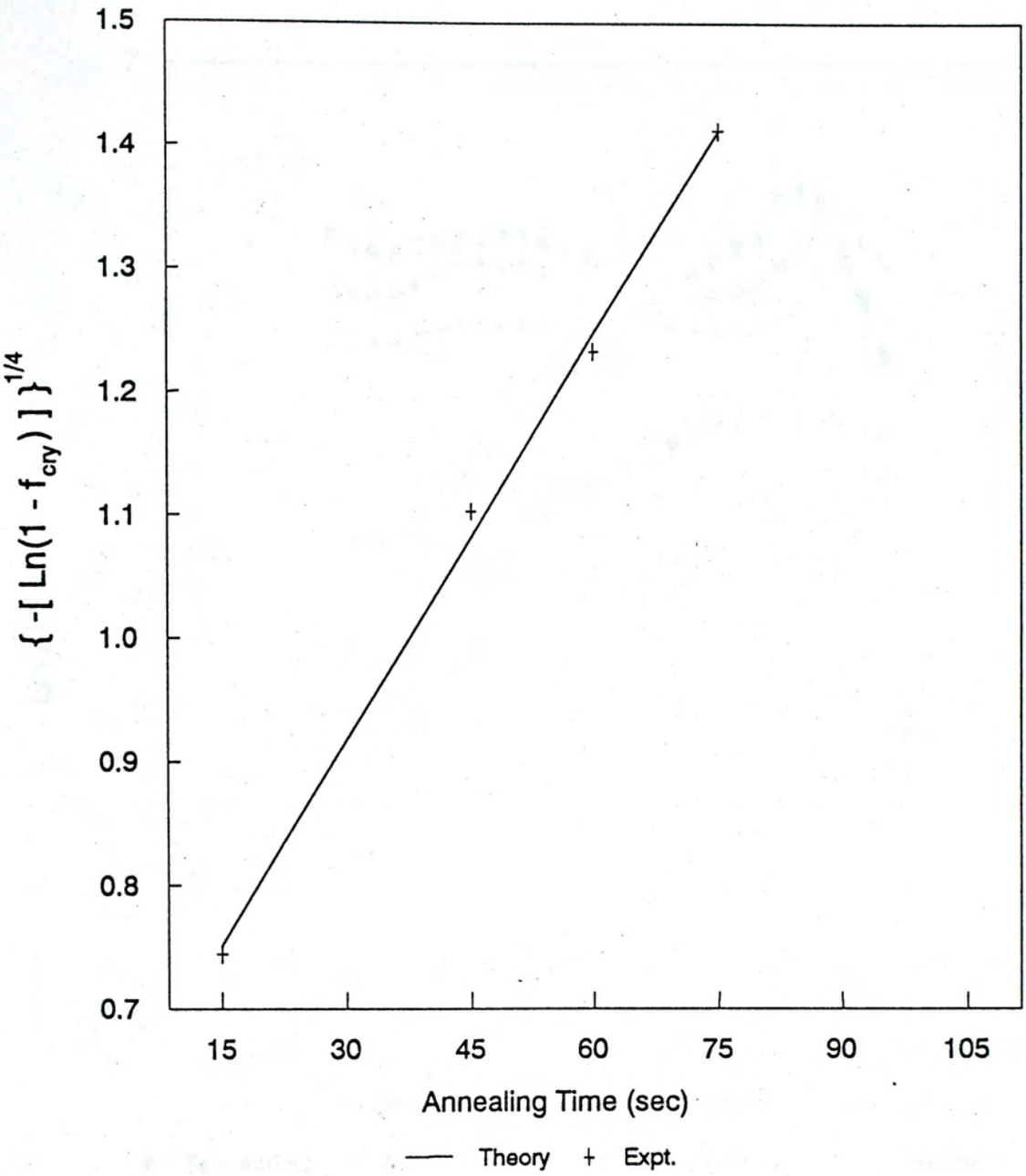

Figure 7-30. A plot of $\left\{\left[-\ \mathrm{Ln}(1-f_{cry})\right]\right\}^{1/4}$ against annealing time.
The solid line was obtained from a nucleation and growth theory.

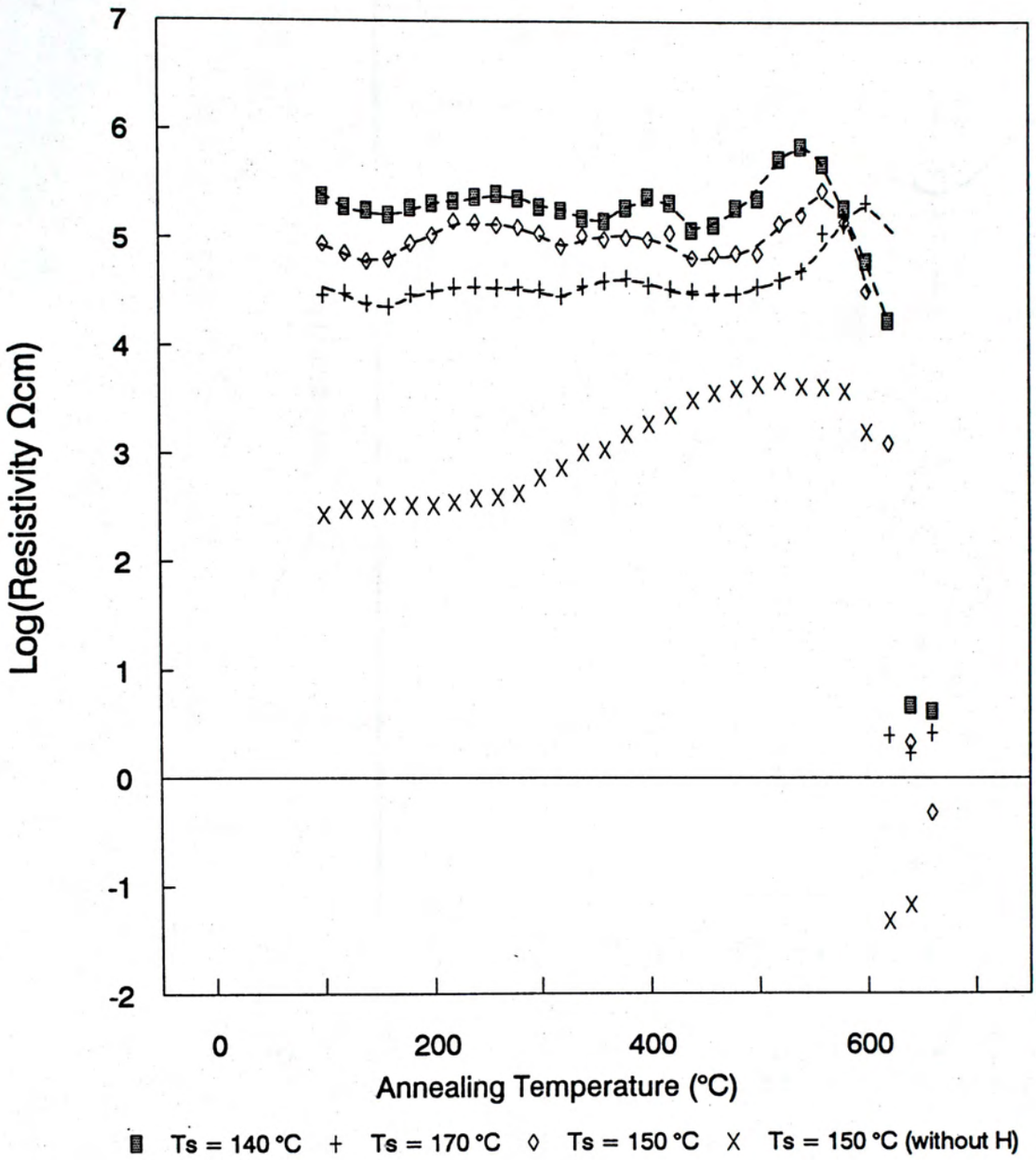

Figure 7-31. Isochronal annealing of a-Ge:H and a-Ge with different substrate temperatures.

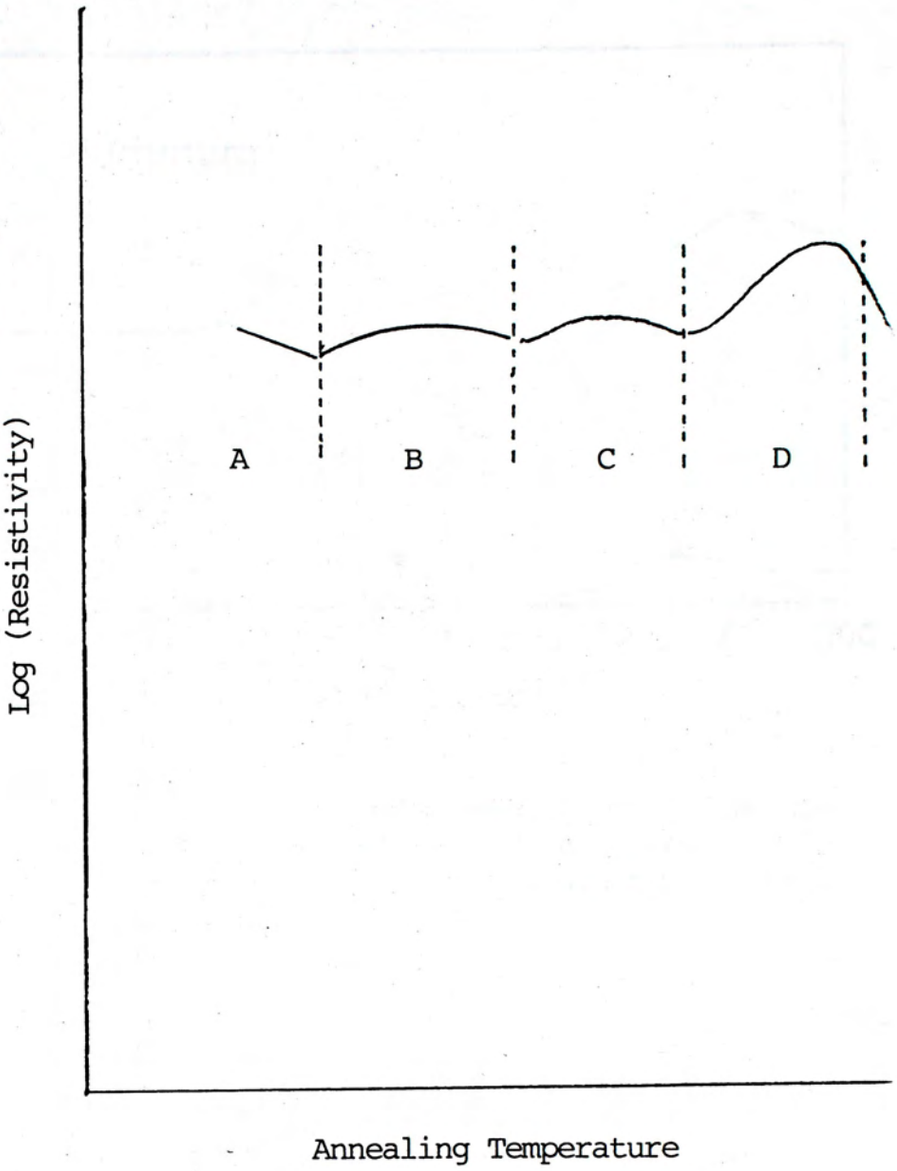

Figure 7-32. A schematic diagram showing the iosochrona annealing behaviour of reactively evaporate a-Ge:H.

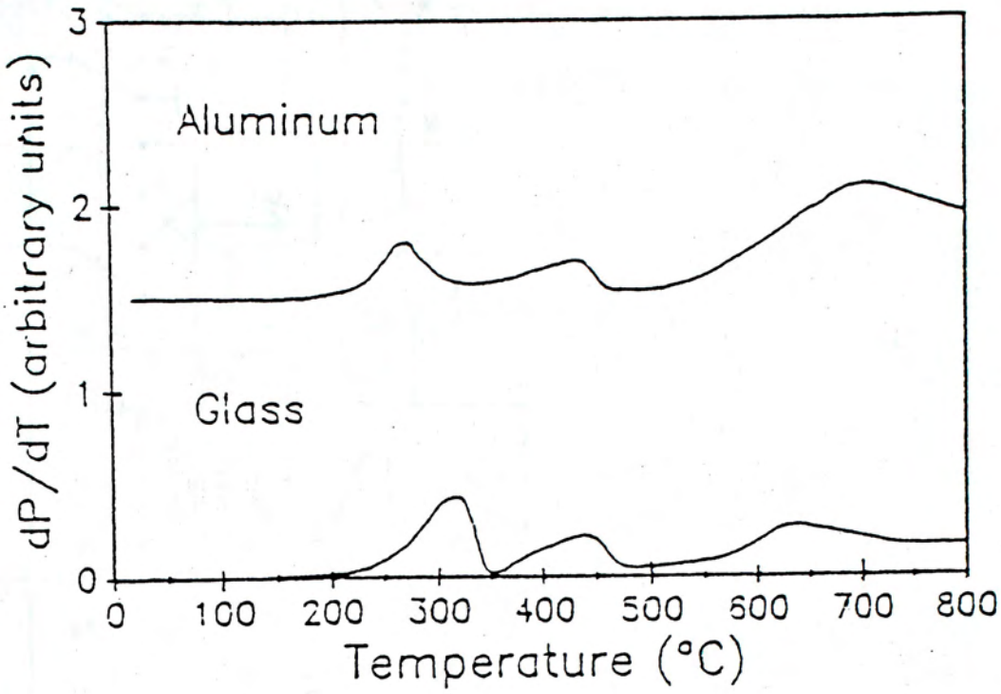

Figure 7-33. Gas evolution spectra of films co-deposited at 250 °C on Corning 7059 glass and Al foil substrates (W. Paul et al., 1990).

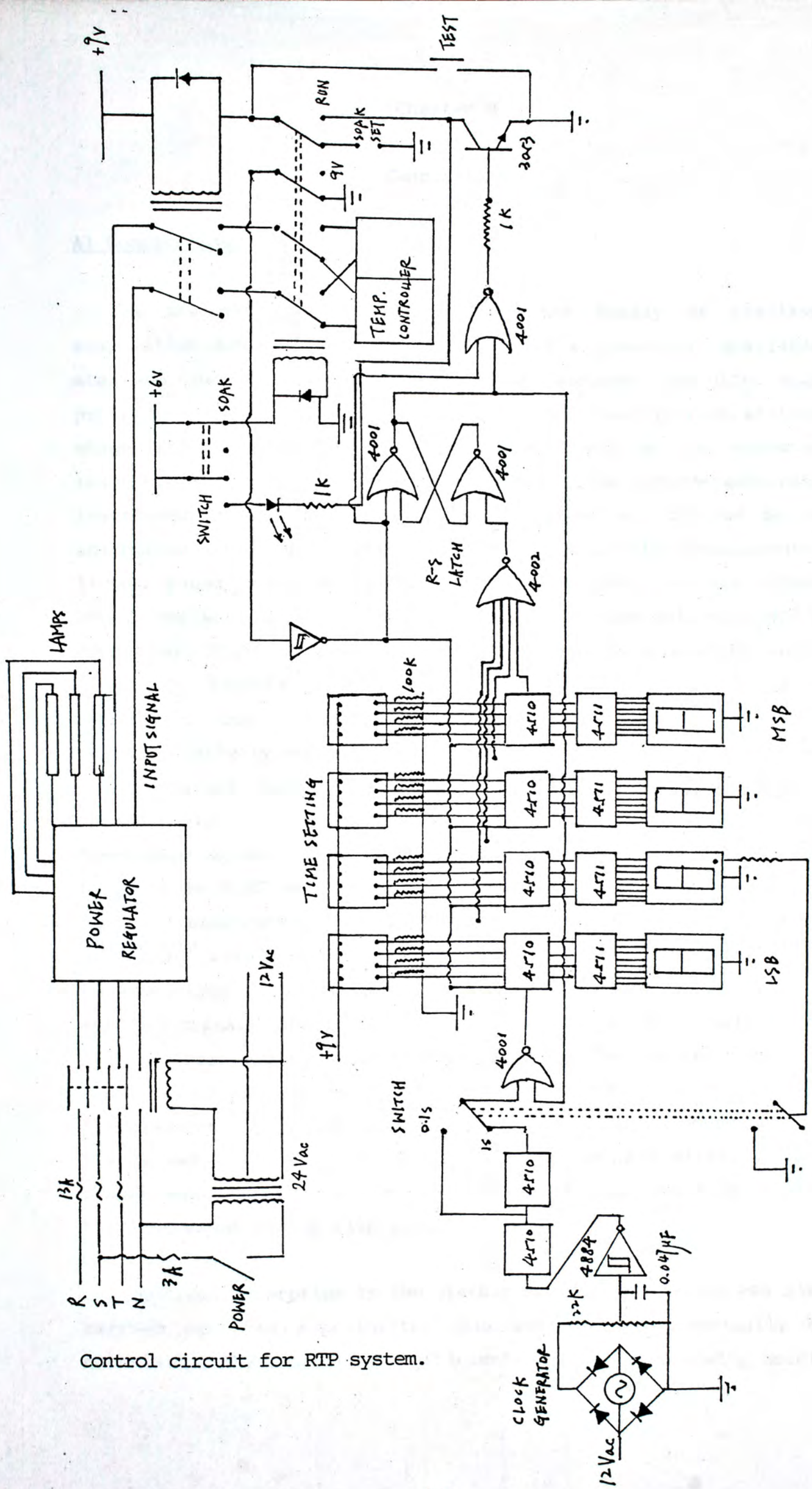

Control circuit for RTP system.

Chapter 8

Conclusions

A) Conclusions:

A new method which belongs to the family of reactive evaporation has been developed. By use of a commercial available atom gun, neutral hydrogen atoms can be produced from ultra high purity hydrogen gas and are allowed to react readily with silicon atoms at the surface of a substrate held at an elevated temperature during the film growth process. The optimum substrate temperature for producing high quality films was checked by IR absorption spectroscopy and electrical conductivity measurements. It was found that the optimum substrate temperature was around 250°C, corresponding to the condition for predominant monohydride formation. Higher T_s leads to less hydrogen incorporation while lower T_s favours polyhydride formation in the film. Both conditions can lead to inferior physical properties. The photoconductivity under AM1 illumination and dark conductivity of the optimized samples were $\cong 2\times10^{-6}$ $(\Omega cm)^{-1}$ and 8.56×10^{-11} $(\Omega cm)^{-1}$ respectively, giving a photosensitivity of $\cong 2.34\times10^{4}$. The corresponding activation energy for extended states conduction was found to be 0.87 eV. Also, ESR measurement indicated that at the optimum substrate temperature, the spin density was about 3×10^{17} cm^{-3} with a g-factor equal to 2.0043, which can be shifted to 2.005 upon illumination by light (LESR). It was proposed that the ESR signals come from T_2^+ and T_3^- centers situated within the mobility gap. The shift in g-factor was explained as the result of electronic transitions between these two centers upon illumination. A growth mechanism for our reactively evaporated a-Si:H was also proposed, and the absence of S-W effect in our sample was ascribed to the passivation of weak bonds by active hydrogen atoms during film growth process.

Optical absorption in the visible and near IR region was also carried out. The experimental data were fitted numerically by calculating the absorption coefficients using the following model,

namely, parabolic bands for extended states, an exponential tail for valence band and two identical gaussian bands for T_2^+ and T_3^- centers within the mobility gap. By deconvolutions of joint density-of-states integrals one obtained an optical gap of ≅ 1.7 eV and a valence band tail width of ≅ 65 meV for our optimized samples, implying a mobility gap of 1.73 eV. The fitting also gave an ESR active spin density of ≅ 1.8×10^{17} cm^{-3}, in close agreement with the measured value of 3×10^{17} cm^{-3} and the position of the Fermi level at 0.86 eV below E_c, also in reasonable agreement with the activation energy found from electrical conductivity data. Moreover, the measured absorption coefficients in the low $h\nu$ region (of order 10^{o} cm^{-1}) is much smaller than those of BARE sample, and highly comparable to those of glow-discharge samples, indicating that a-Si:H produced by the present method is of device grade. Besides being optically stable, the optimized samples were also thermally stable up to an annealing temperature of 510°C. So it can be concluded that the new deposition method used in the present study can successfully fabricate a-Si:H thin films of device quality.

The annealing behaviour of electron beam evaporated a-Ge and reactively evaporated a-Ge:H has been examined by rapid thermal annealing method. For a-Ge deposited at different T_s, it was observed that under isothermal annealing condition samples prepared at lower T_s took longer time to complete crystallization. This may indicate that the absorption of residue oxygen from the high vaccum chamber during film growth process was more serious at low T_s. Also, lower T_s samples tended to have higher final resistivities after complete crystallization. Although a conclusive result concerning the final grain size for completely crystallized germanium films deposited at different T_s could not be obtained, a preferred crystal orientation in <111> was observed. This result was independent of substrate temperature and the annealing methods. Thus it seems that crystallization on an amorphous surface favours the FCC close packing form. Also, it has been observed that upon annealing, uniform strains within the a-Ge film was gradually released, as evident by the gradual shift of 2θ

position of (111) reflections towards the corresponding value of the bulk material. Moreover, the crystallization process as a function of annealing time was also followed closely by X-ray diffraction experiments. The crystallization kinetics can be described by a nucleation and growth process and a negative value of incubation time was obtained. This led one to suspect that nuclei for crystallization were already present after film growth, and hence were probably formed during the film growth process. Finally, the isochronal annealing behaviour of a-Ge:H is different from that of a-Ge. Resistivity plotted against annealing temperature showed three peaks, which can be attributed to the evolution of hydrides of different forms with subsequent lattice reconstruction. The above argument was supported by the fact that the same number of peaks roughly at the same temperatures were observed from the gas evolution experiments reported on glow-discharge produced a-Ge:H.

B) Suggestions On Improvement And Further Development Of The Present System:

One of the severe drawbacks of the present system is the low deposition rate (0.5 Å/s). Such a low value is a result of two reasons: 1) The deposition rate can be increased by increasing the emission current of the electron beam source. In our system, if the emission current is larger than 0.12 A, serious spitting of silicon out of silicon melt occurs. This limits our coating rate attainable. 2) The hydrogen beam current of our gun cannot be varied at will. An increase in deposition rate implies an increase of silicon to hydrogen atoms ratio at the substrate if the hydrogen beam current is fixed. This in turn results in less hydrogen incorporated into the film leading to a decline of film quality. To circumvent the above situations, a better electron beam sweeping unit may be helpful and an atom gun with larger beam current density should be employed. 3) Our atom gun produces hydrogen atom at 5-6 kV energy range. These hydrogen atoms may be too energetic and can create surface defects in the resultant sample during the growth process. So it will be better to use an

atom gun producing lower energy atoms.

Besides producing hydride films, our new method can also be used to make other kinds of films. One example is amorphous silicon nitride. Amorphous silicon nitride (a-SiN_x) films are widely used in micro-electronics and in high temperature applications. One of the characteristics of a-SiN_x films is that their band gap can be tailored by using different nitrogen concentration (J. Kojnok et al., 1992). This can be easily achieved by our method. So there is good reason to study this material by our method in details.

Reference

Adler David, Physical Review Letter, 41, (1978), 1755-1758.

Anderson J.C., Biswas S., and Guo H.J., J. Appl. Phys., 61, (1987), 604-612.

Anderson P.W., Phys. Rev., 109, (1985), 1492.

Brodsky M.H., Cardona M. and Cuomo J.J., Phy. Rev. B, 16, (1977), 3556.

Brodsky M.H. and Title R.S., Physical Review Letters, 23, (1969), 581-585.

Chan P.H., MPhil. Thesis, The Chinese University of Hong Kong, (1988).

Chik K.P., Feng S.Y. and Poon S.K., Solid State Comm., 33, (1980), 1019-1023.

Chik K.P. and Fung S.H., Journal Of Non-crystalline Solids, 24, (1977). 431-435.

Chik K.P. and Lim P.K., Thin Solid Films, 35, (1976), 45-46.

Christian J.W., The Theory Of Transformations In Metal And Alloys, Part 1: Equilibrium And General Kinetic Theory, Pergamon Press, (1975).

Cody G.D., Tiedje T., Abeles B., Brooks B. and Goldstein Y., Physical Review Letters, 47, (1981), 1480-1483.

Cullity B.D., Elements Of X-ray Diffraction, Addison-Wesley Publishing Co, Inc., (1959).

Curtins H. and Favre M., Amorphous Silicon And Related Materials, edited by Fritzche H., World Scientific Publishing Company, (1988).

Demichelis F., Minetti-Mezzetti E., Tazliaferro A. and Tresso, Physical Review B, 33, (1986), 7022-7028.

Dersch H., Schweitzer L. and Stuke J., Physocal Review B, 28, (1983), 4678-4684.

Dersch H., Stuke J. and Beichler J., Phys. Stat. Sol. (b), 107, (1981), 307-317.

Edelman F. and Komen Y., J. Appl. Phys., 72, (1992), 5153-5157.

Elliott S.R., Physics Of Amorphous Materials, 1st edition, Longman Group Limited, (1983).

Eray A. and Tolunay H., Doga Turkish Journal Of Physics, 14, (1990), 222-232.

Guha S. and Hack M., J. Appl. Phys., 58, (1985), 1683-1685.

Jackson W.B., Amer N.M., Boccara A.C. and Fournier D., Applied Optics, 20, (1981), 1333

Jackson W.B., Kelso S.M., Tsai C.C., Allen J.W. and Oh S.-J., The American Physical Society, 31, (1985), 5187.

John P.K., Wong S.K., Gogna P.K., Tong B.Y. and Chik K.P., Journal De Physique C4, 41, (1981), 639-642.

Knights J.C., AIP Conf. Proc., 31, (1976), 296.

Knights J.C., Lucovsky G. and Nemanich R.J., Philos. Mag. B, 37, (1978), 467-475.

Kocka Jan, Journal Of Non-crystalline Solids, 90, (1987), 91-98.

Kojnok J., Gyarmati E., Nickel H. and Szasz A., Journal Of Non-crystalline Solids, 55, (1993), 155-164.

Lucovsky G., Journal Of Non-crystalline Solids, 141, (1992), 241-256.

Lucovsky G., Davidson B.N., Parsons G.N., Wang C., Journal Of Non-crystalline Solids, 114, (1989), 154-156.

Madan Arun and Shaw M.P., The Physics of Applications Of Amorphous Semiconductors, Acadamic Press Inc., (1988).

Morigaki Kazuo, Journal Of Non-crystalline Solids, 141, (1992), 166-175.

Mott N.F. and Davis E.A., Electronic Process In Non-crystalline Materials, 2nd edition, Clarendon Press Oxford, (1979).

Nagels P., Amorphous Semiconductors, Springer-Verlag Berlin Heidelberg, (1979).

Pang Da-Wen, Cui Shu-Fan, Mei Zhen-Hong, Chen Joseph M., J. Appl. Phys., 61, (1987), 1168-1171.

Parker M.A., Conrad K.A. and Schiff E.A., MRS Proc., 70, (1986), 125.

Paul W., Solid State Comm., 34, (1980), 283.

Paul W., Jones S.J. and Turner W.A., Philosophical Magazine B, 63, (1991), 247-268.

Payson J.S. and Guha S., Physical Review B, 32, (1985), 1326.

Ranganathan Radha and Taylor P.C., Journal Of Non-crystalline Solids, 97 & 98, (1987), 707-710.

Ristein J., Hautala J. and Taylor P.C., Journal Of Non-crystalline Solids, 114, (1989), 444-446.

Roozeboom Fred, Parekh N., J. Vac. Sci. Technol. B, 8, (1990), 1249-1259.

Schumm G. Abel C.-D. and Bauer G.H., Journal Of Non-crystalline Solids, 137 & 138, (1991), 351-354.

Shanks H., Fang C.J., Ley L, Cardona M., Demond F.J. and Kalbitzer S., Phys. Status Solidi, 100, (1980), 43.

Shimizu Tatsuo, Kidoh Hideo and Morimoto Akiharu, Japanese Journal of Applied Physics, 28, (1989), 586-592.

Skoog D.A. and Leary J.J., Principle Of Instrumental Analysis, 4th edition, Saunders College Publishing, (1992).

Staebler D.L. and Wronski C.R., J. Appl. Phys., 51, (1980), 3262-3268.

Street R.A., Philosophical Magazine B, 46, (1982), 273-278.

Tang C.Y., MPhil. Thesis, The Chinese University of Hong Kong, (1991).

Triska A., Dehnison D. and Fritzche H., Bull. Am. Phys. Soc., 20, (1975), 392.

Vaid B.A., Sharma K.C. and Sharma D.R., Physics Letters, 102A, (1983), 373.

Veprek S., Sarott F.-A. and Ruckschlos. Journal Of Non-crystalline Solids, 137 & 138, (1991), 733-736.

Wronski C.R., Abeles B., Tiedje T., Cody G.D., Solid State Comm., 44, (1982), 1428.

Wu Y. and Stesmans A., Journal Of Non-crystalline Solids, 90, (1987), 151-154.

Wu Y. and Stesmans A., Physical Review B, 33, (1985), 5046-5049.

Wyrsch N., Finger F., Mc Mahon T.J., Vanecek M., Journal Of Non-crystalline Solids, 137 & 138, (1991), 347-350.

Yamada I., Nagai I., Morie M. and Takagi T., J. Appl. Phys., 54, (1983), 1583-1587.

Zanzucchi P.J., Wronski C.R. and Carlson D.E., J. Appl. Phys., 48, (1977), 5227-5236.